

Lehrstuhl für Steuerungs- und Regelungstechnik
Technische Universität München
Univ.-Prof. Dr.-Ing./Univ. Tokio Martin Buss

Design, Control, and Evaluation of a Family of Kinesthetic Haptic Interfaces

Marc-Walter Ueberle

Vollständiger Abdruck der von der Fakultät für Elektrotechnik und Informationstechnik
der Technischen Universität München zur Erlangung des akademischen Grades eines

Doktor-Ingenieurs (Dr.-Ing.)

genehmigten Dissertation.

Vorsitzender: Univ.-Prof. Dr.-Ing. Fernando Puente León

Prüfer der Dissertation:

1. Univ.-Prof. Dr.-Ing./Univ. Tokio Martin Buss
2. Hon.-Prof. Dr.-Ing. Gerd Hirzinger

Die Dissertation wurde am 15.05.2006 bei der Technischen Universität München eingereicht und durch die Fakultät für Elektrotechnik und Informationstechnik am 28.09.2006 angenommen.

Foreword

This thesis is a result of five years of work in the group of my thesis advisor Prof. Martin Buss. The main part has been accomplished between 2001 and 2005 at the Control Systems Group, Technische Universität Berlin. It has been concluded at the Institute of Automatic Control Engineering, Technische Universität München where I found a good working environment to write down the results of my research.

First of all, I would like to thank my doctoral advisor Prof. Martin Buss for his advice, guidance, and encouragement. He provided me with a perfect research environment and any hardware I needed to put my research ideas into practice.

The realization of the VISHARD devices would not be possible without the support of Mr. Franz Bachmann (TU Berlin). Many thanks for the lengthy discussions greatly helped to improve the design, for making the technical drawings, and for crafting the mechanical parts.

I am also indebted to my colleagues Dr. Dirk Wollherr, Michael Fritschi, and Jan Wolff who helped me to solve many difficulties related to computer hard- and software and encouraged me as friends. To all my students, Martin Ernst, Nico Mock, Daniel Rimmelpacher, Alessandro Bovo, and Chang-Hae Kim, I thank you very much for the extraordinary efforts you took.

In deep gratitude I want to thank my parents, Walter and Christel, my sister Barbara, and my wife Imke for their constant support, encouragement, and words of confidence. Imke completed my life with all the necessary diversions.

Munich, 2006.

Marc Ueberle

to my family

...

Design, Control, and Evaluation of a Family of Kinesthetic Haptic Interfaces

This thesis provides guidelines for the development, control, and evaluation of kinesthetic haptic interfaces with focus on designs offering large workspaces and high force capability. It presents the mechatronic design of a new family of general purpose haptic devices strongly influenced by considerations of versatility and extensibility. The main innovation is the consideration of multiple redundant actuated joints in the kinematical design of haptic interfaces. Among the motivations for kinematical redundancies is the avoidance of interior singularities to increase the workspace while reducing the overall device size. This includes the elimination of wrist singularities resulting in an orientation workspace of 360° around each axis. The control design of the device family employs impedance and admittance control algorithms of varying complexity. The impedance control implementations use an adaptive model-based friction compensation scheme accounting for the nonlinearity and time variability of the viscous and torque dependent sliding friction of the joint components. The compensation of static friction is accomplished with a variable structure force control law. For the control of the hyper-redundant haptic interface developed in this work inverse kinematics solution algorithms based on pseudoinverse control and the inverse function approach are proposed and their applicability for human haptic interaction is explored. Hardware experiments including comparative studies for the performance evaluation of haptic control schemes validate the usability and effectiveness of the design and control concepts elaborated in this thesis.

Design, Regelung und Bewertung einer Familie von haptischen Eingabegeräten

Diese Dissertation bildet einen Leitfaden zu der Entwicklung, Regelung und Bewertung von kinästhetischen haptischen Displays mit Fokus auf Systeme mit einem Darstellungsvermögen von hohen Kräften in großen Arbeitsräumen. Sie stellt das mechatronische Design einer neuartigen Familie von universellen haptischen Eingabegeräten vor, welches von der Zielsetzung nach Einsatzflexibilität und Erweiterbarkeit geprägt ist. Eine besondere Innovation ist die Verwendung von mehreren redundanten Gelenken in der Kinematik von haptischen Displays. Ein möglicher Vorteil ist dabei die Vermeidung von inneren Singularitäten, was eine Vergrößerung des Arbeitsraums bei gleichzeitiger Reduktion der Baugröße ermöglicht. Darüber hinaus können singuläre Handgelenkskonfigurationen umgangen werden, woraus sich ein rotatorischer Arbeitsraum von 360° um jede Achse ergibt. Die Regelung der entwickelten Geräte basiert auf Impedanz- und Admittanzregelungsarchitekturen verschiedener Komplexitätsgrade. Die Impedanzregelungen verwenden eine adaptive modellbasierte Reibungskompensation, die die Nichtlinearität und Zeitvarianz der viskosen und lastabhängigen Gelenkreibung berücksichtigt. Die Kompensation der statischen Reibung wird mittels eines strukturvariablen Kraftregelgesetzes erreicht. Für die Regelung des in dieser Arbeit entwickelten hyper-redundanten haptischen Displays werden Lösungsalgorithmen für die inverse Kinematik basierend auf inversen Funktionen und Verfahren mit der Pseudoinversen erarbeitet und deren Eignung zur haptischen Mensch-Maschine-Interaktion untersucht. Hardware-Experimente, unter anderen Vergleichsstudien zur Leistungsbewertung verschiedener haptischer Regelungsstrategien, validieren die Verwendbarkeit und Leistungsfähigkeit der in dieser Dissertation ausgearbeiteten Design- und Regelungskonzepte.

Contents

1	Introduction	1
1.1	State of the Art in Kinesthetic Haptic Interface Design	2
1.2	Main Contributions and Outline of Thesis	4
2	Hardware Design	7
2.1	Requirements	7
2.2	Kinematical Design	11
2.3	Actuator Technology	13
2.4	Force/Motion Transmission Techniques	15
2.5	Design of the ViSHARD Haptic Interfaces	17
2.5.1	Design Rationale	17
2.5.2	ViSHARD3 Design	19
2.5.3	Design of ViSHARD6	20
2.5.4	ViSHARD10 Design	21
2.6	Summary	25
3	Control Aspects	27
3.1	Classification of Control Schemes	28
3.1.1	Classification of Robot Control Algorithms	28
3.1.2	Classification of Haptic Control Schemes	31
3.1.3	Haptic Control versus Industrial Force Control Tasks	32
3.2	Haptic Control Architectures	32
3.2.1	Impedance Display Mode	33
3.2.2	Admittance Display Mode	34
3.3	Stability Aspects	37
3.4	Control of Haptic Interfaces with Kinematical Redundancies	39
3.4.1	Pseudoinverse Control	40
3.4.2	Inverse Function	45
3.5	Control of the ViSHARD Haptic Interfaces	46
3.5.1	General Control Schemes	46
3.5.2	Virtual Model	47
3.5.3	Inverse Kinematics of ViSHARD10	49
3.6	Summary	60
4	Friction Modeling and Compensation	62
4.1	General Friction Phenomena and Modeling Approaches	63
4.1.1	Classical Friction Models	63
4.1.2	Pre-sliding Hysteresis and Dynamic Friction Effects	65
4.1.3	Advanced Friction Models	67
4.1.4	Stick-Slip and Hunting Oscillations	69

4.1.5	Other Friction Effects	70
4.2	Modeling Harmonic Drive Friction	71
4.2.1	The Principles of Harmonic Drive Operation	71
4.2.2	Transmission Characteristics and Modeling Approaches	72
4.3	Friction Compensation Techniques	74
4.3.1	Joint Torque Feedback	74
4.3.2	Model-based Friction Compensation	76
4.3.3	Dither	78
4.3.4	Disturbance Observer	78
4.4	Friction Model and Compensation Scheme of the ViSHARD3 Device . . .	80
4.4.1	Friction Identification	80
4.4.2	Friction Model	90
4.4.3	Compensation of Static Friction	92
4.4.4	Adaptive Compensation of Sliding Friction	95
4.5	Summary	104
5	Performance Evaluation	106
5.1	Performance Measures	108
5.1.1	Hardware Features	108
5.1.2	Closed Loop Performances	110
5.1.3	Comments	113
5.2	Determination of Performance Indices	114
5.3	Performances of the ViSHARD Devices	115
5.3.1	Output Capability	115
5.3.2	Backdrivability	118
5.3.3	Dynamic Force Precision	127
5.4	Summary	131
6	Conclusions and Future Work	133
6.1	Concluding Remarks	133
6.2	Future work	136
A	Technical Hardware Details	138
A.1	Specifications of Sensors and Joint Components	138
A.1.1	ViSHARD3	138
A.1.2	ViSHARD6	139
A.1.3	ViSHARD10	140
A.1.4	Linear Guide	141
A.2	Dynamic Device Models	142
A.2.1	ViSHARD3	142
A.2.2	ViSHARD6	143
A.2.3	ViSHARD10	147
B	Tracking Performance of Operational Space Position Control Algorithms	154
C	Output Performance Analysis	158

Bibliography

160

Notations

Abbreviations

4R	4 revolute joints
DOF	degrees of freedom
IJC	inverse Jacobian control
IMP	impedance control
JND	just noticeable difference
LF	low pass filter
MR	magneto resistive
PWM	pulse width modulation
RAC	resolved acceleration control
RMS	root mean square
SCARA	selective compliance assembly robot arm
TJC	transposed Jacobian control
VE	virtual environment

Conventions

Scalars, Vectors, and Matrices

Scalars are denoted by upper and lower case letters in italic type. *Vectors* are denoted by upper and lower case letters in boldface type, as the vector \mathbf{x} is composed of elements x_i . *Matrices* are denoted by upper case letters in boldface type, as the matrix \mathbf{M} is composed of elements M_{ij} (i -th row, j -th column).

x	scalar
\mathbf{x}	vector
\mathbf{X}	matrix
$f(\cdot)$	scalar function
$\mathbf{f}(\cdot)$	vector function
$\dot{\mathbf{x}}, \ddot{\mathbf{x}}$	equivalent to $\frac{d}{dt}\mathbf{x}$ and $\frac{d^2}{dt^2}\mathbf{x}$
\mathbf{X}^T	transposed of matrix \mathbf{X}
\mathbf{X}^{-1}	inverse of matrix \mathbf{X}
$\mathbf{X}^\#$	pseudoinverse of matrix \mathbf{X}
\mathbf{X}^*	singularity robust inverse of matrix \mathbf{X}

Subscripts and Superscripts

$\underline{\mathbf{G}}(s)$	linearized dynamic equations \mathbf{G} mapped into the Laplace domain
$\frac{B}{A}\mathbf{R}$	mapping from coordinate system $\{A\}$ to $\{B\}$
\bar{x}	mean of x
x_B	respective the base coordinate system
x_d	desired value of x
x_E	respective the end-effector coordinate system
$\mathbf{x}_l, \mathbf{x}_s$	vector or dynamic equations referring to load or servo side
x_m	measured value of x
x_{\max}	maximum value of x
x_{\min}	minimum value of x
x_x, x_y, x_z	component of vector \mathbf{x} in x -, y -, z -direction
${}^j\mathbf{Z}$	joint space representation of dynamic equations \mathbf{Z}

Symbols and Abbreviations

A	oscillation amplitude
a_{0-2}	coefficients of polynomial describing load dependent friction
α, β, γ	angle of pitch, yaw, roll
C_i	i -th normalized criterion value
\mathbf{C}	matrix of gyroscopic related terms
$D_{\text{rms}}^{\%}$	measure for signal distortion
δ	empirical parameter of Stribeck effect model
$\Delta\mathbf{q}$	quantization of joint angle measurement
$\Delta\mathbf{x}$	position error
$\mathbf{f}, \hat{\mathbf{f}}$	actual, estimated interaction force
$\mathbf{f}(\mathbf{q}, \mathbf{x})$	kinematical constraint functions
f_c	Coulomb friction parameter
F_c, T_c	Coulomb friction force, torque
f_{dist}	disturbance force
f_e	external force
\mathbf{f}_{err}	force error
f_{load}	load dependent friction parameter
f_n	normal force
f_s, τ_s	break-away force, torque
F_{stat}	static friction
F_{Strb}	Stribeck friction
f_u	control input force
f_v	linear viscous friction parameter
f_{visc}	nonlinear viscous friction parameter
F_{visc}	viscous friction
g	cost function
\mathbf{g}	gravitational torques
\mathbf{G}_c	force control law
\mathbf{h}	friction torques

$\mathbf{h}(\boldsymbol{\xi}, \mathbf{x})$	decoding of SCARA segment joint configurations
H	side criterion
\mathbf{I}	identity matrix
\mathbf{J}	Jacobian matrix
J_{mot}	motor inertia
$\mathbf{J}_{\text{rot}}, \mathbf{J}_{xy}$	Jacobian of VISHARD10 wrist, SCARA segment
J_{wav}	wave generator inertia
$\mathbf{J}^{W^{-\frac{1}{2}}}$	weighted Jacobian
$\mathbf{J}^{W\#}$	weighted pseudoinverse of the Jacobian
$\mathbf{J}^{M_q\#}$	inertia weighted pseudoinverse of the Jacobian
$\mathbf{K}_{D,\text{trans}}, \mathbf{K}_{D,\text{rot}}$	virtual translational, rotational damping matrix
$\mathbf{K}_P, \mathbf{K}_D, \mathbf{K}_I$	proportional, derivative, integral controller gain matrices
k_P	proportional gain
κ	gain of null space motion
L	workspace radius
l_i	length of i -th link
λ	weighting factor
\mathbf{M}_{load}	load side joint inertia matrix
$\mathbf{M}_q, \widehat{\mathbf{M}}_q$	joint inertia matrix, approximation
$\mathbf{M}_{\text{trans}}, \mathbf{M}_{\text{rot}}$	virtual mass, inertia matrix
$\mathbf{M}_x, \widehat{\mathbf{M}}_x$	task space mass/inertia matrix, approximation
μ_c	kinetic friction coefficient
μ_s	static friction coefficient
n	number of samples
N	gear ratio
ω	position control bandwidth
ω_0	resonance frequency
$\boldsymbol{\omega}$	end-effector angular velocity
p_{0-4}	coefficients of polynomial describing sliding friction
$\boldsymbol{\phi}$	Euler angles
φ	phase shift
$\boldsymbol{\varphi}$	concatenation of neighbored joint configuration deviations
ψ	composite performance index
q_5^*, q_8^*	absolute angle of VISHARD10 joint 5, 8
q_i	angle of i -th joint
q_{mot}	motor angle
$\mathbf{q}_{\text{rot}}, \mathbf{q}_{xy}$	joint angles of VISHARD10 wrist and SCARA segment
$\dot{\mathbf{q}}_{W^{\frac{1}{2}}}$	weighted joint velocities
\mathbf{R}	rotation matrix
σ_i	i -th singular value
$\boldsymbol{\Sigma}$	component of singular value decomposition
t	time
t_{sw}	switching time
T	temperature
T_{load}	load dependent friction torque
$\boldsymbol{\tau}$	actuation torques

τ_0	initial value of force control integral output
$\boldsymbol{\tau}_{fb}$	output of model-based compensator
$\boldsymbol{\tau}_{in}$	joint torque input
τ_{load}	dynamic load torque
τ_{load}^0	static load torque
$\boldsymbol{\tau}_{out}$	joint torque output
T_{pos}	position dependent friction torque
\boldsymbol{u}	control signal
\boldsymbol{U}	component of singular value decomposition
v	sliding velocity
\boldsymbol{V}	component of singular value decomposition
v_s	Stribeck velocity
w	manipulability index
\boldsymbol{W}	weighting matrix
w_i	i -th weighting factor
x, y, z	end-effector position coordinates
$\ddot{\boldsymbol{x}}_c$	commanded end-effector acceleration
\boldsymbol{x}	end-effector position/orientation
$\boldsymbol{\xi}_i$	coded description of SCARA segment configuration
$\boldsymbol{Z}_d, \boldsymbol{Z}_d^{-1}$	desired impedance, admittance
$\boldsymbol{Z}_{dr}, \boldsymbol{Z}_{dr}^{-1}$	nominal robot impedance, admittance
\boldsymbol{Z}_{EE}	end-effector impedance
$\widehat{\boldsymbol{Z}}_{EE}$	impedance of model-based compensator of end-effector dynamics
$\widehat{\boldsymbol{Z}}_r$	impedance of model-based compensator of robot dynamics
\boldsymbol{Z}_r^{-1}	robot admittance
\boldsymbol{Z}_{rCL}	closed loop impedance
ζ	position control damping ratio

1 Introduction

Virtual reality and telepresence systems offer humans the possibility to interactively explore and manipulate artificial and remote environments. Such systems are most well known to the broad public in the form of video game consoles. These allow users to step into virtual worlds and to experience scenarios where they can do things impossible in reality. In telepresence systems a teleoperator (some robotic system) is controlled at a distance by the human operator through a human-system interface. Due to the human ability to react to unknown and difficult situations these systems are well suited for tasks in unstructured environments. Typical examples are space robotics (Mars Pathfinder mission) or telemanipulator systems for minimally invasive surgery (da Vinci, Zeus). The difference to virtual reality systems is that the feedback to provide to the operator is not calculated by a computer simulation but is measured by the sensors of the remote teleoperator.

As far as the visual and auditory feedback is concerned virtual reality and telepresence systems achieved a high degree of realism as a result of the rapid increase of computational power as well as the availability of low cost but qualified visual displays and sound systems. In the last decade the additional use of haptic feedback in these systems has become increasingly popular allowing the operator to touch virtual or remote objects. The inclusion is motivated by the observation that the majority of interaction tasks of humans with their environment involve haptic sensations comprising the tactile, kinesthetic, and temperature modality. Through the sense of touch we derive object properties such as texture, small shapes, softness, roughness, slip, and vibration. With our kinesthetic sense, which refers to the awareness of our body posture, motion, and the forces supplied by the muscles, we explore object cues as for instance large shapes, weight, inertia, and stiffness. Haptic feedback is therefore believed to be crucial when performing tasks involving active exploration or manipulation of objects [She92, Cut93]. It can result in a more intuitive and dexterous interaction with the virtual or remote environment increasing the task performance by means of completion time and error rate [FBLG96, PPBD06]. The ability to physically interact with objects drastically increases the realism and immersivity of the simulation.

The hardware providing controlled tactile stimuli, kinesthetic sensations, or a combination of both kinds of feedback are called haptic interfaces. Their application potential seems to be enormous. An eminent task domain is virtual prototyping. In the automobile industry physical mock-ups constructed for the evaluation of product designs are increasingly often replaced by digital computer models to lower cost and shorten iteration loops [GZ88]. An intuitive and immersive exploration of these digital mock-ups can be done with virtual reality systems including haptic feedback [HCT⁺]. Other application domains include telesurgery [RHMS99], medical and surgical virtual reality training systems [KcC⁺04], tele- and micromanipulation [GCH⁺01], telemaintenance, scientific visualization [BOYBK90], education [DLR94, ROC97], and entertainment. An application area not related to virtual reality and telepresence is human assistance where force feedback is used to guide or support the operator. Human assistive devices are for example used

for rehabilitation purposes [GBB99] or the extension of the human force capability. An overview on application areas of haptic devices is provided in a recent article of Hayward *et al.* [HACH⁺04].

From a research point of view the field of haptics left its infancy during the last decade. A highly illustrative evidence of this fact is provided by a statement given by Vincent Hayward, one of the leading researchers in the area of haptics:

Ten years ago, I knew of everybody on the planet [in haptics] and now it's become a mainstream research topic. Every big school has a haptics lab. Every big company is doing something.

Hayward, 2002 [Aki02]

This statement is supported by the high increase of the number of related publications as well as the emergence of conferences specialized on haptics research such as the “Haptics Symposium” or the “Eurohaptics”. The growing interest in haptic systems has given rise to the initiation of large research projects worldwide; major European projects include TOUCH-HapSys¹, IMMERSENCE², and the Collaborative Research Centre (SFB) 453 of the German Research Foundation (DFG)³. The most prominent research directions are psychophysics (the study of human haptic perception), haptic rendering of virtual environments, the development and exploration of applications, haptic control design (in particular for telepresence systems), and the development of tactile and kinesthetic haptic hardware. The focus of this thesis is on the design, control, and evaluation of haptic hardware providing kinesthetic force feedback to the human hand. This excludes locomotion and full body feedback interfaces reviewed by Hollerbach [Hol02], devices providing feedback to the operator’s fingers, see [BBPB02, TGTC98, ABFB00] as well as tactile interfaces [JS02, Kam03]. In the following, a brief review on current kinesthetic haptic hardware is given.

1.1 State of the Art in Kinesthetic Haptic Interface Design

Significant research effort has been devoted to the development of kinesthetic feedback devices characterized by a high degree of specialization for certain task domains, in particular medical applications. This includes for instance the Laparoscopic Impulse Engine (Immersion) and the VEST-system VSOOne (Select-IT VEST Systems AG) [KcC⁺04] with kinematical designs and output capability matching exactly the requirements of minimally invasive surgical simulation. This approach aims at the maximization of the device performance for the intended application but, in turn, narrows the range of task domains it can be used for.

The most wide class of haptic interfaces that achieved a highly convenient development status are passive designs providing kinesthetic feedback in small workspaces at moderate force levels. These devices are characterized by highly lightweight mechanical designs requiring no active force feedback control to provide a good backdrivability. The lack of

¹<http://www.touch-hapsys.org>

²<http://www.immersence.info>

³<http://www.sfb453.de/>

force sensing capability greatly reduces the complexity of the control design and the hardware cost. The low mass, size, and force capacity is beneficial in terms of safety aspects and human-friendliness. The commercially most successful passive devices are interfaces used for video games as for instance force reflecting joysticks and steering wheels. Other low-cost haptic devices include force feedback mice. For general tool based applications the PHANTOM devices (SensAble Technologies) developed at MIT [MS94] are the most widely used. They are available in a variety of sizes and 3 or 6 actuated degrees of freedom (*DOF*) and allow interactions through a finger sled or a stylus. Offering low dynamic properties they are able to render free-space in a high-quality. Another passive design with disturbance forces very close to the human perceptual threshold is the Freedom 6S (MPB Technologies), the commercial version of Freedom 7, see [HGG⁺98]. One of the disadvantages of these passive design approaches are a comparatively limited control stiffness due to the low physical damping present in the joints.

As these purely passive devices do not provide force measurement capability they cannot be used for applications that fundamentally require the render of admittances where motion is a response to force input and not vice versa. An example for such an application is a bone drilling training scenario where the surgeon should learn to apply a dedicated constant force to the drill [EYB04]. Interfaces with mildly increased dynamic properties compared to common passive designs but additional force sensing are for instance the commercially available DELTA Haptic Device (FORCE dimension) described in [GCR⁺01] and the VIRTUOSE 6D (Haption). Both provide force feedback in 6 DOF with increased (but still moderate) force capability compared to the 6 DOF PHANTOM devices.

A common deficiency of the majority of currently available haptic devices is their comparatively small workspace and low force capability forbidding for example large ergonomic studies, the display of stiff immovable walls during assembly and disassembly simulations, or the accommodation of heavy end-effectors (e.g. exoskeleton devices providing kinesthetic feedback to the operator's hand or tactile interfaces). One of the reasons is that the design rationale to have low dynamic properties is contrary to other requirements as versatility or large workspace.

For haptic realization of tasks requiring a large workspace and high force capability often off-the-shelf industrial robots are used [CLTM97, HRS02]. These robots are, however, not optimized for interactions with humans; the force capability exceeds by far the strength of a human and the mechanical stiffness is much larger than required for haptic applications. Consequently, these devices show major deficiencies regarding dynamic properties and safety aspects. Interfaces with human matched force capability and workspace, that are devices filling the gap between passive designs and industrial robots, are uncommon and rarely available. Two of the very few examples are the Excalibur device [AMH99] with very high peak stiffness and the *HapticMASTER* (FCS Control Systems) described in [VLFR] showing good performance regarding deceleration capability. Both provide 100 N continuous force in 3 DOF but in a rather limited workspace.

Another approach to provide a large workspace combined with high force are exoskeleton constructions with jointed linkages fixed to the operator. Such interfaces have the additional advantage that they can be used to provide force feedback to constrain the self-motion of a human arm which can for instance be advantageous at assembly/disassembly studies. The workspace is exceptionally high in case of wearable devices as for example the L-EXOS device described by Frisoli *et al.* [FRM⁺05] or the passive masterarm applying electric brakes as actuators presented by Kim *et al.* [KLLK05]. Portable interfaces have,

however, the disadvantage that their weight has to be supported by the operator strongly tightening the requirement for a lightweight design. Furthermore, because wearable haptic interfaces are not grounded to the environment, the net force exerted by the device to the operator equals zero. As a consequence, external forces cannot be rendered adequately. Exoskeletons grounded to the environment, as for instance the SARCOS dexterous master [JSBI91], do not show this deficiency but, in turn, limit the mobility of the operator. For example arm exoskeletons with shoulder joint attached to the environment requires the operator's shoulder to remain at a fixed position. A general drawback of both grounded and portable exoskeleton devices is, that they tend to be quite complex and encumbering. The fact that they are firmly attached to the operator is highly disadvantageous in terms of ergonomics and safety aspects. Another line of research targets at an unlimited workspace by mounting haptic devices on a movable platform [Nit06]. Compared to portable exoskeletons this approach has the advantage that the device weight has not to be supported by the operator. At the downside, this solution drastically increases system complexity. Moreover, the render of high stiffness is challenging due to the typically more compliant coupling of the system to the environment.

1.2 Main Contributions and Outline of Thesis

The work presented in this thesis summarizes design, control, and performance evaluation aspects of kinesthetic haptic hardware for the human interaction with virtual environments as well as the mechatronic design of a new family of haptic interfaces. Contrary to the majority of related work reported in the literature the focus is here not on passive designs but force feedback controlled interfaces with comparatively large workspace and human matched force capability. Workspace enlargement is in fact a considerable challenge in haptic device design as the unavoidable increase in hardware size typically entails a drastic impairment of the dynamic device properties. The preservation of a good closed loop performance therefore requires force feedback control increasing the complexity of the control design as well as the performance evaluation. In the following, a guide through this thesis summarizing the main contributions is given.

Haptic Interface Design

In chapter 2 hardware related aspects of haptic systems are reviewed along with a description of the ViSHARD⁴ kinesthetic feedback devices designed and built by the author. The main innovation is the suggestion of kinematical designs with actuated redundant joints for the increase of the device performance. The additional degrees of freedom can be used to circumvent singular configurations resulting in a significantly larger workspace while reducing the overall device size. Furthermore, kinematical redundancies increase the versatility of haptic interfaces because they offer the possibility to accommodate task specific requirements by dedicated control of the device selfmotion.

The analysis of hardware concepts strongly influenced the hardware design of the ViSHARD family - ViSHARD3, ViSHARD6, ViSHARD10 - of highly versatile, general purpose kinesthetic feedback devices with 3, 6, and 10 actuated DOF. The ViSHARD10 prototype successfully introduces the concept of kinematical redundancies. Among the

⁴Virtual Scenario Haptic Rendering Device

benefits is the unlimited rotational workspace free of singularities that cannot be achieved with nonredundant designs. The realization of a hyper-redundant kinesthetic haptic interface is considered novel.

Control Aspects

The design concept of the VISHARD devices targeted at high versatility in terms of workspace size, output capability, and extensibility necessitates the use of active force feedback control to compensate for the increased natural device dynamics. Aspects related to the control of haptic devices are discussed in chapter 3 and 4.

The focus of chapter 3 is the review and analysis of haptic control schemes with strong emphasis on the control of haptic interfaces with kinematical redundancies. The control of redundant devices requires the definition of a unique mapping of task space forces or motions to the corresponding quantities in the joint space. Two standard approaches for the solution of this inverse kinematics problem, pseudoinverse control and the definition of an inverse function, are discussed. For the VISHARD devices several distinct control schemes are implemented for the purpose of comparison. The proposed inverse kinematics solution approach for the VISHARD10 device is based on a decoupling of the translational from the rotational device motion. Pseudoinverse and inverse function solutions are presented and evaluated for the remaining two separate problems, the inverse kinematics of the positioning and orientation stage.

The discussion of the impedance control scheme given in chapter 3 highlights that friction induced force errors can only be compensated partially by force feedback action. Friction compensation techniques for an additional improvement of the haptic feedback accuracy are subject of chapter 4. It provides a review on friction phenomena and modeling approaches as well as friction compensation techniques for haptic interfaces operated in the impedance display mode. Hardware experiments with the VISHARD devices reveal a significant non-linearity of the load dependent and viscous friction characteristics of the joint components applying harmonic drive gears for speed reduction. Furthermore, a large change of the frictional behavior with time can be observed. In this chapter a novel model-based compensation scheme for the harmonic drive friction is suggested taking in account both, the nonlinearity and time variability of the friction properties. The latter is accomplished by parameter adaptation of the friction model. Contrary to common adaptation algorithms the parameters are not changed iteratively at each sampling instant but re-tuned after a specific number of samples. This technique is justified by the comparatively slow change of the friction behavior. For the compensation of stiction a variable structure force control scheme is proposed and evaluated by hardware experiments. Switching between PID and PD force control this algorithm aims at a good disturbance rejection for the joints at rest while maintaining a good dynamic behavior for moving joints.

Performance Evaluation

The systematic and objective comparison of haptic interfaces and haptic control algorithms requires the univocal definition of quantitative performance measures. Chapter 5 summarizes guidelines and physical performance indices for the evaluation of kinesthetic haptic devices highlighting implications of device nonlinearities and the presence of the human in the control loop. The latter strongly complicates the evaluation of devices applying force

feedback control because load characteristics provided by human operators are difficult to replicate in standardized hardware experiments.

Performance evaluation results for the VISHARD devices reported in this chapter are derived from model-based analysis techniques and hardware experiments. The worst case output capability in terms of the peak force, velocity, and acceleration capacity are calculated applying the algorithm outlined in appendix C. The hardware experiments focus on the comparative performance evaluation of VISHARD haptic control schemes in terms of backdrivability and force control frequency response. This includes a comparison of impedance with admittance control algorithms of varying complexity. In particular, the benefit of acceleration feedforward and feedback linearization in the motion control loop of admittance control implementations is investigated experimentally. In my opinion, the experimental results provide useful hands-on experience for the control design of other haptic interfaces.

2 Hardware Design

In the last decade a great number of kinesthetic haptic interfaces has been developed at educational and research institutions. A comparatively wide but far from complete overview on recent kinesthetic haptic devices is given by Martin and Savall [Mar05]. More detailed but less comprehensive comparisons of haptic hardware can be found in the reviews of Laycock and Day [LD03], Youngblut *et al.* [YJN⁺96], and Burdea [Bur96]). Although there seems to be a consensus in the literature on the requirements of haptic devices, see for instance [HCH97] and [LD03], the contrariness of these performance goals gives rise to a large number of distinct design approaches. The main differences refer to the kinematical design (e.g. parallel [BRB99], serial [PKAS⁺01], hybrid [GBB05]), actuation design (e.g. electric [MS94], hydraulic [JSBI91], pneumatic [TN99], magnetic [BH97], stringed [KBS03]), and control design (e.g. open loop impedance control [HGG⁺98], impedance control with force feedback [BAB⁺94], admittance control [VLFR]).

The main innovation of the following discussion on haptic hardware design approaches, compared other guidelines given in the literature (see e.g. [HCH97] and [Bur96]), is the consideration of actuated kinematical redundancies for an increase of the device performance. The hardware design concept of the ViSHARD kinesthetic feedback devices - ViSHARD3, ViSHARD6, ViSHARD10 - presented in this chapter differs from the vast majority of approaches in that the focus is on versatility and extensibility allowing high force tasks in large operating volumes. The goal of the versatility is to provide a benchmarking testbed for the rapid and cost-effective development and evaluation of novel haptic applications.

The organization of this chapter is as follows: Section 2.1 discusses performance requirements of haptic interfaces followed by a review of hardware aspects related to the kinematical, actuation, and motion transmission design in section 2.2, 2.3, and 2.4, respectively. Finally, section 2.5 describes the design rationale and system design of the ViSHARD device family.

2.1 Requirements

An ‘ideal’ haptic device provides for a large variety of haptic applications a completely transparent interface to the remote or virtual environment, meaning the user cannot detect any difference to the interaction with real objects. The transparency and versatility of haptic devices is affected by a number of design criteria characterizing its performance:

- *Backdrivability*: In unconstrained motion (e.g. free space simulations) no force generated by the natural device dynamics should be felt by the operator. A straightforward approach to increase the acceleration and velocity dependent backdrivability is to reduce the inertia and friction of the mechanical hardware, respectively. In case this is not possible due to other design considerations a further significant lowering of the dynamic properties can be achieved by closed loop control. This approach will be described in detail in Section 3. An unconventional technique to increase backdrivability is the introduction of elastic compliance in the mechanical design. Pratt

and Williamson [PW95] suggested the placement of a significantly compliant elastic torque sensor between the output of the actuator and the robot link in order to decouple the actuator inertia and friction from the link inertia. While at high frequent motion input of the operator the compliancy limits the open loop device impedance to the low stiffness of the elastic coupling and the link inertia, feedback control is applied to lower the output impedance at low frequent input. As pointed out by Robinson [Rob00] an attractive feature of this approach is that it allows rendering very low output impedance across the frequency spectrum even when actuators with poor backdrivability as for instance hydraulic systems are used. Because the sensor flexibility allows comparatively high controller gains an excellent disturbance rejection is achieved resulting in a very clean force output. For manipulators with considerable link inertia this concept can easily be adopted by using an elastic force sensor mounted at the device tip (see e. g. [RPH85]).

- *Stiffness*: The render of high impedances as for example large inertia or stiff virtual walls requires the device tip to move only little in response to the operator force input. In case of common haptic interface designs equipped with position sensors at the motor and not the load side the maximum achievable endpoint stiffness is limited by the mechanical rigidity and the stiffness of the achievable stable control. For the most widely used class of devices employing open loop haptic control schemes due to the lack of force sensing capability the factors affecting the control stiffness have been studied at length in the literature, see for example the work of Colgate and Brown [CB94] and Diolaiti *et al.* [DNB⁺05]. The control stiffness is enhanced by an increase of the physical damping, the sampling rate, the bandwidth of the actuators, the resolution of the position sensors, and by a reduction of computational delay. In particular raising the mechanical viscous friction has found to mitigate stability problems in high gear. Coulomb friction has also a stabilizing effect but can lead to an input dependent stability which is lost when the end-effector velocity exceeds a certain limit. Bounds on the control stiffness of interfaces with force sensing are less severe and therefore rarely studied in the haptics literature. This is due to the increased physical damping usually coming along with these designs and the stabilizing effect of active damping that can be incorporated in the force feedback control algorithm. As a result the maximum control stiffness is likely to exceed the mechanical stiffness by far. Combating mechanical elasticity is possible with active feedback control but requires direct or indirect measurement of the load position.
- *Bandwidth*: In case the operator interacts highly dynamically with the device it is important that backdrivability and stiffness can be provided at a large bandwidth. It is important to note that the bandwidth requirements for unconstrained motions and interactions with stiff environments differ substantially. The render of low impedances needs the control system to suppress disturbance forces due to the operator's motion input and the device natural dynamics. As a result the bandwidth of the disturbances typically corresponds to the bandwidth of the user input. Investigations on the maximum frequency of the operator input have only been little addressed in the literature. For the human fingers a force control bandwidth on the order of 20 to 30 Hz has been reported by Tan *et al.* [TSEC94]. In a review on telerobotic response requirements Brooks [Bro90] reports a bandwidth for the human

ability to control limb motions ranging from 5 Hz for intentionally generated motions and 10 Hz for reflex actions. This comparatively moderate bandwidth requirement for the control system does, however, not hold in case of significant imperfections of the actuation and transmission system. For instance torque ripple of motors and gears can produce high frequent disturbances especially at interactions involving fast motions. Contact situations raise the bar for bandwidth requirements drastically. Hitting a solid wall results in a very sharp force response. Accordingly, a realistic render of such interactions requires the interface force bandwidth to correspond to the bandwidth of the human's somatosensory system which is according to Tan *et al.* around 1 kHz (according to Sharpe [Sha88] the display of very fine surface textures requires even higher feedback frequencies in the range of 5 to 10 kHz). There does, however, exist evidence, that the human ability to discriminate between two force signals degrades at frequencies exceeding 320 Hz [Bro90]. In case of open loop controlled devices the bandwidth characteristics are purely determined by the mechanical design. As described earlier the increase of the backdrivability in the high frequency domain can be achieved by a reduction of the mechanical stiffness. The force bandwidth is, however, widened by lowering the inertia and elasticity as well as the elimination of backlash. In case of closed loop controlled designs the frequency response characteristics can be shaped actively. Leaving stability problems of the controller aside there are also fundamental physical limitations for improvements. In order to increase the backdrivability actively the device has to be able to follow the operator's input motion. Because no actuator has an unbounded torque capability there are limits on the acceleration capability. Thus, the maximum amplitude of a position trajectory the device can follow falls with the frequency due to acceleration saturation. Limits on the force bandwidth can be explained in an analogous way. Accounting for the elasticity present in all physical hardware the generation of force requires some elastic deformation of the device structure. As a result joint motion is needed to control the interaction force actively. Again, the amplitude of the force the device can render reduces with increasing frequency as an effect of acceleration and velocity saturation of the motors. To summarize: widening the bandwidth of the backdrivability and force response by active control is possible but requires an increased velocity and acceleration capability of the actuation. As the bandwidth requirement at contact situations is more stringent than at free space operations the maximization of the open loop force bandwidth is the common design guideline for both, open loop and closed loop controlled haptic interfaces. Needless to say that this does not hold for interfaces with application domains primarily including interactions with soft environments (e. g. soft tissue interaction in medical applications).

- *Output capability:* The device output capability by means of maximum force, velocity, and acceleration defines physical limits for the haptic interactions that can be rendered. Moreover, a low output capability is likely to reduce the robustness of closed loop control due to actuation saturation.
- *Workspace:* The decision for the number of the DOF and the size of the workspace mainly affects the range and variety of applications the interface can be applied for.
- *Extensibility:* Besides the workspace and the output capability the most influential factor for the versatility of the device is its extensibility. The addition of application

specific complex end-effectors (e.g. surgical tools or tactile stimulation actuators) requires sufficient mounting space and torque capability to compensate for the payload.

- *Safety and comfort*: Because haptic devices are in direct physical contact with humans a human friendly design is desired. As pointed out by Zinn *et al.* [ZKRS02] one of the most important safety issues is the avoidance of severe user injury in case of collisions with the device structure. This danger can only be partially mitigated by dedicated software and sensor architectures due to their potential malfunction. More reliable are intrinsically safe hardware designs possessing a high backdrivability in particular at medium to high frequencies. Another common and comparatively reliable procedure is the limitation of the joint velocities to constrain the kinetic device energy. To avoid the intrusion of the interface structure into the operator's workspace by a proper kinematical design one has to take into account varying end-effector grasps (e.g. left or right handed) and potential user movements. Factors adversely affecting the user's comfort are for example acoustic noise, significant intrusion of the device into the visual space, and bulky hardware. Furthermore, an ergonomic positioning of the end-effector should to be considered in the kinematical design to avoid fatigue during operation.

It is intuitively clear that these requirements are contrary and one has to balance amongst them. For example the enlargement of the workspace requires the device to be physically larger, usually entailing an increase in inertia as well as reduced stiffness and force bandwidth. Accordingly, it is increasingly difficult to satisfy the requirements for backdrivability, stiffness, and bandwidth with open loop control when the demands for workspace size and force capability are rising. Feedback control has indeed shown to be able to compensate for the high impedance of larger and more powerful devices but does not solve for safety concerns requiring intrinsically safe hardware.

Zinn *et al.* [ZKRS02] and Bicchi and Tonietti [BT04] pointed out that robots with high inertia require considerable structural elasticity to achieve inherent safety. In order to overcome resultant performance limitations in terms of force bandwidth Bicchi *et al.* suggest a dynamic variation of the mechanical device impedance by using torque transmission mechanisms with programmable stiffness. Zinn *et al.* propose the recover of force bandwidth performance by employing a redundant actuation scheme based on the parallel micro/macro actuator concept introduced by Morrell [Mor96]. In this approach the joint torque is provided by a large and a small actuator acting in parallel (i.e. their torque sums). Whereas the macro actuator is placed at the robot base and coupled to the joint via an elastic transmission mechanism the micro actuator is rigidly connected to the joint. As a result this mechanism combines passive compliance with high frequency torque capability. It has to be noted that the variable stiffness and micro/macro approach does not solely have the potential to increase performance under safety constraints but can also be applied in order to raise the range and accuracy of the impedances a haptic device can render. Indeed, this has been the original motivation of these approaches, see for example the work of Laurin-Kovitz *et al.* [LKCC91], Sharon *et al.* [SHH88], and Morrell [Mor96].

A problem with the design of interfaces applying active feedback control is the fact, that it is hard to give an a priori estimate on the achievable performance improvement. The reason is the high susceptibility of the force control robustness on higher order structural dynamics and nonlinearities inherent in robotic systems. Considerable effort has been put

in solving this problem by increasing the model complexity as for example described in the work of Eppinger [Epp88] and Elosegui [Elo91]. A comparison of these physically motivated models with force transfer functions derived from direct hardware experiments revealed, however, only a limited compatibility [Elo91]. This fact let Elosegui [Elo93] conclude that the complexity of some robotic systems makes the predication of force transfer functions unfeasible and thus direct measurement is needed to derive valid transfer functions. As a consequence, the predication of the stability bounds of a force controller seems to be elusive, thus, making it hard to find an optimal mechanical design that maximizes the closed loop performance for a given control architecture.

2.2 Kinematical Design

One of the most fundamental issues in the conceptual design of a haptic interface is the kinematical configuration because it defines the workspace and basic dynamic properties. Robots can be classified in serial, parallel, and hybrid kinematical chains. In *serial* designs the end-effector is connected to the base via one single opened kinematical chain consisting of a series of links interconnected by joints. *Parallel* devices have at least two independent kinematical chains linking in parallel the end-effector to the base. In case of *fully-parallel* mechanisms the number of these parallel chains equals the number of the end-effector DOF. Mechanisms containing serial-chain and parallel-chain modules connected either in series or in parallel are referred to as *hybrid* kinematical designs.

The main drawback of serial designs is that each axis has to move all succeeding joints and links degrading the inertial properties. Moreover, fully-parallel mechanisms usually allow the location of all actuators at the base further reducing the inertia and simplifying the cabling. The multiple load-bearing paths of parallel designs enhance the force capability and structural stiffness. On the negative side, they are likely to have a significantly smaller workspace, reduced velocity capability, increased number of mechanical parts due to passive joints, susceptibility to link interference, strong coupling of translational and orientation DOF, and highly complex forward kinematics increasing the computational effort for the control.

Therefore, parallel designs can provide highly backdrivable and stiff interfaces with an excellent force bandwidth and high force output in case of moderate workspace requirements. When physical compactness and large workspace size are important design criteria serial designs seem to be more rewarding. The small orientation workspace of many purely parallel devices motivated the design of hybrid haptic interfaces with an orientation stage connected in series to a parallel position stage, see for instance the designs described in Hayward *et al.* [HGG⁺98] and Tsumaki *et al.* [TNNU98]. Other motivations for hybrid kinematics include the incorporation of four or five bar link mechanisms in serial designs to move actuators closer to the base, as for instance employed in the PHANToM device [MS94], or the coupling of several existing devices in parallel to increase the number of DOF [Iwa93].

A maximization of the translational working volume in respect to the length of the kinematical chain requires a serial mechanism with a revolute joint at the base. Indeed, such designs can yield a spherical workspace with radius equal to the length of the robot arm. If the kinematical design is *non-redundant* (i.e. has equal number of actuated joints and DOF at the end-effector) large areas of the workspace will, however, not be available for

haptic simulations due to the existence of *interior singularities*. Singularities are positions in space where the robot loses a DOF. Whereas in common industrial robot applications it is frequently allowed to drive the robot through such singularities it is necessary to circumvent these locations in haptic systems for the following reason: around these positions the dynamic properties of the robot degrade because high joint velocities only produce small end-effector velocities in certain directions. This results in a significant impairment of the end-effector output capability regarding acceleration and velocity. Due to the fact that the device can be moved by the human operator at will motions along these directions cannot be avoided by trajectory planning methods. Singularities are also the reason for the limitation of the angular workspace. It is in general true that an angular workspace of 360° around each axis is not achievable for non-redundant 6 DOF robots [Wam92].

To illustrate the effect of interior singularities the workspace of VISHARD6, a 6 DOF haptic interface [UB02], can be viewed. Figure 2.1 shows the singularity free translational working volume allowing arbitrary orientations of the end-effector in the range of 360° , 90° , and 360° for the angle of roll, pitch, and yaw, respectively. Although the working area is comparatively large an area in the center of the workspace is not available for haptic interaction due to interior singularities. On account of this the unpropitious workspace shape of non-redundant serial designs with revolute joints at the base often diminishes the benefit of their improved workspace volume when compared to mechanisms free of interior singularities as for instance serial 3 DOF linear axes designs or the parallel DELTA mechanism introduced by Clavel [Cla91].

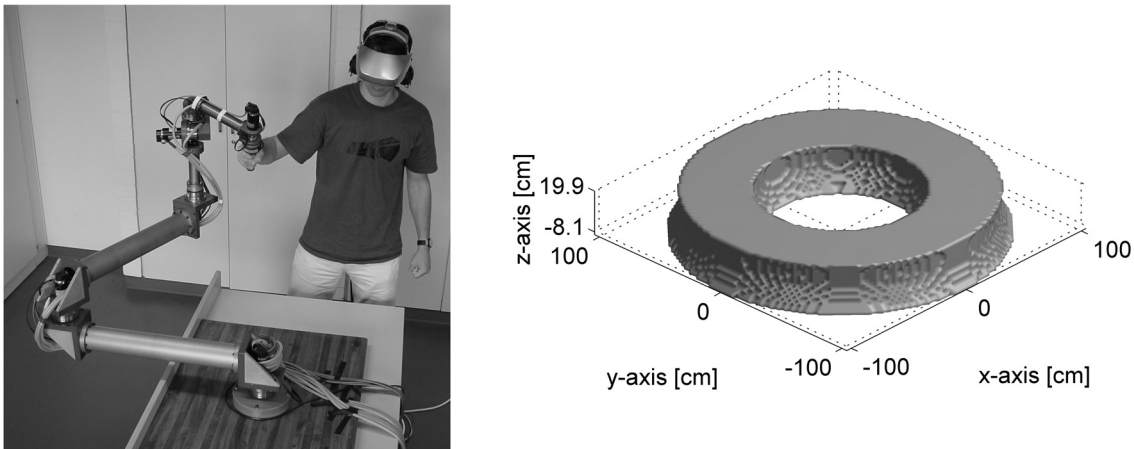


Figure 2.1: VISHARD6 prototype (left) and its singularity free translational workspace for an orientation workspace of 360° , 90° , and 360° for the angle of roll, pitch, and yaw, respectively (right)

A possible solution to this problem is the introduction of actuated kinematical redundancies. Such mechanisms allow for a change of their internal configuration without changing the position and orientation of the end-effector. This kind of motion is called *null space movement* or *selfmotion*. A well directed control of the selfmotion may contribute to increase the overall system performance. The following summarizes some of the well known attractive features available in redundant kinematical designs.

- *Workspace:* The redundant DOF can be used to avoid interior singularities. This can drastically increase the workspace while simultaneously reducing the device size.
- *Dynamic properties:* The selfmotion can be controlled to maximize inertial and bandwidth performance criteria as well as to reduce friction forces at the end-effector. The potential for improvement of the dynamic properties is exceptionally large when dealing with redundant designs forming a macro/micro system comprised of a large (macro) robot carrying a small (micro) robot [SHH88].
- *Output capability:* Also feasible is the maximization of performance criteria affecting the output capability as e.g. force/velocity transmission or acceleration capability.
- *Collision avoidance:* Redundancies offer an increased potential for collision avoidance with the environment and human operator. This can for example be exploited for the prevention of user interference or link interference at dual-arm haptic devices.

In practice, however, kinematical redundancies are rarely used for haptic devices. A possible explanation is the increased cost and complexity of the mechanical design. To control the redundant DOF a computational augmentation is unavoidable. Also, the introduction of additional joints seems to be contrary to the objective of low inertia and high stiffness. The potential reduction of the device size relaxes these disadvantages. Moreover, the removal of the interior singularities allows operating in workspace regions with increased stiffness and output capability. The ViSHARD10 device described in section 2.5.4 is a hyper-redundant haptic interface designed to overcome performance limitations due to interior singularities. Other kinematically redundant haptic devices are off-the-shelf redundant industrial robots and the DLR light-weight robots [HSAS⁺], which are, however, not specifically designed for haptic applications. The target application of the high-end DLR robots are manipulation tasks in space. As a matter of this fact, the main focus of the mechanical design is not on the minimization of the device dynamics but on the reduction of the overall mass. To the best knowledge of the author, the serial macro/micro concept for haptic device design has not been put in practice so far.

2.3 Actuator Technology

Comparative studies of robot actuator technologies are widely reported in the literature. A very extensive comparison of conventional actuation technology has been given by Hollerbach *et al.* [HHB92] and Burdea [Bur96] and a description of the properties of non-conventional actuators can be found in [HL92, MPM99, MVA⁺04].

Traditional actuators for kinesthetic haptic devices comprise hydraulic, pneumatic, and electromagnetic actuators. The main motivation for using hydraulic systems is their outstanding mass power and volume power density (in case the weight of the remotely located hydraulic power supply is not included). As they operate most efficiently at low speed and high force, which is ideal for robotics, no speed reducing mechanism has to be applied to yield an excellent force to mass ratio. Particularly with regard to haptic feedback applications hydraulic actuators have, however, significant drawbacks. First, hydraulic systems have typically very high impedance coming from the low compressibility and high inertia of hydraulic fluid, the difficulty in back-flowing through a servo valve, and the

high sliding friction and stiction due to tight seal tolerances required to reduce leakage. Consequently, backdrivability relies purely on active feedback control. Secondly, common hydraulic actuators for robotics employ spool valves regulating the fluid flow rate proportional to the control signal. Thus, hydraulic actuators usually resemble velocity rather than force sources forbidding open-loop force control and standard dynamic model based position control schemes that typically rely on the accurate generation of the actuator torque according to the control signal. Hence, the overall performance of haptic interfaces employing hydraulic actuation strongly depends on the performance of the active force feedback control. Whereas force control of standard hydraulic systems has been widely recognized as a very difficult problem [NS01] the experimental results reported by Boulet *et al.* [BDHN93] as well as Mougnet and Hayward [MH95] show that an impressive force response in terms of accuracy and bandwidth (around 100 Hz) can be achieved with specialized hydraulic actuators. The final drawbacks include the high material overhead (pumps, valves, bulky and heavy hoses and pipes for fluid transport), requirement for regular and skilled maintenance to keep a clean sealed system, tendency to leakage, and the high cost of qualified hydraulic systems.

Pneumatic actuators are very similar to hydraulic systems. The difference between them is the use of compressible gas (typically air) as the medium for energy transmission. They are operated at pressure levels orders of magnitude smaller than hydraulics because the large amount of potential energy stored in compressed air raises safety concerns. Accordingly, the mass and volume power is inferior to hydraulics but still superior to electromagnetic actuation. As air is a clean operating medium pneumatic actuators do not require return lines for fluid (the air can simply be released to the surroundings) greatly reducing the system complexity and mass. In general, the setup, operation, and maintenance are significant easier and the cost is lower compared to hydraulics. At the downside, these systems typically produce large amount of acoustic noise and suffer from a low force bandwidth due to the high compliancy of air. Even when closed loop pressure control is implemented the force bandwidth seems to be limited to less than 20 Hz [BDS95] which is insufficient for a realistic render of stiff environments.

Electromagnetic motors exhibit the lowest mass and volume power amongst the conventional actuators. Moreover, they operate inefficiently at low speed and high torque making mechanical speed reduction mechanisms (see Section 2.4) necessary to yield an acceptable torque to mass ratio. Even so, electromagnetic motors are the preferred actuators for the vast majority of kinesthetic interfaces because they are clean and quiet as well as easy to install, operate, and control which is especially true for DC motors. High performance DC motors show very low torque ripple resulting in a comparatively accurate proportional relationship between motor current and torque. As high bandwidth current control is a comparatively simple task these actuators provide an excellent torque source over a wide frequency range. Furthermore, a comparison with pneumatic and hydraulic actuators given in [Bur96] reveals superior performance in terms of mechanical bandwidth. Since they also show good backdrivability and low impedance they are perfectly qualified for open loop force control.

Viewing non-conventional actuators it can be observed that they show low compatibility to the requirements of kinesthetic haptic hardware. Most of these technologies (e.g. piezoelectric and magnetostrictive actuators, conducting polymers, shape-memory alloys) suffer from small motions requiring specialized mechanisms to generate large displacements. Their application to micro robots as for example tactile interfaces seems to be more ap-

pealing. Actuators with larger strain show other shortcomings including for instance low stiffness (e.g. dielectric elastomers, thermal liquid crystal polymers, electrostatic actuators). It has to be noted, that many of these technologies are still at a very early research state and far from being mature. Future work may improve their compatibility to macro robots.

2.4 Force/Motion Transmission Techniques

The comparatively low force to mass and force to volume ratio of electromechanical motors limits the use of direct drive actuation where the joints are directly driven by the motor axes. This is especially true for serial designs with significant number of DOF where the comparatively large, heavy, inefficient, and also expensive direct drive motors placed at joints distant to the base add too much inertial and gravitational load. As a consequence, the majority of haptic interface designs employs mechanical transmission mechanisms to boost the motor torque (speed reduction), to transmit the actuator power over some distance to the joint, or both. Among the drawbacks of these transmission techniques are the added dynamics and energy dissipation degrading the mechanical bandwidth and output force accuracy of the actuation system. The application of speed reduction mechanisms has the additional disadvantage that the reflected inertia seen at the output of the speed reducer increases by the square of the reduction ratio. This characteristic has to be considered at the optimization of the overall device inertia.

Common transmission mechanisms include for instance gear drives, tendons, chains, toothed-belts, and linkages. Transmission mechanisms converting rotary motion into linear movement as for instance leadscrews are excluded from the following discussion. For the purpose of speed reduction gear drives represent the most compact mechanisms. Typical gear drives employed for kinesthetic haptic devices are planetary and the (more expensive) harmonic drive gears. Standard planetary gear drives typically suffer from backlash. It is, indeed, possible to eliminate the backlash by preloading but this, in turn, increases the friction. Harmonic drive gears are in general preloaded, thus offering zero backlash. A comparison of gear trains for industrial robots presented by Rosenbauer [Ros95] indicates lower efficiency and higher inertia of harmonic drives compared to planetary gear trains. It has, however, to be noted, that the increased inertia does not seem to be a significant disadvantage because it is usually small compared to the motor inertia. On the positive side harmonic drives show a higher torque to mass ratio, compactness, overload capability, and reduced hysteresis. Despite of their built-in flexibility, the flexspline, a superior stiffness and mechanical bandwidth could be observed. A possible explanation is the significantly larger zone of tooth engagement (around 30%). A large benefit of harmonic drive gears is their flat geometry which seems to ideal for compact robot joint designs. Moreover, hollow-shaft versions are available that allow routing the cabling through the center of the joint when combined with a hollow-shaft motor. This offers the possibility to locate the entire cabling at the inside of the device structure. The main downside of speed reduction using gear trains is the torque ripple inevitable coming along with tooth systems. Torque ripple can be high frequent in particular at high joint velocities and is therefore hard to compensate with force feedback control. One has, however, to consider, that gear trains have been typically optimized for precise transmission of motion instead of force feedback application. As the reductions of torque and velocity ripple are somewhat contrary requirements it can be

expected that a significant lowering of the torque ripple can be achieved with dedicated mechanical designs.

Tendon transmission systems have also been widely used in haptic hardware designs to yield speed reduction. As no toothing is used these systems are virtually free from backlash and torque ripple. On the other hand, they show a drastically reduced compactness because the diameter of the capstan cannot be made arbitrary small to avoid tendon fatigue; this requires a very large driven pulley or a multiple staged design to realize high reduction ratios. The study of Rosenbauer [Ros95] reveals that a significant effort is required to yield a torsional stiffness comparable to precision gear drives when using toothed belts. This indicates that also tendon based speed reducers are likely to have inferior stiffness characteristics.

The most attractive feature of tendon transmission systems is their ability to transmit the motor torque over some distance to the joint offering the possibility to mount the motors at the device base to lighten the interface structure. Moving the often bulky motors away from the joint can improve the compactness and ergonomics of the design. Moreover, it may allow using large and heavy motors driving the joint without speed reducer (also called semi-direct drive actuation) possibly significantly improving the interface backdrivability. It is, however, increasingly difficult to realize a stiff transmission when the tendon length is rising. Viewing combinations of tendon based mechanisms for force transmission over distances with speed reduction mechanisms (e. g. harmonic drive gears) Townsend [Tow88] pointed out that it is advantageous in terms of transmission stiffness to place the speed reducer not at the actuator but as close to the joint as possible. The reason is the decreased tension in the (high-speed) transmission part spanning most of the distance. Moreover, the elastic displacement of the high speed part produces only little displacement at the joint output due to the reduction ratio of the speed reducer.

The price of communicating torque over distances with tendons is usually an increase in friction, additional and complex transmission dynamics, and a higher system complexity. Whereas it is in principal possible to keep the friction level very low by sophisticated mechanical design, see for instance the results of the Freedom 7 haptic interface presented by Hayward *et al.* [HGG⁺98], this is, in fact, not a trivial task as for example shown by the practical experience reported by Gosselin *et al.* [GGB05]; they decided to replace the tendon transmission of the first prototype by an actuation system located close to the end-effector to solve performance limitations due to the high friction level. The realization of low friction is particularly difficult for serial kinematical designs of high DOF because cumulative routing of the tendons is required to drive the distal joints. As a matter of this fact Marcheschi *et al.* [MFAB05] assumed the friction induced by the multiple idle pulley bearings of the PERCRO L-EXOS exoskeleton haptic interface to dominate in high gear over the friction of the planetary gear drives the tendon transmission system is connected to. The demand for low friction requires tendon routings via idle pulleys instead of sheaths (guide tubes). The downside of idle pulleys is their need for mounting surfaces, reduced reliability, and increase of complexity of the mechanical design. Jacobsen *et al.* [JKID90] briefly reviewed types of tendon drive configurations showing that in order to prevent the tendons to go slack active tensioning is preferable to passive pretensioning because it reduces the average tension resulting in lower friction. This advantage goes along with a simplified assembly, tuning, as well as improved reliability and work life [HCH97]. The most favorable configuration employs two actuators per driven joint each pulling an opposing tendon in agonist/antagonist fashion. Clearly, the increased number of actuators results

in a more expensive system. The potential augmentation of the transmission dynamics due to tendon drives has been studied by Prisco and Bergamasco [PB97]. The authors identified and quantified a dynamic coupling between motor and joint variables in serial multi-DOF robots that is not present in serial robots with actuators located on the joints.

On account of the above discussion tendon mechanisms seem to be primarily rewarding for haptic interface designs small in physical size and low DOF because in case of large devices the weight of the mechanical structure (links, joint bearings, etc.) typically dominates over the actuator weight due to the requirements on structural rigidity. Another approach to communicate torque over distances is the use of linkages. Whereas most of the difficulties related to tendon transmissions do not apply to linkages they tend to be more bulky and heavy. By reason of complexity they are usually only applied to move the motor closer to the preceding actuated joint; transmitting motor torque to more distal joints is hardly done. The most common implementations of linkage transmissions are planar four and five bar mechanisms. The parallelism inherent in these mechanisms usually results in an improved in-plane but poor out-of-plane mechanical stiffness of the segment.

2.5 Design of the ViSHaRD Haptic Interfaces

2.5.1 Design Rationale

The driving motivation for the design of the ViSHARD devices is the vision of a general-purpose haptic interface that can be used in a large variety of application domains. The benefit of this versatility is twofold: First, in certain task domains versatility seems to be mandatory to yield an acceptable cost-value ratio. Such an example is medical training simulation. The use of specialized interfaces would require an excessive number of hardware devices due to the large number of medical interventions (e. g. minimal-invasive surgery, open hand surgery, bone-drilling, palpation of body segments, reanimation) the students have to practice. Second, such a general-purpose interface provides a benchmarking testbed and experimental environment for the rapid and cost-effective development and evaluation of novel haptic applications. When the task domain requires a certain workspace or force capability the device can be constrained to these specifications by appropriate controller design. Once the new haptic application has been rudimentarily developed and the feasibility is verified, a tailored, highly specialized haptic display with exactly matching mechanical properties can be developed.

The most influential factors for the versatility of haptic interfaces are the workspace size, output capability, and extensibility. Therefore, the target specifications of the ViSHARD devices include a human matched force capability as well as a high payload capability to accommodate various (actuated) application specific end-effectors as for instance surgical tools like drills [EYB04] and scissors or tactile stimulation actuators for combined kinesthetic and tactile feedback to support realistic direct interaction between the operator's finger or hand and virtual objects. The main difference between the ViSHARD devices is the workspace size. The ViSHARD3 interface provides an 3 DOF translational workspace of an size somewhere between the operating volume of the PHANToM Premium 1.5 and 3.0 but with a significantly increased force capability. ViSHARD6 offers force and torque feedback in full 6 DOF in a slightly increased translational workspace. The largest workspace has the ViSHARD10 device: the actuated kinematical redundancies offer an unlimited

Table 2.1: Technical hardware specifications of the ViSHARD device family

Property	ViSHARD3	ViSHARD6	ViSHARD10
transl. workspace	$0.6 \times 0.25 \times 0.4$ m	$0.86 \times 0.3 \times 0.3$ m	$\varnothing 1.7 \times 0.6$ m ¹
rot. workspace	not applicable	360°, 60°, 360°	360° for each rotation
peak force	86 N	178 N	170 N
peak torque	not applicable	pitch, yaw: 54 Nm roll: 4.8 Nm	pitch, yaw: 13 Nm roll: 4.8 Nm
transl. velocity	1.0 m/s	0.61 m/s	>1 m/s
rot. velocity	not applicable	2.96 rad/s	
transl. acceleration	14.7 m/s ²	7.5 m/s ²	
rot. acceleration	not applicable	38.6 rad/s ²	
max. payload	6.5 kg	7.5 kg	7 kg
mass of moving parts	≈ 5.5 kg	≈ 20 kg	≈ 23 kg

orientation workspace free of singularities and a translational operating volume of 1.3 m³. The versatility of ViSHARD10 is particularly high because the null space movement can be adapted to the specific needs of the application. This includes for instance a control of the selfmotion to achieve collision avoidance which is advantageous at dual-arm haptic interactions to avoid interference of the two devices. The ViSHARD devices have in common that the kinematical design is purely serial due to the superior workspace characteristics when compared to parallel kinematics. Furthermore, all interfaces employ force sensing at the device tip to actively compensate for the increased device impedance coming along with the demand for versatility. The technical specifications of the ViSHARD device family are summarized in table 2.1. Further details on the sensor and actuator specifications are given in appendix A.1.

The scope of the hardware developments was the preparation of first prototypes for the rapid evaluation of the design concept. Striving for a moderate hardware complexity the design has been influenced by considerations of modularity. As a matter of this fact, the kinematical design of the ViSHARD interfaces is based solely on revolute joints. The modular joint components employ DC motors coupled with off-the-shelf harmonic drive units. As described in section 2.4 these gears benefit from zero backlash as well as a higher torque to mass ratio and compactness compared to planetary gears. Although the ViSHARD interfaces show good results in terms of the closed loop performance, the intentionally limited hardware complexity leaves much room for improvement. For instance most components parts are constructed from aluminium. A significant reduction of the mass and inertia can be achieved when using fiber composite (e. g. carbon fibre robot links). Additional room for improvement gives the housing of the harmonic drive gears. Because the body of the harmonic drive units is made from steel a considerable reduction in mass can be achieved when using harmonic drive component sets with a custom enclosure made from light metal. The results of recent investigations on the development of light weight harmonic drive gears and units is presented by Koenen [Koe04] and Kropp [Kro04b]. These studies indicate a potential for the weight reduction of the component sets down to 50 %

¹The ViSHARD10 workspace size depends on the inverse kinematics algorithm. The given specification applies to the target workspace possible in theory. The currently implemented control law provides a smaller translational workspace with the dimension $0.85 \times 0.71 \times 0.6$ m, see section 3.5.3 for details.

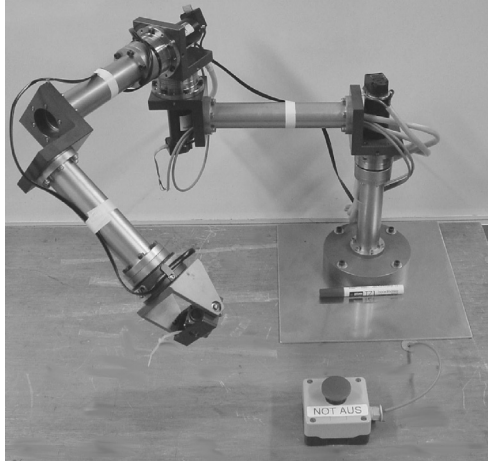


Figure 2.2: ViSHARD3

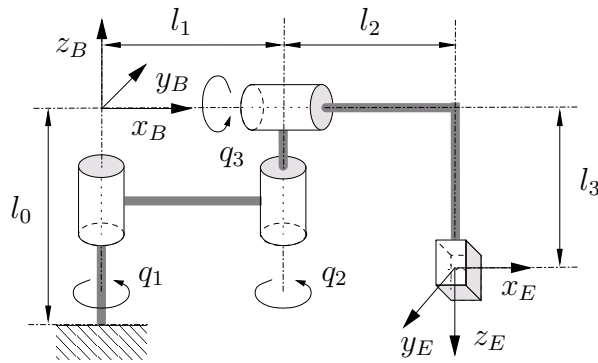


Figure 2.3: ViSHARD3

and of the units to 46% of the standard version. Further improvements can be obtained with the use of high-end motors as for example the DLR RoboDrive motor [HSAS⁺] offering compared to off-the-shelf motors a highly superior torque to mass ratio, reduced power loss at zero speed, and an advantageous flat geometry.

2.5.2 ViSHARD3 Design

In figure 2.2 and 2.3 the hardware and kinematical design of the ViSHARD3 prototype is shown. The first two joints are arranged in a SCARA-configuration with vertical axes avoiding the need for a compensation of gravitational loading with motor torque. The links 1,2,3 have an equal length of 0.3 m. For detailed information on the kinematical and inertial parameters see appendix A.2. The end-effector is a gimbal mounted thimble with three passive, freely rotating DOF. The human finger-tip can be placed on the end-effector to allow pointwise interaction with the device. The mass of the moving parts is around 5.5 kg giving inside the rectangular workspace of $0.6 \times 0.25 \times 0.4$ m in width, depth, and height an apparent inertia at the end-effector ranging from 1.9 to 18 kg.

The torque capability is provided by 150 W Maxon DC motors coupled with harmonic drive units. To compensate for the device dynamics a 12 DOF JR3 force/acceleration sensor is mounted at the tip. The acceleration sensing capability allows for example to distinguish between inertial forces generated by accelerations of the end-effector and the

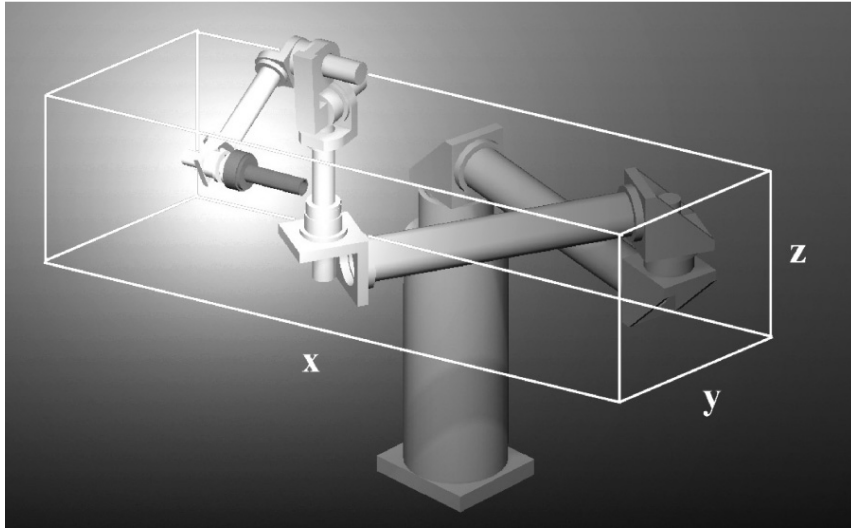


Figure 2.4: ViSHARD6

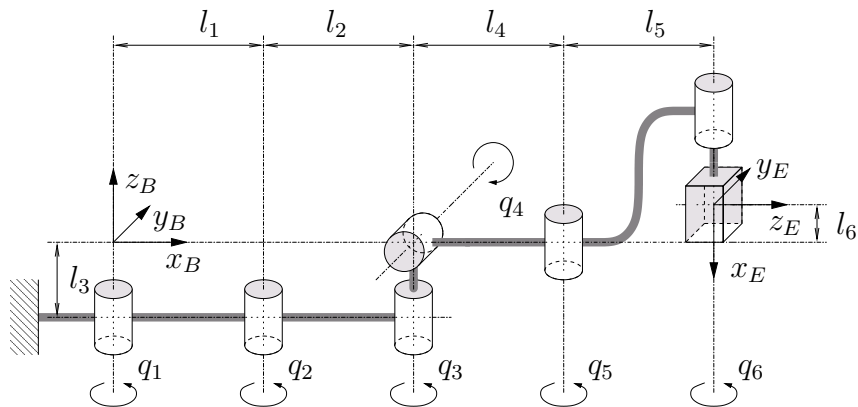


Figure 2.5: ViSHARD6

interaction forces of the operator with the device. Since this sensor provides a bandwidth of 8 kHz at a comparatively low noise level and the current control of the pulse width modulated (*PWM*) amplifiers act at a bandwidth of 2.5 kHz, a sampling rate of more than 2 kHz for the force feedback control can be achieved. The joint angles are measured by optical encoders with a resolution of 2 000 counts per revolution, after quadrature, resulting in an accuracy of $\pi \cdot 10^{-5}$ rad when multiplied with the gear ratio of 100:1. Accordingly, the joint velocities can be approximated with a resolution of 0.063 rad/s at a sampling rate of 2 kHz. Details on the ViSHARD3 mechatronic design along with the kinematic equations are presented in [Fri02]. The hardware design described in [Fri02] has later been modified by the addition of auxiliary bearing support at the base joint to increase the device stiffness.

2.5.3 Design of ViSHARD6

Figure 2.4 presents the CAD drawings of ViSHARD6 along with the dextrous rectangular workspace that can be included in the device working area. The hardware realization

Table 2.2: Link length design of ViSHARD6

Link i	Length
$l_1 = l_2$	0.6275 m
l_3	0.32 m
l_4	0.084 m
l_5	0.255 m
l_6	0 m

and complete singularity free translational operating volume is shown in figure 2.1. The ViSHARD6 kinematics is illustrated in figure 2.5. The design is similar to ViSHARD3; the first (three) joints are in a SCARA configuration offering a high payload capability; employs similar joint components (150 W Maxon DC-motors coupled with harmonic drive units, optical encoders); uses a JR3 force/torque sensor but without acceleration measurement capability.

The drawback of the SCARA-segment is a strong coupling of the translational with the rotational DOF. For instance rotations around the angle of yaw requires considerable motion of the SCARA-segment to keep the position in the x - y -plane. Another example are rotations around the pitch angle entailing a motion of joint 5 to hold the end-effector height. Details on this coupling along with an optimization of the link length design maximizing the workspace volume is presented in [UB02] and [Ern02] (see table 2.2 for the optimal link parameters and appendix A.2 for the inertial parameters). The ViSHARD6 kinematic equations are summarized in [Ern02]. A removal of the coupling can be achieved by the use of a prismatic joint for the adjustment of the end-effector height.

Similar to the modifications of the ViSHARD3 device ViSHARD6 has been extended by an additional bearing support at the base joint to increase the stiffness. The second hardware change compared to the prototype described in [UB02] is the replacement of the direct drive actuation of the last joint by a geared motor raising the torque capability for the angle of roll.

2.5.4 ViSHaRD10 Design

The first considerations regarding the kinematical design of a redundant interface have been focused on the class of standard kinematical designs consisting of a 3-jointed spherical shoulder, a single elbow joint, and a 3-jointed spherical wrist. These arms can be described as anthropomorphic after [Hol84]. Exemplarily, a configuration with a wrist in roll-pitch-roll configuration is illustrated in figure 2.6. The strength of these mechanisms is the size of the workspace which is optimum for 7 DOF robots in terms of the ratio of the arm length to the working volume. The translational workspace is a sphere with an interior singularity at the center. The angular workspace is 360° around each axis since singularities in the wrist can be avoided by rotating the elbow around the line from the shoulder to the wrist. A kinematic analysis of the design shown in figure 2.6 is presented in [KDLS90]. Among the drawbacks we identified for 7 DOF anthropomorphic arms are:

- *Gravitational load:* Only the first joint axis is designed to be vertical for arbitrary positions and orientations of the end-effector. As a consequence high motor torque is required to compensate for gravitational load.

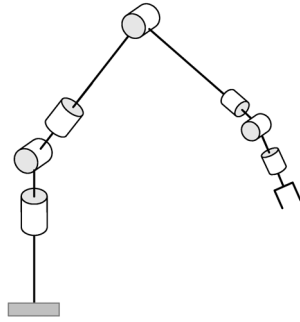


Figure 2.6: Typical 7 DOF anthropomorphic robot arm

Table 2.3: Link length design of VISHARD10

Link i	Length
$l_1 = l_2 = l_3 = l_4$	0.25 m
$l_{5h} = l_8$	0.47 m
l_{5v}	0.71 m
$l_6 = l_7$	0.212 m
l_9	0.15 m
l_{10}	0.15 m

- *Interior singularity:* The singularity in the center of the workspace impairs the dexterity and thus the performance of the device when moving the end effector close to the shoulder. An elimination of this singularity requires at least two additional redundant joints placed between the shoulder and the wrist.
- *Safety:* The most critical deficiency is the selfmotion of anthropomorphic 7 DOF arms, the rotation of the upper and forearm. Especially in case of operating with the end-effector close to the shoulder the elbow-orbit may deeply intrude into the operator's workspace bearing the risk for severe conflicts between the elbow joint and the user. The safety aspect can be solved by using a 4-jointed roll-yaw-pitch-roll wrist as described in [Wil94]. Then, the position of the elbow can be controlled to prevent collisions with the operator because singular wrist configurations can be avoided with the selfmotion of the redundant wrist. This 8 DOF solution, however, intensifies the deficiency regarding gravitational load significantly.

In order to circumvent these deficiencies of anthropomorphic arms it has been finally decided for a mechanism without a 3-jointed spherical shoulder. The kinematic structure of the hyper-redundant design with 10 DOF, VISHARD10, is depicted in figure 2.7, the link length design is summarized in table 2.3. It shows the reference configuration with all joint angles q_i defined to be zero. The inertial parameters are provided in appendix A.2. In figure 2.8 the prototype is shown in a typical operational configuration.

In the same way as in the VISHARD3 and 6 design the kinematical chain begins with a SCARA configuration to avoid the need for an active compensation of gravity. This segment is assigned for the positioning of the end effector in the x - y -plane. Although a SCARA segment with three links is sufficient for the elimination of the singularity in the

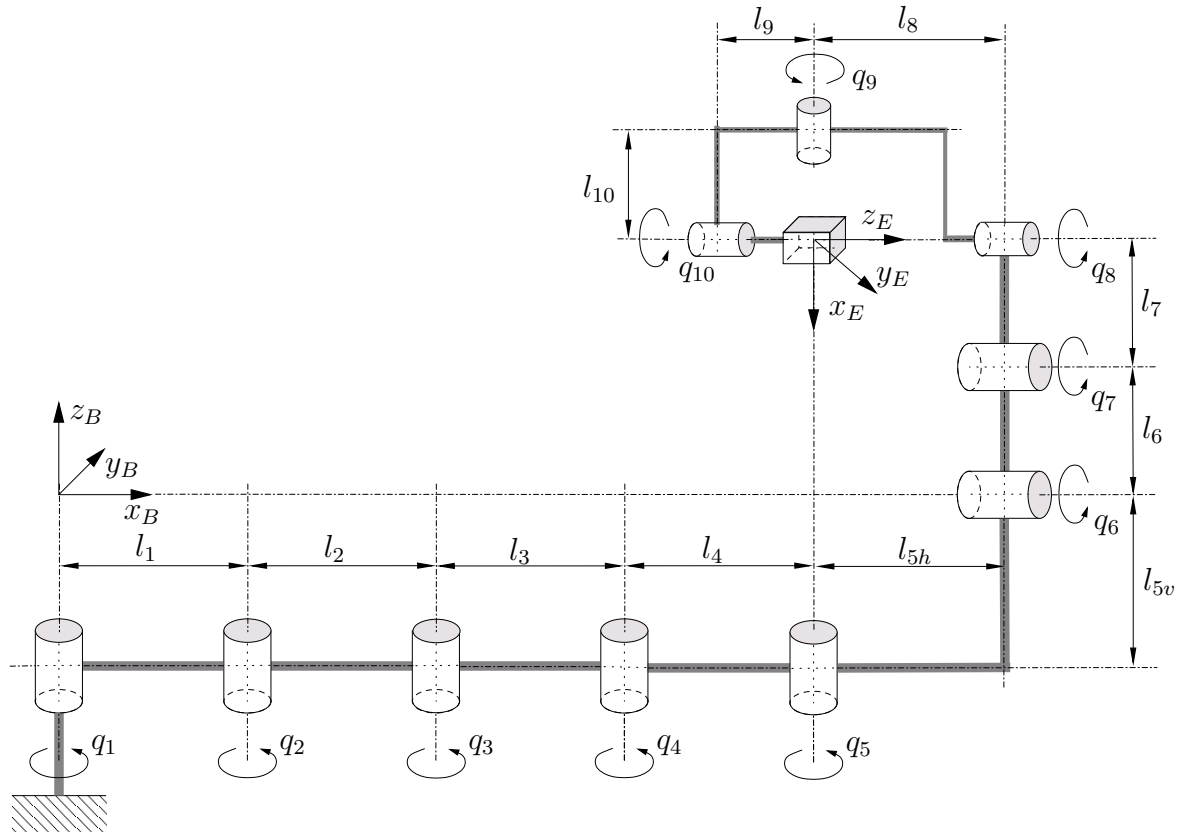


Figure 2.7: Kinematical model of ViSHARD10

center of the planar workspace we decided for an arm with 4 revolute joints ($4R$) for two reasons: First, it is well known that the $4R$ arm provides improved dexterity compared to the $3R$ arm [DMH99] and second, the avoidance of user interference is much simpler to achieve.

Alternatively we weighed up the use of a 2 DOF linear axes design for the positioning in the x - y -plane as this also provides an interior singularity free workspace. This mechanism, however, suffers from a significantly reduced workspace; two prismatic joints with a length of one meter are required to achieve a workspace of $1 \times 1 \text{ m}^2$ whereas an $4R$ arm with a total length of two meters can provide a sphere with radius 2 m. Moreover, as the base of the $4R$ arm is less bulky it is better suited for two arm simulators with two haptic devices.

Joints 6 and 7 are assigned to adjust the height of the end-effector. One simple inverse kinematics solution for them is the imitation of a prismatic joint by means of not changing the end-effector position in the x - y -plane. The decision for two revolute joints over one prismatic joint is amongst other things due to the fact that off-the-shelf prismatic joints matching our requirements regarding low friction, mass, stiffness, velocity, and zero backlash could not be found on the market and modularity of the rotational joint components is kept.

Joint 5 is used to prevent singular configurations in the spherical wrist formed by joints 8, 9, 10. Despite tending to an increased wrist size we decided for a yaw instead of roll orientation for joint 8 to obtain decoupling of the wrist configuration from the end-effector height. This mechanism has a singularity when the axes of joint 5 and 9 as well as of joint 8 and 10 have the same orientation. Whereas the first condition cannot be avoided

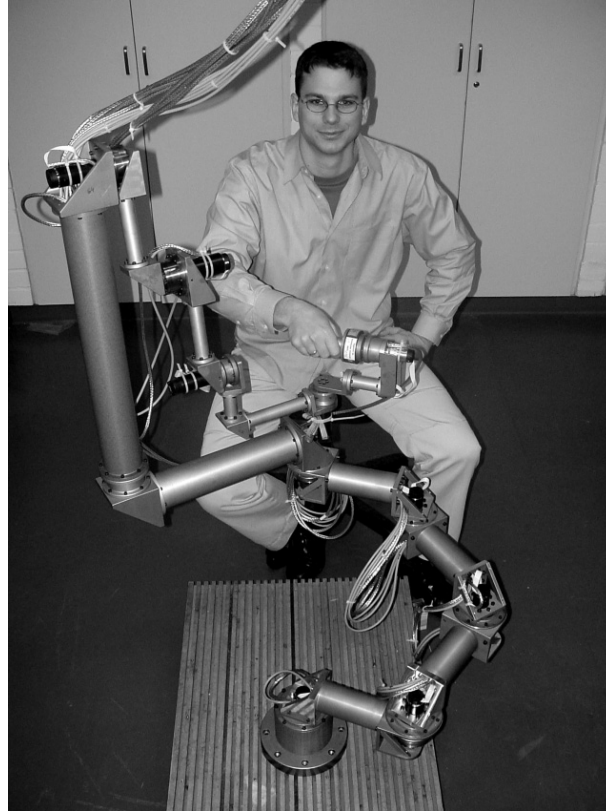


Figure 2.8: Haptic display VISHARD10

when holding the end-effector in a horizontal orientation the second can be avoided by a rotation of joint 5.

The axes of joint 5, 8, 9, 10 intersect at one point which is located 5 cm in front of the force-torque sensor (assuming that the motion of joint 6 and 7 is controlled accordingly). This enables the operator to grip the end-effector at the point where the angular DOF are mechanically decoupled from the translational ones as for example desired for simulations involving direct haptic interactions with the finger or hand. Alternatively, the user can hold the device at an other location of the end-effector to simulate the exploration of a remote or virtual environment with the tip of a tool. The benefit of such a decoupling of the positioning from the orientation mechanism is twofold: first, it results in reduced natural dynamics of the orientational DOF and second, it allows for taking different output capability requirements of these DOF into account; the maximum torque exerted by the operator to the end-effector is usually bounded by the low torque capability of the human wrist whereas the high torque capability of the human shoulder joints allows for comparatively high forces.

The mechanical realization of this kinematical design is without joint angle limits and possibility for collision between parts of the structure. One important goal pursued with the kinematical design of VISHARD10 has been to provide the option to partition the inverse kinematics problem into two separate problems: the inverse kinematics for the positioning and the orientation stage. This can decrease the computational power required for the redundancy resolution significantly. The decoupling of the translational from the rotational movement is achieved when controlling joint 6 and 7 to mimic the operation of a

prismatic joint. The distance between joint axis 10 and joint 9 is 0.1 m providing sufficient mounting room for end-effectors of moderate size. The link length design (see table 2.3) gives an overall system size similar to VISHARD6. The dexterous workspace, however, which is a cylinder with $\varnothing 1.7\text{ m} \times 0.6\text{ m}$, is significantly larger. Further details on the kinematical design including the kinematic equations are provided in [Moc04], [Moc05].

Like the other VISHARD interfaces the joint components comprise DC motors coupled with harmonic drive gears. The moment stiffness of all gears in the SCARA segment is increased by additional bearing support in order to avoid damage due to deflection in the harmonic drive component sets. Again, the device is equipped with a six-axis JR3 force-torque sensor to shape the device dynamics as needed by active control. The joint angles are measured by digital magneto resistive (*MR*) encoders with a resolution of 4 096 counts per revolution, after quadrature, resulting in a comparatively high position resolution when multiplied with the gear ratio varying from 100:1 to 160:1. Detailed specifications of the sensors and joint components are given in appendix A.1.

2.6 Summary

In this chapter several design aspects of haptic interfaces have been discussed. For the majority of application domains the most rewarding design guideline is the maximization of the device open loop force bandwidth because at contact situations bandwidth requirements are higher than at unconstrained motions. For rising demands for workspace size and output capability the inclusion of feedback control seems to be unavoidable in order to mitigate a degradation of the haptic feedback accuracy due to the increased natural device dynamics. Safety issues can, however, not be solved entirely by dedicated feedback control concepts due to their potential malfunction. Accordingly, human friendly hardware designs are desirable for the realization of haptic interactions in large operating volumes as off-the-shelf industrial robots bear a considerable risk for the operator.

For the realization of large workspaces with devices of moderate physical size serial kinematical designs seem to be more rewarding than parallel designs. The improved workspace characteristics are particularly high when kinematical redundancies are introduced to circumvent interior singularities. Redundant designs can also be beneficial in terms of safety aspects; a micro/macro concept where a micro actuator is placed on an intrinsically safe macro actuator to recover the force bandwidth performance; a well-directed control of the selfmotion to avoid user interference.

As far as technical solutions for the actuation are concerned it can be concluded that in case of highest requirements on the device performance hydraulic actuation is a rewarding option due to the outstanding mass power and volume power density. By reason of the highly challenging force control characteristics of hydraulic actuators and the requirement for regular and skilled maintenance electromagnetic actuators are, however, almost exclusively preferred. Viewing mechanisms for the transmission of forces it can be summarized that gears have in comparison to tendon transmission systems superior stiffness characteristics and higher compactness. This is in particular true in case of harmonic drive gears showing a higher torque to mass ratio, compactness, overload capability, stiffness, and bandwidth than planetary gear drives. At the downside, gear drives suffer from torque ripple. Transmitting power over distances with tendon mechanisms usually increases friction, adds complex transmission dynamics, and rises the hardware complexity. In case of large

devices the benefit of the remote location of the actuators in terms of inertia reduction is less significant as the weight of the mechanical structure typically dominates over the actuator weight.

Based on the above review on hardware solutions for kinesthetic haptic feedback mechanisms a family of haptic devices has been developed striving for human friendly general-purpose designs filling the gap between passive interfaces and industrial robots. These prototypes are directed towards versatility and extensibility to provide a testbed and experimental environment for a rapid evaluation of haptic applications. The versatility of the ViSHARD10 device is particularly high due to the introduction of kinematically redundant joints permitting the adaptation of the null space motion to the specific needs of the haptic interaction task. Control concepts of haptic interfaces along with experimental results for performance evaluation of the ViSHARD devices are provided in the following chapters.

For haptic interaction tasks requiring 3 DOF translational force feedback in a moderate workspace the application of ViSHARD3 is most rewarding. The advantages compared to ViSHARD6 and 10 are the smaller physical size and lower natural device dynamics. The improved backdrivability allows for a more accurate render of unconstrained motions (see section 5.3.2 for a comparative study of the closed loop backdrivability of the ViSHARD interfaces). The ViSHARD3 prototype has been successfully integrated in a virtual reality skill training system for bone drilling [EYB04]. The setup largely benefits from the ViSHARD3 capability to measure and display high forces. One ViSHARD3 prototype has been sold to the Department of Mechanical and Systems Engineering of the Gifu University in Japan. Taking advantage of the device high payload capability it has there been extended with a complex end-effector providing 3 actuated rotational DOF. ViSHARD6 is preferable to ViSHARD3 in case of tasks requiring an increased operating volume², higher interaction forces, or additional rotational DOF. Compared to the ViSHARD10 interface it provides a better capability for the display of low translational inertia (this statement applies to the currently implemented inverse kinematics algorithm of ViSHARD10 and can change in the future). In case of high demands on the performance of the orientational DOF in terms of workspace size and backdrivability ViSHARD10 is the best choice due to the redundant spherical wrist design. Moreover, it features the largest translational workspace. The ViSHARD10 interface has been presented to the public at major exhibitions (IST Event 2004, CeBIT 2005). It is currently employed for a dual arm telemanipulation system [PUB06] as well as for a virtual reality multi-user training system [EYB07]. The successful application of the device for the render of haptic interactions with deformable objects such as soft tissue is reported in [EYB06]. One ViSHARD10 prototype has been extended by end-effectors providing tactile feedback to the operator [FEB06]. It is used at the Max Planck Institute for Biological Cybernetics in Tübingen for psychophysical research. The focus is on the investigation of tactile suppression effects [VEF06].

²The specifications given in table 2.1 indicate similar translational workspace characteristics for ViSHARD3 and 6. One has, however, to consider that a significant enlargement of the ViSHARD6 operating volume can be achieved when narrowing the permitted rotational workspace.

3 Control Aspects

Most commercially available kinesthetic interfaces as for instance the PHANTOM devices (SensAble Technologies) developed at MIT [MS94] do not incorporate force sensing capability in the hardware; the desired interaction forces with the human operator measured from remote teleoperator environments or computed by a virtual reality application software is provided by open loop force control. Accordingly, a large body of literature on haptic device control is focused on the analysis of this class of control algorithms, see for example [Hog89], [CB94], [Has01], and [DNB⁺05]. In order to afford an accurate force feedback this control strategy relies on a lightweight mechanical interface design with low friction to reduce disturbance forces due to the natural device dynamics. As described in section 2.1 such a passive design is increasingly difficult to achieve when the demand for versatility in terms of workspace size, output capability, and extensibility is rising. Furthermore, open loop force control requires appropriate actuators; for instance common hydraulic actuators cannot be used because they resemble velocity rather than force sources, see section 2.3

The inclusion of force sensing in haptic hardware design seems to receive increasing attention from the developers. It is only quite recently that commercially available interfaces with largely increased output capability and workspace emerged, see for example the DELTA Haptic Device (FORCE dimension) [GCR⁺01], the VIRTUOSE 6D (Haption), and the *HapticMASTER* (FCS Control Systems) [VLFR]. In contrast to the passive designs active force feedback is applied to compensate errors due to the natural dynamics. A review on common closed loop haptic control schemes for virtual reality applications has been presented by Carignan and Cleary [CC00]. Control algorithms for haptic interfaces with kinematical redundancies are rarely discussed in the literature.

In case of telepresence systems the control architecture is more complex due to the additional control loop of the remote manipulator as well as the communication network exchanging the command and sensor signals between the haptic device and the teleoperator. Such systems are not subject of this thesis. For a comparison and discussion of telepresence control architectures see [HZS01], [Law93], and [Kro04a]. Robust stabilization of these systems in the presence of communication unreliability as for instance caused by time-varying delay and packet loss is studied by Hirche [Hir05].

The main innovation of this chapter is the discussion of control algorithms of haptic interfaces with kinematical redundancies. Based on a review of standard approaches for the control of redundant manipulators compatible with haptic human-device interaction, control algorithms for the VISHARD10 device introduced in section 2.5.4 are presented.

This chapter is structured as follows: It starts with a classification of general robot and haptic control schemes (section 3.1) and proceeds in section 3.2 with an analysis of impedance and admittance control implementations. Section 3.3 discusses briefly the sources for performance limitations of active feedback control due to stability problems. The control of haptic interfaces with kinematical redundancies is addressed in section 3.4. The control design of the VISHARD device family described in section 2.5 is outlined in section 3.5.

3.1 Classification of Control Schemes

In this section classification schemes of general robot control algorithms and haptic control concepts are presented. For the specific task of haptic control usually approaches are adopted that are originally motivated by industrial robot applications that implicitly require the control of the robot interaction force¹ with the workpiece (e. g. assembly, polishing, grinding, handling flexible parts). Accordingly, theoretical and experimental evaluations and analyzes of haptic control algorithms presented in the literature are mostly in the framework of these industrial applications. One goal of this section is to highlight the common ground of these general robot control approaches and haptic device control.

3.1.1 Classification of Robot Control Algorithms

Classification 1: The following classification scheme for general robot control algorithms has been adopted from Volpe [Vol90]. Contrary to the original formulation of Volpe's categorization the term 'position' has been replaced by 'motion' in terms of a generalization of position, velocity, and acceleration:

- motion control

- force control
 - explicit force control
 - * open loop explicit force control
 - * force-based explicit force control
 - * motion-based explicit force control
 - impedance control
 - * impedance control without force feedback
 - * impedance control with force feedback

- hybrid control

Motion controlled robots are commanded to follow a desired motion trajectory while rejecting internal (e. g. joint friction) and external (e. g. due to interaction with environment) forces. In contact situations with objects the motion error induced by contact forces is tried to be compensated by high-gain motion feedback control entailing larger interaction forces. Thus, contact with stiff and immovable objects may result in large interaction forces possibly causing actuator saturation, instability, damage of the manipulator or object.

¹Throughout the thesis force stands for both, force and torque, while position refers to both, translational and angular positional quantities.

Robot control algorithms not considering external forces as disturbances are called *force control*. Force control schemes can be grouped in *explicit force control* and *impedance control* approaches. In explicit force control the desired interaction force with the environment is commanded. Explicit force control algorithms using no force feedback to regulate the commanded force are called *open loop explicit force control*. The other implementation forms compare the commanded force \mathbf{f}_d with the measured force \mathbf{f}_m giving the control error. The control error is then either processed by a control law providing directly an actuation signal \mathbf{u} to the plant (*force-based explicit force control*) or it is first transformed into a reference motion $\dot{\mathbf{x}}_d$ through an admittance² \mathbf{Z}_d^{-1} and possibly an integrator or differentiator which is then the input of a motion controller (*motion-based explicit force control*). The latter approach is also known as *admittance control* in the literature. Dependent on the physical quantity on that the inner motion control loop is closed this technique can be called *position-, velocity-, or acceleration-based explicit force control*. In case of *open loop acceleration-based explicit force control* (i.e. no acceleration feedback is used to produce the reference acceleration) the assignment to motion- or force-based explicit force control is not clear-cut because the differential equations relating the force error to the reference acceleration together with the open loop acceleration control law can also be considered as a force controller. Figure 3.1 and 3.2 show the block diagram of force- and position-based explicit force control (the modification to other types of motion-based explicit force control is straightforward). Both approaches are usually extended by model-based compensations of certain device dynamics (e.g. friction and gravitational forces), force-based explicit force control additionally by force feedforward. Unlike shown in Figure 3.2 it is also common to form the motion error in joint space instead of operational space.

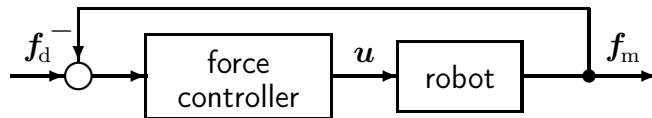


Figure 3.1: Force-based explicit force control

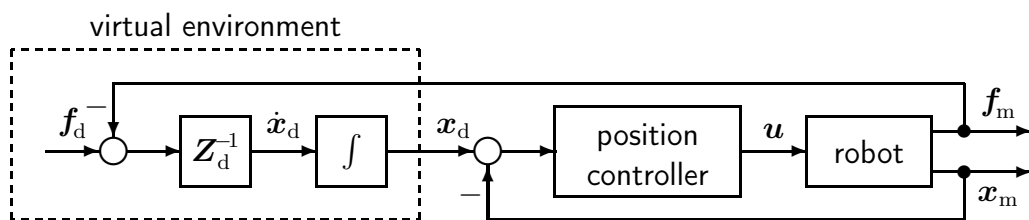


Figure 3.2: Position-based explicit force control

Impedance control proposed by Hogan [Hog85] aims at providing a dynamic relationship between the deviation of the robot's actual from the commanded motion and the interaction force with the environment. This is realized by transforming the motion error through a differentiator or integrator and an impedance \mathbf{Z}_d into a reference force signal. Note, that impedance control is a generalization of stiffness [Sal80] and damping (or accommodation) control [Whi77] where the target impedance takes that of a spring and a damper system,

²In this thesis admittance is defined to be the relation \mathbf{Z}^{-1} between velocity and force: $\dot{\mathbf{x}} = \mathbf{Z}^{-1}(\mathbf{f})$.

Conversely, impedance is defined as the relationship \mathbf{Z} between velocity and force: $\mathbf{f} = \mathbf{Z}(\dot{\mathbf{x}})$

respectively. The impedance control approach does not necessarily require force measurement. Algorithms not involving force measurement (also called *implicit force control* or *open loop impedance control*) can actually be considered as motion control with the motion error formed in operational space and the control gains adjusted to achieve a desired compliance of the robot to external forces. Figure 3.3 shows an impedance controller with the motion error formed in the position domain. It illustrates that impedance control contains an explicit force controller. Again, the control law can be extended by force feedforward and model-based compensations of device dynamics.

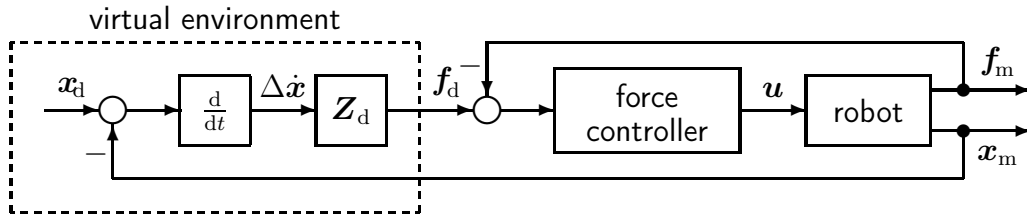


Figure 3.3: Impedance control with force feedback

The *hybrid control* approach proposed by Raibert and Craig [RC81] takes into account that the robot interaction with the environment does not necessarily require force control in all but only in constrained directions. Thus, the space including all feasible directions of displacement is partitioned into an unconstrained subspace in which motion control is used and a constrained subspace in which the robot is force controlled.

Classification 2: An alternative classification scheme for robotic force control algorithms involving force measurement has been proposed by Maples and Becker [MB86]. Their categorization is based on two classifications:

- Loop closure: Classification between algorithms where the inner-most control loop is based on force, velocity, or position
- Coordinate System: Grouping in whether the error between the manipulator's desired and actual position or velocity is formed in operational or joint space.

For completion the potential loop closure on acceleration should be added to the original formulation of Maples and Becker. As the main disadvantage of joint based algorithms the authors highlighted the fact that a compliancy defined linear in joint space is curved in operational space. As a consequence, the stiffness of a position controller linear in joint space results in a nonlinear control stiffness in operational space that also varies with the end-effector position. On the other hand joint space control implementations typically benefit from less computational effort. Another potential advantage is that disturbance forces due to unmodeled actuator and transmission dynamics (e.g. friction effects) are originated in the joint space. For the suppression of these kind of disturbances the definition of control gains in the joint space seems to be more straightforward.

3.1.2 Classification of Haptic Control Schemes

The haptic simulation of a human's bilateral interaction with a virtual or remote environment requires the control of the motion-force relation between the operator and the robot. Accordingly, haptic control algorithms belong to the group of force control schemes. The dashed box in Figure 3.2 and 3.3 indicates how the application haptics fits into these general robot force control schemes. In Figure 3.2 the virtual environment (VE) acts as an admittance (accepts force input and yields motion output, i. e. the environment reacts compliant to force input). The commanded force \mathbf{f}_d can be interpreted as an internal bias force, i. e. induced by gravitational load of a virtual mass. The VE in the impedance control scheme behaves as an impedance (accepts motion input, yields force output, i. e. the environment behaves like a resistance to motion). Here the commanded position \mathbf{x}_d can be considered as the position where a virtual spring is attached.

Classification 1: Haptic control schemes can be classified according to the *implementation type of the VE* and the *control algorithm* used to track the VE-output. The five³ different combinations can be termed as follows:

- *Open loop impedance control* (VE: impedance; controller: open loop explicit force control)
- *Impedance control with force feedback* (VE: impedance; controller: force-based explicit force control)
- *Motion-based impedance control* or *admittance control with motion feedback* [CC00] (VE: impedance; controller: motion-based explicit force control)
- *Admittance control* (VE: admittance; controller: motion control)
- An implementation of the last possible combination (VE: admittance; controller: impedance control with force feedback) has to the best knowledge of the author not been reported in the literature. As a term for this control scheme *force-based admittance control* is suggested.

Classification 2: The environment in industrial manipulation tasks corresponds in haptic systems to the human operator. Hence, haptic systems have to be considered as two manipulators, the device and the operator, acting in series. The most common classification of haptic control schemes refers to whether the *robot acts as an admittance or an impedance* [CLTM97]:

- *Admittance display mode:* The human acts as impedance and the device as admittance. Admittance and motion-based impedance control belong to this group. The admittance display mode requires force feedback.
- *Impedance display mode:* The human acts as admittance and the robot as impedance. Open loop impedance control, impedance control with force feedback, and force-based admittance control are examples for this kind of display mode. This approach does not necessarily require force measurement.

³A combination with impedance control without force feedback has not been considered due to the similarity to motion control.

In other words, haptic control schemes where in the inner-most control loop the device motion is controlled are in the admittance and where force is controlled in the impedance display mode. The terminology does not refer to the implementation form of the virtual environment. In case of a combination of a virtual impedance with open loop acceleration-based explicit force control an assignment to the admittance or impedance display mode is not clear-cut. When using force measurement also the classification scheme of Maples and Becker described above can be used to categorize haptic control algorithms. Actually, it can be considered as a refinement of this comparatively crude classification as it distinguishes between the different types of loop closure on motion.

Similar to the hybrid control approach the impedance and admittance mode can be combined by partitioning the space in directions applying loop closure on motion and directions where the inner-most loop is closed on force. Buttolo *et al.* implemented such a control law that additionally makes use of switching between different control algorithms in a virtual prototyping system [BSM02].

3.1.3 Haptic Control versus Industrial Force Control Tasks

There are two main differences between the conventional robot force and haptic control task: First, the end-effector typically contacts a very stiff environment in case of industrial force control applications whereas the haptic interface is grasped by a human operator providing a comparatively compliant connection. Accordingly, many stability problems of robot force control caused by low grip compliance do not apply for haptic control tasks. Second, the goal of common industrial force control tasks is the generation of a dedicated contact force. In case of impedance or position-based explicit force control the desired robot dynamics is freely chosen by the control designer to maximize the performance of the force controller. In other words, it is chosen as a means of satisfying a superordinated control goal. This is different at haptic control task where the generation of the motion-force relation between operator and device is the intrinsic control goal. The target impedance or admittance is dictated by the VE and is usually subject to strong dynamical variations.

3.2 Haptic Control Architectures

In this section several haptic control schemes are described in more detail. Clearly, this covers just a small subset of feasible solutions. For a broader discussion see the surveys of Whitney [Whi85] and Chiaverini *et al.* [CSV99].

The dynamic model-based algorithms consider the robot manipulator to be rigid. The dynamic model can be written in the form

$$\mathbf{M}_q(\mathbf{q})\ddot{\mathbf{q}} + \mathbf{C}(\mathbf{q}, \dot{\mathbf{q}})\dot{\mathbf{q}} + \mathbf{h}(\mathbf{q}, \dot{\mathbf{q}}) + \mathbf{g}(\mathbf{q}) = \boldsymbol{\tau} - \mathbf{J}^T(\mathbf{q})\mathbf{f} \quad (3.1)$$

where \mathbf{M}_q is the symmetric joint inertia matrix, \mathbf{q} is the vector of joint angles, $\mathbf{C}\dot{\mathbf{q}}$ the vector of Coriolis and centrifugal torques, \mathbf{h} the vector of friction torques, \mathbf{g} the vector of gravitational torques, $\boldsymbol{\tau}$ the vector of actuation torque, \mathbf{f} the vector of external force exerted by the human operator, and \mathbf{J} the Jacobian matrix relating joint velocities $\dot{\mathbf{q}}$ to the vector of end-effector velocities $\dot{\mathbf{x}}$.

3.2.1 Impedance Display Mode

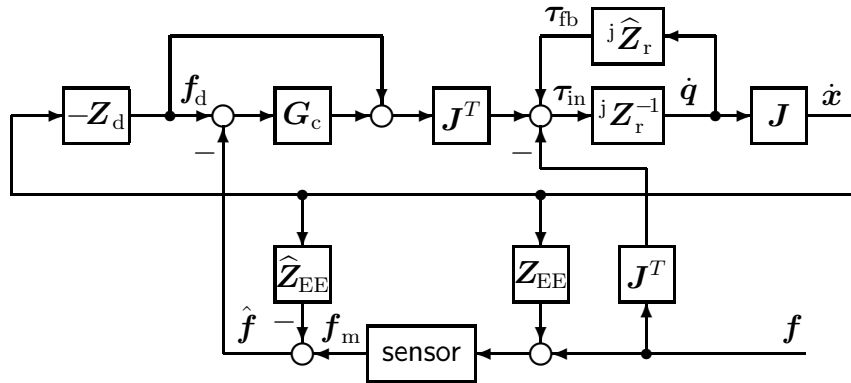


Figure 3.4: Impedance control with force feedback and model-based compensation

In Figure 3.4 the block diagram of a impedance control scheme with force feedback is given. The matrices $\underline{\mathbf{Z}}_d$ and ${}^j\mathbf{Z}_r^{-1}$ represent the impedance of the virtual model and the admittance of the natural robot dynamics, respectively. The index j indicates that the admittance is defined in joint space, i. e. gives the relationship between the joint torque input $\boldsymbol{\tau}_{in}$ and the angular velocity output $\dot{\mathbf{q}}$. Note, that $\mathbf{Z}_r^{-1} = \mathbf{J} {}^j\mathbf{Z}_r^{-1} \mathbf{J}^T$ gives the manipulator admittance in operational space. The matrix ${}^j\hat{\mathbf{Z}}_r$ is the impedance of the model-based compensator. In the literature, this model-based compensator is also (wrongly) called *model feedforward*. In fact, $\boldsymbol{\tau}_{fb}$ is a feedback torque as it is derived from sensor measurements (directly or by state observers). Its objective is the compensation of the device dynamics. Taking into account that the force sensor usually does not measure the operator's interaction force \mathbf{f} directly because an end-effector is located between the force sensor and the operator, an estimation $\hat{\mathbf{f}}$ of this quantity is derived from $\dot{\mathbf{x}}$ and the measured force \mathbf{f}_m using $\hat{\mathbf{Z}}_{EE}$, a model of the end-effector impedance \mathbf{Z}_{EE} .

Linearizing the system around the current working point the following equation can be obtained from the block diagram

$$s\mathbf{X} = \mathbf{J} {}^j\mathbf{Z}_r^{-1} \left(\mathbf{I} - {}^j\hat{\mathbf{Z}}_r {}^j\mathbf{Z}_r^{-1} \right)^{-1} \mathbf{J}^T \left(-\mathbf{F} - \underline{\mathbf{Z}}_d s\mathbf{X} - \underline{\mathbf{G}}_c \left(\underline{\mathbf{Z}}_d s\mathbf{X} + \mathbf{F} + \left(\mathbf{Z}_{EE} - \hat{\mathbf{Z}}_{EE} \right) s\mathbf{X} \right) \right), \quad (3.2)$$

where $\mathbf{X}(s)$ and $\mathbf{F}(s)$ denote the device position and interaction force mapped into the Laplace domain, the underlined variables indicate that the corresponding dynamic equations are linearized and mapped into the Laplace domain, and $\underline{\mathbf{G}}_c(s)$ is the transfer function of the linearized force control law. The closed loop impedance $\underline{\mathbf{Z}}_{rCL}(s)$ relating the device velocity $s\mathbf{X}(s)$ to the force $\mathbf{F}(s)$ applied by the operator is:

$$\underline{\mathbf{Z}}_{rCL} = \underline{\mathbf{Z}}_d + (\mathbf{I} + \underline{\mathbf{G}}_c)^{-1} \left(\underline{\mathbf{Z}}_r - \hat{\underline{\mathbf{Z}}}_r + \underline{\mathbf{G}}_c \left(\mathbf{Z}_{EE} - \hat{\mathbf{Z}}_{EE} \right) \right) \quad (3.3)$$

This equation clearly exhibits the role of the force feedback and model-based compensator concerning the accuracy of the haptic device. Without force feedback ($\underline{\mathbf{G}}_c = \mathbf{0}$) the difference between the desired impedance $\underline{\mathbf{Z}}_d$ and the closed loop impedance $\underline{\mathbf{Z}}_{rCL}$ is the device natural impedance reduced by the dynamic terms predicted by $\hat{\underline{\mathbf{Z}}}_r$. A reduction of the inertia is without force or acceleration measurement hardly possible. Therefore, open loop

can be implemented as a combination of a virtual impedance \mathbf{Z}_{d1} relating the reference end-effector velocity $\dot{\mathbf{x}}_d$ to the reference interaction force \mathbf{f}_d and a virtual admittance \mathbf{Z}_{d2}^{-1} relating the force error to $\dot{\mathbf{x}}_d$. The resulting impedance of the VE is given with

$$\underline{\mathbf{Z}}_d = \underline{\mathbf{Z}}_{d1} + \underline{\mathbf{Z}}_{d2} \quad (3.5)$$

where $\underline{\mathbf{Z}}_{d2}$ is the inverse function of \mathbf{Z}_{d2}^{-1} . Again, the underlined variables denote that the corresponding dynamic equations are linearized and mapped into the Laplace domain. Such a virtual coupling enables for admittance control the use of haptic rendering software modelling impedances. In fact, most application software is of impedance type because commercially available haptic devices are rarely equipped with force sensing capability and thus necessarily have to be controlled in the impedance mode. Needless to say, that the virtual coupling network can also be replaced by a haptic rendering engine of admittance type directly relating the interaction force to the desired motion, meaning that $\mathbf{Z}_{d2}^{-1} = \mathbf{0}$.

Assuming the gain of the inner-loop position controller is sufficiently large that $\dot{\mathbf{x}} \approx \dot{\mathbf{x}}_d$ holds (which, in practice, is mostly given) then the closed loop impedance of the system is

$$\mathbf{Z}_{rcl} \approx \mathbf{Z}_d + \mathbf{Z}_{EE} - \widehat{\mathbf{Z}}_{EE}. \quad (3.6)$$

As a result of the high gain inner position-control loop the nonlinear disturbances due to the natural device dynamics are effectively compensated. Thus, it is possible to shape the impedance error to a dedicated form without acceleration measurement, the use of a dynamic device model, or without both. This control scheme seems to be particularly well suited for devices with hard nonlinearities and large dynamic properties compared to the virtual environment being emulated. Contrary to haptic displays operated with standard impedance control laws applying no model-based inertia compensation it is possible to render an isotropic closed loop dynamic behavior in order to provide the operator a somewhat more ‘natural feeling’.

A drawback of this control law is that the relation from the force error to the desired position \mathbf{x}_d adds more poles than zeros and thus an additional phase lag to the open loop transfer function of the system. Acceleration feedforward as shown in Figure 3.5 can be used to fasten the system response but usually impedance control algorithms give a superior closed loop bandwidth.

An increase in bandwidth can also be achieved when closing the inner loop on velocity or acceleration instead of position. Then, however, an accurate tracking of the device reference motion is harder to obtain which usually results in an increased impedance error. Also, a drift between \mathbf{x}_d and \mathbf{x} can be expected when using a controller without integral action. This causes a corresponding drift of e.g. virtual walls because the VE application software assumes an erroneous end-effector position. To avoid this problem motion-based impedance control can be used differing from admittance control in that that $\dot{\mathbf{x}}$ instead of $\dot{\mathbf{x}}_d$ is the input to \mathbf{Z}_{d1} (illustrated in Figure 3.5 by the dashed line).

Motion-based impedance control schemes allow an interesting interpretation of the acceleration feedforward term. Assuming that no motion feedback is used, i.e. in case of open loop acceleration-based explicit force control, the control scheme is equivalent to impedance control with force feedback. Hence, motion-based impedance control with motion feedback and acceleration feedforward can be interpreted as impedance control with force feedback acting in parallel with motion-based impedance control. The gain of the motion controller can then be interpreted as a weighting factor of the two different haptic control schemes acting in parallel.

For haptic control implementations based on an inner loop closed on position standard position control algorithms can be applied. Most conventional single looped position control laws can be split in a block amplifying the control error (e. g. a PD controller) and a block converting the output signal to commanded motor torque. When interpreting the output of the first block (in Figure 3.5 named “position controller”) as a desired end-effector acceleration the latter (“AccContr”) can be considered as an open loop acceleration control law. Adding the sensed force mapped in joint space to the acceleration controller output aims at the compensation of the force applied by the operator. This positive force feedback can greatly reduce position errors due to interaction forces. Thus, virtual springs can be rendered with a stiffness exceeding by far the position controller stiffness. The benefit of external force compensation in position-based force control schemes is well known, see for example [GW95, CS94]. As the positive force feedback increases the computational effort only very little it should be included even in simple position control laws. Standard operational space position control laws, namely *resolved acceleration*, inverse Jacobian, and transposed Jacobian control, are discussed in the following. An experimental comparison of the position tracking performance of these algorithms is provided in appendix B.

Resolved Acceleration Control

Resolved acceleration control (*RAC*) can essentially be considered as an open loop acceleration control law incorporated in a PD position control in operational space. The commanded manipulator end-effector acceleration $\ddot{\mathbf{x}}_c$ is chosen with

$$\ddot{\mathbf{x}}_c = \ddot{\mathbf{x}}_d + \mathbf{K}_P (\mathbf{x}_d - \mathbf{x}) + \mathbf{K}_D (\dot{\mathbf{x}}_d - \dot{\mathbf{x}}), \quad (3.7)$$

where \mathbf{K}_P and \mathbf{K}_D denote the position and velocity gain matrices, respectively. Based on the inversion of (3.1) the actuation torque is then given by

$$\ddot{\mathbf{q}}_c = \mathbf{J}^{-1}(\mathbf{q}) \left(\ddot{\mathbf{x}}_c - \dot{\mathbf{J}}(\mathbf{q})\dot{\mathbf{q}} \right) \quad (3.8)$$

$$\begin{aligned} \boldsymbol{\tau} &= \mathbf{M}_q(\mathbf{q})\ddot{\mathbf{q}}_c + \mathbf{C}(\mathbf{q}, \dot{\mathbf{q}})\dot{\mathbf{q}} + \mathbf{h}(\mathbf{q}, \dot{\mathbf{q}}) \\ &\quad + \mathbf{g}(\mathbf{q}) + \mathbf{J}^T(\mathbf{q})\mathbf{f}. \end{aligned} \quad (3.9)$$

Equation (3.8) relates the end-effector acceleration to the manipulator joint accelerations. In case of a perfectly accurate model the open loop acceleration control law given by Equation (3.8) and (3.9) yields $\ddot{\mathbf{x}} = \ddot{\mathbf{x}}_c$, i.e. the plant together with the acceleration control law results in a double integrator system. Thus, the gain matrices are usually chosen with $\mathbf{K}_P = \omega^2 \mathbf{I}$ and $\mathbf{K}_D = 2\zeta\omega \mathbf{I}$ where ω is the desired bandwidth and ζ the desired damping ratio of the position control.

Resolved acceleration control is strongly related to *computed torque control*. In this scheme the commanded motor torques are also derived from equation 3.9 but the commanded joint acceleration $\ddot{\mathbf{q}}_c$ is the output of a joint space position controller:

$$\ddot{\mathbf{q}}_c = \ddot{\mathbf{q}}_d + \mathbf{K}_P (\mathbf{q}_d - \mathbf{q}) + \mathbf{K}_D (\dot{\mathbf{q}}_d - \dot{\mathbf{q}}). \quad (3.10)$$

Inverse Jacobian Control

In inverse Jacobian control (*IJC*) the commanded motor torque is

$$\boldsymbol{\tau} = \widehat{\mathbf{M}}_q \mathbf{J}^{-1} \ddot{\mathbf{x}}_c + \mathbf{h}(\mathbf{q}, \dot{\mathbf{q}}) + \mathbf{g}(\mathbf{q}) + \mathbf{J}^T(\mathbf{q})\mathbf{f}, \quad (3.11)$$

where $\widehat{\mathbf{M}}_q$ is an approximation of the device joint inertia matrix \mathbf{M}_q ; usually a constant diagonal matrix not considering couplings and the dependence on the manipulator configuration is applied. By comparison with Equation (3.8) and (3.9) one can see that inverse Jacobian control can be regarded as a crude approximation of resolved acceleration control as this open loop acceleration control law is based on $\widehat{\mathbf{M}}_q$ and neglects the gyroscopic term, that is $(\mathbf{C} - \mathbf{M}_q \mathbf{J}^{-1} \dot{\mathbf{J}}) \dot{\mathbf{q}}$.

Transposed Jacobian Control

Although inverse Jacobian control results in a significant reduction of computational effort compared to resolved acceleration control the calculation of \mathbf{J}^{-1} may become complicated when the DOF of the robot are increasing. This calculation can be avoided when applying an approximation of the manipulator mass/inertia matrix in task space, $\widehat{\mathbf{M}}_x$. Taking into account that the relation between the manipulator mass and inertia matrix is given with

$$\widehat{\mathbf{M}}_x = \mathbf{J}^{-T} \widehat{\mathbf{M}}_q \mathbf{J}^{-1}, \quad (3.12)$$

one can derive a computationally less demanding control law based on the transposed Jacobian matrix (*TJC*):

$$\boldsymbol{\tau} = \mathbf{J}^T \widehat{\mathbf{M}}_x \ddot{\mathbf{x}}_c + \mathbf{h}(\mathbf{q}, \dot{\mathbf{q}}) + \mathbf{g}(\mathbf{q}) + \mathbf{J}^T(\mathbf{q}) \mathbf{f}. \quad (3.13)$$

A drawback is that \mathbf{M}_x is usually varying much stronger with the robot configuration than \mathbf{M}_q impairing the accuracy of an approximation with a constant matrix.

3.3 Stability Aspects

It has been shown in Section (3.2) that the accuracy of the haptic feedback improves with an increase of the controller gains. Most theoretical investigations of force control schemes that assume the robot's mechanical structure to be rigid and the implementation of the control law continuous in time allow controller gains to go to infinity without producing instability [AH87, MB86, Epp88]. In practice, however, the gains cannot be increased beyond some limit. Among the possible sources for stability problems of haptic devices are:

- sampling rate of time discrete implementation
- stiction and Coulomb friction
- actuator saturation and bandwidth
- sensor noise
- flexibility of robot joints and links
- sensor dynamics
- virtual environment dynamics
- human arm dynamics

- operator's dynamic force/motion input

González and Widman [GW95] investigated the effect of the time discrete implementation of force control algorithms. It is shown that the interaction of a robot with a stiff environment possibly results in a fast highly underdamped closed loop system that requires very high sampling rates to maintain stability. The inclusion of environmental force compensation by force feedforward (see Section (3.2.2)) is proposed to slower the apparent dynamics of the plant. The role of damping regarding the robustness of discrete time control implementations is discussed by Qian and De Schutter [QD92b, QD92a]. They propose the introduction of active linear and nonlinear damping to increase the robustness [QD92a] and the use of low pass filtering to cope with insufficient sampling rates [QD92c]. They prove low pass filtering with a cut off frequency sufficiently below the system open loop resonance frequency to guarantee stability. Such a method is certainly not rewarding for the control of haptic interfaces due to the stringent requirement for an high force bandwidth.

The effect of nonlinear damping due to Coulomb friction and stiction on force-based explicit force controlled robots are investigated by Townsend [Tow88] with focus on integral control. He points out that Coulomb friction can have a stabilizing effect by means of extending the stability bounds of the controller gain but may lead to an input dependent stability (as a remedy they propose to apply a saturation to the force error signal). Stiction may reduce the stability bounds below the bounds set by Coulomb friction. Moreover, it can cause the applied force to enter a limit cycle. In [QD92b] the effects of stiction and Coulomb friction on the time discrete implementation of proportional force-based explicit force control is studied. A stabilizing effect of Coulomb friction due to its addition of positive damping to the system is identified. Stiction adds a negative damping to the system and therefore may cause instability. However, this destabilizing effect becomes smaller with increase of the manipulator inertia, feedback gain, and the environment stiffness the robot is interacting with. This analysis suggests that stiction is rarely the cause of stability bounds observed for robots under proportional force-control.

The effect of control signal saturation is addressed by González and Widman [GW92]. Applying standard phase plane analysis techniques stability for proportional force-based explicit force control is proven when the forward loop gain is sufficiently large. Moreover, an significant extension of the stability bounds for discrete time implementations is observed. However, the effect of saturation in case of position-based explicit force control where the force error is usually integrated twice is not investigated. A limited actuator bandwidth clearly has a potential destabilizing effect. But for high bandwidth systems using high-bandwidth current amplifiers the actuator dynamics do not seem to be the factor causing stability problems [Epp88].

The possibly destabilizing effect of flexibility in the robot structure is described by Eppinger [Epp88]. A problem in force controlled robots using force feedback is the *non-collocation* of the actuator and the force sensor (i. e. they are not attached to the same point on the robot arm). The flexibility of the joints or links results in dynamics between the actuator and the sensor adding more poles than zeros to the open-loop transfer function from the actuator to the sensor. This additional phase lag causes the open-loop phase to drop below -180° clearly predicting an upper bound for the gain of proportional force-feedback control. It is also illustrated that flexibilities not physically located between the sensor and actuator (e. g. mounting base and end-effector compliance, the dynamics of the human arm) add poles and zeros in equal number. Therefore, they do not necessarily

adversely affect the system performance. Control approaches for the compensation of non-collocated vibration modes are described in [Rea94].

Ensuring stability of haptic systems is a challenging task since the device is in feedback with the virtual environment and the human operator. The dynamics of the virtual environment may vary over a large range of impedances/admittances and can be highly nonlinear. Modelling the human arm impedance seems to be elusive considering that the parameters vary with muscle activity [Hog89, KH94]. Moreover, to model the human as a static impedance is neglecting possible influences of the operator's dynamic inputs. These uncertainties and nonlinear components in the dynamics of the environment and operator result in rather conservative stability conditions as for instance presented by Kazerooni and Her [KH94]. A stability analysis of an one DOF haptic system considering all dynamic parameters of the virtual environmental and the operator to be known has been presented by Lawrence and Chapel [LC94]. A further problem is that the virtual environment dynamics are often rendered by an application software which is not customized for the specifications of the haptic device by means of taking into account the range of target impedances to which the device can response without producing instability. A solution proposed by Adams and Hannaford [AH02] is the use of passivity networks ensuring passivity as a sufficient condition for stability of the system. Hannaford and Ryu [HR02] introduced a control scheme based on the concept of a 'Passivity Observer' measuring the net energy of the network representing the haptic system and a 'Passivity Controller' which is an adaptive dissipative element absorbing net energy output. However, passivity based approaches have the drawback that the dynamics of the system is changed and thus transparency is at least partially lost.

3.4 Control of Haptic Interfaces with Kinematical Redundancies

The mapping

$$\dot{\mathbf{x}} = \mathbf{J}\dot{\mathbf{q}} \quad (3.14)$$

relates the n -dimensional joint velocity vector $\dot{\mathbf{q}}$ to the m -dimensional end-effector velocity vector $\dot{\mathbf{x}}$, where \mathbf{J} is the $m \times n$ Jacobian matrix of the manipulator. If $n > m$ the manipulator is said to be redundant with respect to the end-effector task and $n-m$ DOF are available to solve the redundancy on the condition that \mathbf{J} is full rank. In this case the range space of \mathbf{J} is the entire \mathbb{R}^m and the $n-m$ dimensional null space is spanned by the last $n-m$ input vectors \mathbf{v}_i of the matrix \mathbf{V} , which can be found by the singular value decomposition

$$\mathbf{J} = \mathbf{U}\mathbf{\Sigma}\mathbf{V}^T, \quad (3.15)$$

where $\mathbf{\Sigma} = [\mathbf{S} \ \mathbf{0}]$ is the $m \times n$ matrix with \mathbf{S} containing the singular values σ_i of \mathbf{J} on its diagonal. The columns of \mathbf{U} and \mathbf{V} are, respectively, the left (output) and right (input) singular vectors for the corresponding singular values. The columns of \mathbf{V} corresponding to vanishing singular values form an orthonormal basis of the null space of \mathbf{J} whereas the columns of \mathbf{U} corresponding to non-zero singular values span the range of \mathbf{J} . As \mathbf{J} approaches rank deficiency the singular value σ_m tends to zero and the end-effector velocity produced by a fixed joint velocity inline with \mathbf{v}_m decreases. At singular configurations (i. e.

$\text{rank}(\mathbf{J}) < m$) the range of \mathbf{J} does not cover the entire \mathbb{R}^m meaning that no end-effector motions can be achieved in certain directions.

The implications of kinematical redundancies on the haptic control schemes discussed above are as follows: Admittance control architectures involve a mapping of the end-effector motion to the joint motion requiring the inverse of the relation described by equation (3.14). A solution to this inverse kinematics problem, the calculation of the joint from the end-effector motion, is not uniquely determinable because there are fewer equations than unknowns. Impedance control implementations have a similar characteristic. The mapping of the end effector force to the joint torques via \mathbf{J}^T is only one of an infinite number of solutions as discussed by Khatib [Kha95]. Considering the haptic interface to be at rest and the operator exerting the force \mathbf{f} on the end-effector. Then, the motor torques calculated with $\boldsymbol{\tau} = \mathbf{J}^T \mathbf{f}$ keep the entire device at equilibrium. There exists, however, an infinite number of joint torque vectors causing no end-effector motion but a device selfmotion. In other words, a desired interaction force at the device tip can be produced by an infinite number of motor torque vectors.

In haptic human-device interaction local inversion methods have to be employed giving joint paths depending only on the local behavior of the end-effector path. The global trajectories are not known in advance because the device is moved by the operator at will. In the following, standard local solution approaches for the inverse kinematics problem, namely pseudoinverse control and the definition of an inverse function, are discussed. The characteristics of the inverse function method also applies for the much broader class of cyclic inverse kinematics techniques, because all these algorithms can also be formulated as inverse functions [BW88]. Cyclic algorithms have the property that every closed path in the end-effector space is tracked only by closed paths in the joint space.

3.4.1 Pseudoinverse Control

Resolution at the Kinematic Level

As proposed by Whitney [Whi69] a solution to equation (3.14) can be found by using the Moore-Penrose generalized inverse $\mathbf{J}^\#$ of the Jacobian matrix, which yields

$$\dot{\mathbf{q}} = \mathbf{J}^\# \dot{\mathbf{x}} \quad \text{with} \quad \mathbf{J}^\# = \mathbf{V} \boldsymbol{\Sigma}^\# \mathbf{U}^T, \quad (3.16)$$

where $\boldsymbol{\Sigma}^\#$ is the transpose of $\boldsymbol{\Sigma}$ with every non-zero singular value replaced by its reciprocal. Although the motion is pointwise optimal in a least squares sense, meaning that the solution minimizes the quadratic cost functional of joint velocities

$$g(\dot{\mathbf{q}}) = \frac{1}{2} \dot{\mathbf{q}}^T \dot{\mathbf{q}}, \quad (3.17)$$

there is no guarantee that the manipulator does not approach singular configurations. In order to avoid excessive joint velocities at operations in the neighborhood of singularities the use of the *singularity robust inverse* \mathbf{J}^* has been proposed [Nak91]. Contrary to the pseudoinverse it does not provide an exact solution to equation (3.14) but yields joint velocities minimizing

$$g(\dot{\mathbf{q}}, \dot{\mathbf{x}}) = (\dot{\mathbf{x}} - \mathbf{J}\dot{\mathbf{q}})^T (\dot{\mathbf{x}} - \mathbf{J}\dot{\mathbf{q}}) + \lambda^2 \dot{\mathbf{q}}^T \dot{\mathbf{q}}, \quad (3.18)$$

where the scalar λ determines the weighting between the exactness of the end-effector motion and the velocity of the joints. The joint motion is then computed by solving the following equation:

$$\dot{\mathbf{q}} = \mathbf{J}^* \dot{\mathbf{x}} \quad \text{with} \quad \mathbf{J}^* = \mathbf{J}^T (\mathbf{J}\mathbf{J}^T + \lambda \mathbf{I})^{-1}. \quad (3.19)$$

An inverse kinematics algorithm based on the singularity robust inverse has for example been used in a telepresence system where it successfully enabled operations of the redundant telemanipulator near singularities [PUB06]. Its application to the control of haptic interfaces is, however, less rewarding because a deviation of the actual from the target end-effector motion deteriorates the transparency of the haptic feedback. More convenient are algorithms avoiding singular configurations by dedicated control of the null space motion. Such a redundancy resolution technique has been introduced by Liegeois [Lié77]. He proposed the additional usage of the null space projection operator

$$\dot{\mathbf{q}} = \mathbf{J}^\# \dot{\mathbf{x}} + (\mathbf{I} - \mathbf{J}^\# \mathbf{J}) \dot{\mathbf{q}}_0, \quad (3.20)$$

to project the joint velocities $\dot{\mathbf{q}}_0$, defined by a suitable choice of some side criterion, onto the null space of \mathbf{J} . It can be shown that this solution minimizes the following cost functional (see e.g. [SS00]):

$$g_{\dot{\mathbf{q}}_0}(\dot{\mathbf{q}}) = \frac{1}{2} (\dot{\mathbf{q}} - \dot{\mathbf{q}}_0)^T (\dot{\mathbf{q}} - \dot{\mathbf{q}}_0) \quad (3.21)$$

The meaning of this equation is, that a solution to the inverse kinematics problem is chosen that is in a least squares sense as close to the vector $\dot{\mathbf{q}}_0$ as possible. The potential function $H(\mathbf{q})$ depending on the joint angles \mathbf{q} can be used as a side criterion, which has to be extremized using the gradient minimization or maximization of potential fields. Thus, the joint velocities $\dot{\mathbf{q}}_0$ can be defined as

$$\dot{\mathbf{q}}_0 = \kappa \nabla H(\mathbf{q}). \quad (3.22)$$

Because $(\mathbf{I} - \mathbf{J}^\# \mathbf{J})$ is positive semi-definit equation (3.20) yields a selfmotion maximizing the objective function for a positive value of the real scalar κ and minimizing $H(\mathbf{q})$ for $\kappa < 0$. The gain κ does not have to be a static variable but can be dynamically changed. For example Li *et al.* [LGZY01] dynamically modified κ to ensure that the joint velocities of the inverse kinematics solution remain within the admissible operating range of the joint components.

A vast variety of side criteria $H(\mathbf{q})$ has been proposed in the literature. Hooper *et al.* [HT95] list 30 criteria covering the evaluation of the manipulator inertial, geometric, compliance, and kinetic energy performance as well as the distance from physical constraints. The combination of multiple optimization criteria is easily achieved by the formulation of one single composite performance index ψ as for example by using the weighted sum

$$\psi = w_1 C_1(\mathbf{q}) + w_2 C_2(\mathbf{q}) + \dots + w_n C_n(\mathbf{q}), \quad (3.23)$$

where $w_i > 0$ are the weighting factors and C_i normalized criteria values.

The most widely used side criterion for the avoidance of singular configurations is the *manipulability index*. The term manipulability can be understood as a definition of how easily and uniformly the manipulator can move around the workspace. Yoshikawa [Yos85b] first introduced a quantitative measure of manipulability as

$$w = \sqrt{\det \mathbf{J}\mathbf{J}^T} = \sigma_1 \sigma_2 \cdot \dots \cdot \sigma_m, \quad (3.24)$$

where σ_i are the singular values obtained by the singular value decomposition (3.15) of \mathbf{J} ; w can be used as a potential function $H(\mathbf{q})$. Examples for alternative side criteria for singularity avoidance are an index based on the *dynamic-manipulability ellipsoid* [Yos85a] evaluating the input-output transmission of accelerations as well as the Jacobian condition number or minimum singular value as a measure for the directional uniformity of the input-output transmissivity of velocities and the worst case transmissivity, respectively.

Weighted Pseudoinverse

Common modifications to the inverse kinematics solution described by equation (3.20) include the application of a *weighted Jacobian* resulting from a scaling of the joint velocity vector:

$$\dot{\mathbf{q}}_{\mathbf{W}^{\frac{1}{2}}} = \mathbf{W}^{\frac{1}{2}} \dot{\mathbf{q}} \quad \text{with} \quad \mathbf{W} = \mathbf{W}^{\frac{1}{2}} \mathbf{W}^{\frac{1}{2}} \quad (3.25)$$

The matrix $\mathbf{W}^{\frac{1}{2}}$ is the symmetric positive-definite square root of the symmetric positive-definite weighting matrix \mathbf{W} and $\dot{\mathbf{q}}_{\mathbf{W}^{\frac{1}{2}}}$ the weighted joint velocity vector. The end-effector velocity is then given with

$$\dot{\mathbf{x}} = \mathbf{J} \mathbf{W}^{-\frac{1}{2}} \dot{\mathbf{q}}_{\mathbf{W}^{\frac{1}{2}}} = \mathbf{J}_{\mathbf{W}^{-\frac{1}{2}}} \dot{\mathbf{q}}_{\mathbf{W}^{\frac{1}{2}}} \quad (3.26)$$

where $\mathbf{J}_{\mathbf{W}^{-\frac{1}{2}}}$ is called the weighted Jacobian. Considering, that at kinematically nonsingular configurations the Moore-Penrose pseudoinverse can be calculated with

$$\mathbf{J}^{\#} = \mathbf{J}^T (\mathbf{J} \mathbf{J}^T)^{-1} \quad (3.27)$$

the inverse kinematics solution when solving equation (3.26) with the technique described by equation (3.16) and mapping the result to back to the unweighted joint velocity space is:

$$\dot{\mathbf{q}} = \mathbf{W}^{-\frac{1}{2}} \mathbf{J}_{\mathbf{W}^{-\frac{1}{2}}}^{\#} \dot{\mathbf{x}} = \mathbf{W}^{-1} \mathbf{J}^T (\mathbf{J} \mathbf{W}^{-1} \mathbf{J}^T)^{-1} \dot{\mathbf{x}} = \mathbf{J}^{\mathbf{W}^{\#}} \dot{\mathbf{x}} \quad (3.28)$$

The matrix $\mathbf{J}^{\mathbf{W}^{\#}}$ is also called the *weighted pseudoinverse*. Its solution produces a joint motion minimizing the cost functional

$$g_{\mathbf{W}}(\dot{\mathbf{q}}) = \frac{1}{2} \left(\mathbf{W}^{\frac{1}{2}} \dot{\mathbf{q}} \right)^T \mathbf{W}^{\frac{1}{2}} \dot{\mathbf{q}} = \frac{1}{2} \dot{\mathbf{q}}^T \mathbf{W} \dot{\mathbf{q}}. \quad (3.29)$$

In the same way, the solution approach described by equation (3.20) applied to equation (3.26) produces the following result:

$$\dot{\mathbf{q}} = \mathbf{W}^{-\frac{1}{2}} \left(\mathbf{J}_{\mathbf{W}^{-\frac{1}{2}}}^{\#} \dot{\mathbf{x}} + \left(\mathbf{I} - \mathbf{J}_{\mathbf{W}^{-\frac{1}{2}}}^{\#} \mathbf{J}_{\mathbf{W}^{-\frac{1}{2}}} \right) \mathbf{W}^{\frac{1}{2}} \dot{\mathbf{q}}_0 \right) = \mathbf{J}^{\mathbf{W}^{\#}} \dot{\mathbf{x}} + \left(\mathbf{I} - \mathbf{J}^{\mathbf{W}^{\#}} \mathbf{J} \right) \dot{\mathbf{q}}_0. \quad (3.30)$$

The solution is then optimal in terms of minimizing the cost functional

$$g_{\mathbf{W}, \dot{\mathbf{q}}_0}(\dot{\mathbf{q}}) = \frac{1}{2} (\dot{\mathbf{q}} - \dot{\mathbf{q}}_0)^T \mathbf{W} (\dot{\mathbf{q}} - \dot{\mathbf{q}}_0). \quad (3.31)$$

When applying the weighted pseudoinverse for the calculation of the homogeneous solution of the inverse kinematics problem one has to consider that the weighted pseudoinverse null space transformation $(\mathbf{I} - \mathbf{J}^{\mathbf{W}^{\#}} \mathbf{J})$ is usually not symmetric and thus non-definite. Definiteness is, however, needed to ensure that the homogeneous solution extremizes the performance criterion. As shown in [Nem97] semidefiniteness can be assured when multiplying the gradient of the side criterion with \mathbf{W}^{-1} :

$$\dot{\mathbf{q}}_0 = \mathbf{W}^{-1} \kappa \nabla H(\mathbf{q}). \quad (3.32)$$

Further insight into the effect of the weighting can be obtained when considering that equation (3.30) partitions the joint velocity space into two subspaces: one subspace including all homogeneous solutions, the range of $\mathbf{J}^{W\#}\dot{\mathbf{x}}$, and another subspace including the particular solutions, the range of $(\mathbf{I} - \mathbf{J}^{W\#}\mathbf{J})$. The first is also referred to as the *active joint velocity space* and the latter the *null joint velocity space*. From (3.30) one can see that the active joint velocity space depends on the choice of the weighting matrix. Vectors lying entirely in the active joint velocity space are perpendicular to the columns of $(\mathbf{I} - \mathbf{J}^{W\#}\mathbf{J})$. Needless to say, that null joint velocity space is not affected by the weighting as it equals the null space of the Jacobian. The effect is as follows: Consider a joint velocity vector yielding a non-zero end-effector velocity. Then, it depends on the definition of the weighting matrix whether the joint velocity is a purely active velocity or a combination of active and null joint velocity components. Only in case of no end-effector motion $\dot{\mathbf{q}}$ is by definition entirely in the null joint velocity space.

The use of a weighted pseudoinverse can be beneficial in several ways: One option is the scaling of the joint velocities with a diagonal weighting matrix to increase or penalize the influence of certain joints on the end-effector motion. This is for example advantageous in case of significant differences in the velocity capability amongst the joints. Chan and Dubey [CD95] use an dynamic weighting matrix to improve the joint limit avoidance capability by means of increasing the weights connected to joints approaching joint limits. As a consequence, the performance criterion is also considered in the particular solution of the inverse kinematics problem. Another approach is the application of the joint inertia matrix \mathbf{M}_q as weighting matrix. The resultant weighted pseudoinverse $\mathbf{J}^{M_q\#}$ is also called *inertia weighted pseudoinverse* or *dynamically consistent inverse* of the Jacobian matrix. It produces a particular solution that minimizes the instantaneous kinetic energy as emphasized by Hollerbach and Suh [HS85].

Resolution at the Acceleration Level

The resolution of the redundancy at the acceleration level is for example required in admittance control architectures with inner operational space motion control (e.g. resolved acceleration control) where the controller output has the physical meaning of an acceleration in the operational space. Please note, that these control algorithms provide a largely different closed loop behavior when compared to implementations with joint space control. As a loop closure in joint space aims at keeping the entire device structure at the target configuration it renders a stiff device structure. Operational space position control specifies the end-effector position but not the complete device posture. As a matter of this fact disturbance forces caused for example by operator interference with the device structure effect a corresponding null space motion. This added compliancy is advantageous in terms of safety aspects.

At redundancy resolution in the acceleration domain the inverse of the following relation has to be found:

$$\ddot{\mathbf{x}} = \mathbf{J}\ddot{\mathbf{q}} + \dot{\mathbf{J}}\dot{\mathbf{q}}. \quad (3.33)$$

The general inverse solution to this equation can be obtained by differentiating equation (3.30) with respect to time:

$$\begin{aligned}\ddot{\mathbf{q}} &= \mathbf{J}^{W\#} \ddot{\mathbf{x}} + \dot{\mathbf{J}}^{W\#} \dot{\mathbf{x}} + (\mathbf{I} - \mathbf{J}^{W\#} \mathbf{J}) \ddot{\mathbf{q}}_0 - (\mathbf{J}^{W\#} \dot{\mathbf{J}} + \dot{\mathbf{J}}^{W\#} \mathbf{J}) \dot{\mathbf{q}}_0 \\ &= \mathbf{J}^{W\#} (\ddot{\mathbf{x}} - \dot{\mathbf{J}} \dot{\mathbf{q}}) + \mathbf{J}^{W\#} \dot{\mathbf{J}} \dot{\mathbf{q}} + \dot{\mathbf{J}}^{W\#} \dot{\mathbf{x}} + (\mathbf{I} - \mathbf{J}^{W\#} \mathbf{J}) \ddot{\mathbf{q}}_0 - (\mathbf{J}^{W\#} \dot{\mathbf{J}} + \dot{\mathbf{J}}^{W\#} \mathbf{J}) \dot{\mathbf{q}}_0.\end{aligned}\quad (3.34)$$

With (assuming \mathbf{J} to have full rank)

$$\mathbf{J}^{W\#} \dot{\mathbf{J}} + \dot{\mathbf{J}}^{W\#} \mathbf{J} = \frac{d}{dt}(\mathbf{J} \mathbf{J}^{W\#}) = \frac{d}{dt}(\mathbf{I}) = \mathbf{0} \quad (3.35)$$

and substituting $\dot{\mathbf{q}}$ with equation (3.30) the final solution is:

$$\ddot{\mathbf{q}} = \mathbf{J}^{W\#} (\ddot{\mathbf{x}} - \dot{\mathbf{J}} \dot{\mathbf{q}}) + (\mathbf{I} - \mathbf{J}^{W\#} \mathbf{J}) (\dot{\mathbf{J}}^{W\#} \dot{\mathbf{x}} - \dot{\mathbf{J}}^{W\#} \mathbf{J} \dot{\mathbf{q}}_0 + \ddot{\mathbf{q}}_0) \quad (3.36)$$

The first term of this equation renders the active and the second the null joint acceleration. The advantage of using the inertia weighted pseudoinverse of the Jacobian is the fact, that it is the only one where the application of external forces at the end-effector produces pure active and no null joint accelerations [FK97]. The validity of this property can be verified by showing that joint accelerations induced by arbitrary external end-effector forces are perpendicular to the columns of the null space term $(\mathbf{I} - \mathbf{J}^{W\#} \mathbf{J})$. Substituting $\ddot{\mathbf{q}}_0$ by $(-\mathbf{M}_q^{-1} \mathbf{J}^T \mathbf{f})$ gives:

$$\begin{aligned}- (\mathbf{I} - \mathbf{J}^{M_q\#} \mathbf{J}) \mathbf{M}_q^{-1} \mathbf{J}^T \mathbf{f} &= - (\mathbf{I} - \mathbf{M}_q^{-1} \mathbf{J}^T (\mathbf{J} \mathbf{M}_q^{-1} \mathbf{J}^T)^{-1} \mathbf{J}) \mathbf{M}_q^{-1} \mathbf{J}^T \mathbf{f} \\ &= - (\mathbf{M}_q^{-1} \mathbf{J}^T - \mathbf{M}_q^{-1} \mathbf{J}^T (\mathbf{J} \mathbf{M}_q^{-1} \mathbf{J}^T)^{-1} \mathbf{J} \mathbf{M}_q^{-1} \mathbf{J}^T) \mathbf{f} \\ &= - (\mathbf{M}_q^{-1} \mathbf{J}^T - \mathbf{M}_q^{-1} \mathbf{J}^T) \mathbf{f} = \mathbf{0}.\end{aligned}\quad (3.37)$$

In [BK00] Bruyninckx and Khatib revealed that the application of the inertia weighted pseudoinverse has also a strong physical meaning. Consider a redundant robot with freely rotating joints not actuated by motor torque. When exerting external forces on the end-effector and assuming zero gravitational torques the device joint motion follows exactly the joint accelerations predicted by the particular solution using the inertia weighted pseudoinverse. In other words, with this weighting externally induced end-effector accelerations can only generate purely active and no null joint accelerations. The inertia weighted pseudoinverse is therefore considered by the authors as the ‘natural’ solution to the inverse kinematics problem.

A detailed description of an implementation of resolved acceleration control involving redundancy resolution at the acceleration level is given by Natale *et al.* [NSV99]. The proposed algorithm includes a control of the null space acceleration guarantying stable null space motion and offering the possibility for the optimization of a side criterion.

Resolution at the Torque Level

At impedance control implementations the control of the selfmotion in addition to the end-effector force trajectory tracking can be achieved by the use of the dynamically consistent relationship between the operational force and the joint torques introduced by Khatib [Kha95]:

$$\boldsymbol{\tau} = \mathbf{J}^T \mathbf{f} + (\mathbf{I} - \mathbf{J}^T \mathbf{J}^{M_q\#T}) \boldsymbol{\tau}_0. \quad (3.38)$$

This equation can be applied to the impedance control architecture discussed in section (3.2.1) when setting \mathbf{f} as the sum of the force feedforward and the force controller output. The use of the inertia weighted pseudoinverse $\mathbf{J}^{M_q\#T}$ is needed to achieve the property of the null space term $(\mathbf{I} - \mathbf{J}^T \mathbf{J}^{M_q\#T}) \boldsymbol{\tau}_0$ to produce no end-effector acceleration for an arbitrarily chosen joint torque vector $\boldsymbol{\tau}_0$. Indeed, Featherstone and Khatib [FK97] revealed some equivalence between redundancy resolution in the torque and acceleration level when using the inertia weighted pseudoinverse. As a matter of this fact, the application of a suitable $\boldsymbol{\tau}_0$ yields a null space movement that is dynamically decoupled from the force control task in the operational space. In [Kha95] the gradient of a side criterion is used for $\boldsymbol{\tau}_0$ to yield a well-directed selfmotion.

3.4.2 Inverse Function

Another approach to solve the redundancy is defining off-line a single inverse function relating to each point in a specified subset of the end-effector space a unique joint coordinate vector. Because the inverse function is defined at the position level this inversion approach yields *cyclic* (also called *conservative*) motion. Cyclic motion means that every closed path in the end-effector space is tracked only by closed paths in the joint space. This is in contrast to pseudoinverse control. Although equation (3.26) relates at a given joint configuration a unique joint rate to the end-effector velocity, it does not, in general, make the joint vector a function of the tip position, even not in case the device motion is always started from a predefined initial configuration. This statement can easily be proven by simulation experiments (an analytical prove has been provided by Klein and Huang [KH83]; an in-depth analysis of the joint angle drift produced by pseudoinverse control has been provided by Luo and Ahmad [LA92]). The addition of a null space term to optimize a side criterion, see equation (3.30), yields a dependence of the device posture at the target end-effector position not on the path only but also on the speed of the path following. On the other hand, at low end-effector speed and high gain of the selfmotion term the device posture can be kept very close to the side criterion minimum producing approximately a cyclic motion.

The main advantage of cyclic inversion methods is the fact, that the analysis of the kinematical and dynamical device performance is equivalent to non-redundant manipulators. This allows for example the systematic determination of a dextrous workspace along with a specification of the output capability. In case of repetitive end-effector motions the requirements on the joint force and velocity capability, for instance, can be derived from a single simulation or hardware experiment. For non-conservative algorithms the verification of performance specifications is very hard to obtain because resultant joint configurations can be exceedingly difficult to predict. As a consequence, the appropriateness of these algorithms is typically only shown by extensive simulation experiments and hardware tests providing, however, no proof for the compliance with the specifications. This approach lacks of systematics; the identification of qualified test scenarios depends strongly on the intuition and experience of the experiment designer.

At the downside, Baker and Wampler [BW88] revealed fundamental restrictions on the invertible workspace achievable with inverse functions (and all other conservative inversion methods as for instance the extended Jacobian method introduced by Baillieul [Bai85]). The main statement of Baker and Wampler in view of the inverse kinematics solution of the VISHARD10 device is the fact, that it is not possible to define an inverse function or

an extended Jacobian algorithm without singularities for a 3 DOF orientation workspace covering the entire sphere, no matter how much redundant joints are used. In this context the term ‘singularity’ does not refer to kinematical singularities but to *algorithmic singularities*. At algorithmic singularities the manipulator is far from a kinematical singularity but the inversion algorithm produces unbounded joint velocities when moving through these locations along certain directions.

Restrictions on planar workspaces are presented by Wampler in [Wam88]. This article shows high relevance on the ViSHARD10 control because it considers planar serial manipulators with n revolute joints. It is proven that a necessary condition for an invertible workspace with the shape of a disk centered on the origin is a radius not exceeding $\sum l_i - 2l_{\max}$, where l_i is the length of the i -th link and l_{\max} the maximum link length. The implications for the ViSHARD10 control are as follows: Consider, that joint 6 and 7 are controlled to mimic the operation of a prismatic joint adjusting height only. Then, the positioning of the end-effector is solely determined by the posture of the SCARA segment and the above statement constitutes that cyclic inverse kinematic solution algorithms allowing arbitrary end-effector motions cannot enclose a horizontal disk centered at the base with a radius larger than 0.5 m. Allowing the use of joint 6 and 7 for positioning in the horizontal plane virtually adds a fifth link of variable length (including negative values) to the SCARA segment. Because the arguments of Wampler’s proof apply also for such systems the bound for the workspace radius is increased by the maximum length of the projection of link 6 and 7 on the horizontal plane. This, however, results in a strong coupling of the translational with the orientational DOF.

Despite of these fundamental restrictions the application of the inverse function approach can be rewarding for applications that do not require maximum workspace sizes. It also has to be noted, that the redundant DOF provide freedom in the design of the inverse function offering the option to consider application specific requirements.

3.5 Control of the ViSHaRD Haptic Interfaces

3.5.1 General Control Schemes

The control schemes of the ViSHARD devices essentially conform to the algorithms described in section 3.2.1 and 3.2.2. For ViSHARD3 and 6 both, impedance and admittance control, has been implemented. The focus of the ViSHARD10 control has been solely on admittance control because in account for the significant nonlinearities and large dynamic properties of this interface the implementation of impedance control characterized by an inferior disturbance rejection capability has been considered as less rewarding.

The impedance control algorithms employ a PD force controller along with model-based compensation of friction and gravity (for a detailed description of the friction compensator see section 4.4). A model-based compensation of gyroscopic effects has not been included because it turned out to provide a very strange haptic sensation. A possible reason is the correspondence of the closed loop with the natural device dynamics in case of no such compensation. The nonlinear disturbance forces are therefore easy to anticipate for the operator. With the elimination of gyroscopic effects the closed loop dynamics remains highly nonlinear during end-effector accelerations but tends to zero at steady tip velocity, a behavior that does not fit to the operator’s experience and expectation. In admittance

control, however, the elimination of gyroscopic effects is highly convenient because it goes along with a feedback linearization of the operational space mass matrix.

At high control gains the impedance control of the ViSHARD3 interface shows the susceptibility to produce poorly damped force oscillations around $\omega_0 = 29$ Hz. This frequency approximately corresponds to the mechanical resonance frequency of the joint components in isometric conditions, that is with locked gear output. A simple heuristic remedy is the application of a notch filter to the commanded motor torque. The ad hoc design of the filter has the transfer function

$$G_{\text{notch}}(s) = \frac{s^2 + 2 \cdot 0.01\omega_0 + \omega_0^2}{s^2 + 0.4\omega_0 + \omega_0^2}. \quad (3.39)$$

As the application of two filters acting in series could completely eliminate the force oscillations no further optimization of its design has been undertaken.

The admittance control algorithms of ViSHARD3 and 6 employ resolved acceleration control in the inner control loop. For comparison purposes also \mathbf{J}^{-1} and \mathbf{J}^T control has been implemented for ViSHARD3 and a computed torque scheme for ViSHARD6. The ViSHARD10 control scheme is illustrated in figure 3.6. The inner position control loop applies the computed torque scheme described by equation (3.10) and (3.9). The desired joint acceleration for the acceleration feedforward of the position control is obtained by numerical differentiation of $\dot{\mathbf{q}}_d$, the output of the inverse kinematics solution algorithm. In the following sections the implementation of the virtual model and the inverse kinematics solution approaches are described.

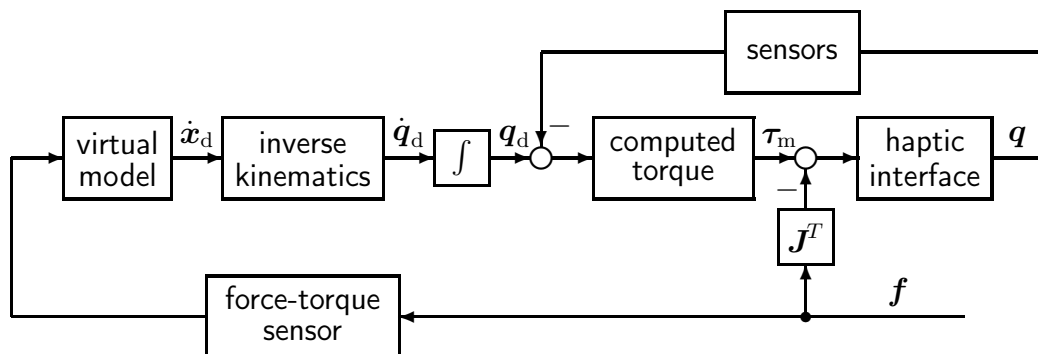


Figure 3.6: Admittance control scheme of ViSHARD10

3.5.2 Virtual Model

As the majority of commercially available haptic interfaces does not provide force sensing capability most haptic rendering software tools accept motion input and provide force output. It is therefore straightforward to interface these rendering engines with the ViSHARD devices when operated in the impedance mode. As already discussed in section 3.2.2 a connection of this type of rendering software to the admittance control scheme can be accomplished with a virtual coupling as illustrated in figure 3.7. Usually the virtual impedance \mathbf{Z}_{d1} is used to define the desired spring/damper characteristics of the virtual model whereas the definition of the mass and inertial parameters are left to the virtual admittance \mathbf{Z}_{d2}^{-1} . An increase of \mathbf{Z}_{d2}^{-1} decreases the deviation between the target impedance \mathbf{Z}_{d1} provided

by the virtual rendering engine and the actual closed loop dynamics. One has, however, to consider, that the minimum target inertia of the device is bounded by stability, see chapter 5.3.2. Without fail this fact has to be incorporated into the virtual model design. The same is true when using haptic rendering software of admittance type that directly relates the interaction force to motion.

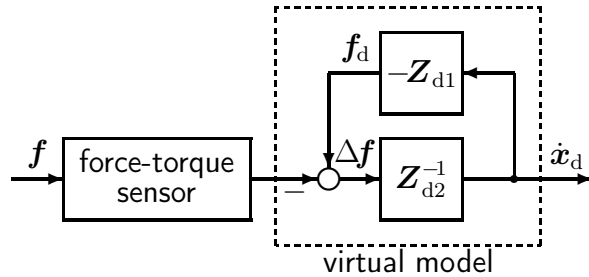


Figure 3.7: Virtual admittance implemented as coupling between impedance and admittance

The implementation of the virtual admittance is illustrated in figure 3.8. The render of the VISHARD6 and 10 rotational inertia and damping is based upon the well known Euler's dynamical equations of rotation. The indices B and E indicate the corresponding quantity to be defined respective the coordinate system $\{B\}$ and $\{E\}$ defined in figure 2.3, 2.5, and 2.7. The rotation matrices ${}^E_B\mathbf{R}$ and ${}^B_E\mathbf{R}$ map vectors from the base to the end-effector coordinate system and vice versa. The matrix ${}^E\dot{\mathbf{R}}$ yields a transformation from ω_d^E to the time derivative of a set of Euler angles $\dot{\phi}$. Further details on these transformations along with closed form solutions are provided in [Moc05] and [Kim05]. The virtual mass, inertia, translational, and rotational damping is defined by the matrices $\mathbf{M}_{\text{trans}}$, \mathbf{M}_{rot} , $\mathbf{K}_{D,\text{trans}}$, and $\mathbf{K}_{D,\text{rot}}$, respectively. These parameters can be adjusted via a graphical user interface or passed as variables to the control algorithm. Possible extensions to this virtual admittance are for example the implementation of virtual spring forces to constrain the workspace of the haptic interface.

It depends on the control algorithm which output variables of the virtual admittance are used. Whereas $\dot{\phi}$ can be integrated to obtain a variable, that describes the end-effector orientation, the integral of ω_d^B does not have a physical meaning. Therefore, the Euler angles are used in case of operational space position control, that requires the calculation of an orientation error, or when applying an inverse kinematics solution operating at the angular position level. The well known disadvantage of Euler angles are representation singularities. These can, however, be avoided when using a set of Euler angles where these critical configurations correspond to the kinematical device singularities. Another undesirable property of Euler angles is the effect that a stiffness defined in the Euler space results in an equivalent operational space elasticity that is dependent on the end effector orientation [CNSV99]. For position control purposes in haptic control this does not seem to be problematic because the control stiffness typically exceeds the target stiffness defined by the virtual model by far. Thus, variations in the control stiffness are virtually impossible to perceive by the operator. In case of joint space position control no operational space orientation representation is required. Then, ω_d^B is directly mapped into the joint space allowing a transformation to the position domain by simple integration.

In order to compare the full with the partitioned inverse kinematics solution approach a large number of simulation experiments has been accomplished. In [UMB03] end-effector trajectories along horizontal circles centered at the origin have been investigated. Moreover, the performance of different side criteria for selfmotion optimization has been studied. Circular trajectories intersecting the center of the workspace have been analyzed in [UMB04]. As the height of the horizontal paths has been varied conclusions regarding the dependency of the results on the end-effector height could be drawn. Finally, the influence of the end-effector speed has been investigated in [UB06]. The results of the simulation experiments confirm an increased manipulability and effective singularity avoidance for the investigated end-effector paths when adding to pseudoinverse control a null space motion optimizing the manipulability index or the condition number of the Jacobian matrix. In fact, both optimization criteria produced similar results. The experiments also revealed two effects emphasizing that these solution approaches are local inversion methods not necessarily producing optimal joint motions: At certain end-effector heights the device configuration was trapped in a local minimum preventing a null space motion towards more dextrous configurations. Second, at high end-effector velocities the addition of the optimized selfmotion could give inferior results than pseudoinverse control without null space term. This is due to the fact, that the control of the selfmotion cannot account for future end-effector motions. A comparison of the full solution approach with the partitioned inverse kinematics solution indicates a significant potential for performance improvement when solving for all 10 DOF simultaneously.

Despite the superior potential of full inverse kinematics solutions hardware experiments have, so far, been restricted to the application of partitioned solutions. The non-consideration of full solution techniques is founded by safety concerns related to the coupling of the translational and rotational selfmotion producing joint motions more difficult to understand and anticipate for the operator. In the following, inverse kinematics algorithms for the wrist and the SCARA segment are described.

Wrist Inverse Kinematics

Inverse function: A simple inverse function for the redundant wrist can be defined when setting joint angle 5 to $q_5 = q_{5,0} - \sum_{i=1}^4 q_i$. Then, a unique solution for the remaining wrist joints can be determined. The benefit compared to nonredundant wrists is the possibility to place the interior singularities at any orientation in the horizontal plane by means of a proper choice of the constant $q_{5,0}$. This particular inverse function has the property that the orientation of link 5 respective the base coordinate system $\{B\}$ remains fixed for arbitrary motions of the positioning and orientation stage. This is advantageous in terms of collision avoidance; potential interference of the device structure with the operator is easy to anticipate; at bimanual interaction tasks collisions of the two devices are more easy to avoid.

Pseudoinverse control: Hardware experiments with pseudoinverse control revealed a significant dependency of the appropriateness of the produced solution on the choice of the weighting matrix in equation (3.30). A reasonable weighting has to consider the largely differing inertia around the wrist axes. Especially fast accelerations of joint 5 have to be avoided because the high inertial torques can excite flexible modes of the device structure. Moreover, these motions involve the rotation of large parts of the device structure which

is likely to disturb the operator. Conversely, the increase of the contribution of \mathbf{q}_{10} to the solution is rewarding due to the exceptionally low inertia around this axis. In [Moc05] a set of hardware experiments for the identification of a suitable weighting matrix is described in detail. The results indicate a benefit when scaling \dot{q}_8 , \dot{q}_{10} down and \dot{q}_5 up. The easement of motions around q_{10} relative to q_5 is necessary to avoid that rolling motions of the end-effector cause significant motions in q_5 . This is especially important when the end-effector orientation is close to vertical. Scaling down the velocity of joint 8 significantly reduces \dot{q}_5 in the particular solution when rotating the end-effector around the axis of joint 8. The penalization of \dot{q}_5 relative to \dot{q}_9 is important at rotations around the vertical axis when the end-effector orientation is close to horizontal. An appropriate choice of the weighting matrix is given with $\mathbf{W}^{\frac{1}{2}} = \text{diag}(3, 0.2, 1, 0.1)$.

Singularity avoidance by the optimization of a suitable side criterion requires the definition of the gain κ . This gain directly affects the speed of the null space motion yielding a fast approach of the locally optimal joint configuration for high values. This is desirable in order to avoid that fast end-effector motions drive the wrist in critical configurations. At the downside, large gains can result in null space motions producing high accelerations of joint 5. Hardware experiments revealed, that an appropriate balancing of the singularity avoidance robustness and the smoothness of the resultant joint 5 trajectories is indeed highly difficult to achieve with the application of side criteria based on the manipulability index or the condition number of the wrist Jacobian. Although parameter settings could be identified providing a convenient device response for almost arbitrary end-effector paths there was still one single critical motion producing undesirable high accelerations of joint 5.

This motion is illustrated in figure 3.9. It is created by rotating the end-effector from a vertical orientation ($z_E \parallel z_B$) around the axis of joint 9 into a horizontal orientation. In case of a fast end-effector rotation a considerable velocity of joint 5 is required to prevent the approach of a singular configuration (i. e. q_8^* and q_9 approach a multiple of π ; the first criterion is virtually automatically satisfied for horizontal end-effector configurations). The demand for high \dot{q}_5 is evident when considering that the effect of a slow selfmotion can easily be compensated by a corresponding adaptation of the end-effector trajectory. In other words, the singularity avoidance will be hard to achieve with moderate speeds of joint 5 if the operator tries to drive the end-effector in such a configuration at will.

Despite the accomplishment of a large number of hardware experiments applying various different weighting matrices and gains for the selfmotion no parameter set could be determined providing a good singularity avoidance at acceptable accelerations of joint 5 at these critical end-effector motions. One of the reasons for the unsatisfactory performance of the singularity avoidance based on the optimization of the manipulability index or condition number is the fact, that these side criteria are functions of q_8^* and q_9 . Thus, the nullspace motion can move joint 9 away from $q_9 = \pi(1/2 + k)$ (recalling, that singular configurations require $q_9 = k\pi$, these joint angles maximize the distance to singular configurations). The motion of joint 8 has, however, no impact on the distance to a singular configuration: singular configurations require the end-effector to be in a horizontal orientation. In these orientations \dot{q}_8^* does not lie in the nullspace of \mathbf{J}_{rot} causing q_8^* to remain fixed to the critical angle. The distance to the singularity is therefore solely determined by the position of joint 9.

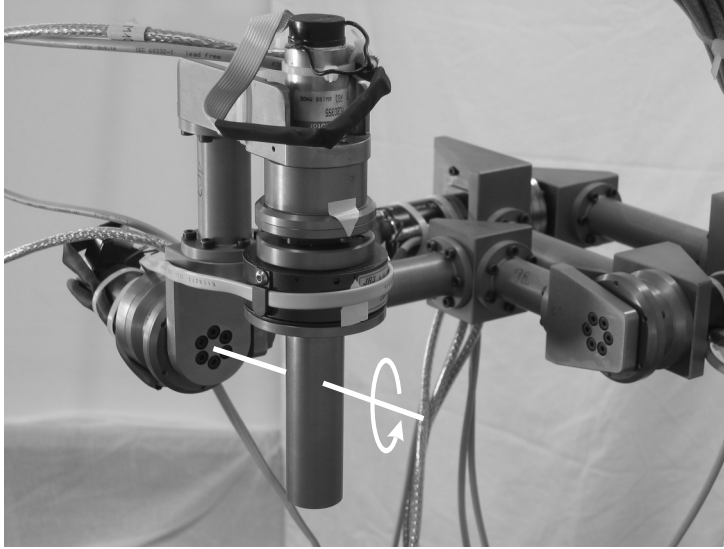


Figure 3.9: Critical end-effector motion: rotation around the axis of joint 9 drives the wrist towards a singular configuration producing high accelerations of joint 5

The actual implementation of the wrist pseudoinverse control applies therefore a side criterion directly maximizing the distance to singular configurations:

$$H(\mathbf{q}_{\text{rot}}) = q_9^2 - \pi q_9. \quad (3.43)$$

The minimization of this comparatively simple performance measure gives a selfmotion driving joint 9 towards $q_9 = \pi/2$. Practical experience confirmed that this side criterion provides significantly better results than the manipulability index and condition number: the singularity avoidance does not only require less peak acceleration of joint 5 but also turned out to be simpler to understand and predict by the operator.

Studying the performance of this redundancy resolution at the critical motion shown in figure 3.9 one can see, that a rotation of the end-effector from the horizontal orientation exactly around joint axis 9 produces no selfmotion at all because \dot{q}_9 does not lie in the nullspace of \mathbf{J}_{rot} . As a consequence, the wrist is driven into a singular configuration. In practice, however, the end-effector rotation is rarely exactly around the axis of joint 9. Hence, the singularity avoidance is typically successful, but the selfmotion can induce undesirable high accelerations of joint 5 for fast end-effector motions. This can be avoided by placing a virtual wall keeping q_9 within the bounds $[0^\circ + \zeta \quad 180^\circ - \zeta]$ with $0^\circ < \zeta < 45^\circ$, where ζ is a measure for the distance of the 3R wrist from a singular configuration. Because the side criterion given in equation (3.43) causes the selfmotion to drive this wall away from the current end-effector orientation, contacts with the virtual wall are likely to occur only in case of critical end-effector trajectories. The wall will then, however, avoid undesirable fast selfmotions.

The emphasize of the above discussion on the critical end-effector trajectories may cloud the fact that these motions rarely occur in practice. At all other interactions a robust singularity avoidance has been achieved. Therefore it can be concluded, that the pseudoinverse control approach can indeed offer an unlimited orientational workspace. Moreover, as the resultant selfmotion is simple to anticipate this solution appears to be well suited for human-system interaction.

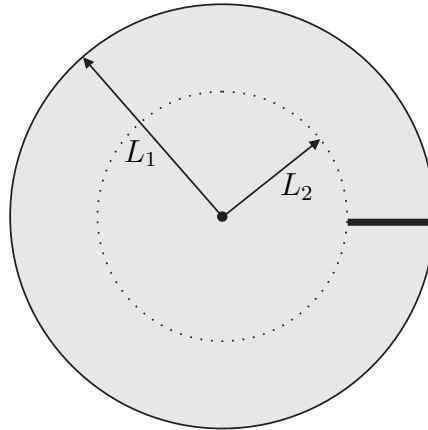


Figure 3.10: Exclusion of workspace area (thick line) to satisfy Wampler's necessary conditions for invertibility; $L_1 = 0.85$ m, $L_2 = 0.5$ m

Inverse Kinematics of the SCARA segment

Inverse function: The simplest inverse function is defined by controlling the SCARA segment to mimic the operation of two prismatic joints

$$q_1 = \arccos \frac{y}{2l_1} - \frac{3}{2}\pi, \quad q_2 = -2 \arccos \frac{y}{2l_1} + 2\pi, \quad (3.44)$$

$$q_3 = \arccos \frac{x}{2l_3} - q_1 - q_2, \quad q_4 = -2 \arccos \frac{x}{2l_3} + 2\pi, \quad (3.45)$$

where x and y are the end-effector position coordinates respective the coordinate system $\{B\}$ defined in figure(2.7). Considering the target specification of a translational velocity capability not less than 1 m/s the resulting workspace size is 0.85 m in the x - and 0.71 m in the y -direction (the admissible operating range of joint 2 and 4 is bounded by 0.9 rad/s and 1.2 rad/s, respectively).

Clearly, this workspace is much smaller than the target workspace specified in table 2.1 which is a disk with a radius of 0.85 m. From the discussion in section 3.4.2 it is known, that such a large area is not invertible. The fundamental restriction discussed by Wampler [Wam88] do, however, not forbid the inversion of larger workspaces when the motion through certain areas is not allowed. This idea is illustrated in figure 3.10 showing a circular workspace with 0.85 m radius centered at the origin that does not violate Wampler's necessary conditions for invertibility. The excluded area is indicated by the thick line. This restriction can be understood as a virtual wall placed inside the workspace area. In the following, the attempt to find an inverse function providing such a workspace is described.

The followed strategy was the construction of an inverse function in the form of a look-up table based on the results of numerical search algorithms. A comparatively straightforward way is to apply these search algorithms to an optimization problem of the following form:

$$\min_{\mathbf{q}} g(\mathbf{q}) \quad \text{such that} \quad \mathbf{f}(\mathbf{q}, \mathbf{x}) = \mathbf{0}, \quad (3.46)$$

where $\mathbf{x} \in \mathbb{R}^{2 \times 1}$ is a vector including the coordinates of i end-effector points on a predefined mesh in the workspace, $\mathbf{q} \in \mathbb{R}^{4 \times 1}$ the vector with the joint coordinates associated with

these points, \mathbf{f} the set of constraint functions ensuring that all related \mathbf{x}_i and \mathbf{q}_i satisfy the forward kinematics, and g the objective function evaluating the appropriateness of the inverse mapping.

As the avoidance of excessive joint velocities was deemed to be the most fundamental requirement for the applicability of the inverse function, objective functions evaluating the difference of the joint configurations of neighbored end-effector positions have been used. The comparison between two neighbored joint configurations $\mathbf{q}_a, \mathbf{q}_b$ is accomplished by forming the difference $\Delta\mathbf{q}_a^b = (\mathbf{q}_a - \mathbf{q}_b)/\Delta x_a^b$, where Δx_a^b is the cartesian distance between the related end-effector positions. Concatenating the difference vectors of all neighbored points into one single vector $\boldsymbol{\varphi}$, the objective function is given with

$$g(\mathbf{q}) = \|\boldsymbol{\varphi}(\mathbf{q})\|_p \quad (3.47)$$

where $\|\cdot\|_p$ denotes a suitable vector norm as for instance a p - or infinity norm.

It has to be noted, that (3.46) is hard to solve due to the high dimension of the search space and the nonlinear constraint functions. A drastic reduction of the complexity can be achieved when exploiting the fact, that only two parameters are needed to describe the configuration of the SCARA segment in the null space. Specifying for instance the position of joint 3 respective the coordinate system $\{B\}$ allows the computation of the complete set of joint angles (assuming an a priori agreement on the remaining discrete choices for ‘elbow up’ or ‘elbow down’ configurations). Accordingly, (3.46) can be reformulated as an optimization problem with inequality constraints within a search space of lower dimension. The inequality constraints are needed to verify that the parameters remain within the admissible search space. In case of using the cartesian position of joint 3 the permitted search space is given by the intersection of two circles with 0.5 m radius centered at the base and the tip of the SCARA segment.

A further improvement of the formulation of the optimization problem can be achieved by a proper coding of the joint 3 position coordinates yielding a rectangular search space independent on the end-effector position. This allows the application of efficient algorithms for bound-constraint optimization. The coding used in the following is explained in figure 3.11. The line g_1 connects the intersection points of the circles centered at the base and the tip. The cartesian distance between these points is given with $2\xi_{1,i}^*$. The line g_2 is the perpendicular to g_1 passing through the position of joint 3. The distance between the intersection points of g_2 with the circles is $2\xi_{2,i}^*$. In the used coding $\boldsymbol{\xi}_i^T = [\xi_{1,i} \quad \xi_{2,i}]$ the first entry $\xi_{1,i}$ describes the position of the intersection point of g_1 with g_2 along g_1 ranging from -1 to 1 when scaled with $\xi_{1,i}^*$. The second variable is a coding for the position of joint 3 on g_2 . Again, a scaling with $\xi_{2,i}^*$ yields values within the interval $[-1, 1]$. The optimization problem has then the following form:

$$\min_{\boldsymbol{\xi}} g(\mathbf{h}(\boldsymbol{\xi}, \mathbf{x})) \quad \text{such that} \quad \mathbf{x} \in [-\mathbf{1}, \mathbf{1}] \quad (3.48)$$

The vector $\boldsymbol{\xi} \in \mathbb{R}^{2i \times 1}$ concatenates the vectors $\boldsymbol{\xi}_i$ related to the i end-effector positions and \mathbf{h} is a set of nonlinear functions calculating the joint configurations \mathbf{q} from $\boldsymbol{\xi}$ and \mathbf{x} .

Figure 3.12 shows the workspaces for that the construction of an inverse function has been tried. Starting with an inversion of the darker area the workspace has been consecutively increased by addition of the brighter areas. The idea is to approach gradually an operating area with a shape similar to the workspace shown in figure 3.10. The dots

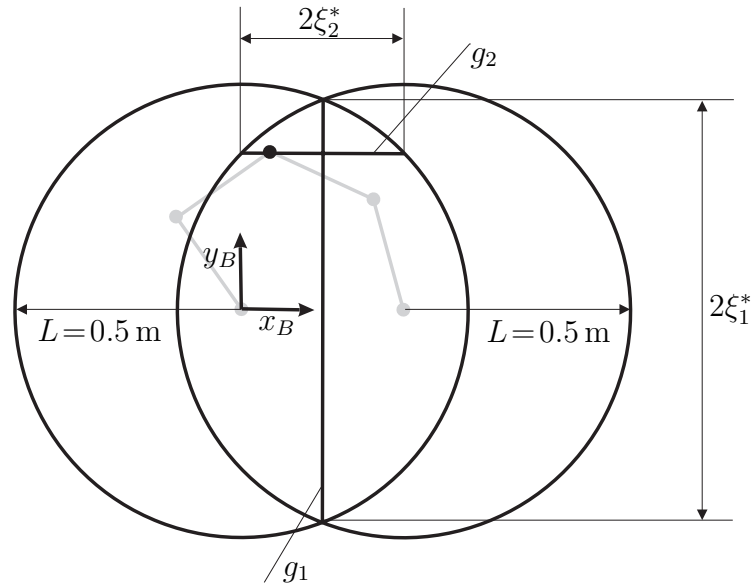


Figure 3.11: Coding of the joint 3 position to obtain a rectangular search space

indicate the mesh of end-effector positions considered in the optimization routine. As a local optimization algorithm⁴ has been applied to (3.48) it is not surprising that initial joint configurations chosen at random could not produce any useful results. A qualified initial solution has been obtained by separately identifying with numerical optimization 16 inverse functions, each for end-effector positions lying on one of the radial lines from the origin to the outer circle. In order to obtain similar solutions for neighbored lines and to avoid a singularity of the initial solution at the origin, the joint configuration at the start and endpoint has been predefined: The joint configuration at the origin has been set equal for all lines; the endpoint solutions differ only in the angle of joint 1. The predefined solutions have been obtained by maximization of the manipulability index. Due to the comparative low computational complexity of the resultant 16 optimization problems solutions close to optimum could be found by repetitive application of a local optimization algorithm from a large number of randomly generated initial solutions (also referred to as *multistart* technique for global optimization).

The norm used in the objective function (3.47) was the infinity norm in order to minimize the worst case joint rate for bounded end-effector velocities. As it is well known that gradient based search algorithms are inappropriate for this kind of functions the solution has been created by gradually increasing the norm from $\|\cdot\|_2$ to $\|\cdot\|_\infty$ by means of changing the norm when the optimization algorithms converged to a (local) minimum.

An evaluation of the results obtained by numerical optimizations in terms of the value of the objective function is summarized in table 3.1. The workspace number refers to the number of bright colored areas added to the dark workspace (see figure 3.12). Recalling, that the infinity norm is applied, this value corresponds to the maximum difference in the scaled joint angles between neighbored configurations. As the scaling applies the cartesian distance between the corresponding tip positions, this value can be interpreted as a lower bound on the maximum joint rate per end-effector velocity (lower bound because the mesh of considered tip positions is not infinitely dense).

⁴'fmincon' of the MATLAB optimization toolbox

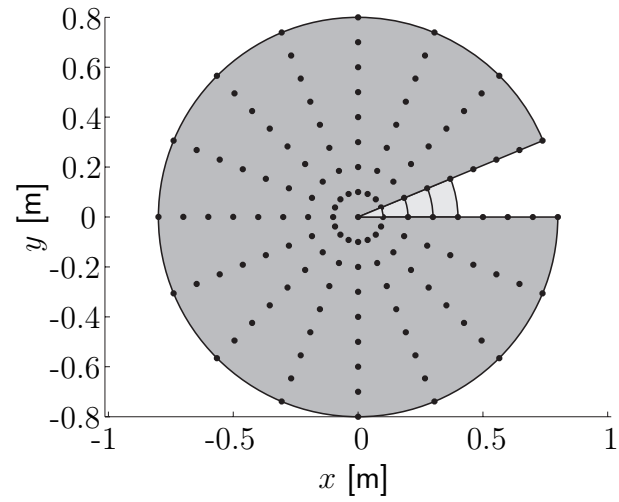


Figure 3.12: Inverted workspace; the dots indicate the mesh of end-effector positions considered in the optimization routine

Table 3.1: Optimization results

workspace	maximum joint rate per tip velocity
#0	> 4.767 rad/m
#1	> 5.836 rad/m
#2	> 7.366 rad/m
#3	> 9.849 rad/m
#4	> 12.408 rad/m

The results show an acceptable performance of the calculated inverse functions only for workspace #0. Considering, that the maximum velocity of joint 1 is 3.67 rad/s, the resultant (worst case) device velocity capability is around 0.77 m/s. An increase of the workspace results in a significant lowering of the velocity capability. The reason for the large dependency of the performance on the workspace size can be seen when viewing figure 3.13 and 3.14 showing the inverse solution obtained for workspace #0 and #2, respectively. Tip positions at the outer circle require an ‘outstretched’ configuration of the SCARA segment restricting possible solutions for joint angle 1 to a comparatively small range. Accordingly, there exist radial tip trajectories from the origin to the outer circle where joint 1 has to traverse almost 180°. Furthermore, there are neighbored radial trajectories with different sign in the motion of joint 1. This is apparent in figure 3.13 where already at the inner circles the solutions for joint 1 cover a large range. Please note, that the configurations plotted with the darkest and brightest color have neighbored tip positions. This fast spreading is prevented in the solution presented in figure 3.14 because the added workspace requires also the brightest and darkest line to have similar joint angles at circles with radii up to 0.2 m. As a matter of this fact, faster motions of joint 1 are needed to approach the final configuration required at the outer circle. Obviously, further increase of the workspace size gives an additional deferment of the joint 1 motion.

Pseudoinverse control: Even though simulation studies indicated a robust singularity avoidance of pseudoinverse control with optimization of the manipulability index, it turned out that the approach of such configurations could easily be accomplished when the device is guided by a human operator actively reacting to the selfmotion. Modifications of the weighting matrix and the gain of the null space term could prevent excessive joint velocities along certain critical trajectories but, in turn, produced susceptibility for singular configurations at other end-effector motions. A series of hardware experiments revealed three sources for the discontenting performance of the selfmotion control (an analysis of two exemplary joint configurations confirming the following observations is presented in [Moc05]).

One is related to the existence of local minima of the objective function forcing the selfmotion to converge to solutions far from an optimal configuration. Another disadvantage is caused by symmetries: The SCARA segment configuration obtained by reflection along the line drawn from the origin to the tip has the same manipulability index as the source configuration. Due to this symmetry there always exist at least two optimal joint configuration for a given end-effector position. At certain configurations a subtle change of the joint angles can change the direction of the selfmotion and the solution to which it converges. In practice, this renders the null space motion hard to predict for the operator. As the direction of the selfmotion can also be changed by little end-effector motions it provides a somehow restive feeling. The third identified problem is similar to the characteristic also observed for the wrist control when applying the manipulability index as side criterion: This objective function does not necessarily maximize the ‘distance’ to singular configurations: it can produce joint configurations where moderate end-effector motions can drastically reduce the manipulability index and drive the system in a singularity. Such unfavorable configurations are typically generated when the selfmotion changes the direction of the curvature of the SCARA segment from purely right to left or vice versa. This is likely drive joint angle 2, 3, or 4 to a multiple of π reducing the degree of redundancy.

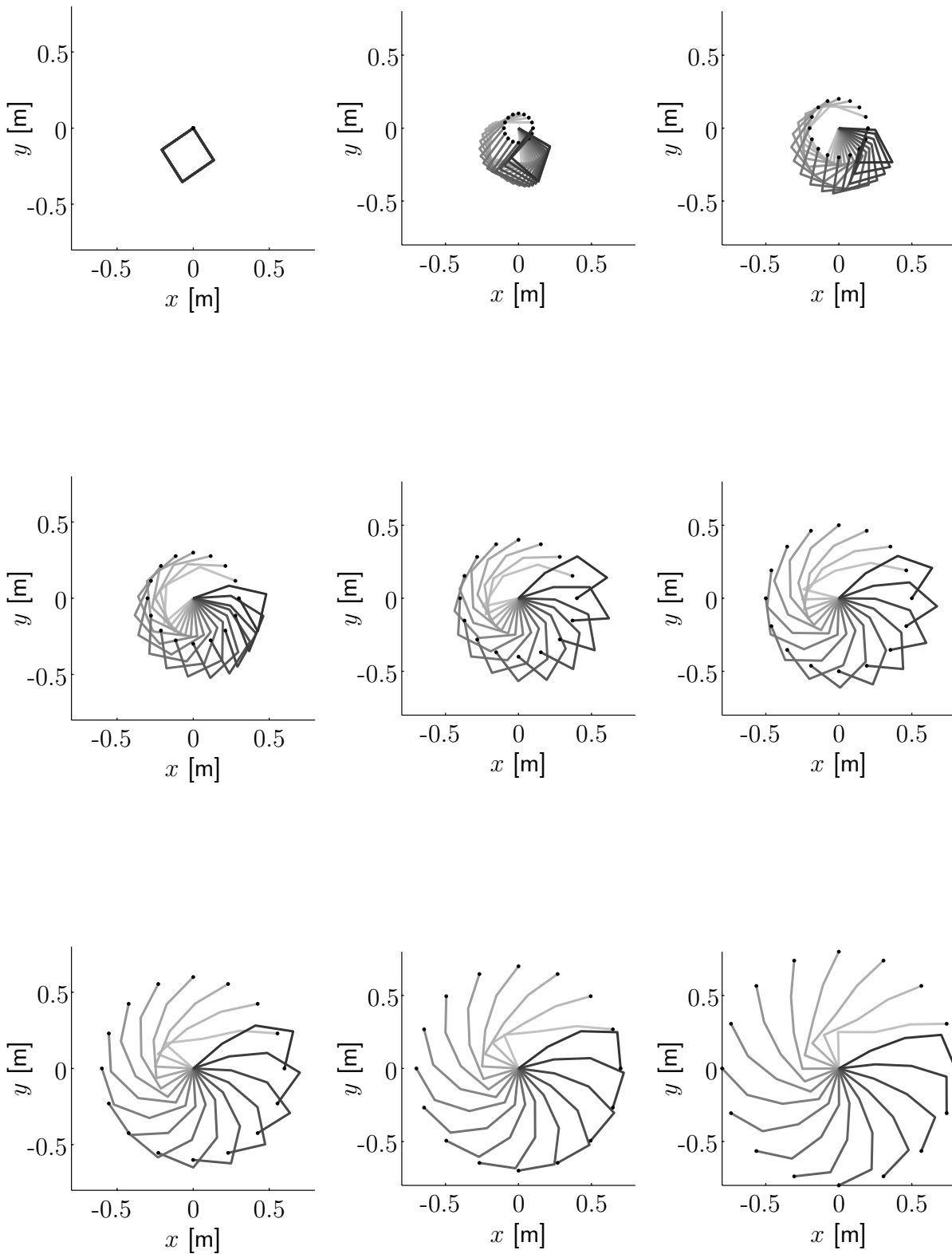
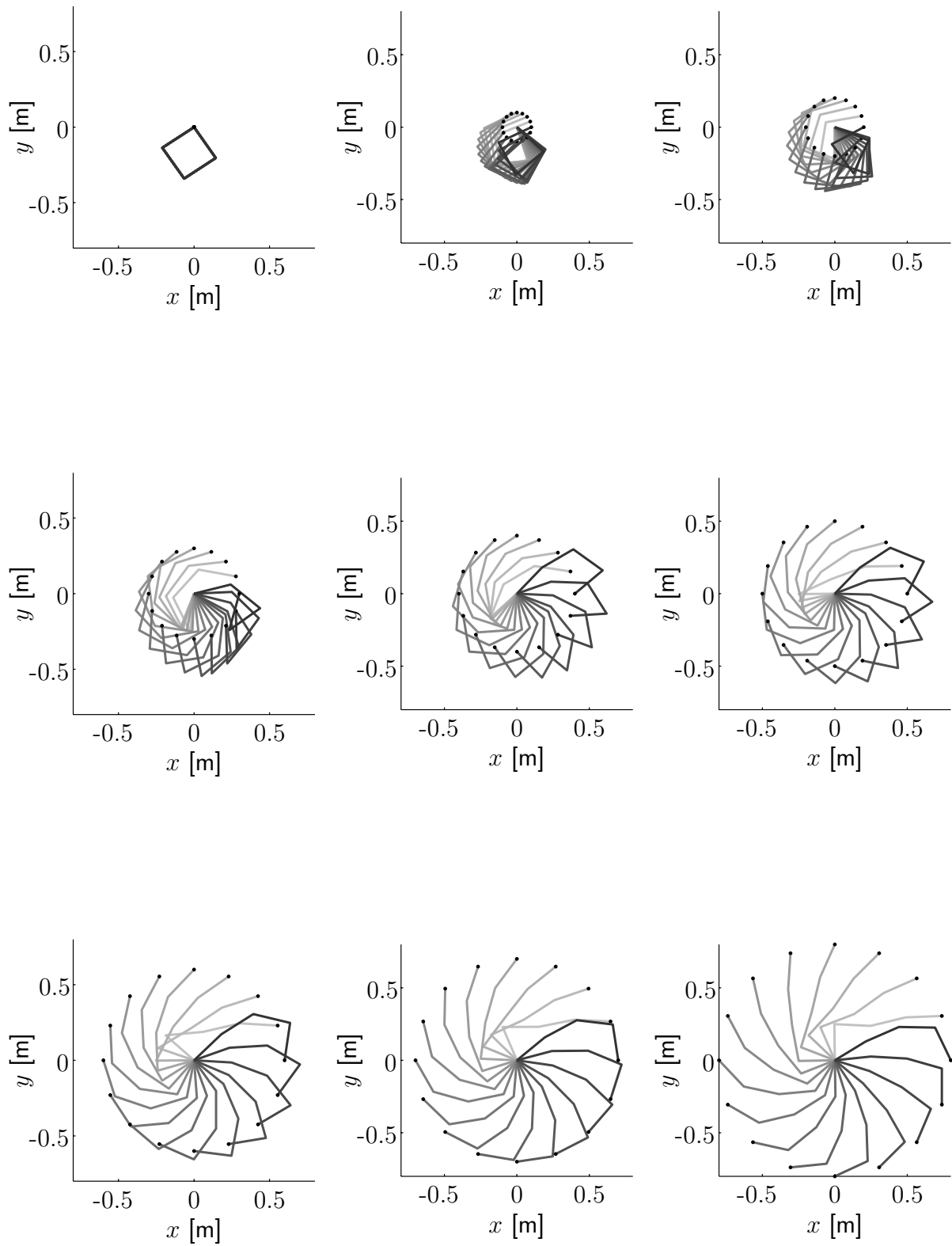


Figure 3.13: Inverse function for workspace #0

**Figure 3.14:** Inverse function for workspace #2

Then, it is easy to react by an end-effector motion further folding the device structure and yielding a singular configuration.

3.6 Summary

One of the objectives of this chapter is to provide a brief overview on haptic device control approaches including designs with kinematical redundancies. To emphasize the common ground of industrial force and haptic control a set of generic classification schemes for general robot and haptic control algorithms has been presented. An analysis of the impedance display mode has shown that the impedance error perceived by the operator is inversely related to the gain of the force feedback controller. A dedicated shaping of the closed loop inertia is based on a dynamic interface model and requires either acceleration measurement, which is rarely provided by haptic hardware, or the measurement of force. In the latter case, the resultant force control law aims ‘in its heart’ at the control of the device acceleration and can therefore also be classified as admittance control. Contrary to impedance control all admittance control implementations form the closed loop inertia. To achieve this neither acceleration feedback nor the application of a dynamic device model is required. In common implementations the active shaping of the closed loop inertia is a result of high gain velocity or position feedback control in an inner control loop. It is therefore possible to render an isotropic closed loop dynamic behavior providing a ‘natural’ haptic sensation. It has also been pointed out that motion-based impedance control with acceleration feedforward can be interpreted as impedance control and admittance control acting in parallel.

A discussion of sources for stability problems forbidding an arbitrary reduction of the closed loop inertia has been presented. The most influential factor is possibly the flexibility of the robot structure; non-collocated modes add more poles than zeros to the open-loop transfer function producing additional phase lag. Accordingly, the device flexibility has to be considered in any realistic stability analysis of haptic devices. Such a stability analysis of haptic systems is complicated by the presence of the operator, the virtual environment in the control loop as well as hard nonlinearities for example due to stiction and Coulomb friction.

The control of haptic devices with actuated kinematical redundancies requires the definition of a mapping of operational space forces or motions to the corresponding joint space quantities. As the interface tip is moved by the operator at will the resultant trajectory is not known in advance. Accordingly, no globally optimal path inversion methods can be applied to solve the inverse kinematics problem. Local inversion methods can be defined at the force, velocity, acceleration, or position level. Conservative inverse kinematics solution approaches, assigning an unique device posture to each end-effector configuration, have the advantage that the analysis of the kinematical and dynamical device performance is equivalent to non-redundant interfaces. For non-conservative algorithms as for instance pseudoinverse control the verification of performance specifications is very hard to obtain because resultant joint configurations can be exceedingly difficult to predict. At the downside, conservative algorithms have fundamental restrictions on the achievable invertible workspace that do not exist for non-conservative inversion methods.

The kinematical design of the hyper-redundant haptic interface ViSHARD10 allows for a decoupling of the translational from the rotational device movement enabling the parti-

tioning of the inverse kinematics problem in two subproblems that can be solved separately. Despite solving for all 10 DOF simultaneously has shown to have a significant potential for performance improvement hardware experiments have, so far, been restricted to the application of this partitioned solution approach because decoupled translational and rotational null space motions seem to be easier to understand and anticipate for the operator. Moreover, the partitioned solution permits independent testing of inverse kinematics algorithms for the wrist and SCARA segment. For the orientational DOF the application of pseudoinverse control with the additional use of a side criterion directly maximizing the distance to a singular wrist configuration is proposed. Practical experience at hardware experiments reveal that this side criterion provides significantly better results by means of singularity avoidance when compared to the well established manipulability index or the condition number. This control algorithm provides an unlimited orientational workspace with a selfmotion simple to understand for the operator. For the control of the SCARA segment the results are less satisfactory: At hardware experiments no robust avoidance of singular configurations could be achieved with the application of pseudoinverse control with optimization of the manipulability index. Moreover, the resultant null space motion turned out to be hard to predict for the operator. Good results could be achieved with the inverse function approach defined at a rectangular workspace of moderate size. The construction of inverse functions for larger workspaces has been accomplished by the application of numerical search algorithms. The results indicate that an inverse kinematics function with acceptable performance can be defined for a circular workspace with 0.8 m radius excluding positions with polar angle in the interval $[0 \text{ rad } \pi/8 \text{ rad}]$. Further increase of the operating area in terms of reducing the workspace void by allowing tip positions with small radial coordinate results in a significant lowering of the device velocity capability. The implementation and experimental validation of the inverse functions obtained by numerical optimization is subject to future research. Further research needs are extended studies of non-conservative redundancy resolution approaches for the control of the SCARA segment as well as hardware experiments for the investigation of the suitability of the full solution approach for human-device interaction.

4 Friction Modeling and Compensation

The discussion of haptic control architectures in section 3.2 indicates the importance of accurate friction compensation in case of impedance control. According to equation (3.3) the force feedback action can only partially eliminate the impedance error induced by the device friction because the controller gain is bounded by stability. For a further reduction of errors caused by friction the force controller has to be combined with additional friction compensation techniques. In case of admittance control the degradation of the haptic feedback fidelity due to friction is typically less dramatic. The reason is the high gain of the inner motion control loop yielding a largely improved disturbance rejection capability when compared to impedance control. Although additional friction compensation actions can significantly enhance the tracking performance of the inner motion control loop the impact on the force feedback quality perceived by the operator tends to be marginal.

Model based friction compensation requires a comparatively precise knowledge on the frictional characteristics of the joints. Compared to gravitational, gyroscopic, and inertial forces the accurate estimation of friction forces is, however, much more challenging due to the complexity of the physical processes involved and its dependency on temperature and the microscopical properties of the contacting surfaces which can change dramatically with time as a consequence of wear. In fact, the study of tribology, the science of friction, lubrication, and wear, is a comparatively active research area with a large community. A survey on friction modeling and control systems with friction has been presented by Armstrong-Hélouvry *et al.* [AHDC94]. This article provides an excellent overview on this subject including an extensive bibliography. A more detailed discussion on dynamic friction models is given by Olsson *et al.* [OrC⁺98] and a recent review on friction compensation schemes in robotics by Bona and Indri [BI05]. Friction modeling and compensation schemes for harmonic drive gears (harmonic drives are used in the joint components of the ViSHARD devices described in section 2.5) are for instance discussed in [GGD02], [Dha03], [TB88], [KD05], [VAL01], [ZD04], and [HHM04].

Friction compensation techniques for haptic interfaces along with performance evaluation are little discussed in the literature. Bernstein *et al.* [BLP05] suggest a hybrid controller in terms of combining force feedback action with compensation torques derived by a comparatively simple Coulomb type friction model. The innovative aspect is a gain scheduling technique altering the force feedback gain at low velocity motion. Further results on model-based friction compensation are given by Bi *et al.* [BLTW04] and Marcheschi *et al.* [MFAB05]. Kwon and Woo [KW00] present an experimental performance comparison of model-based friction compensation with the use of a disturbance observer. A sliding mode friction estimator and compensator is discussed by Ando *et al.* [ASKH02].

The innovation of this chapter is the development of a friction compensation scheme applying nonlinear models for the viscous and load torque dependent friction based on forth and second order polynomials, respectively. The time varying nature of the friction behavior is taken into account by adapting the parameters of the friction model. As the change of the friction characteristics due to temperature shift is a process of moderate

speed the friction model is not adapted iteratively at each sampling instant as done at traditional adaptive compensation schemes but re-tuned after a specified number of samples. For the compensation of stiction a variable structure force control law is proposed that switches between PID and PD control. This algorithm aims at providing a good stiction compensation while maintaining a good dynamic behavior of the joints in motion.

This chapter starts with a description of the most well known friction phenomena and modeling approaches relevant for the control of machines with friction (section 4.1). Section 4.2 briefly reviews modeling approaches for harmonic drive gears and section 4.3 friction compensation approaches for haptic interfaces in the impedance display mode. Finally, section 4.4 presents the VISHARD3 friction model derived from identification experiments (section 4.4.2) along with an outline and evaluation of the static friction compensation scheme (section 4.4.3) as well as the adaptation mechanism of the sliding friction compensator (section 4.4.4).

4.1 General Friction Phenomena and Modeling Approaches

4.1.1 Classical Friction Models

Among the most classical descriptions of friction is the *Coulomb friction* model given with

$$F_C(v, f_n) = f_c \operatorname{sgn}(v) \quad \text{with} \quad f_c = \mu_c f_n, \quad (4.1)$$

where F_C is the the Coulomb friction (or *kinetic friction*), v the sliding velocity, and f_c the Coulomb friction parameter dependent on the constant kinetic friction coefficient μ_c and the normal force f_n . This model captures friction phenomena typically observed at sliding motions of unlubricated (dry) bodies: the friction force opposes motion, is proportional to the normal load, and is independent of contact area and velocity. These characteristics can be explained by the inherent roughness of the contacting surfaces. When the peaks of the roughness, also called *asperities*, come in touch, they deform until the contact area of the asperity junctions has grown large enough to take up the normal load. As a result, the true contact area of the two surfaces is dependent on the normal load and the hardness of the bodies in contact. The friction force is then given by the shear strength of the surface materials times the junction area. This explains the increase of the friction force with the normal load and the independence on the sliding velocity and size of the apparent contact area.

The Coulomb friction model does not describe friction forces at static operations. Friction effects for zero velocity are typically modeled as a function of the external force f_e :

$$F_{\text{stat}}(f_e, f_n) = \begin{cases} f_e & \text{if } v = 0 \text{ and } |f_e| < f_s \\ f_s \operatorname{sgn}(f_e) & \text{if } v = 0 \text{ and } |f_e| \geq f_s \end{cases} \quad \text{with} \quad f_s = \mu_s f_n \quad (4.2)$$

For external forces lower than the *break-away force* f_s , which is dependent on the normal load and the static friction coefficient μ_s , the static friction F_{stat} (shorthand: *stiction*) prevents the initiation of motion from rest. Usually, but not necessarily, the break-away force is larger than the Coulomb friction required to sustain the motion. A heuristic explanation of the difference between μ_s and μ_c is that collisions between contacting asperities during

sliding motions cause impulses with upward components. This produces highly asymmetric normal oscillations increasing the normal separation between the surfaces. The reduced asperity penetration decreases the average area of contact entailing lower shear forces [Tol67].

The joint elements used for robots are typically lubricated with oil or grease in order to reduce wear and friction. At dynamic operations a fluid layer of lubricant is built up exchanging dry sliding friction for viscous friction. The friction forces between the parts in motion is dependent on the fluid layer thickness which is a function of the surface properties, lubricant viscosity, and sliding velocity. A common model of the friction forces at high velocities, where the thickness of the fluid layer is large enough to completely separate the contacting surfaces (*full fluid lubrication*), is the *viscous friction* model. It describes the friction component generated by hydrodynamic effects in the fluid film as proportional to velocity. With f_v representing the viscous friction parameter this friction component is calculated with

$$F_{\text{visc}}(v) = f_v v. \quad (4.3)$$

Within the transition from static friction to full fluid lubrication the velocity dependent friction component typically differs considerably from equation (4.3). For very low sliding velocities no fluid film is built up between the surfaces. In this velocity domain, the friction forces are dependent on the shear strength of the solid boundary layer. The boundary layer is a solid film covering the surface of the bodies in contact. It is formed by oxidation or chemical reactions with the lubricant. During *boundary lubrication* the shear forces are independent of the sliding velocity. For higher sliding motions a fluid film builds up. The velocity regime producing a fluid layer thinner than the height of the asperities results in *partial fluid lubrication* where still some solid-to-solid contact occurs. If the shear strength of the solid boundary layer is higher than the shear forces of the fluid film the friction force will decrease continuously with increasing velocity. After the work of Stribeck [Str02] this characteristic is also called the *Stribeck effect*. At higher velocities hydrodynamic effects usually become dominant resulting in an increase of the friction with rising velocity. The existence and significance of the Stribeck effect depends strongly on the lubricant applied. Due to the lack of a theoretically motivated mathematical model a number of empirical parameterizations of the Stribeck effect have been suggested to describe the friction effects within the boundary and partial fluid lubrication regime [AH91]. A widely used mathematical description is the model proposed by Bo and Pavelescu [BP82]

$$F_{\text{Strb}}(v, f_n) = (f_s - f_c) e^{-|v/v_s|^\delta} \text{sgn}(v) \quad (4.4)$$

and the Lorentzian model of Hess and Soom [HS90]

$$F_{\text{Strb}}(v, f_n) = \frac{f_s - f_c}{1 + (v/v_s)^2} \text{sgn}(v), \quad (4.5)$$

where v_s (also called the *Stribeck velocity*) and δ are empirical parameters. Setting $\delta = 2$ (*Gaussian model*) the difference between both models becomes marginal.

Friction models applied for control design are mostly some combination of the components described above. They are also called *static friction models* as they describe a static map between velocity or the external force and the friction force. Figure 4.1 shows a set of common combinations. The Coulomb friction parameter and break-away force is usually

assumed to be constant neglecting their dependency on the normal force. The addition of the Stribeck effect has the advantage to eliminate the discontinuous variation of the friction force at the transition from rest to motion. The impact of the parameter settings in the model of Bo and Pavelescu is illustrated in figure 4.2. It shows for several models the friction as a function of the steady state velocity (also referred to as *Stribeck curve*). The thick line represents the reference Stribeck curve. The other curves have been obtained by varying separately parameters from the reference model. It can be observed that the increase of δ (thin line) enlarges the region of boundary lubrication with friction nearly independent of velocity. Decreasing parameter v_s (dashed curve) reduces the domain of sliding velocities in that the Stribeck effect is significant. The dotted line has been obtained by lowering the break-away force f_s below the Coulomb friction parameter f_c . It reveals the capability of the model to describe systems exhibiting no Stribeck effect. It has to be noted that unlubricated bodies can also show decreasing sliding friction with increasing velocity almost equivalent to the Stribeck effect. A physical explanation to this phenomenon is provided by Al-Bender *et al.* [ABLS04].

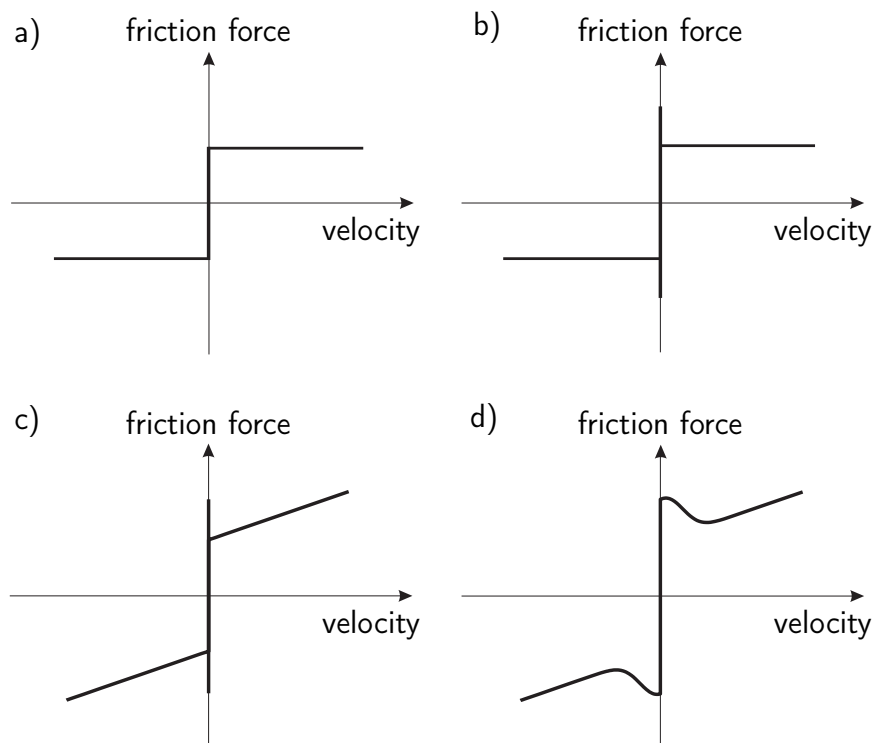


Figure 4.1: Static friction models: a) Coulomb friction; b) Coulomb plus static friction; c) Coulomb plus static plus viscous friction; d) Coulomb plus viscous friction plus Stribeck effect.

4.1.2 Pre-sliding Hysteresis and Dynamic Friction Effects

Viewing the static friction regime at a microscopic level it can be observed that the assumption of zero motion between the contacting surfaces is not correct. In fact, the compliancy of the asperities gives rise to microscopic motions without sliding (*pre-sliding displacement*

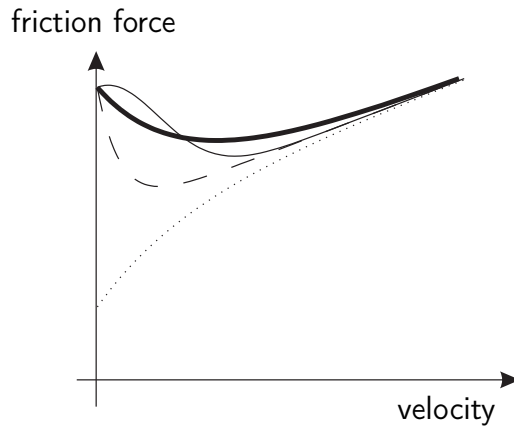


Figure 4.2: Effect of δ , v_s , and f_s on the shape of the Stribeck curve: the thick line is the reference Stribeck curve; thin: increased δ ; dashed: decreased v_s ; dotted: decreased f_s ($f_s < f_c$)

or *micro-slip*). Experimental investigations of the pre-sliding displacement regime presented by Courtney-Pratt and Eisner [CPE57] and Dahl [Dah68] indicate that the asperity junctions first deform elastically and then plastically resulting in a hysteretic friction - displacement relationship similar in shape to the stress-strain curve of solid brittle materials. Recent experiments as for example reported by Symens and Al-Bender [SAB05b] evince a velocity-independent hysteretic behavior with nonlocal memory of the position by means of a dependency of the force not only on the current value of the relative displacement between the contacting surfaces but also on past extremum values of it (see [SAB05a] for a theoretical analysis of this effect). The phenomenon of purely elastic pre-sliding hysteresis is illustrated in figure 4.3. As the external force increases, more and more asperity junctions start to break causing a continuous transition to the sliding regime where all junctions are broken. The spring-like behavior of the contact under static friction is also called the *Dahl effect*.

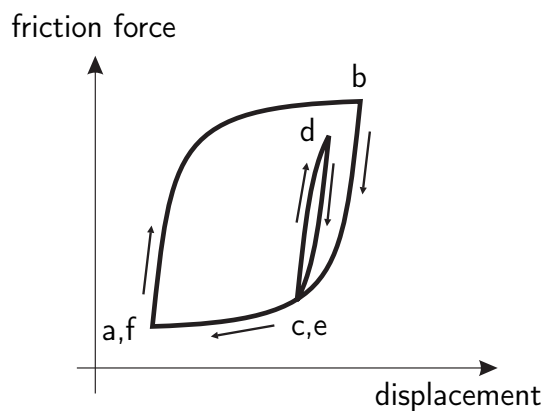


Figure 4.3: Pre-sliding hysteresis: Typical static friction for a displacement trajectory within the elastic pre-sliding displacement regime; the motion starts from point a, follows b-c-d-e and arrives at point f

Pre-sliding hysteresis is not the only memory effect observed in friction behavior. Hess and Soom [HS90] investigated friction dynamics within the partial fluid lubrication regime. In their experiments they superimposed a bias velocity to a periodic time-varying velocity to yield unidirectional motion (i. e. no velocity reversal). Examining the relation between friction force and velocity, a loop with friction force larger for acceleration than for deceleration could be identified. This is illustrated in figure 4.4. The width of the loop increased with the frequency of the velocity variation. Their observations indicate that in the partial fluid lubrication regime friction does not change simultaneously with a change in velocity but is lagging behind. This effect, which is called *frictional lag* or *frictional memory*, could be described comparatively precisely by a time delay in the relation between velocity and friction that increases with increasing lubricant viscosity and with increasing normal load. Among the physical explanations for this effect is the time required to modify the lubricant film thickness. This illustration, however, cannot explain the frictional lag also observed in dry friction experiments where no lubrication has been used.

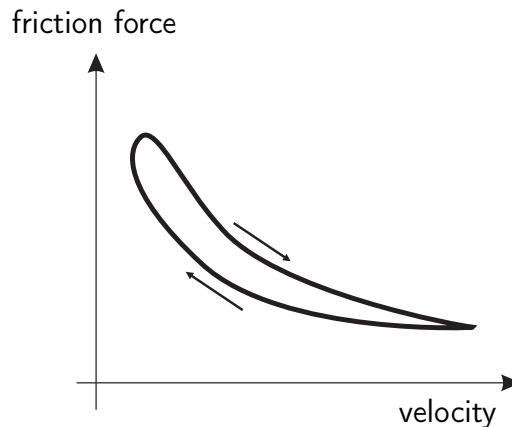


Figure 4.4: Frictional lag: Friction-velocity relation for unidirectional sinusoidal velocity input within the partial fluid lubrication regime

Another phenomenon pointing to dynamics within the physical processes that determine friction is the dependence of the break-away force on the rate of the external force application as qualitatively shown in figure 4.5. This effect has been demonstrated by the work of Johannes *et al.* [JGB73] and Richardson and Nolle [RN76]. Moreover, their investigations show evidence that, at least in case of short time periods, the break-away force is not affected by the time of stationary contact (dwell time) as stated by many authors. The results obtained by Richardson and Nolle indicate that for large force rates the static friction coefficient tends to be equal to the kinetic friction coefficient.

4.1.3 Advanced Friction Models

Various empirical models have been proposed to account for the friction phenomena discussed above. Armstrong-Hélouvy [AHDC94] suggested an extension of the classical friction models shown in figure 4.1. By introducing a time delay in the description of the Stribeck effect and temporal dependencies for stiction it includes frictional lag and varying break-away force. Stiction is modeled by a separate equation describing the friction force as a function of displacement to account for micro-slip. Pre-sliding hysteresis is, however,

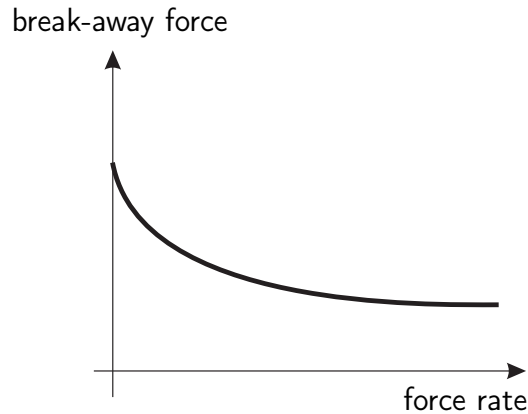


Figure 4.5: Dependency of the break-away force on the rate of force application

not captured by this model. Another drawback is the fact that no switching mechanism for transitions between the equation describing sliding friction and the equation characterizing the micro-slip regime is incorporated in the model.

An alternative approach to describe dynamic aspects of friction behavior is the use of dynamic friction models, also called *state variable friction models*. This class of models introduces one or more internal state variables, which in combination with the sliding velocity are used to derive the friction force. The time-dependent evolution of the state variables is described by a set of differential equations. A discussion on several dynamic friction models is presented by Olsson *et al.* [OrC⁺98]. Widely used dynamic models are the Dahl model introduced in [Dah68] and the LuGre model (Lund Grenoble) suggested by Canudas de Wit *et al.* [CO_rL95]. Dahl's model has been extensively used in simulation studies. It captures pre-sliding displacement, pre-sliding hysteresis, varying break-away force, and Coulomb friction. Also, it renders a continuous and smooth transition from micro-slip to gross sliding. This is accomplished without a switching function. The LuGre model can be considered as an extension of the Dahl model in terms of allowing the inclusion of arbitrary steady-state velocity-friction characteristics to introduce for instance viscous friction and the Stribeck effect while keeping the characteristics of the Dahl model in the pre-sliding regime. Moreover, the interaction of the dynamics with the Stribeck effect generates frictional lag. Despite the richness of captured friction phenomena the LuGre model has a comparatively simple structure easy to implement and low number of parameters. This explains its appeal for simulation studies and theoretical formulations. The LuGre model is, however, not without shortcomings. Swevers *et al.* criticized an unprecise replication of pre-sliding hysteresis [SABGP00]. They suggested an extension of the LuGre model, also called *Leuven model*, featuring pre-sliding hysteresis with nonlocal memory and the incorporation of arbitrary force-displacement curves in the micro-slip regime. In [LSAB02] Lampaert *et al.* present the *generalized Maxwell slip friction model*, a modification to the Leuven model providing a computationally more efficient implementation of the hysteresis effect. Another drawback of the LuGre model identified by Dupont *et al.* [DHA00] is the fact that it renders pre-sliding displacements always with a plastic component. As a consequence, the LuGre model predicts a system subjected to an arbitrarily small force oscillation superimposed on an arbitrarily small bias force to drift. This unbounded motion is contrary to practical experience. The authors propose the *elasto-plastic friction model*, a class of single-state friction models in which pre-sliding displacement is first purely elastic

before getting plastic. Compared to the LuGre model it is able to render stiction more adequately.

4.1.4 Stick-Slip and Hunting Oscillations

In motion controlled systems friction can induce two widely recognized and discussed phenomena, namely stick-slip and hunting oscillations. *Stick-slip motion*, a periodic cycle of alternating sliding and sticking, can for instance be observed for spring-mass-damper systems in contact to a moving surface or, which is equivalent, at low constant velocity tracking tasks of sliding masses under PD position control. A typical stick-slip motion is shown in figure 4.6. At the beginning the system stays at rest due to the static friction counteracting the applied force. The position error and applied force increase linearly until the break-away force is reached and sliding is initiated. Then, the system starts to accelerate rapidly because the Coulomb friction is smaller than the static friction. As the position error gets smaller, the applied force reduces to a value below the Coulomb friction and begins to decelerate. If the control damping is not sufficiently large the velocity will approach zero again. The phenomenon then repeats again. A detailed analysis of the conditions under which stick-slip motion occurs is presented by Armstrong-Hélouvry [AH91]. The dominant contributors for the stick-slip limit cycle are stiction and the drop of the friction force at the transition from stiction to sliding. Frictional lag and the decrease of the break-away force with the force rate have a stabilizing effect. In [AH94] it is shown that the presence of frictional lag is a sufficient and also necessary condition for the widely observed phenomenon that stick-slip or chatter can be extinguished by altering the position controller stiffness. Another well known effect is the elimination of stick-slip with increased sliding velocity: because a higher velocity also raises the force rate, the break-away force is lowered.

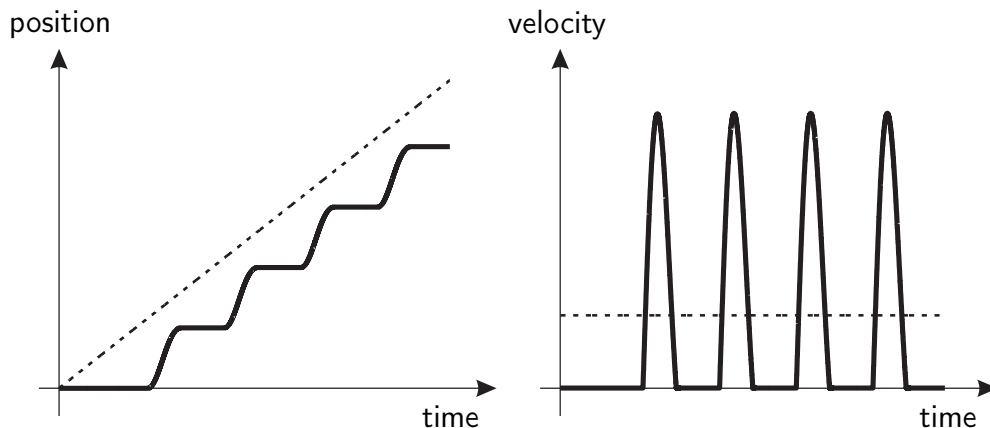


Figure 4.6: Stick-slip motion at low constant velocity tracking under PD position control; dashed line: desired motion; solid line: actual motion

Hunting oscillations as shown in figure 4.7 are friction induced limit cycles around the target position at positioning tasks when control algorithms with integral action (e. g. PID control) are applied. A detailed study of the hunting phenomenon has been presented by Hansen [Han02]. The author concludes that minor changes in the parameters settings of the Stribeck effect can cause severe changes in the conditions for the existence and

stability of limit cycles as well as the stability properties of the equilibrium points. In contrast, the inclusion of pre-sliding hysteresis and dynamic friction effects (frictional lag, rate dependent break-away force) shows only little effect.

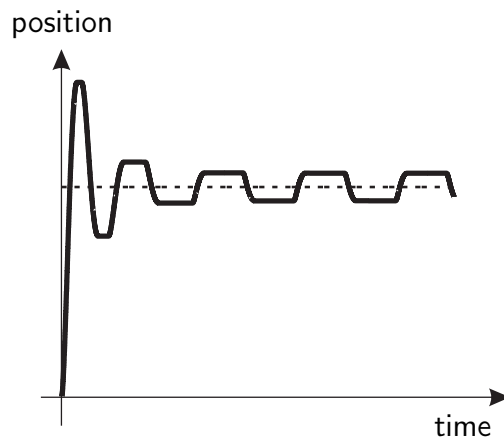


Figure 4.7: Hunting oscillations under PID position control; dashed line: desired position; solid line: actual position

4.1.5 Other Friction Effects

The description of friction effects given so far is not complete. Other phenomena observed include:

- *Temperature dependency:* Friction characteristics can be highly dependent on the operating temperature (e. g. due to changing physical properties of the lubricant).
- *Nonlinear viscous friction term:* Often the sliding friction at high velocities is inadequately described by a linear dependence on velocity.
- *Load dependency:* All friction parameters can be dependent on the instantaneous normal force and its history. Moreover, this dependency can be nonlinear.
- *Asymmetry:* The friction properties can be different in the different directions of motion.
- *Position dependency:* In some mechanisms friction is position dependent. This is for example a typical characteristic of gear drives where the contact geometry and normal force changes with position.
- *Change with time:* Due to wear and lubricant contamination friction properties can change largely with time. This change is particularly significant during the run-in period of the mechanism.
- *Dependency on normal contact dynamics:* There exist indications that friction is strongly influenced by the normal motion of the contacting surfaces, see [MOSo90].

- *Frictional noise:* Even perfect friction models cannot account for friction effects arising at random as for instance due to wear debris and other small particles between the contacting surfaces. The mean value of frictional noise is typically not zero because these disturbances result in a temporal increase but never in a decrease of the sliding friction.

4.2 Modeling Harmonic Drive Friction

The modular joint components of the ViSHARD devices described in section 2.5 apply harmonic drive gears. Their main benefits are zero backlash and a higher torque to mass ratio, compactness, overload capability, stiffness, and bandwidth than planetary gears. The following sections provide a description of the principle of the harmonic drive operation along with a brief review on transmission characteristics and modeling approaches provided in the literature.

4.2.1 The Principles of Harmonic Drive Operation

The harmonic drive transmission mechanism incorporates three concentric components: the elliptical *wave generator*, a nonrigid flexible cylinder with external teeth also referred to as *flexspline*, and the *circular spline*, a rigid ring with internal teeth. These basic components of harmonic drive gears are shown in figure 4.8. At the joint components of the ViSHARD devices, where the harmonic drive gears are used as speed reducing mechanisms, the wave generator is firmly attached to the motor shaft. In assembled condition the compliant flexspline deforms to the elliptical shape of the wave generator resulting in a teeth engagement with the circular spline along the major axis of the ellipse as illustrated in figure 4.9. When the wave generator is rotated the zone of tooth engagement travels with the major elliptical axis. As the flexspline has two fewer teeth than the circular spline a full rotation of the wave generator (relative to the circular spline) yields a relative travel of the flexspline to the circular spline of two teeth in the opposite direction.

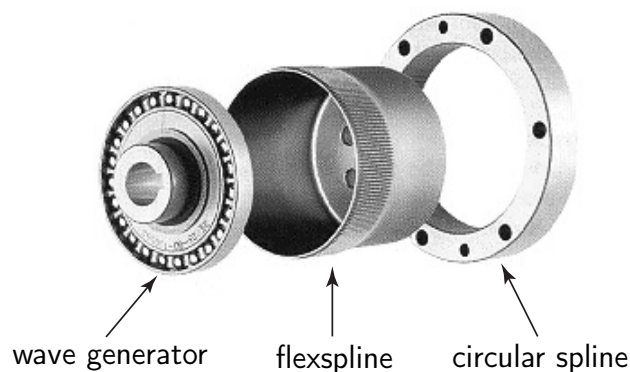


Figure 4.8: Harmonic drive gear components (source: Harmonic Drive AG)

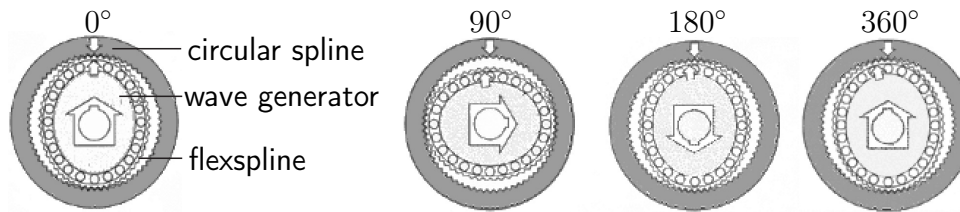


Figure 4.9: Harmonic drive gear principle of operation (source: Harmonic Drive AG)

4.2.2 Transmission Characteristics and Modeling Approaches

A substantial body of research aiming at the identification, understanding, and modelling of the harmonic drive transmission characteristics has been reported in the literature. Among the difficulties in the study of harmonic drive friction properties is the fact, that the energy dissipation is introduced by a number of distinct friction sources. These include for instance the wave-generator bearing, the tooth meshing area, the structural damping of the flexspline, and the output bearing. The frictional losses at these locations are virtually impossible to measure directly. The same is true for the internal state variables of the transmission mechanism that cannot be seen at the gear in- and output. Note, that the internal states differ from the external ones due to mechanical compliancy. Harmonic drive transmission characteristics reported in the literature include:

- *Nonlinear flexibility with hysteresis*: Among the main sources of the torsional compliance are the flexspline elasticity, the gear-tooth engagement zone, and wave-generator deformation. The torque versus torsion curve of harmonic drive gears shows rising stiffness with increasing torsion. The low stiffness at low applied torques is also referred to as *soft-windup*. The second common attribute is the hysteresis in the torque-torsion curve. Several authors proposed the description of structural damping as a function on the rate of the torsional displacement in order to match the observed hysteresis curve, see for example [KG97, Tag97, GGD02]. Yielding a hysteresis-like phenomenon these approaches, however, ignore that hysteresis is by definition a rate independent memory effect [Vis94]. Dhaouadi *et al.* [DGG03] conducted experiments where the gear output is locked and the input position is commanded to follow a sinusoidal function with zero mean value. Repeating the experiment at different input frequencies but constant amplitude it could be seen that all torque-torsion curves are indeed almost identical. These observations cannot be explained with rate dependent descriptions of structural damping.
- *Kinematic error*: The kinematic error of harmonic drive gears can be defined as the deviation between the actual output position from the expected position, which is the input position scaled by the gear ratio. This error can be decomposed in a component due to position dependent gear ratio variations, which forms the basic component of the kinematic error, and a contribution induced by torsional flexibility. The origin of gear ratio variations has not yet been fully understood [Tut92]. Among the possible sources are manufacturing imperfections of the three transmission elements (out-of-roundness, tooth-placement errors of the circular spline and flexspline), assembly imperfections (misalignment of the components), but also the operating principle

itself. The error waveform shows typically frequency components at two cycles per revolution of the wave-generator relative to the circular spline and the wave-generator relative to the flexspline along with several subsequent harmonics. As the flexspline moves comparatively slowly relative to the circular spline the error waveforms due to circular spline and flexspline gear-errors have slightly different frequencies. This explains amplitude modulations of observed position error waveforms. Although the amplitude of the kinematic error is small it can result in comparatively high output acceleration fluctuations at high wave-generator velocities. Due to the elasticity of the harmonic drive the kinematic error can excite significant resonance vibrations resulting in surprising transmission dynamics [Tut92].

- *Nonlinear viscous friction:* A typical behavior of harmonic drive friction is that the slope of the Stribeck curve is not constant in the full fluid lubrication regime. A common observation is a decrease with increasing velocity, see for instance [SMA95, Tut92].
- *Stribeck effect:* Results of friction identification procedures reported for example in [Tag97, GGD02, Pee03, KD05] indicate only little significance of the Stribeck effect. Moreover, the measurements of [Tag97, KD05] show that harmonic drives can have a break-away force lower than Coulomb friction. As a consequence, harmonic drives show little susceptibility to stick-slip motions.
- *Position dependent friction:* The position dependency of the friction can easily be felt when backdriving the harmonic drive with the hand. Gandhi *et al.* [GGD02] developed a model for position dependent friction based on the measurements at velocity tracking experiments at low velocities. The results indicate a rising amplitude of the friction fluctuation with the motor position for increasing velocities. Similar to the kinematic error the position dependent friction waveform shows a dominant frequency component at two cycles per revolution of the wave-generator. Furthermore, there also seems to be a dependence on the load (output) position. A similar identification procedure and result is presented by Kennedy and Desai [KD05]. The position dependent friction term suggested by Tuttle [Tut92] differs in that it varies at one cycle per output revolution of the harmonic drive output. As this term has been introduced in order to capture observations in the wave generator velocity data obtained in response to step commands to the motor current it most likely describes other effects than the previous models.
- *Load dependent friction:* The load dependency of harmonic drive friction is typically ignored in models reported in the literature. The load dependent friction term can, however, be significant in case of high applied torques. The experimental results presented by Zhu and Doyon [ZD04] indicate a quadratic relationship between load dependent friction and the applied torque. A linear load dependency has been included in the friction models of Albu-Schäffer [AS02] and Peer [Pee03]. Tuttle [Tut92] considered the geometry of the tooth meshing. Assuming a linear relationship of the Coulomb friction between the rubbing teeth surfaces on the normal force the resultant friction model is load dependent. The model could successfully account for the drastic enhancement of frictional losses during resonance vibrations as these go along with increased torque levels.

- *Temperature dependent friction:* As harmonic drives are lubricated with oil or grease a change of the Stribeck curve with the operating temperature can be observed. This effect can be explained by a dependency of the physical properties of the lubricant (e.g. the viscosity) on temperature. The friction identification results reported by Visioli *et al.* [VAL01] indicate an increase of the sliding friction with rising temperature. An experimental identification of the relationship between the friction parameters and temperature is difficult because the temperature at the tooth meshing area is hard to measure.
- *Torque saturation:* Kircanski and Goldenberg [KG97] observed that the torque transmitted by a harmonic drive saturates at a value far below the maximum allowable torque when the gear output is fixed to a stiff and immobile environment. Studying the dependence of the saturation level (critical torque) on the rate of the applied input torque a lower critical torque for a reduced input rate could be identified. The phenomenon of torque saturation is not present at interactions with soft environments.

The modeling approaches for harmonic drive gears proposed in the literature vary largely in complexity. The most advanced approach has possibly been provided by Gandhi *et al.* [GGD02]. Table 4.1 compares several suggestions in terms of the transmission characteristics included in the model.

4.3 Friction Compensation Techniques

As noted earlier the application of friction compensation schemes is particularly important in case of impedance control implementations because stability bounds on the force feedback gain enable only a partial elimination of friction induced impedance errors. In the admittance display mode the high gain of the inner motion control loop can more effectively compensate for friction forces diminishing the benefit of additional compensation procedures. In fact, the test persons in our lab had not been able to notice any difference in the haptic sensation when switching between admittance control with and without model-based friction compensation at a free space simulation. As a consequence, the following discussion of friction compensation approaches targets at implementations within impedance control architectures.

4.3.1 Joint Torque Feedback

The force sensor of haptic devices is typically placed as close to the end-effector as possible. This keeps the impedance Z_{EE} low (see figure 3.4) allowing for a good estimation of the operator's interaction force. The large distance (and thus considerable non-collocated dynamics) between the force sensor and the actuators is, however, probably the main reason for the comparatively low stability bounds of the force control law. Torque sensors placed directly at the joint outputs allow significantly larger feedback gains. At the downside, it is difficult to separate the measured signals in components induced by end-effector forces and by device dynamics lying outside the joint torque feedback loop (load side dynamics). A model-based separation would require a model of the load dynamics and knowledge on the

Table 4.1: Comparison of modeling approaches for harmonic drive transmissions

transmission characteristics	Tuttle [Tut92]	Seyfferth <i>et al.</i> [SMA95]	Kircanski and Goldenberg [KG97]	Taghirad [Tag97]	Gandhi <i>et al.</i> [GGD02]	Kennedy and Desai [KD05]
multiple friction sources	✗	✓	✓	✓	✓	✗
compliance	nonlinear stiffness	✓	✓	✗	✗	✓
	structural damping	✗	✓	✓	✓	✗
	hysteresis	✗	✓	✗	✗	✗
kinematic error	✓	✗	✗	✗	✓	✗
Stribeck effect	✗	✗	✗	✓	✓	✓
nonlinear viscous friction	✓	✓	✗	✗	✗	✗
friction dynamics	✗	✗	✗	✗	✓	✗
position dependent friction	✓	✗	✗	✗	✓	✓
load dependent friction	✓	✗	✗	✗	✗	✗
temperature dependent friction	✗	✗	✗	✗	✗	✗
torque saturation	✗	✗	✓	✗	✗	✗

load acceleration. As a consequence, joint torque feedback control typically compensates only for the servo dynamics (including joint friction and the inertia of the actuator).

A combination of the advantages of endpoint force feedback with the improved friction compensation capability of joint torque feedback can be achieved with the use of both kinds of sensors as illustrated in figure 4.10. For the sake of clarity the impedance \mathbf{Z}_{EE} of the device structure located between the endpoint force sensor and operator has been omitted in this block diagram. The outer control loop is almost identical to the control scheme shown in figure 3.4: The desired interaction force \mathbf{f}_d is, together with the output of controller $\mathbf{G}_{c,1}$, mapped into the joint space and added to the model-based feedback torque $\boldsymbol{\tau}_{fb,l}$. The difference is in $\boldsymbol{\tau}_{fb,l}$ aiming at the compensation of the load dynamics only (device dynamics without servo dynamics). In the common case of no acceleration measurement $\boldsymbol{\tau}_{fb,l}$ typically comprises Coriolis, centrifugal, and gravitational torques. The second difference is, that the desired torque $\boldsymbol{\tau}_d$ is not the commanded motor torque but the input to an inner control loop closed on $\boldsymbol{\tau}_{out}$, the torque at the joint outputs. Equivalent to the outer interaction force control loop, model-based feedback and torque feedforward is passed to the inner control loop for performance increase. The model-based feedback targets at the compensation of the servo dynamics. Because acceleration measurement is usually not provided the model-based feedback $\boldsymbol{\tau}_{fb,s}$ is mostly limited to friction torques.

The high gain of the inner loop controller $\mathbf{G}_{c,2}$ yields an improved friction and servo inertia attenuation performance when compared to endpoint force feedback alone [EDS90]. Despite less effective than an inner loop closed on motion this control scheme does not suffer from additional phase lag in the system open loop transfer function due to integration. Hence, it typically yields a better closed loop bandwidth than admittance control algorithms.

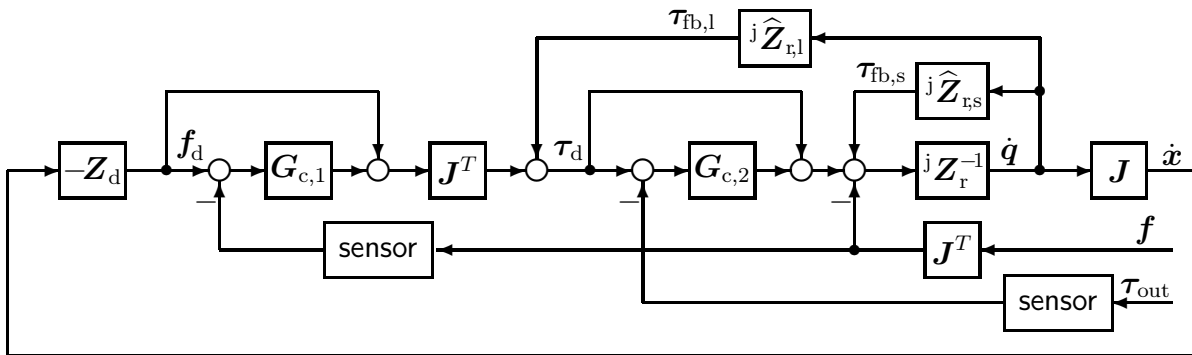


Figure 4.10: Impedance control with endpoint force and joint torque feedback

4.3.2 Model-based Friction Compensation

Model-based friction compensation, that is the addition of the estimated friction torque to the commanded motor torque, has been part of the control schemes shown in figure 3.4 and 4.10. The input variables to the friction models depend strongly on the model structure and the control scheme in that it is incorporated. In general, these inputs can be commanded (*feedforward compensation*), measured (*feedback compensation*) or estimated values (e. g. by state observers). For instance in case of admittance control both, feedforward and feedback compensation, can be used for the friction estimation. In particular at low sliding velocities

the use of the commanded velocity is often favored over the measured velocity because sensor noise can for instance give an erroneous sign of the measured velocity producing a friction compensation in the wrong direction [CNA⁺89]. Feedforward compensation is not possible in case of impedance control as no motion commands are present in this control scheme. The objective of observers is the estimation of variables that are not measured or the reduction of sensor noise. A typical example for variables impossible to measure are the internal states of state variable friction models.

Common difficulties when using static friction models as shown in figure 4.1 are the compensation of static friction and the switching between stiction and sliding. The calculation of the static friction force is mostly based on the applied tangential force (see equation (4.2)) or the displacement between the contacting surfaces. Both quantities are, however, difficult to obtain. This is particularly true for pre-sliding displacement as it requires the accurate measurement of the load side position in addition to the motor position. The direct measurement of the applied force needs force sensing located at the friction node. Its estimation from endpoint force sensing demands for a precise dynamic model of the robot and acceleration measurement (see e. g. [GW92]).

Switching at zero velocity from sliding to some static friction model requires the accurate detection when velocity is zero. In practice, the velocity is usually a measured signal tainted with sensor noise. In case of analog sensing the sampled velocity data will rarely be exactly zero. A widely used solution to this problem is switching to the stiction regime in a velocity interval around zero as suggested by Karnopp [Kar85]. More advanced switching functions as for instance relay functions can be applied to avoid high frequent switching between the stiction and sliding regime in the presence of sensor noise. Because static friction models often render a discontinuous friction force at the transition from sliding to stiction such a high frequent switching can result in undesirable actuation force oscillations that may produce acoustic noise and the excitation of higher order dynamics.

The solution approaches for problems related to switching between stiction and sliding described above do not agree with the true characteristics of friction. An approach better accounting for the behavior of friction is the use of dynamic friction models that accomplish a smooth transition from sliding to micro-slip without switching function. Well known examples are the Dahl and LuGre model. At the downside, dynamic models require some estimation procedure of the internal friction states that cannot be measured. As such a state observer includes feedback action it is often hard to detect whether the friction compensation performance attributes to the model design or the contribution of the feedback gain. The design and analysis of an observer estimating the unknown inner state of the LuGre friction model has been presented by Olsson and Åström [Or96].

The benefit of model-based friction compensation is largely dependent on the accuracy of the friction model. In most cases its parameters are determined off-line with identification experiments along dedicated excitation trajectories producing a high coupling of the measured signals to the sought parameters. Such identification procedures have for example been described by Armstrong-Hélouvry [AH91], Johnson and Lorenz [JL92], and Canudas de Wit and Lischinsky [CL97]. Another approach is the estimation of the friction parameters from the data acquired during the ordinary device operation. On-line identification allows to track changes and to update the model parameters during the task execution to account for the time-varying nature of friction (e. g. due to wear and changes in temperature and humidity). The main drawback of such adaptive control algorithms is the fact, that the device motions at ordinary operations can be highly unsuitable for

friction identification in terms of insufficient excitation of the model parameters. Moreover, the estimation of the friction force at operations involving significant accelerations is a considerable practical challenge due to lacking acceleration sensing of common haptic hardware. A brief overview on adaptive friction compensation approaches has been presented by Armstrong-Hélouvry *et al.* [AHDC94] and Bona and Indri [BI05]. An adaptation algorithm for the LuGre friction model has been given by Canudas de Wit and Lischinsky [CL97].

4.3.3 Dither

A simple technique to smooth out the discontinuity of friction around zero velocity is the use of high frequent *dither* superimposed on the command or control signal. Typical dither signals are sinusoidal, square wave, triangular, sawtooth, and trapezoidal. Setting the frequency of the dither signal well beyond the system bandwidth while remaining below the actuator bandwidth its high-frequency behavior is filtered out before reaching the joint output. The oscillation across the nonlinearity, however, effects an averaging of the nonlinearity. This smoothing effect can result in an replacement of the zero velocity discontinuity of friction force by an equivalent linear viscous damping characteristics. Another potential benefit is the elimination of the Stribeck effect yielding the suppression of stick-slip and hunting oscillations. Recent analyses of the effect of dither on frictional systems using the method of averaging have been given by Thomsen [Tho99] and Chatterjee *et al.* [CSK04]. Experimental validation of the smoothing effect and stick-slip elimination has been presented by Feeny and Moon [FM00]. Among the practical problems of dither is the excitation of vibrations that can result in acoustic noise as well as fatigue and failure of the actuators and mechanical parts.

4.3.4 Disturbance Observer

Another approach to compensate friction forces is the use of a *disturbance observer*. In this control concept the actual output of the robot is compared with the output of a nominal model. The deviation is considered to be caused by disturbance forces, torques, or accelerations applied to the nominal model. An observer is used to estimate and cancel out these disturbances in order to give the robot the dynamics specified by the impedance \mathbf{Z}_{dr} of the nominal model.

Figure 4.11 illustrates the control scheme discussed in section 3.4 augmented by a disturbance observer with the structure proposed by Kaneko *et al.* [KKO94]¹. The impedance \mathbf{Z}_{EE} of the device structure located between operator and the force sensor has been omitted in this block diagram. This type of disturbance observer, the disturbance force observer in the operational space, defines the nominal manipulator model as

$$\dot{\mathbf{x}} = \mathbf{Z}_{\text{dr}}^{-1}(\mathbf{f}_u) - \mathbf{f} \quad (4.6)$$

where \mathbf{f}_u is the control input force and \mathbf{f} the external force exerted by the human operator. Introducing a disturbance force \mathbf{f}_{dist} accounting for the difference between the response of

¹Several alternative structures in joint or Cartesian space have been developed differing in whether the disturbance is modelled as force or acceleration.

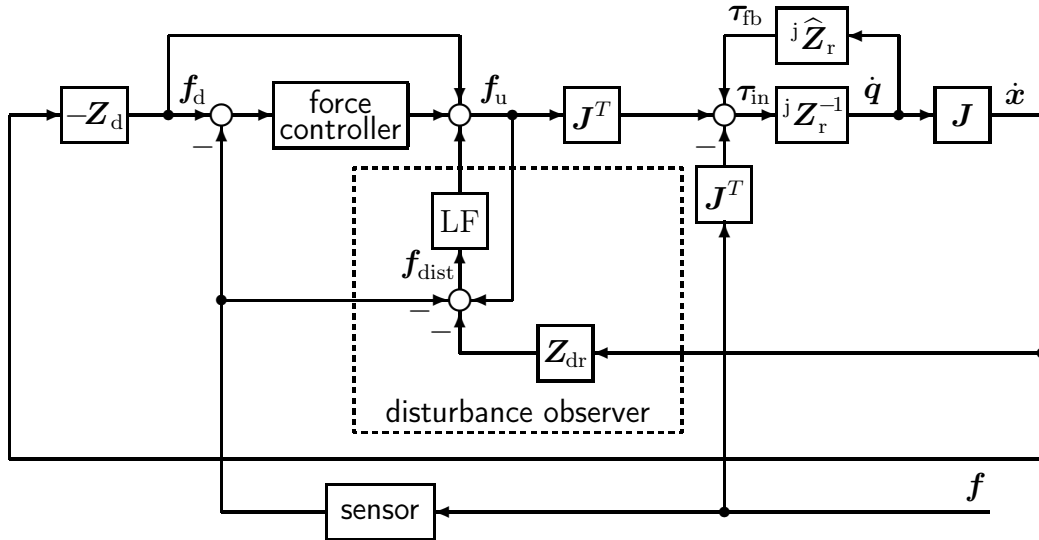


Figure 4.11: Impedance control with disturbance observer

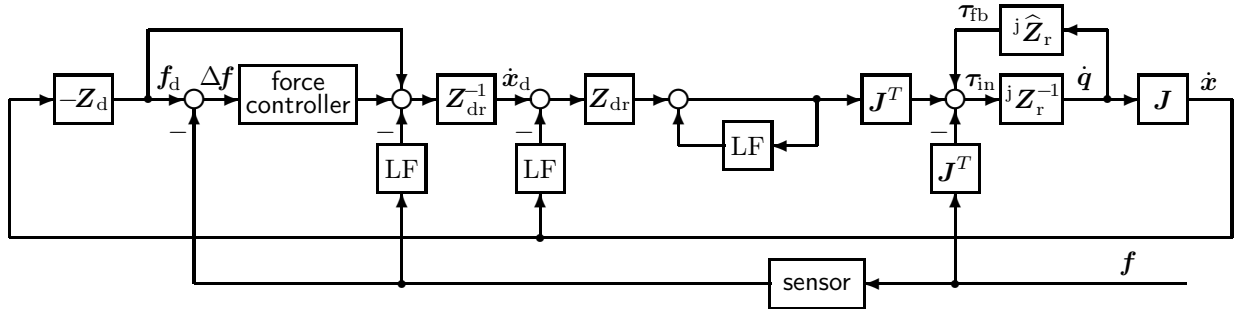


Figure 4.12: Rearranged diagram of impedance control with disturbance observer

this nominal model and the real system including model feedback the dynamic equation of the real system can be written as follows:

$$\dot{\mathbf{x}} = \mathbf{Z}_{dr}^{-1}(\mathbf{f}_u - \mathbf{f} - \mathbf{f}_{dist}). \quad (4.7)$$

The disturbance force is then estimated by

$$\mathbf{f}_{dist} = \mathbf{f}_u - \mathbf{f} - \mathbf{Z}_{dr}(\dot{\mathbf{x}}) \quad (4.8)$$

and fed back to the control input force. If the nominal model describes accurately the robot dynamics without friction, \mathbf{f}_{dist} will correspond to the friction force. As it is typically some second order system the calculation of the disturbance force requires the estimation of the end-effector acceleration $\ddot{\mathbf{x}}$. At implementations where the acceleration is not measured directly but obtained by differentiation of position or velocity a low pass filter LF is inserted to reduce the high frequency noise included in \mathbf{f}_{dist} . Experimental results of the disturbance observer concept applied to haptic device control have been reported by Kwon and Woo [KW00]

An analogy to position-based impedance control emerges when rearranging the block diagram as depicted in figure 4.12. This rearrangement assumed a linear nominal impedance

\mathbf{Z}_{dr} and low pass filter. The force control law together with the admittance $\mathbf{Z}_{\text{dr}}^{-1}$ of the nominal model acts as trajectory generator for the end-effector motion providing the input of an inner control loop. Assuming the frequency of \mathbf{f} to be much below the cut-off frequency of LF and the use of a proportional force control law with gain \mathbf{K} the commanded tip position is

$$\dot{\mathbf{x}}_{\text{d}} \approx \mathbf{Z}_{\text{dr}}^{-1} ((\mathbf{I} + \mathbf{K}) \Delta \mathbf{f}). \quad (4.9)$$

The structure of the inner control loop reveals one of the major deficiencies of this control scheme. The comparatively simple control law is based on the nominal model. In case of large deviations between the impedance of the real system and the nominal impedance this control law may produce comparatively poor results. In general there does not seem to be a conceptual advantage of the observer based approach over multiple loop algorithms applying a control law based on computed torque in the inner-most control loop.

4.4 Friction Model and Compensation Scheme of the ViSHARD3 Device

The friction compensation approach used for the impedance control of the ViSHARD3 device is a combination of model-based friction attenuation (see section 4.3.2) and force feedback action. Hardware experiments for the study of the ViSHARD3 joint friction characteristics are described in section 4.4.1. Based on these results a friction model structure is proposed in 4.4.2. Section 4.4.3 discusses the static friction compensation scheme and section 4.4.4 an adaptation algorithm for the friction model parameters accounting for the time-varying nature of the sliding friction.

4.4.1 Friction Identification

The interaction with haptic interfaces typically includes a wide spectrum of motions ranging from zero motion over low velocities to fast motions with frequent velocity reversal. This points to the demand for a model covering a high richness of friction phenomena: accurate modeling of Coulomb and viscous friction to cope with medium and high velocity motions; of stiction effects to manage velocity reversals and to reduce the steady-state force error at zero motion; of the Stribeck effect, frictional lag, stiction, and the rate dependency of the break-away force to realize slow motions within the partial fluid lubrication regime. Less significant seems to be the inclusion of pre-sliding displacement and hysteresis due to the moderate requirements regarding positioning accuracy.

In addition to the control task the sensor capability of the hardware has an important influence on the choice of the model complexity. Advanced friction compensation schemes for harmonic drives proposed in the literature are typically implemented and tested at dedicated testbeds with sensors not available at practical hardware setups. For example the control law suggested by Gandhi *et al.* [GGD02] requires measurement of the gear output position to account for the structural damping of the flexspline. The ViSHARD3 device only provides sensing of the motor positions with incremental encoders and of the interaction force at the end-effector. As the motor velocity is obtained via numerical differentiation no adequate velocity estimation within the partial fluid lubrication regime is available due to large quantization errors. This impairs the benefit of an inclusion of the

Stribeck effect and frictional lag to the model. Our decision to do without these effects has been backed up by the fact, that ViSHARD3 showed very little susceptibility to stick-slip motions.

To be able to define an appropriate friction model for the ViSHARD3 device several hardware experiments have been carried out in order to study the significance of certain friction phenomena: nonlinearity and asymmetry of the Stribeck curve and its variation over time and temperature as well as the torque and position dependency of friction.

Stribeck Curve

Common experimental procedures for the identification of the Stribeck curve (i. e. friction as a function of the steady state velocity) proceed either by closed loop control of constant velocities and observation of the average motor torques or, vice versa, by the application of steady motor torques and monitoring of the average resulting velocities. The closed loop approach has the disadvantage that the controller action typically gives rise to a high noise content of the commanded motor torque. For instance quantization errors of the velocity measurement can cause high frequent motor torque fluctuations in case of high gain velocity control. On the other hand, closed loop experiments can be obligatory for measurements within the partial fluid lubrication regime due to sticking effects. Moreover, they better reflect the fact, that friction is a function of the steady state velocity and not vice versa (note, that this function is not necessarily invertible). This had been the main motivation for the decision to exercise the closed loop technique.

Conducting identification experiments at a discrete set of constant velocities it could be observed, that the motor torque needed to keep the velocity steady did not remain constant but decreased with time. This is illustrated in figure 4.13 showing the progression of the commanded actuation torque required to keep joint 3 of ViSHARD3 at the constant velocity of π rad/s. The change of the actuation torque is particularly rapid within the first ten seconds where it decreases from 4.6 to 4.3 N m. The overall decrease of the friction within 20 min is around 0.9 N m. Among possible explanations for this effect is a variation of the operating temperature modifying the physical properties of the grease. In order to reduce the measurement time and the temperature shift during the experiment it has been decided to identify the Stribeck curve along a velocity ramp instead of discrete velocities. The slope of the ramp has been selected sufficiently small so that inertial torques are negligible.

The measurement result obtained for the ViSHARD3 haptic interface is presented in figure 4.14. It shows the commanded motor torque multiplied with the gear ratio versus the measured joint velocity. The result of joint 2 is not given because it is very similar to the frictional behavior of joint 3. The shape of the curve obtained for joint 2 and 3, which is characterized by a steady decrease of the slope with increasing velocity, is particularly typical for these kind of joint components (Maxon motors coupled with HFUC harmonic drive gears). A similar nonlinear shape of the Stribeck curve has been identified for most joints of ViSHARD6 and ViSHARD10 (this also agrees with the findings of other authors, see e. g. [SMA95], [Pee03]). The viscous friction curve of joint 1 differs from the others through a distinct inflection point. Such a characteristic, whose identification has been reproducible, has been observed only for a few joints of the ViSHARD devices. A Stribeck curve with similar shape has been identified by Visioli *et al.* [VAL01]. None of the joints of the ViSHARD interfaces showed the highly nonlinear behavior described by

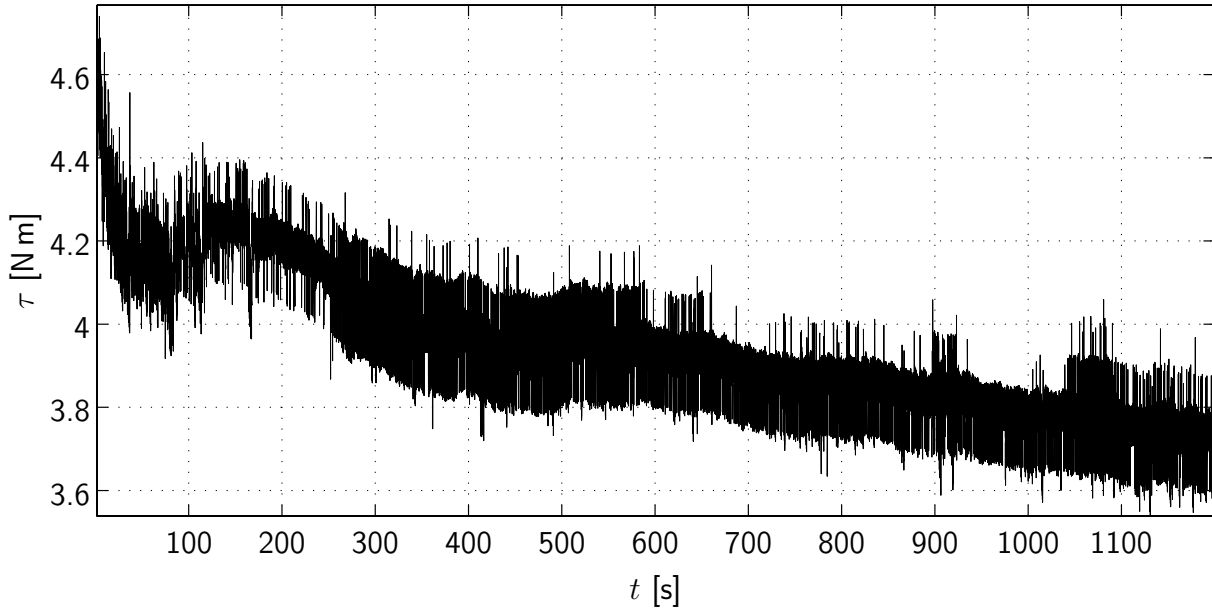


Figure 4.13: Variation of friction with time (joint 3 of ViSHARD3, $\dot{q} = \pi$ rad/s)

Tuttle [Tut92]. The odd characteristics noted by Tuttle has been assumed to be caused by significant resonance losses around certain joint velocities.

Although all ViSHARD3 joints have identical component parts it can be felt that the sliding friction of joint 1 is significantly lower than the friction of the other joints when backdriving them with the hand, an observation attributed to the large susceptibility of the harmonic drive friction behavior on manufacturing and assembly tolerances. This indicates the need for an experimental friction identification rather than a modeling approach purely based on cataloged empirical data. The difference between the sliding friction of the joints is hard to quantify due to the strong dependence of the results on the operating conditions. For instance the measurement results presented in figure 4.14 have been obtained after some warm-up of the interface. As the temperature at the tooth meshing area of the gears has not been accessible for measurement it has not been possible to verify similar test conditions.

A qualitative study of the effect of the operating temperature on the Stribeck curve has been conducted for a 7 DOF telemanipulator designed at the Control Systems Group of the Technische Universität Berlin (see [SB04] for a detailed description of the hardware design). To analyze the dependence of the Stribeck curve on the direction of motion the joints have been commanded to follow a triangular velocity trajectory, see figure 4.15. At the start and end of each experiment the temperature at the gear housing has been measured. Although this temperature does not correspond with the temperature at the tooth meshing area it allows a qualitative study of the influence of temperature on the frictional behavior. The measurement results of joint 6, that has the same component parts as the ViSHARD3 joints, are shown in figure 4.15. It indicates a considerable decrease of the viscous friction with increasing temperature whereas variations of the Coulomb friction term are less significant. The initial and final temperature at each experiment along with the coefficients of a 4th order polynom fitting the measurement data best in a least squares sense is provided in table 4.2. In order to study the symmetry of the Stribeck curve the result for the different segments of the commanded trajectory are shown in common plots,

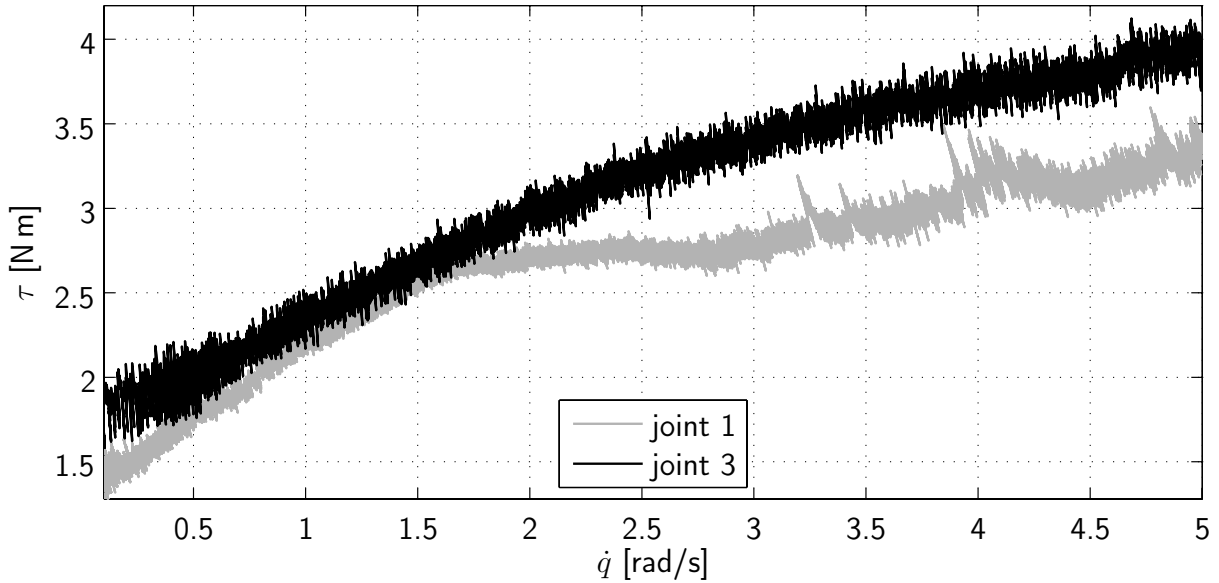


Figure 4.14: Stribeck curve of joint 1 and 3 of the ViSHARD3 device

Table 4.2: Analysis of the measurement results presented in figure 4.15 ($\dot{q} > 0$, $\ddot{q} < 0$)

temperature	initial temperature	final temperature	coefficients of polynomial fit
26 °C	24.9 °C	26.3 °C	$[-0.0037 \ 0.0487 \ -0.2642 \ 1.008 \ 1.183]$
32 °C	31.6 °C	32.6 °C	$[-0.0041 \ 0.0500 \ -0.2427 \ 0.808 \ 1.050]$
36 °C	35.6 °C	35.9 °C	$[-0.0019 \ 0.0257 \ -0.1509 \ 0.619 \ 1.033]$

see figure 4.16. It can be observed that the shape of the curves is nearly identical for positive and negative joint velocities. Their difference has mainly the form of a constant offset of approximately 0.2 N m. A possible explanation of this deviation is an offset of the PWM amplifier current control.

During the perennial use of the ViSHARD3 device several adjustments of the friction model had been necessary to account for the tendency of the sliding friction to decrease with time. The variation of the Stribeck curve with time has been particularly substantial during the run-in period. A documentation of this effect is presented in figure 4.17 comparing the Stribeck curve of joint 1 of ViSHARD10) measured after a few hours of operations at a low velocity with the result after an additional run-in of six hours at a high velocity. In order to avoid differences due to dissimilar operating conditions the measurements have been conducted after an adequate warm-up of the joints. Whereas the Coulomb friction term did not change significantly, the viscous friction has been lowered drastically due to the increased time of operation.

Break-Away Torque

In order to identify the break-away torque of the joints the actuation torque has been commanded to follow a ramp with a slope of 0.1 N m/s. To provide similar operating conditions the joints have been warmed up and driven to a reference motor position via

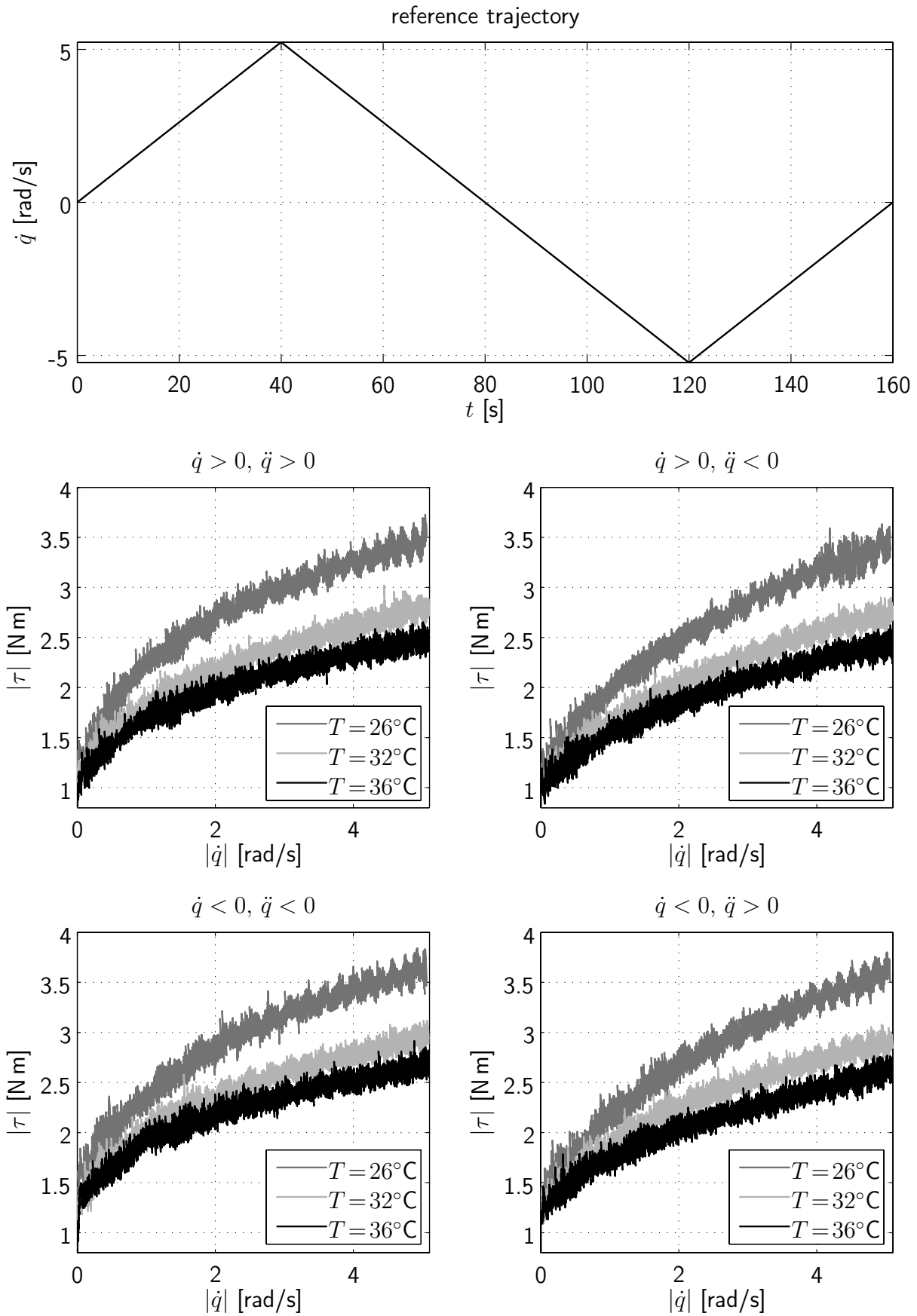


Figure 4.15: Temperature dependency of the Stribeck curve (joint 6 of the 7 DOF telemanipulator presented in [SB04])

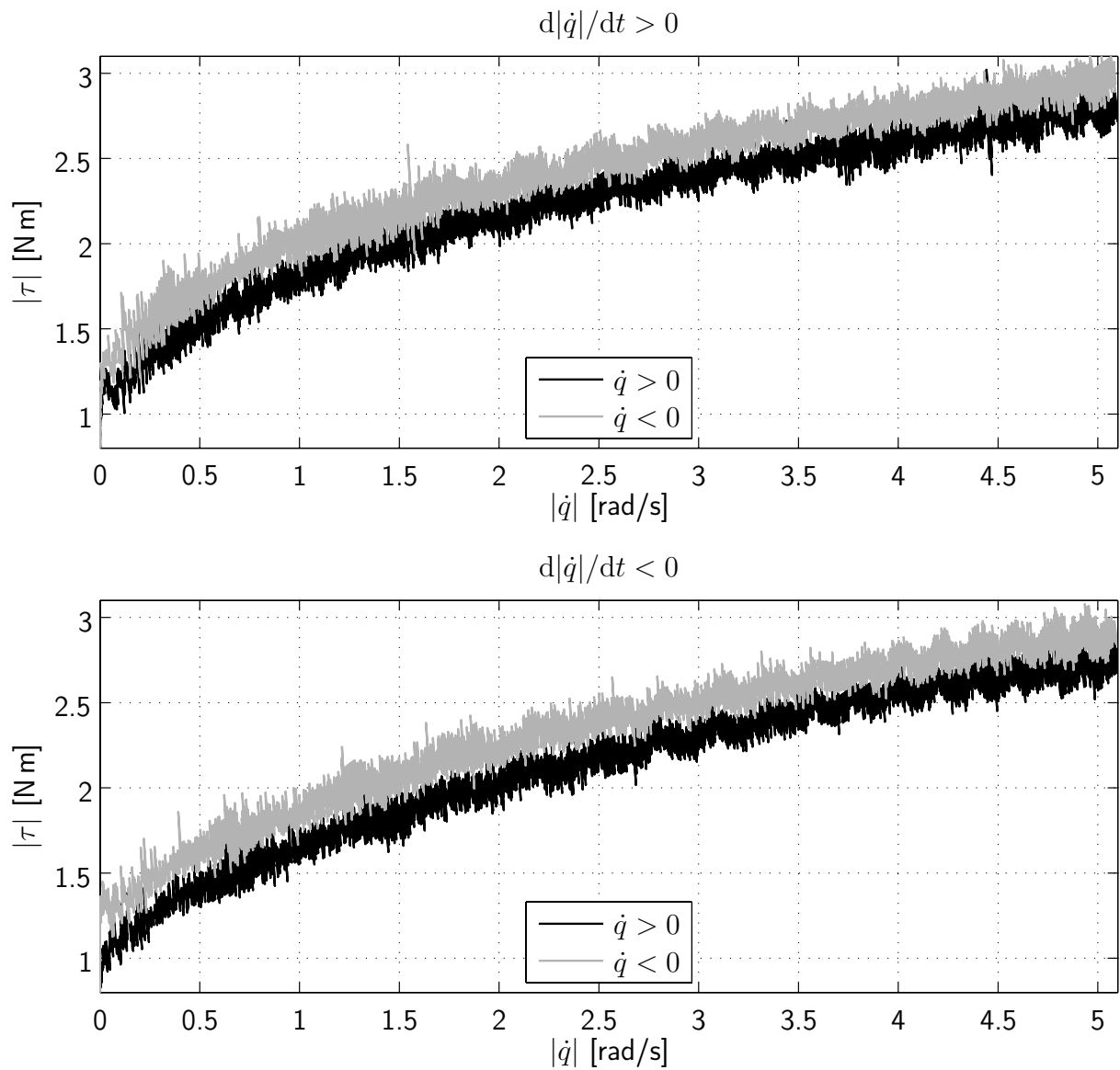


Figure 4.16: Symmetry of the Stribeck curve (32°C, joint 6 of the 7 DOF telemanipulator presented in [SB04])

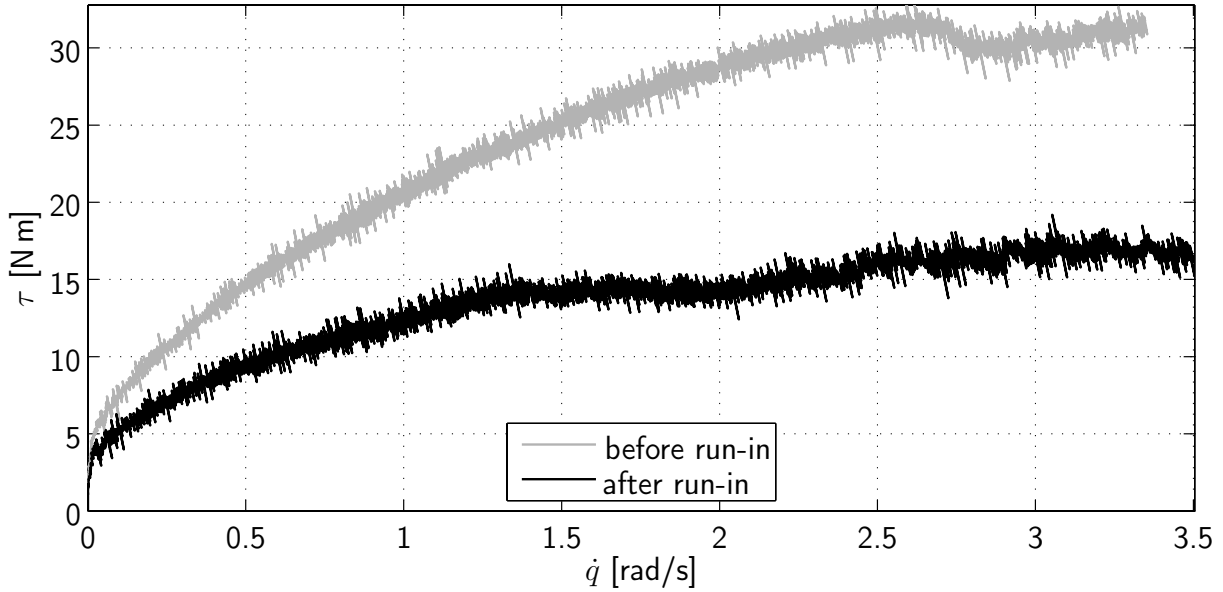


Figure 4.17: Change of frictional behavior during the run-in period (joint 1 of ViSHARD10)

integral closed loop control. Figure 4.18 shows the results of four successive experiments accomplished with joint 1 of ViSHARD3. It reveals two difficulties in determining the break-away torque: First, the transition from rest to sliding is not clear-cut but characterized by a stick-slip motion initiated at an actuation torque around 0.5 N m. This behavior can possibly be explained by the multiple mechanical parts and friction sources inherent in the joints. Second, the repeatability of these experimental results turned out to be comparatively low. Defining the break-away torque τ_s as the actuation torque where the joint motion is initiated without falling back to rest, it varies from 1.19 N m (2nd measurement) over 1.24 N m (3rd measurement) and 1.46 N m (4th measurement) to more than 1.5 N m (1st measurement). Due to this large variation it has been decided to set the break-away torque equal to the Coulomb friction term (the Coulomb friction of joint 1 of ViSHARD3 is given with $T_C = \pm 1.4$ N m, see figure 4.14).

Torque Dependency

As no dedicated testbed with torque sensing capability for the analysis of the load dependency of the joint friction had been available, joint 1 and 3 of ViSHARD3 have been rigidly coupled via link 2 as shown in figure 4.19. The experiment proceeded by commanding the torque of joint 1 to follow a ramp with a slope of 1 N m/s to generate a load torque while controlling joint 3 to maintain a constant velocity. The experiments have been operated at different joint velocities and with commanded joint torque trajectories in and opposed to the direction of rotation. The load independent friction term (Coulomb and viscous friction) of both joints has been compensated with model feedforward. Assuming this compensation to be ideal and the load dependent friction torque T_{load} equal for both joints the torque balance is according to figure 4.20 given with

$$\tau_3 = 2T_{\text{load}} + \tau_1, \quad (4.10)$$

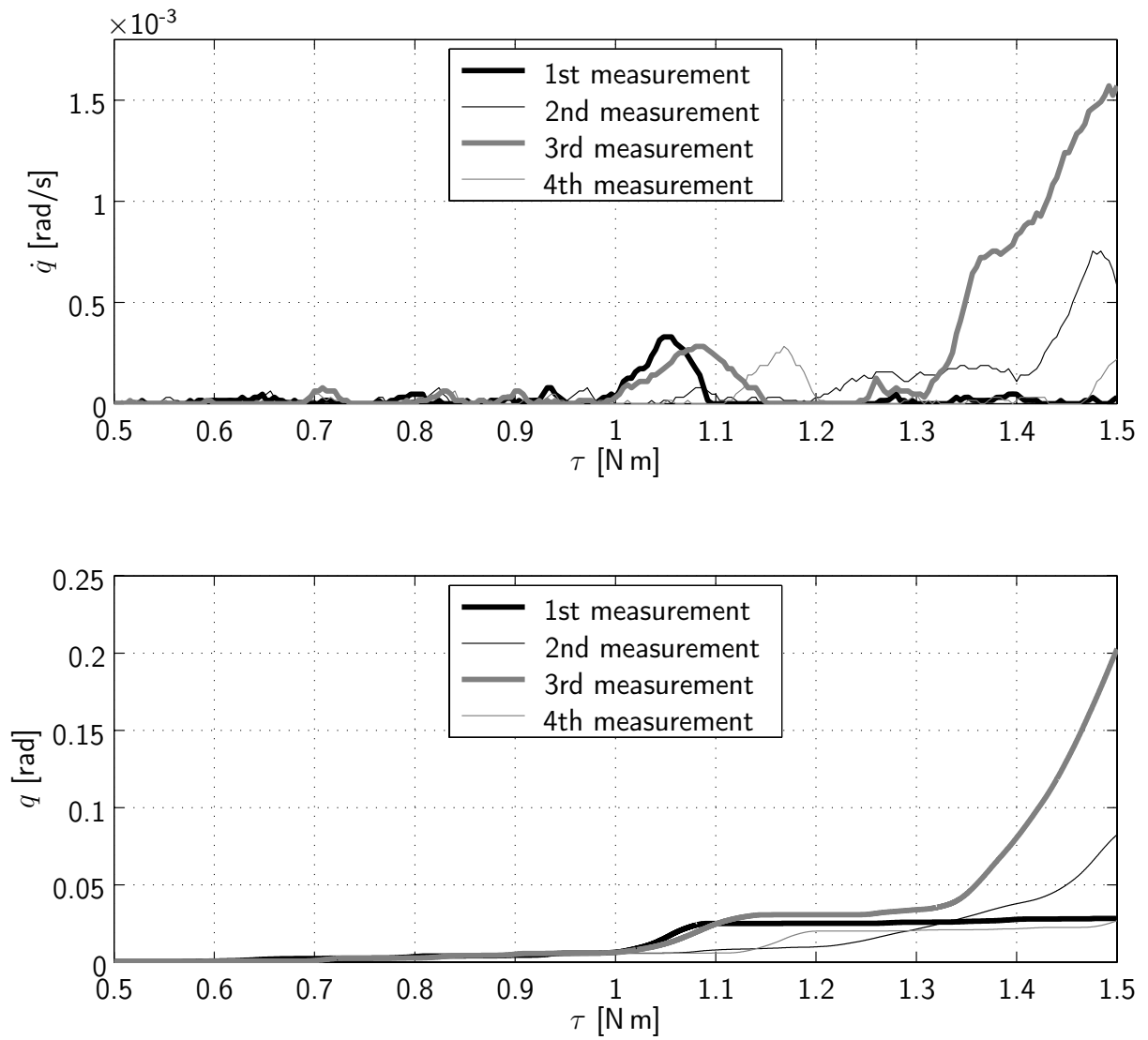


Figure 4.18: Results of break-away force identification experiments (joint 1 of ViSHARD3).

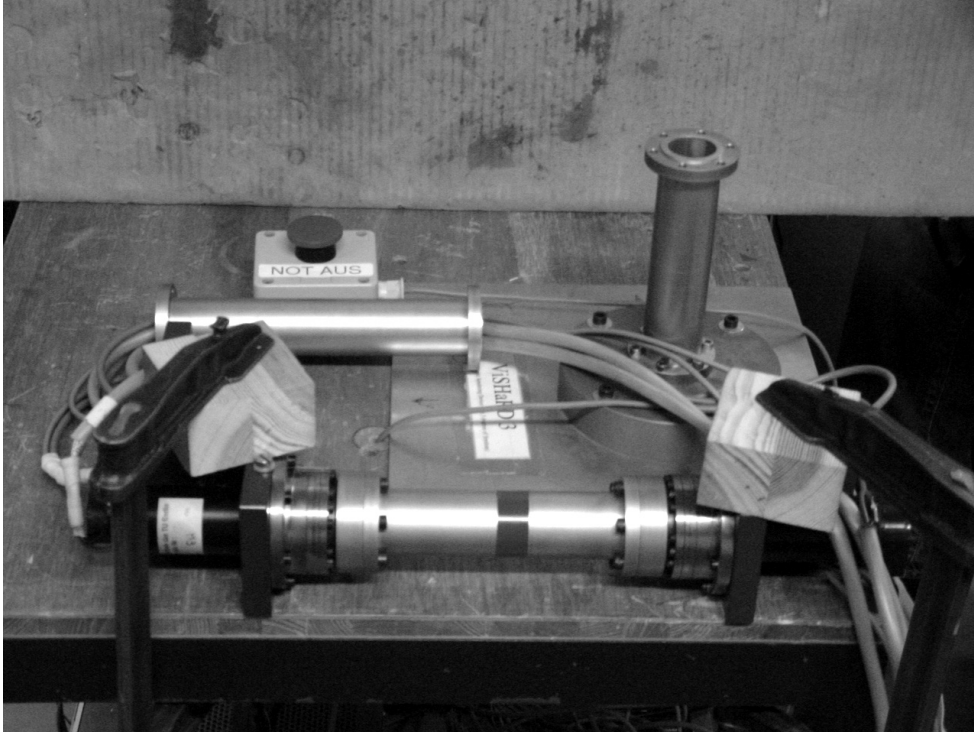


Figure 4.19: Hardware setup for identification of load dependent friction

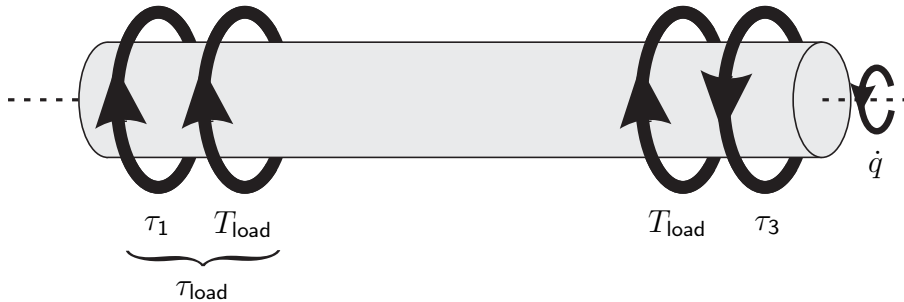


Figure 4.20: Torque balance: the load dependent friction T_{load} opposes the motion \dot{q} .

where τ_1 and τ_3 are the commanded torques (without friction feedforward term) of joint 1 and 3, respectively. Note, that T_{load} is always directed opposed to the direction of motion. The torque dependent friction is then calculated with

$$T_{\text{load}} = \frac{1}{2} (\tau_3 - \tau_1) \quad (4.11)$$

and τ_{load} , the torque applied at the load side of the joints, with

$$\tau_{\text{load}} = \tau_1 + T_{\text{load}}. \quad (4.12)$$

Figure 4.21 presents experimental results measured at the joint velocity $\dot{q} = \pi/4$ rad/s. It reveals slight differences for the different directions of the commanded torque of motor 1. Among possible explanations is that the assumption of an identical torque dependent friction behavior of both joints does not hold accurately. These results evidence a convenient description of the load dependent friction by a second order polynomial as indicated by

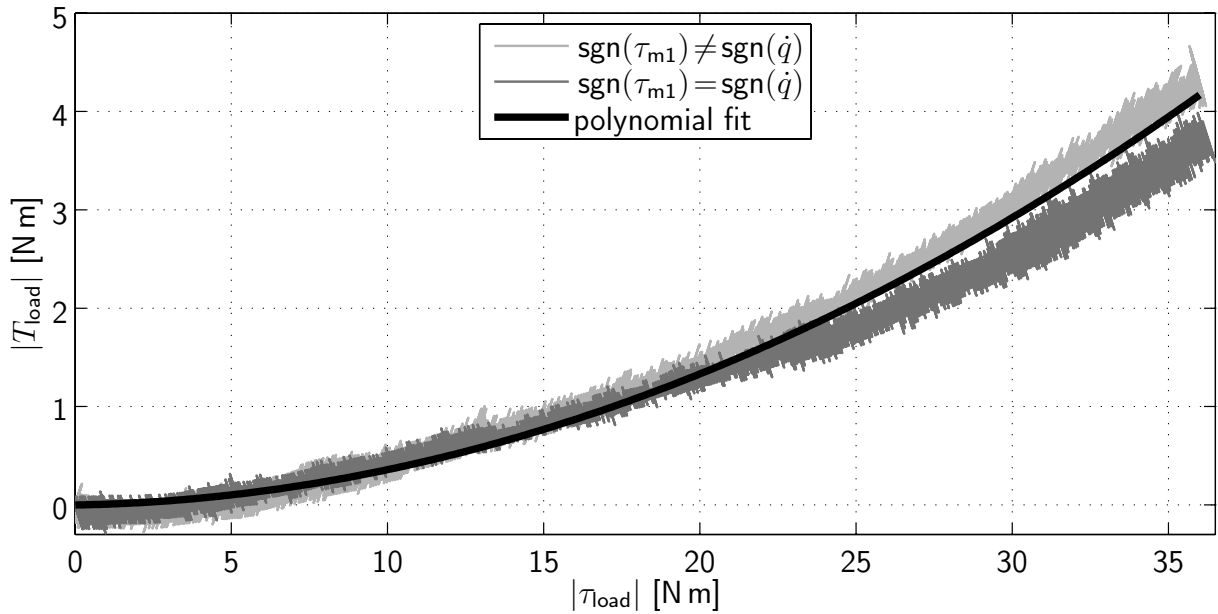


Figure 4.21: Load dependent friction torque of the ViSHARD3 joints

the black line in figure 4.21. Multiple experiments at different joint velocities confirmed a high repeatability and low dependency of the results on the velocity and the operating conditions.

Position Dependency

Gandhi *et al.* [GGD02] investigated the position dependency of harmonic drive friction by conducting velocity tracking experiments at very low velocities. To provide a good tracking accuracy along with a low noise content of the commanded motor torque these experiments require velocity measurement at a very high resolution. An alternative approach is the application of a constant motor torque and observation of the resulting velocity. Figure 4.22 shows the velocity progression of joint 3 of ViSHARD3 measured for a motor torque of 2.8 N m. One can see that the resultant joint velocity is not constant but oscillating. The amplitude and time for two cycles is indicated by the dashed lines. A comparison with the motor position q_m suggests a dominant frequency component at two cycles per motor revolution. Please note, that these observations also hold for the other parts of the measured trajectory. According to figure 4.22 a simple approximation of the velocity trajectory can be expressed with

$$\dot{q} = \bar{\dot{q}} + A \sin(2\dot{q}_{\text{mot}} + \varphi) \approx 0.37 \text{ rad/s} + 7.5 \cdot 10^{-3} \sin(24\pi t \text{ rad/s} + \varphi) \text{ rad/s} \quad (4.13)$$

where $\bar{\dot{q}}$ is the mean of the joint velocity, A the amplitude of the oscillation, \dot{q}_{mot} the mean of the motor velocity, and φ the phase shift. The joint acceleration is then given with

$$\ddot{q} = 2\dot{q}_{\text{mot}}A \cos(2\dot{q}_{\text{mot}} + \varphi) \approx 0.18\pi \cos(24\pi t \text{ rad/s} + \varphi) \text{ rad/s}^2. \quad (4.14)$$

Assuming that position dependent friction torques T_{pos} are the only origin of these joint accelerations, the maximum of T_{pos} is calculated with

$$\max(T_{\text{pos}}) = 2\dot{q}_{\text{m}}AN^2(J_{\text{mot}} + J_{\text{wav}}) \approx 0.18\pi 100^2(0.134 \text{ kg cm}^2 + 0.079 \text{ kg cm}^2) \approx 0.12 \text{ N m} \quad (4.15)$$

where N is the gear ratio, J_{mot} the motor inertia, and J_{wav} the wave generator inertia. Clearly, this is just a crude estimation of the maximum torque loss due to position dependent friction. For example the quantization of the velocity measurement has been approximately $4.7 \cdot 10^{-3}$ rad/s as it has been derived from the position measurement by finite differentiation. As a matter of this fact, the amplitude A of the oscillation may, in the worst case, be underestimated by this value (giving then $\max(T_{\text{pos}}) = 0.19$ N m). Another inaccuracy comes with the neglect of other sources for joint accelerations in the above analysis as for instance the kinematic error and flexibility with hysteresis.

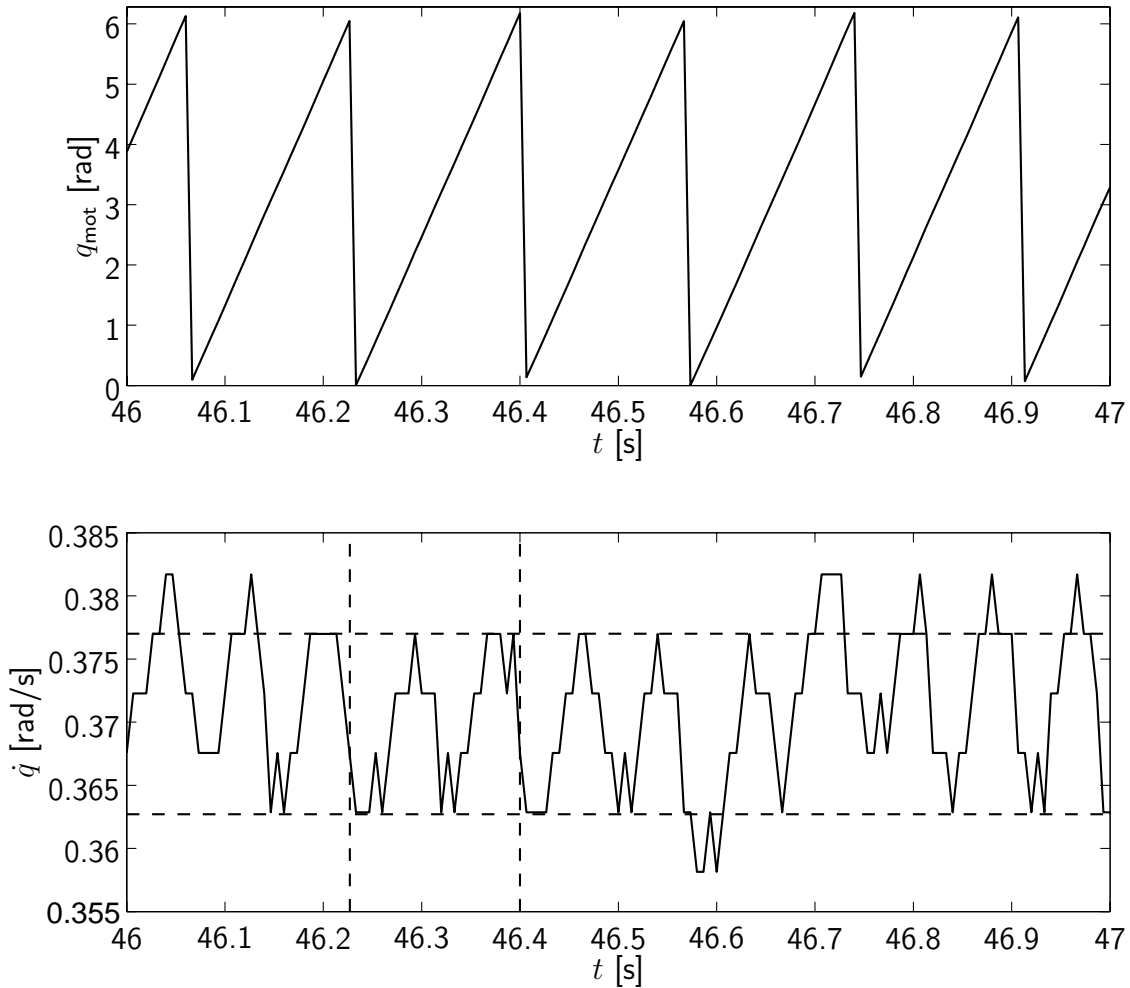


Figure 4.22: Joint velocity progression measured for a constant actuation torque of 2.8 N m (joint 3 of ViSHARD3). Velocity oscillation points to position dependency of friction.

4.4.2 Friction Model

As reported before the friction effects specific to the partial fluid lubrication regime (Stribeck effect and frictional lag) have not been included into the model due to the large quantization error of the velocity measurement and the low observed susceptibility of the joints to stick-slip motions. Pre-sliding hysteresis has been omitted because the requirements for position accuracy are in general low for haptic devices. The almost identical shapes

of the Stribeck curve for the different directions of motion (see figure 4.16) motivated a symmetric model of the sliding friction.

Although the experimental results displayed in figure 4.22 indicate a comparatively low amplitude of the position dependent friction this friction effect causes a significant disturbance to the haptic sensation due to its high frequency. The limited accuracy of the velocity sensing of VISHARD3 made an in-depth study of this friction behavior difficult. A model-based compensation approach of the VISHARD3 friction assuming a sinusoidal relationship between motor position and position dependent friction did not provide a noticeable improvement of the transmission behavior (see [Rim04] for experimental results). Among the reasons for the little success seems to be the too low accuracy of the model. The measurement results reported by Gandhi *et al.* [GGD02] indicate a much more complex relationship between motor position and position dependent friction. Despite of the considerable identification and modeling effort practised by Gandhi *et al.* still no significant reduction of the tracking error could be achieved by the inclusion of a position dependent friction compensation. The authors presume, that the limited benefit is caused by an unmodeled dependence of the friction waveform on the load position. Due to the difficulty in position dependent friction compensation it has not been included in the VISHARD3 model.

Significant friction characteristics revealed by the identification experiments are the load dependency as well as the nonlinearity of the Stribeck curve and its variation with the operating conditions and time. The friction model is therefore given with

$$h(\dot{q}, \tau, \tau_{\text{load}}, \tau_{\text{load}}^0) = \begin{cases} \tau - \tau_{\text{load}}^0 & \text{if } \dot{q} = 0 \text{ and } |\tau - \tau_{\text{load}}^0| < f_c + f_{\text{load}} \\ \text{sgn}(\tau - \tau_{\text{load}}^0)(f_c + f_{\text{load}}) & \text{if } \dot{q} = 0 \text{ and } |\tau - \tau_{\text{load}}^0| > f_c + f_{\text{load}} \\ \text{sgn}(\dot{q})(f_c + f_{\text{visc}} + f_{\text{load}}) & \text{if } \dot{q} \neq 0 \end{cases} \quad (4.16)$$

with

$$f_{\text{visc}}(\dot{q}) = p_4 |\dot{q}^4| + p_3 |\dot{q}^3| + p_2 |\dot{q}^2| + p_1 |\dot{q}|; \quad f_c = p_0 \quad (4.17)$$

and

$$f_{\text{load}}(\tau_{\text{load}}) = a_2 |\tau_{\text{load}}^2| + a_1 |\tau_{\text{load}}| + a_0 \quad (4.18)$$

where p_i and a_i are the parameters of a 4th and 2nd order polynomial, τ the motor torque multiplied with the gear ratio, τ_{load} the dynamic, and τ_{load}^0 the static load torque at the gear output. The static differs from the dynamic load torque in that the acceleration of the corresponding joint is assumed to be zero:

$$\tau_{\text{load},i} = \mathbf{J}_i^T(\mathbf{q})\mathbf{f} + g_i(\mathbf{q}) + \mathbf{M}_{\text{load},i}(\mathbf{q})\ddot{\mathbf{q}} + \mathbf{C}_i(\mathbf{q}, \dot{\mathbf{q}})\dot{\mathbf{q}} \quad (4.19)$$

$$\tau_{\text{load},i}^0 = \mathbf{J}_i^T(\mathbf{q})\mathbf{f} + g_i(\mathbf{q}) + \sum_{\substack{k=1 \\ k \neq i}}^n (m_{\mathbf{q},ik}(\mathbf{q})\ddot{q}_k + c_{ik}(\mathbf{q}, \dot{\mathbf{q}})\dot{q}_k) \quad (4.20)$$

In these equations $\tau_{\text{load},i}$ is the dynamic and $\tau_{\text{load},i}^0$ the static load torque of the i th joint of a manipulator with n joints. \mathbf{J}_i^T , $\mathbf{M}_{\text{load},i}$, and \mathbf{C}_i are the i th row of the device transposed Jacobian, load side inertia matrix, and the matrix describing Coriolis and centrifugal torques, respectively. The variables g_i , $m_{\mathbf{q},ik}$, and c_{ik} are the appropriate elements of the vector of gravitational torques, the joint inertia matrix $\mathbf{M}_{\mathbf{q}}$, and \mathbf{C} . \mathbf{M}_{load} differs from $\mathbf{M}_{\mathbf{q}}$ in that the wave generator and motor inertia is not included.

The model of the static friction term basically conforms to the approach described by equation (4.2). The only disagreement is the characterization of the break-away torque as a combination of a load dependent with a constant term. An explanation for the torque independent component is a load torque due to the preloading of the gear not included in τ_{load}^0 . The difference between the torque applied at the gear in- and output, $\tau - \tau_{\text{load}}^0$, corresponds to f_e . In many publications this term is simplified to the applied motor torque (see e. g. [JL92]). In haptic applications such an approximation is not justified due to the high load torques generated by the human operator.

The description of the Stribeck curve with a 4th order polynomial offers a comparatively precise agreement with the measured behavior. In case of simpler shapes without distinct inflection points also a simpler model of the viscous friction term given with

$$f_{\text{visc}} = b_1 |\dot{q}| + b_2 \sqrt{|\dot{q}|} \quad (4.21)$$

provides a well approximation (the inferior accuracy at very low velocities is in practice harmless due to the large quantization error of the velocity measurement). Because the models for the Stribeck curve and the load dependent friction are linear in their parameters they can be derived from identification measurements by standard linear least squares techniques. The variation of the Stribeck curve with the operating condition and time has been taken into account by adaptation of its parameters as described in section 4.4.4.

A difficulty with the consideration of the load dependent friction is the lacking joint torque sensing capability of the VISHARD interfaces. The calculation of τ_{load} using equation (4.19) requires the joint accelerations to be known. Their estimation from shaft encoder measurements requires significant filtering action to reduce the sensor noise. Thus, the achievable bandwidth of the load torque estimation is fairly limited. A model-based forward computation of τ_{load} without acceleration measurement is difficult as the joint accelerations themselves are dependent on the frictional losses (and thus also on τ_{load}). Solving the dynamic equation (3.1) for $\ddot{\mathbf{q}}$ and substituting the result in equation (4.19) renders it implicit in the load torque (see also [Dup90]). A possible solution approach is to iteratively compute τ_{load} . As $|\mathbf{f}_{\text{load}}|$ is small compared to $|\tau_{\text{load}}|$ a fast convergence of the iterative process can be expected.

4.4.3 Compensation of Static Friction

The model-based compensation of static friction is less straightforward than the reduction of the sliding friction. The hassle is caused by the fact, that the static friction is not a function solely on the system states but also on the applied motor torque. Thus, the static friction is directly affected by the compensation torques added to the motor torque. In many published control schemes this fact is ignored. For example in the friction compensation scheme presented by Johnson and Lorenz [JL92] the static friction is calculated based on the motor torque commanded by the output of the position controller and an acceleration feedforward term. The contribution of the friction compensation torque is not included. As a consequence, this approach is likely to provide too low compensation torques. As an example consider a joint at rest with zero torque applied at the load side. If the motor torque desired to be transmitted to the joint output is well below the break-away torque this compensation scheme will only double the applied motor torque. This is far from the ideal correction, that adds the break-away torque. The consequence of such an

uncomplete stiction compensation is the haptic sensation of an ‘snapping in’ at slow velocity reversals (this is particularly true in case of a good compensation of the sliding friction). Although it is theoretically possible to implement an ideal compensation algorithm this does not seem to be applicable in practice. As the commanded motor torque is mostly the output of a feedback controller it is typically tainted with a considerable noise content. At low commanded torques this effects a high frequent switching of the sign. Because in case of ideal stiction compensation the change of the sign is likely to produce a discontinuous change of the correction torque the noise is amplified strongly causing chattering.

As our experiments with ViSHARD3 confirmed the substantial conflict between chattering avoidance and the performance of model-based stiction compensation alternative approaches have been tried. The addition of a high frequent dither signal offered some reduction of stiction forces but produced significant acoustic noise interfering strongly the immersivity of the system. It turned out that a rather simple and convenient technique for the suppression of stiction effects is the application of dedicated force feedback control. This approach has been motivated by the observation that admittance control implementations with inner velocity or position control loop successfully eliminate static friction disturbances due to the integral action involved in the transformation of the force error $\Delta \mathbf{f} = \mathbf{f}_d - \hat{\mathbf{f}}$ to the commanded velocity or position (see figure 3.5). A similar good disturbance rejection can be achieved when using a force control law with integral action within the impedance control architecture. Such a control law has, however, the drawback to reduce the closed loop bandwidth of the system significantly. A possible way to mitigate this disadvantage is the removal of the integral action as soon as the motion of the joint initiates. The resultant control law aims at offering a good disturbance rejection for the joints at rest while maintaining a good dynamic behavior of the joints in motion. The proposed control algorithm has the following form:

$$\tau_i(t) = \begin{cases} \mathbf{J}_i^T \left(\mathbf{f}_d + \mathbf{K}_P \Delta \mathbf{f} + \mathbf{K}_D \Delta \dot{\mathbf{f}} \right) + g_i(\mathbf{q}) + h_i(\dot{q}_i, \tau_{\text{load},i}) & \text{if } |\dot{q}_i| \geq |\dot{q}_i|_{\text{min}} \\ \mathbf{J}_i^T \left(\mathbf{f}_d + \mathbf{K}_P \Delta \mathbf{f} + \mathbf{K}_D \Delta \dot{\mathbf{f}} \right) + g_i(\mathbf{q}) + \tau_{0,i} + \int_{t_{\text{sw},i}}^t \mathbf{J}_i^T \mathbf{K}_I \Delta \mathbf{f} dt & \text{if } |\dot{q}_i| < |\dot{q}_i|_{\text{min}} \end{cases} \quad (4.22)$$

with

$$\tau_{0,i} = h_i(\dot{q}_i(t_{\text{sw},i}), \tau_{\text{load},i}(t_{\text{sw},i})) \quad (4.23)$$

where \mathbf{K}_P , \mathbf{K}_D , and \mathbf{K}_I are the controller gain matrices, $|\dot{q}_i|_{\text{min}}$ defines the threshold for switching between PD- and PID-control, and $t_{\text{sw},i}$ is the point in time at that the integral action is added and the model-based friction compensation term $h_i(\dot{q}_i, \tau_{\text{load},i})$ removed. The inclusion of the term $\tau_{0,i}$ prevents discontinuities in the commanded motor torque at the transition from PD- to PID-control (assuming that the initial value of the integrator output is defined to be zero). By setting integration limits a bound for jumps in τ_i can be achieved for the other transition direction.

To assess the benefit of integral control addition at low joint velocities the end-effector of ViSHARD3 has been firmly coupled to a linear guide, see figure 4.23. Technical specifications of the linear guide are given in appendix A.1.4. Whereas ViSHARD3 has been controlled in the impedance mode with zero target impedance (zero interaction force for arbitrary motions) the linear guide has been position controlled forcing the end-effector to follow a sinusoidal motion with an amplitude of 0.05 m and frequency of 0.1 Hz. For comparison the control has been switched after 20 seconds from conventional PD force control

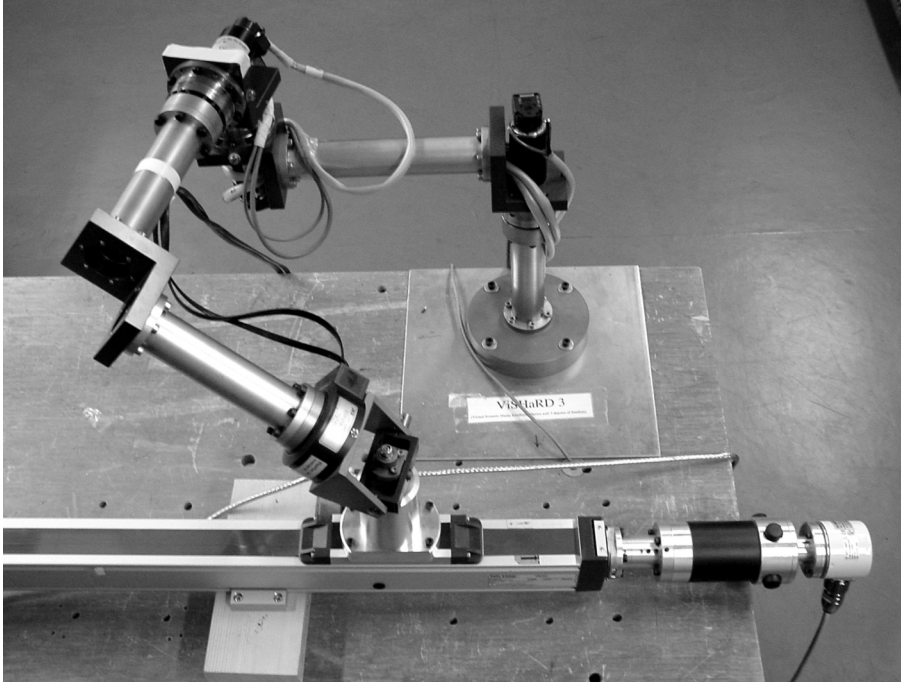


Figure 4.23: ViSHARD3 coupled to a linear guide

to the algorithm given in equation (4.22). To bound the contribution of the integral action, integration limits have been set at 2 Nm.

The enforced velocity trajectory of joint 2 is shown in figure 4.24. Viewing the unfiltered measurement signal reveals a general problem with the switching function defined in equation (4.22). As the joint velocity is computed by finite differentiation of the quantized position measurement it is tainted with serious quantization noise. The typical consequence is high frequent switching between discrete velocity values. Accordingly, such a simple switching function results in high frequent switching between PD- and PID-control. A simple and effective remedy is the use of a more advanced switching mechanism as for instance relay functions. The measurement results presented in figure 4.24 have been obtained with switching from PID- to PD control when $|\dot{q}_i|$ increases to $4\Delta\dot{q}_i$ and changing back to PID-control when it goes down to zero. The variable $\Delta\dot{q}_i$ denotes the quantization interval of \dot{q}_i . As the measured velocity never reaches the switching threshold the control algorithm remains in the PID mode.

The resultant load torque of joint 2, that is the measured end-effector force mapped to joint 2 (inertial load torques are negligible due to the low acceleration), has a large noise content due to the derivative action in the position control of the linear guide and the force control of ViSHARD3. Therefore, also the filtered measurement signal using a first order low-pass filter with 50 rad/s cut-off frequency is shown. One can detect a partial compensation of the friction torque due to the gain of the PD-control ($|\tau_{\text{load}}|$ remains well below the Coulomb friction torque). The addition of the integral action, however, almost eliminates the stiction and the sliding friction. A good performance of the proposed algorithm could also be observed when the device is driven by a human operator. The integral action successfully removed any force threshold required to initiate motion which greatly eased interaction tasks requiring fine-positioning of the end-effector. In the experiments no degradation of performance and stability properties could be detected.

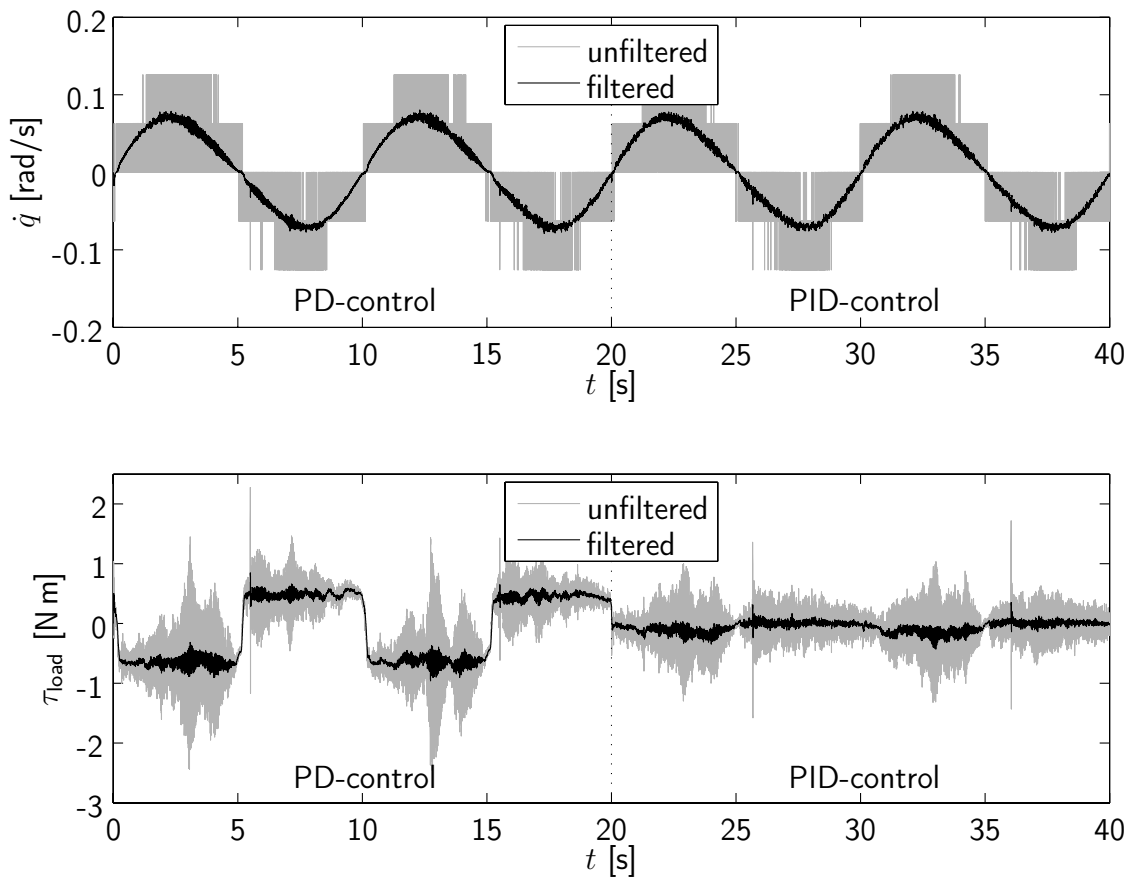


Figure 4.24: Stiction compensation: Friction reduction at very low velocities through addition of integral action to the PD control-law (joint 2 of ViSHARD3)

These included highly dynamic motions in free-space simulations as well as collisions with virtual walls, an interaction that is characterized by high-speed velocity reversal and a demanding requirement on force bandwidth.

4.4.4 Adaptive Compensation of Sliding Friction

A possible way to track slow changes of the frictional behavior (e.g. due to wear) are occasionally executed identification experiments where the device is controlled to move along a pre-planned excitation trajectory. Off-line identification is, however, not capable of accounting for the dependence of the Stribeck curve on the operating conditions typically changing significantly during the task execution. Consequently, fixed parameter models require to be quite conservative to avoid friction overcompensation. A typical effect of friction overcompensation at small velocities are low frequent oscillations when trying to hold the end-effector fixed with a loose grip (moderate overcompensation at higher velocities is less severe because it usually does not produce limit cycling). The implemented fixed parameter friction compensator of the ViSHARD3 device is therefore based on identification experiments conducted at high operating temperatures. This effects an uncomplete friction compensation at the start of operation gradually improving with time, a behavior that could be readily noticed during hardware experiments. As opposed to typical indus-

trial robots applications haptic tasks frequently take only a short time this approach can be unsatisfactory. More convenient seems to be an adaptation of the friction model during the task execution.

Most of the research on adaptive friction compensation reported in the literature is focused on continuous adaptation of the friction compensator by means of describing the adapted parameters by some differential or finite difference equation. Among the challenges arising with these approaches are the guaranty of robust stability of the parameter adaptation algorithm in the presence of unmodeled high-order dynamics, convergence to the real parameters in case of poor excitation, and the adaptation of parameters entering the model in a nonlinear way.

The observation that the change of the frictional behavior due to temperature shift is a process of moderate speed motivated the study of an alternative concept in that the friction model is re-tuned from time to time. The idea is to estimate and also to record the friction force at each sampling instant. Contrary to common adaptation approaches the model parameters are not updated iteratively but are determined after a specified number of samples from the stored data by some curve fitting algorithm and then presented to the friction compensator. This technique offers several rewarding possibilities:

- Postprocessing of the stored data: Before the measured friction data are presented to the curve fitting algorithm they can be preprocessed. For instance data can be deleted in order to attain a balanced excitation of the parameters. In case of a very poor excitation of certain parameters the data set can be complemented with information derived from the previous parameter settings. Another option is the application of noncausal filtering to reduce the noise content of the data.
- Usage of more sophisticated friction models: Curve fitting procedures do not require the parameters of the friction model to enter linearly. As there are no stringent limits for the computation time advanced nonlinear optimization algorithms can be applied. It is also easy to identify models with a high number of parameters as for example look-up charts or interpolations with splines.
- Large freedom in the design of the fitting algorithm: It is for example possible to apply algorithms for constrained optimization to increase the reliability of the solution.
- Switching between friction models identified off-line: Because the friction model is not changed continuously the best curve fit can also be chosen from a discrete set of parameter settings derived from off-line identification experiments. This approach may enhance the reliability of the model in terms of its capability for extrapolation.
- Evaluation of the identified friction model prior to the update of the friction compensator: In case of mistrust regarding the reliability of the identified model (e. g. due to insufficient excitation of parameters or significant deviations from expected values) corrections yielding a more conservative setting or the suspension of the update can be made.

As the parameter identification procedure is not part of the control loop it does not affect stability issues. Also switching the parameter settings of the friction compensator does not seem to be problematic because it has an effect similar to a slight hit exerted on the end-effector. The main concern should be devised to the avoidance of friction overcompensation.

Friction Estimation

The sum of the Coulomb and viscous friction is estimated using equation (3.1) and 4.16

$$\mathbf{T}_C + \mathbf{T}_{\text{visc}} = \boldsymbol{\tau} - \mathbf{J}^T(\mathbf{q})\mathbf{f} - (\mathbf{M}_q(\mathbf{q})\ddot{\mathbf{q}} + \mathbf{C}(\mathbf{q}, \dot{\mathbf{q}})\dot{\mathbf{q}} + \mathbf{g}(\mathbf{q}) + \text{sgn}(\dot{\mathbf{q}})f_{\text{load}}), \quad (4.24)$$

where the load dependent friction term is calculated according to equation (4.18) and 4.19. The joint velocity and acceleration is estimated from shaft encoder measurements by numerical differentiation. To reduce the quantization error the Euler approximation uses encoder measurements tracing back forty sample steps. Accordingly, the external force and commanded actuation torque is averaged over the last forty samples. A suitable number of backward steps balancing the quantization noise level and the bandwidth of the friction estimation has been determined experimentally. The phase lag introduced by the filtering action is not problematic as the estimate is not directly used for friction compensation. With a control sampling rate of 2 kHz and a quantization of the joint angle measurement of $\Delta q = \pi \cdot 10^{-5}$ the resultant quantization of the acceleration measurement is

$$\Delta \ddot{q} = \frac{\pi \cdot 10^{-5} \text{ rad}}{(40 \cdot \frac{1}{2000} \text{ s})^2} = 0.025 \text{ rad/s}^2 \quad (4.25)$$

In addition to the filtering action and sensor noise modeling errors of the device dynamics and kinematics are the main sources for friction estimation errors. In particular the assumption of a rigid robot does not hold in practice due to the significant joint flexibilities. Figure 4.25 illustrates the high noise content of the friction estimate. It shows the calculated friction torque versus the joint velocity measured during a free space simulation in a time period of forty seconds. While the end-effector was moved by the operator's hand the device was controlled in the impedance mode as described in section 3.2.1. It can be noticed, that the scatter of the friction estimates is largest for joint 1 and smallest for joint 3. This can be explained by the increased inertial load of the joints placed closer to the device base effecting an inferior mechanical bandwidth. Moreover, the higher complexity of the load dynamics can result in larger modeling inaccuracies. The measurement results agree with the previously observed lower friction level of joint 1. Except for joint 1 figure 4.25 indicates an acceptable reliability of the friction estimation with the proposed algorithm. A direct addition of the estimated friction to the actuation torque², however, produced unsatisfactory results due to the high noise content and the lag introduced by the filtering action.

Adaptation of the Stribeck Curve

The approximation of the Stribeck curve is based on the friction estimates collected within a predefined period of time. As the joint friction model is symmetric the sign of the data points (comprising joint velocity with related friction torque) measured at negative joint velocities is changed. The algorithm proceeds by computing for each quantized joint velocity the average of all related friction torque estimates. The parameters of the friction model given in equation (4.17) are then determined by applying a standard least squares technique. The averaging prior to the curve fitting aims at avoiding a deterioration of the

²In fact, such a compensation scheme is a specific implementation of the disturbance observer approach described in section 4.3.4.

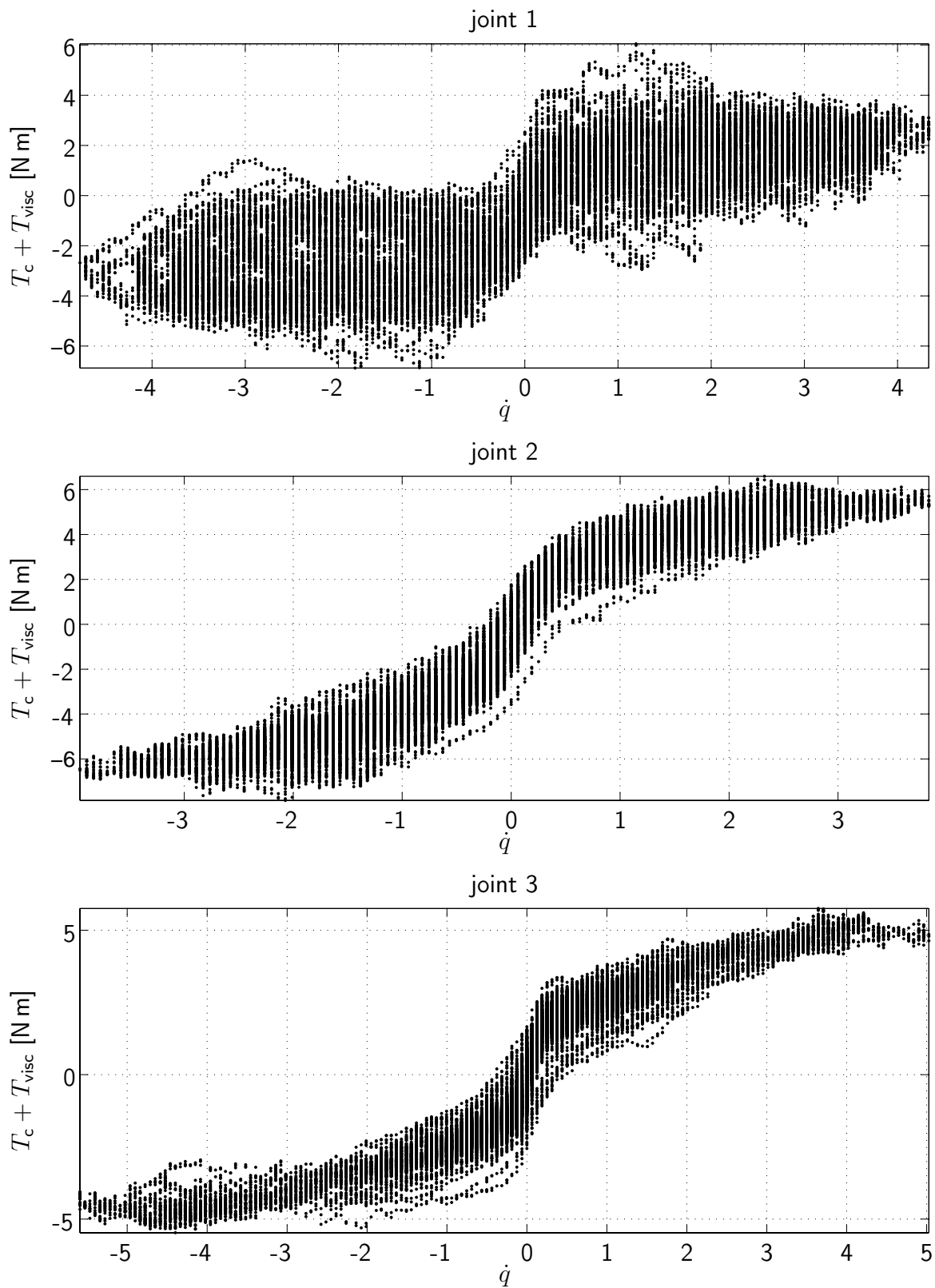


Figure 4.25: Friction torques estimated during a free space simulation in a time period of forty seconds

approximation accuracy at velocity regions where only few measurements are available. As soon as the computation of the new parameter set is finalized an update of the friction compensator is initialized. Because polynomials are typically characterized by very steep slopes at high velocities their extrapolation capability is limited. As a matter of this fact, the sliding friction is hold constant for joint velocities exceeding the highest velocity included in the measurement. In case of joint 2 and 3 characterized by a Stribeck curve of comparatively simple shape also the application of the alternative friction model described with equation (4.21) seems to be rewarding. The moderate slope of this function family at high velocities seems to provide a favorable extrapolation capability.

Experimental Results

To assess the adaptation scheme experiments with a run-time of ten minutes have been performed. In these investigations the ViSHARD3 device was controlled in the impedance mode rendering free space interaction. The time span between the parameter updates of the friction compensator has been set to forty seconds. After five minutes of operation the experiment has been interrupted and immediately repeated with the initial friction parameter settings in order to study possible effects of the friction compensation action on the friction estimation. In the first experiment the device has been moved by a human operator. The identified friction models are presented in figure 4.26. For the sake of clarity not all friction curves are shown. The dashdotted line represents the initial Stribeck curve being used for the friction compensation in the time period of 0-40s and 300-340s. The initial parameter settings have been derived from identification experiments described in section 4.4.1. Viewing the results for joint 2 and 3 a gradual decrease of the estimated sliding friction with run-time can be observed. This is in accordance with the expectations as the operating temperature is rising throughout the experiment. The identified lowering of the friction is not an effect of the friction compensator adaptation because the reinitialization of the parameters does not interfere with this progression. Considering that the joint trajectories differed substantially in each measurement phase as the device has been moved by the operator at will the identified Stribeck curves are quite similar in shape pointing to a convenient repeatability of the friction identification. An evaluation of the friction identification accuracy of joint 2 and 3 is difficult because the true friction is not known. The subjective impression of the operator was an improvement of the compensation performance when switching from the initial friction model to the identified parameters. Later adaptations changed the haptic sensation only marginally. The results for joint 1 are less satisfactory. The large deviation between the friction curves points to a low reliability of the identification.

In order to study the progression of the frictional behavior for repetitive motions the end-effector of ViSHARD3 has been coupled to a linear guide (see figure 4.23) that has been controlled to move along a sinusoidal trajectory. The resultant joint motions and the identified friction curves are given in figure 4.27. Joint 3 remained at rest as the linear guide was oriented horizontally. The results for joint 2 clearly show the change of the friction characteristics with operation time. Again, this change is not an effect caused by the adaptation of the control because the reinitialization of the compensator after five minutes does not seem to affect the friction estimation. The estimation results are quite similar to the friction curves measured during the human induced joint motions indicating a promising degree of reliability of the proposed identification scheme. The

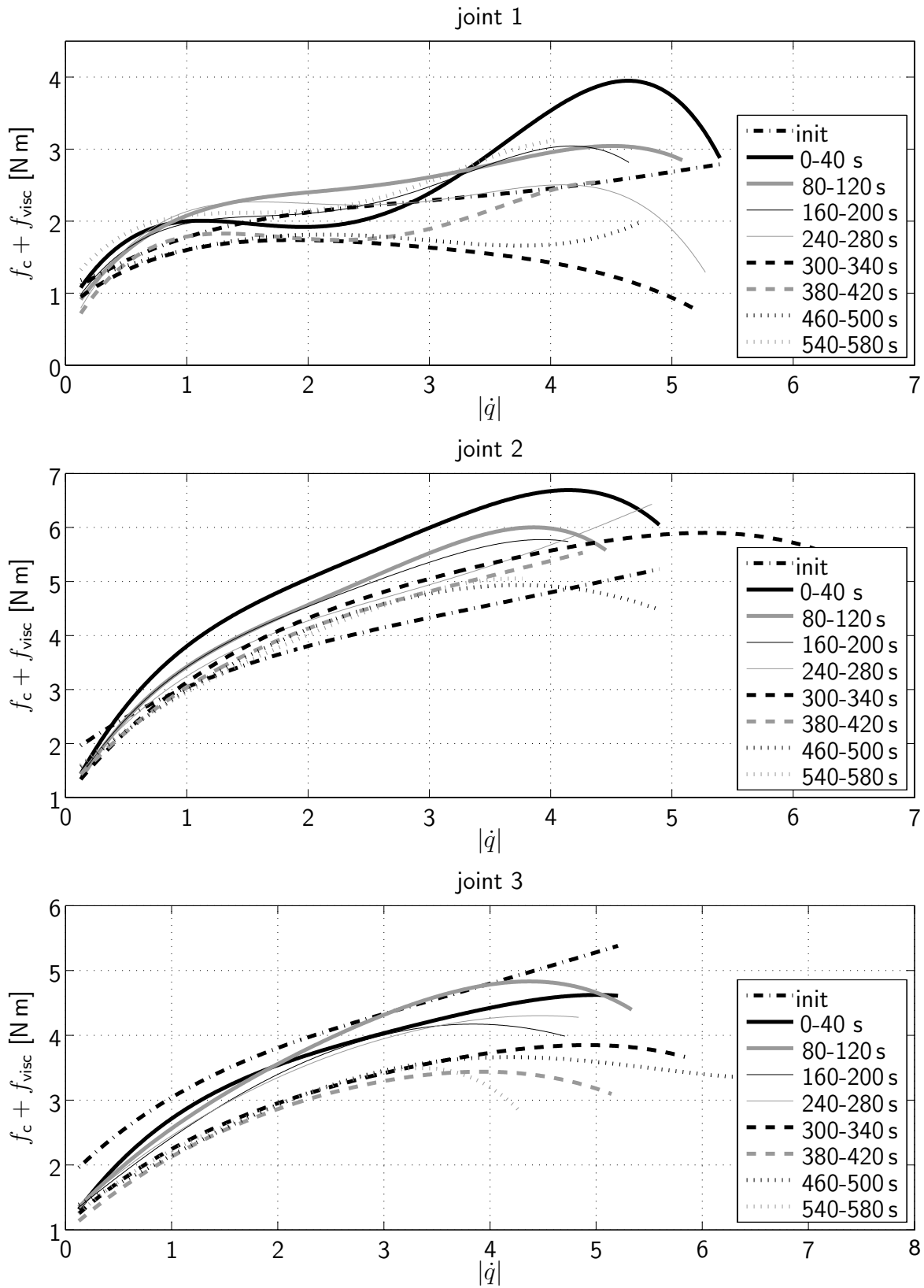


Figure 4.26: Estimation of the ViSHARD3 Stribeck curve during motions induced by a human operator

Stribeck curves obtained for joint 1 are all comparatively similar showing no significant change with operation time. The shape of the curve differs significantly from the results of the previous experiment; the friction curve has a negative slope for low velocities; the friction torque is much higher. This observation indicates again the limited reliability of the joint 1 friction identification.

As the interaction force of this enforced device motion is largely dominated by inertial forces the sensor measurements do not allow an evaluation of the friction compensation performance. Moreover, the added dynamics due to the linear guide PD control and unavoidable compliancy of the coupling introduces noise to the force measurement. For these reasons the compensation accuracy has been studied by means of position tracking experiments. Prior to the position control the device has been controlled in the impedance mode and moved by the operator for one minute in order to identify the current friction behavior. The position tracking experiment started with the application of computed torque control with acceleration feedforward but without friction compensation. Then, the static friction compensation derived from identification experiments described in section 4.4.1 has been added. Finally, the parameters of the friction compensator are switched to the previously identified values. The commanded trajectory is a sinusoidal motion of joint 2 with an amplitude of 0.6π at a frequency of 2.2 rad/s. The remaining joints are controlled to keep a steady position. In figure 4.28 the resultant performance of the friction compensation is shown by means of the commanded motor torque due to the feedback control law. In other words, τ_{PD} is the motor torque without the component provided by the acceleration feedforward and the friction compensation. Due to the high noise content of τ_{PD} also the filtered signal using a first order low-pass filter with 50 rad/s cut-off frequency is shown. The results reveal a drastic lowering of the feedback control action due to the inclusion of model based friction compensation. The differences between the static and adapted friction compensation is only marginal: At high velocities the adapted compensation gives an improvement around 10% whereas at low velocities the compensation gives inferior results. Needless to say, that this difference depends on the operating conditions.

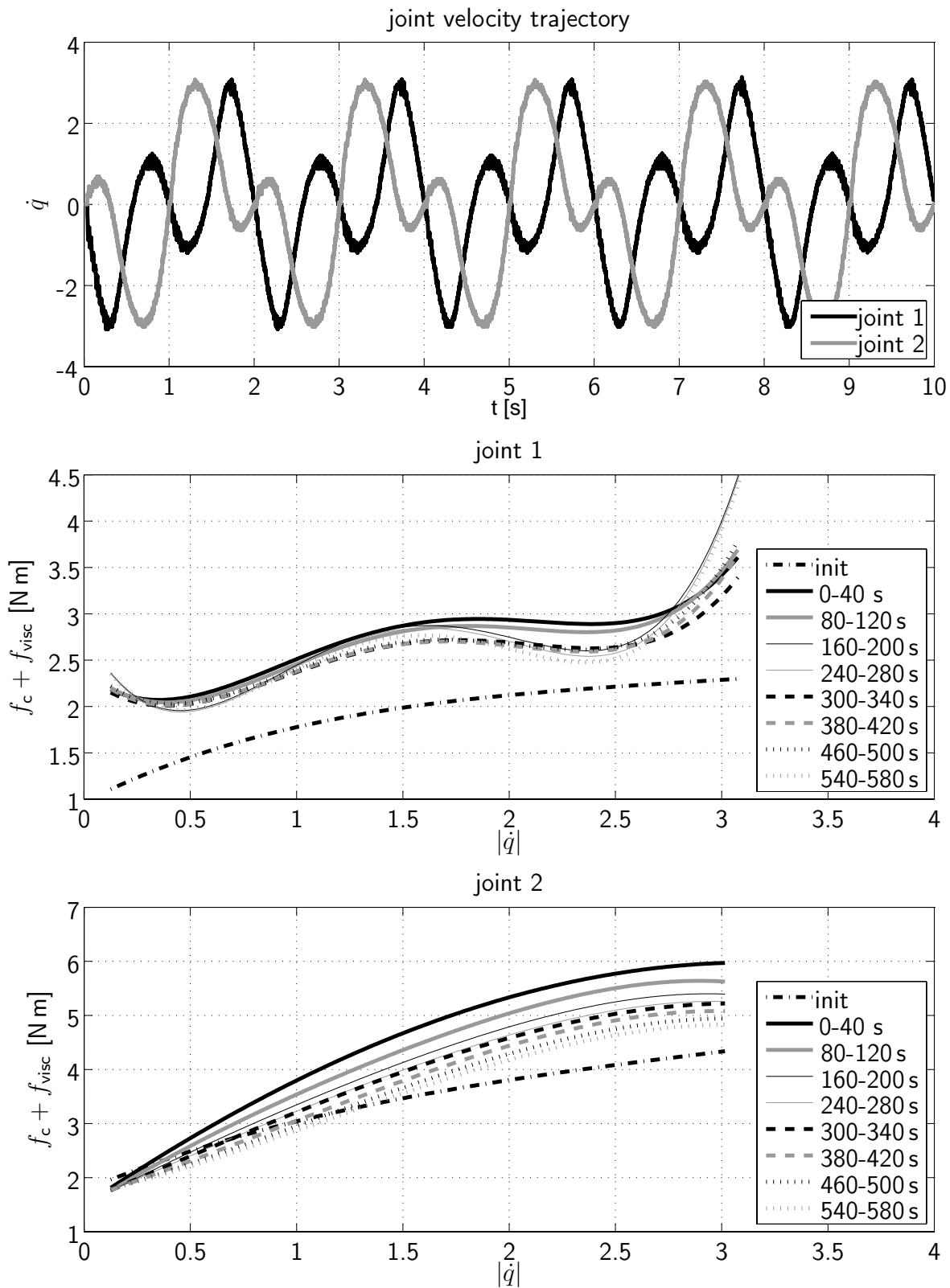


Figure 4.27: Estimation of the VISHARD3 Stribeck curve during motions induced by a linear guide

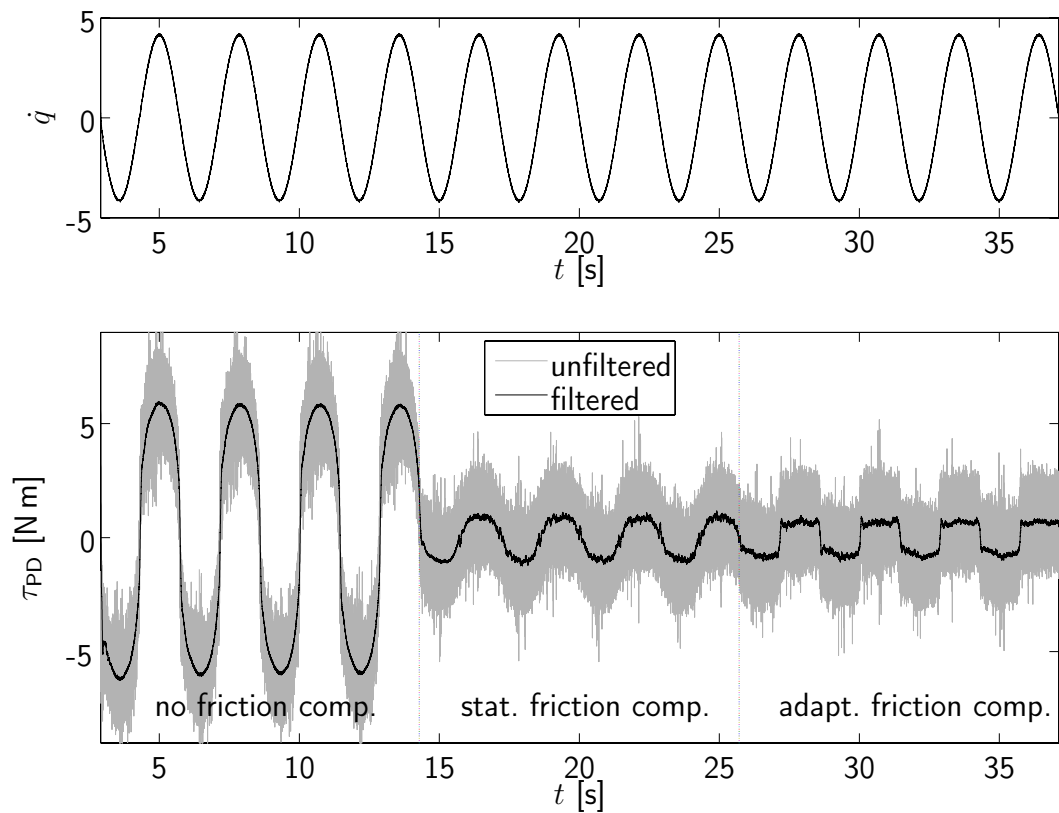


Figure 4.28: Reduction of the feedback control action due to friction compensation (joint 2 of the VISHARD3 device)

4.5 Summary

Based on hardware experiments and a review on general friction phenomena, modeling, and compensation approaches a control scheme for the attenuation of the ViSHARD3 haptic device joint friction has been developed. Viewing general friction compensation concepts it can be summarized that model-based friction compensation can mitigate friction induced disturbance forces in high gear. Further improvement can be achieved by the use of joint torque feedback. The application of dither is less rewarding because it produced significant acoustic noise interfering strongly the immersivity of the system. The disturbance observer concept has been shown to result in a control scheme very similar to admittance control. Haptic displays operated in the admittance mode typically do not require friction compensation techniques because the high gain of the inner motion control loop provides an effectual disturbance rejection capability. On account of these facts the ViSHARD3 impedance control scheme relies on force feedback control along with a model-based friction compensator.

As far as model-based friction compensation of haptic devices is concerned an inclusion of pre-sliding hysteresis into the friction model does not seem to be beneficial due to the moderate requirements on positioning accuracy. Because the harmonic drive gears used in the joint components of the ViSHARD devices show an insignificant Stribeck effect and low susceptibility to stick-slip motion also the modeling of dynamic friction effects is considered to be nonessential for haptic applications. Significant effects confirmed by hardware experiments are, however, the strong dependency of the harmonic drive friction behavior on the load torque and temperature. Furthermore, a considerable nonlinearity of the viscous friction could be observed. These behaviors are disregarded in most harmonic drive transmission models reported in the literature. Other unfavorable characteristics include large changes of the friction behavior with time, significant dependencies on manufacturing and assembly tolerances and position dependent friction torques.

On account of these observations the ViSHARD3 friction compensator applies a static model describing the nonlinear viscous and torque dependent friction with forth and second order polynomials, respectively. The variation of the Stribeck curve with the operating condition and time is taken into consideration by adapting the parameters of the friction compensator. As the change of the frictional behavior due to temperature shift is a process of moderate speed the friction model is not adapted iteratively at each sampling instant but re-tuned after a specified number of samples. The results of hardware experiments indicate a convenient performance of the proposed adaptation scheme in case of joint 2 and 3. The results for joint 1 are less satisfactory revealing a low reliability of the friction identification. A systematic evaluation of the adaptive friction compensation requires either the direct measurement of the true friction (e. g. by joint torque measurement) or in-depth psychophysical studies analyzing the benefit regarding the fidelity of the haptic sensations perceived by the operator.

Stiction effects have been excluded from the model because model-based stiction compensation is likely to introduce chattering. Instead, a variable structure force control scheme is applied to compensate for static friction. Switching between PID and PD control this compensator aims at offering a good disturbance rejection for the joints at rest while maintaining a good dynamic behavior of the joints in motion. Hardware experiments indicate a good performance of the proposed algorithm. Another effect not included into the model-based compensation scheme is position dependent friction. One can observe

that torque ripple can provide a noticeable disturbance to the haptic sensation due to its high frequency at high joint velocities. A model-based compensation of position dependent friction is, however, fraught with difficulties: The experimental results reported by Gandhi *et al.* [GGD02] indicate that the position dependent friction waveform is highly complex. Although the authors have spent a considerable effort on the identification and modeling of this effect no significant improvement of the tracking performance could be achieved with a model-based compensator. In fact, the torque ripple characteristics of harmonic drive gears is only little studied in the literature; its in-depth understanding can essentially be considered as an open research question. This applies in particular for the analysis of backdriving motions where the actuation torque is exerted to the gear output.

5 Performance Evaluation

The report of newly developed kinesthetic haptic hardware typically goes along with the presentation of a number of technical specifications characterizing its performance. Such performance measures are required for the assessment of the qualification of an haptic interface for a certain task as well as for the comparison of devices. Moreover, they can support the design process by providing a quantitative evaluation of different solutions regarding the hardware design (see chapter 2) and the control algorithm (see chapter 3). A systematic comparison of haptic interfaces requires the definition of a set of standardized performance indices and measurement procedures compatible to different hardware concepts and control schemes. In practice, however, one can observe, that a comparison of haptic interfaces is difficult because the performance indices provided in the literature and manufacturer data sheets vary largely in detail. Whereas the specification of the workspace and force capacity is common, important information on for example the velocity and acceleration capability as well as the backdrivability and frequency response characteristics is in particular for commercially available devices rarely provided. Furthermore, the given indices are in large part autonomously chosen and can differ from those presented for other devices or can be obtained under different measurement conditions. Often the interpretation of these performance indices is left to the reader as the methodology used to derive them is not described properly.

As an example for an unprecise performance specification the data sheets of the widely used PHANToM devices with 6 DOF obtainable from the manufacturer's webpage¹ can be viewed: The very good results for the rotational workspace reveal that it contains interior singularities. This important fact is, however, not indicated in the data sheets making this specification quite misleading. Moreover, no information is given on the coordinate system respective it is defined. As a result, the meaning of the rotational workspace specification is unclear; possibly it describes the admissible range of the corresponding joints. Other performance indices of the PHANToM devices are presented for the "nominal position" only; worst case results for the entire workspace are not specified. Viewing the performance measure for the device stiffness no information is given whether the mechanical, maximum control, or closed loop stiffness is described.

A more detailed evaluation of the PHANToM Premium 1.5 device has been presented by Çavuşoğlu *et al.* [ÇFT02] adding an analysis of the device manipulability and frequency response characteristics. Frequency response measurements of haptic devices along with other performance indices are also reported in [BH97], [CWH05], [VLFR], and [FB03]. These studies have been accomplished under isotonic conditions meaning that the end-effector is unloaded (zero interaction force). Despite such experiments give information on the mechanical device bandwidth they are not qualified for the assessment of the backdrivability (where the device motion is at least partially generated by external forces instead solely by motor torques) or the closed-loop frequency response characteristics of devices employing force feedback control (at zero interaction force the force controller is not active).

¹<http://www.sensable.com>

More meaningful for the evaluation of haptic devices seems to be the analysis of the force frequency response to force commands or end-effector motions providing insight to the device closed loop force bandwidth or impedance, respectively. Force bandwidth measurement results for an open loop controlled device are presented by Hayward *et al.* [HGG⁺98]. Ellis *et al.* [EIL96] give experimental results for an interface employing impedance control with force feedback. No information is, however, given on the influence of the control design on the results. Direct measurement of an haptic device impedance frequency response has, to the best knowledge of the author, not yet been reported in the literature. Performance measures striving for a comparison of large and powerful with small passive designs have for example been proposed by Van der Linde *et al.* [VLFR] and Colgate and Brown [CB94]. Instead of evaluating one single performance requirement the ratio of concurrent performance goals is formed (e.g. the maximum divided by the minimum closed loop impedance, the workspace divided by the third power of the position resolution, the force capability divided by the force precision).

In order to make a systematic comparison of kinesthetic haptic devices possible Hayward and Astley [Hay96] proposed a set of physical performance measurements aiming at moving towards standardization in haptic hardware evaluation (a more illustrative description of many of these measures is presented in [Mor96]). Their suggestions do, however, leave many open questions: The practicability of these indices is not confirmed by hardware experiments (many of the proposed performance indices involve substantial hardware equipment). Second, the discussion almost exclusively focuses on haptic devices controlled in the impedance mode. Finally, the evaluation of the closed-loop performance is just little addressed. A less complete but comparatively practical set of performance indices and measurement procedures assessed by hardware experiments has been described by Ellis *et al.* [EIL96]. However, as some of the identification procedures involve the interaction of a human operator the proposed performance evaluation lacks reproducibility and systematics. An entirely different approach is followed by task specific evaluations of haptic systems based on performance measures such as task completion time, accuracy, or success rate, see for example [KD02], [RC99], and [Kro04a]. Such an evaluation relies on the results of experiments where the human operator is asked to perform the task of interest. Because the results are dependent on factors like the operator's skill and period of training this method, also called "statistical survey" by Guerraz *et al.* [GLR03], requires a large number of experiments for a meaningful evaluation.

The innovation of this chapter is the presentation of hardware experiments for the comparative performance evaluation of haptic control schemes applied to the VISHARD interfaces introduced in section 2.5. This includes measurement of the force control frequency response and backdrivability accomplished for various admittance and impedance control implementations described in section 3.2.1 and 3.2.2. Furthermore, some open research questions concerning the performance evaluation of haptic interfaces are highlighted.

The chapter is organized as follows: Section 5.1 describes a set of performance measures for haptic interfaces. General guidelines for the determination of these indices are given in section 5.2. Section 5.3 presents performance results of the VISHARD devices regarding output capability (section 5.3.1), backdrivability (section 5.3.2), and force control frequency response (section 5.3.3).

5.1 Performance Measures

The haptic device properties characterizing its performance can be classified in specifications being purely determined by the hardware selection, in the following referred to as *mechanical hardware features*, and properties deeply affected by the action of the controller, the *closed loop performances*. Table 5.1 summarizes the performance measures detailed in the following sections.

Table 5.1: Performance measures for haptic interfaces

	performance criterion	performance specification ¹
hardware features	dextrous workspace, free of singularities	number and nature of DOF translational workspace: simple geometric shapes orientation workspace: e. g. range of Euler angles
	output capability	maximum peak and continuous force maximum velocity maximum acceleration maximum payload
	sensorial capability	measured quantities resolution at the human body interface
closed loop performances	force precision	maximum steady state force error at zero motion
	dynamic force precision	force control frequency response: - bandwidth - distortion (RMS)
	backdrivability	minimum apparent inertia at the tip maximum force error due to friction maximum force error due to gyroscopic effects condition number of closed loop mass matrix maximum angle between tip acceleration and resultant inertial interaction force impedance frequency response: - integral norm - distortion (RMS)
	stiffness	apparent stiffness at the human body interface

¹ worst case value in the entire specified workspace

5.1.1 Hardware Features

Workspace

The variety of applications a haptic interface can be applied for is deeply affected by the number and nature of the DOF along with their admissible operating range. In case of devices providing no rotational degrees of freedom the end-effector workspace can be expressed as (preferably simple) geometrical shapes as for example rectangular boxes, spheres, ellipsoids. A meaningful specification of the workspace should not consider the entire *reachable workspace*, that is the set of all points in the operational space the end-effector can reach using all admissible joint configurations, but only areas in that the other

evaluation criteria, in particular the output capability, have admissible performance. This excludes for example regions in the neighborhood of singular configurations. One has to consider, that the specification of the workspace strongly affects the other performance indices expressed in terms of worst case values in the entire operating volume.

In case of devices offering translational and rotational DOF it is important to express the position and orientation workspace independently from each other, meaning that for each position included in the translational workspace all orientations of the angular workspace have to be reachable and vice versa (also referred to as *dextrous workspace*). The translational and rotational workspace should be defined respective a suitable task space coordinate system. For most tool-based haptic interfaces this is a stationary world coordinate system not moving with the device configuration. The definition of a suitable representation of orientations depends strongly on the kinematical device design. Usually it is convenient to specify the orientation workspace in terms of the admissible ranges of the Euler angles of a practical Euler convention.

Output Capability

Like the workspace size also the output capability in terms of maximum force, velocity, and acceleration defines physical limits on interactions that can be performed with the device. High force and acceleration capability is particularly important at the exploration of rigid objects to avoid intrusion into immovable walls due to force saturation and to convincingly render hard stops requiring rapid changes of the velocity. A high velocity capability is needed for unconstrained motions involving high end-effector speeds.

The device maximum output capability should be specified for the location at that the human contacts the haptic device (device body interface). In case of devices providing both, translational and rotational DOF, the analysis of the maximum translational output should consider only input vectors producing no rotational output. Conversely, the maximum rotational output should be specified with the constraint that no translational output is generated. Due to the device nonlinearities the maximum output capability typically varies strongly with the end-effector location and the direction of manipulation. A meaningful measure for the output performance with one single parameter is therefore the specification of the worst case value in the entire workspace. A method for calculating at a given end-effector location the worst case output capability by means of considering the most adverse direction of interaction is presented in appendix C.

A related performance index is the payload capability. The payload capability equals the maximum continuous force capability in the direction of the acceleration due to gravity.

Sensorial Capability

The sensorial capability describes what physical quantities are measured along with the resolution in terms of the smallest measurable change in the corresponding quantity at the device body interface. In case the sensor is not directly placed at the end-effector the resultant resolution can vary with the device configuration and the measurement direction. Again, a meaningful specification considers the worst case in the entire operating volume.

5.1.2 Closed Loop Performances

Force Precision

Force precision denotes the steady state force control error at a constant force command with the device at rest. The main sources for such force errors are frictional losses and, typically less intense, imperfections of the open loop control of the motor torque (e. g. due to torque ripple, cogging, or imprecise knowledge of the torque constant). The force precision is therefore highly dependent on the capability of the control scheme to attenuate static friction effects. If no friction compensation and force or acceleration feedback is applied, the force precision will usually be around the apparent break-away force at the device tip.

Force feedback can significantly improve the force precision, see equation (3.3). The inclusion of integral action in the force control law at zero joint motion as proposed in section 4.4.3 almost completely eliminates the force error (see the experimental results given in figure 4.24). Then, the force error virtually corresponds to the resolution and accuracy of the force sensor. The same statement holds for admittance control implementations with inner velocity or position control loop due to the integral action involved in the transformation of the force error to the commanded velocity or position.

Clearly, a meaningful specification of the force precision should consider the worst case figure in the entire workspace. The smallest force error humans are capable to perceive has been found to be roughly linearly dependent on the level of the commanded force [Jon89], [TPD92]. In the literature, the perceptual discrimination threshold (also called *just noticeable difference*; shorthand: *JND*) for forces is therefore mostly expressed as percentage with respect to the desired value ranging from 5 % to 15 % [BS02]. Accordingly, a low force resolution is particularly critical for the render of small interaction forces.

Dynamic Force Precision

The dynamic force precision describes the performance of the force controller to track dynamically changing force commands while the device tip is hold stationary (clamped end-effector). In practice, the fixture of the end-effector cannot be made infinitively stiff. The effect of the contact stiffness on the open loop force control bandwidth has been analyzed by Townsend [Tow88]. It is suggested to select the contact stiffness to a value where further increase does not significantly improve the force control bandwidth. As the tracking capability is highly dependent on the frequency of the force command it is hard to describe this performance criterion conveniently with one single parameter. A feasible approach is the measurement of the device frequency response to sinusoidal force commands (details on a possible realization of such experiments are given in section 5.3.3). An evaluation of the results with one parameter can for example be expressed in terms of the force bandwidth, the frequency where the amplitude of the force response drops to -3 dB. A high force bandwidth is needed to provide a crisp haptic sensation at the render of hard stops (e. g. collisions with virtual walls). Clearly, the specification of the force bandwidth alone does not provide information on the existence of resonance magnification or the progression of the signal phase.

The measurement results obtained with the frequency response experiments can also be used to quantify the distortion of the rendered force signal caused for example by sensor noise. A common evaluation of the signal distortion is obtained by computing for each

frequency the percent² RMS value of the deviation between the measured signal and its (in a least squares sense) best sinusoidal fit, see section 5.3.3 for details.

The estimation of the frequency response along with the analysis of the signal distortion provides rich insight to the dynamic force tracking capability. One has, however, to consider, that haptic devices are nonlinear systems where these measurement results do not only vary with the end-effector location and direction of the force command but also with the amplitude of the excitation (e. g. due to the nonlinear stiffness of gears or tendons). This can necessitate the specification of the force bandwidth and signal fidelity for different force levels. Again, the worst case figure in the entire workspace should be considered.

Backdrivability

Another property describing the dynamic accuracy of the haptic feedback is the backdrivability, that is the minimum closed loop impedance the device can render without producing instability. Whereas a good dynamic force precision is needed for a realistic display of dynamic interactions with rigid objects, backdrivability is required for the accurate emulation of impedances falling below the natural impedance of the haptic interface (e. g. free space simulations).

In case of typical impedance control implementations applying a force control law without integral action (e. g. PD control) the minimum impedance essentially corresponds to the device natural dynamics reduced by model-based feedback terms and a factor proportional to the force gain, see equation (3.3). A highly descriptive way to quantify the impedance is to subdivide it with respect to the originating physical effects and then to define a meaningful measure for each contribution. This includes for example the maximum inertia and uncompensated friction force (in the range of admissible end-effector velocities) displayed at the tip while the interface is controlled to render zero force. Another possible measure is the specification of the worst case force error due to gyroscopic effects (again, for the entire range of admissible end-effector velocities). As described in section 3.5.1 hardware experiments with the VISHARD3 device indicated a limited practical use of the model-based compensation of gyroscopic forces because it turned out to provide a very strange haptic sensation difficult to anticipate for the operator. Therefore, the specification of the force error due to gyroscopic effects seems to have limited value.

In addition to the magnitude of the impedance also its directional characteristics in terms of isotropy and cross couplings should be considered because disturbance forces in directions diverging strongly from the direction of the end-effector acceleration provide an unnatural and unexpected force sensation. The isotropy of inertial disturbances can be evaluated by means of the condition number of the closed loop mass matrix and the cross couplings in terms of the maximum angle between the direction of the end-effector acceleration and the resultant interaction force.

The proposed grouping in inertial, frictional, and gyroscopic disturbances gives a meaningful and plain description of the backdrivability for interactions at moderate bandwidth. At higher excitation frequencies the closed loop impedance characteristics can change significantly: For example the exceedance of the force control bandwidth removes the active increase of the backdrivability; structural device elasticities act as mechanical high-pass filters increasing the backdrivability at high excitation frequencies. Typically, however,

²percentage of the RMS value of the sinusoidal fit

the force control as well as the mechanical bandwidth is higher than the frequencies of the operator's motion input which, in practice, rarely exceeds 10 Hz [Bro90].

Another approach for the evaluation of the backdrivability is the specification of the device impedance response by means of the force frequency response to a sinusoidal end-effector velocity while the device is controlled to render minimum impedance. The motion is enforced by a velocity source firmly connected to the tip. Obviously, the resultant amplitude response provides insight into the dependency of the backdrivability on the excitation frequency. On the negative side, the result is harder to interpret as no explicit assignment to the originating physical effect is given. Moreover, nonlinear effects as for instance uncompensated friction forces (usually these are far from linear damping) are not described properly. A meaningful evaluation of the impedance response by one single parameter can be expressed by some integral norm in the frequency domain as suggested by the telepresence community to quantify transparency, see for instance [WLW⁺05], [Hir05]. Again, the measurement results can be used to quantify in terms of percent RMS values distortions of the rendered impedance due to sensor noise as well as nonlinearities of the actuators and force transmission (e. g. force ripple, high frequency vibrations). Please note, that the human perception of distortion is comparatively good.

In admittance control implementations the qualitative description of the backdrivability is comparatively simple: At motion input with moderate bandwidth the high gain of the inner control loop closed on motion effectively compensates for disturbance forces due to the natural device dynamics. Accordingly, the closed loop dynamics corresponds relative accurately to the commanded impedance (assuming negligible deviation between the measured and real interaction force, meaning that no parts of the device structure with significant impedance Z_{EE} , see figure 3.5, are located between the sensor and the operator). In fact, the display of impedances with zero friction and gyroscopic effects as well as with uniform inertia without cross coupling effects can be realized. The requirements on the tracking performance of the inner motion control loop are comparatively low due to the limitations of the human's sensing capability of position, motion, and mass: the investigations of Jones and Hunter indicate a JND for the perception of position and motion with the arm in the range of $8 \pm 2\%$ and $8 \pm 4\%$, respectively [JH92]; Beauregard and Srinivasan identified a JND of $21 \pm 5\%$ for the perception of mass with the fingers [BS95]. As a result of this discussion a convenient measure for the backdrivability of haptic interfaces operated in the admittance display mode seems to be the specification of the minimum inertia that can be commanded without producing instability. As shown by Nitzsche [Nit06] the stability bound for the lowering of the target inertia depends on the virtual damping. It is therefore suggested to consider the worst case, that is the render of a pure inertia with zero damping and stiffness. Additional impedance response experiments can be accomplished to determine the bandwidth of the active shaping of the closed loop impedance along with the RMS value of the signal distortion.

Stiffness

The device capability for the realistic render of rigid objects is in addition to the force bandwidth determined by the maximum closed loop stiffness. At the majority of haptic interfaces the end-effector position is not directly measured but derived from encoders placed at the motors. For a meaningful measure of the maximum stiffness not the control stiffness seen from these encoders should be considered but the actual endpoint stiffness

including all sources of mechanical device elasticity. In case of control algorithms not compensating for the mechanical elasticity the resultant endpoint stiffness is given by the serial connection of the control and mechanical stiffness. The stiffness threshold beyond no difference to infinite stiffness can be perceived has been found to be within the range of 15 300 to 41 500 N/m [TSEC94].

5.1.3 Comments

Many of the proposed measurement procedures (force and impedance frequency response) are accomplished under isometric conditions: the haptic interface is firmly connected to a very rigid reference device (Hayward and Astley [Hay96] suggest a milling machine) generating dedicated end-effector motions. It is, however, well known that the stability of force feedback control is highly dependent on the compliance of the environment the robot is interacting with (see e.g. [Whi85], [AH87], [Epp88], [EDS90]). Because the required stiffness exceeds by far the stiffness of a human arm it is most likely that the control gains have to be reduced significantly to maintain stability. Needless to say, that the reduction of the control gain is associated with a decrease of the closed loop performance. The potential incompatibility of isometric measurement procedures to force feedback controlled haptic interfaces reveals that performance indices based on such experimental result do not allow an objective comparison of devices with different construction and arbitrary control schemes.

Aiming at more realistic testing conditions Ellis *et al.* [EIL96] proposed to measure the device force bandwidth while the end-effector is grasped by a human operator. Whereas this approach is close to the way the interface is meant to be used it lacks reproducibility and systematics. Another method proposed by Hayward and Astley [Hay96] is the coupling of the end-effector to a material with well defined physical properties approximating the features of a human grasp (e.g. some shock absorbing polymer or silicon gel). This method strives for realistic testing conditions producing consistent results. A suggestion for a suitable material along with experimental validation has, however, to the best knowledge of the author not yet been given in the literature. Ellis *et al.* experimented with a Sorbothane-faced stiff jig but this solution was deemed to be unrealistic and has been found to produce poor results in terms of adding resonances [EIL96]. The definition of a realistic and well-defined testing condition is still an open but very important research question. The solution to this problem seems to be a pre-requisite for a standardized performance evaluation.

Another open problem is the evaluation of redundant haptic devices. For these devices most performance measures are not only dependent on the end-effector working point and the direction of manipulation but also on the manipulator configuration in the nullspace. A performance analysis as described above is therefore only possible when defining a single inverse kinematics function assigning an unique device posture to each end-effector configuration as described in section 3.4.2. In case of non-conservative inverse kinematics solution approaches as for instance pseudoinverse control (see section 3.4.1) the closed loop performance will be highly dependent on the capability of the null space motion to drive the interface to dextrous configurations.

5.2 Determination of Performance Indices

The proposed performance indices can either be determined by direct measurement or derived by the analysis of an appropriate device software model. Direct measurement as suggested by Hayward and Astley [Hay96] has the advantage to be more reliable in particular in case the investigated performance criterion is susceptible to modeling inaccuracies. This applies for example for frequency response investigations that are highly dependent on the stiffness of all involved mechanical parts (e. g. gears, bearings, tendons, links, ...). The accurate modeling of the (typically nonlinear) device stiffness characteristics is a very demanding task that is prone to error. In case the haptic interface applies active force feedback control virtually all closed loop performance measures are difficult to predict without hardware experiments. This is founded by the strong dependence of the results on the control gain. It is, however, hard to give a valid estimate on the stability bound of the control gain because the force control robustness is highly susceptibility to higher order structural dynamics and nonlinearities that are difficult to model [EDS90], [Elo93].

At the downside, the identification of worst case figures is hard to obtain with direct measurement. Due to the nonlinearity and anisotropy of most interfaces with multiple DOF the measurement results vary strongly with the device configuration and direction of interaction. A systematic analysis of the performance requires therefore an excessive number of experiments. Another problem is the incompatibility of isometric measurement procedures to force feedback controlled devices as discussed earlier.

On account of this discussion it seems to be reasonable and pragmatic to do hardware experiments whenever necessary but to make use of model-based performance estimation whenever possible. A purely model-based performance evaluation is rewarding for all measures described in section 5.1.1: The analysis of the velocity capability requires only a kinematic device model along with the velocity capability of the joint components. The derivation of the maximum output force depends on the kinematics, the torque capability of the actuators, gravitational load, and the frictional losses. Although a precise friction model is virtually impossible to obtain, see section 4, modeling errors are usually small compared to the torque capability of the actuators. The determination of the acceleration capability requires in addition a model of the device inertia that can be derived comparatively precisely from CAD along with multibody simulation tools. The results of a systematic analysis based on the computer model may then be validated by a few hardware experiments.

The calculation of the closed loop performance measures required knowledge of the admissible control gain. The most relevant gain is here the proportional force gain (impedance control) or the minimum target inertia (admittance control). A rather heuristic way to identify these gains are hardware experiments with the device coupled to a human operator. This approach provides maximum realistic testing conditions but lacks of systematics and reproducibility. In particular, robustness properties of the control cannot be verified. The identification of the control gain does then allow for a model-based estimation of the backdrivability in terms of the closed loop inertia (magnitude and directional characteristics) and the maximum force error due to gyroscopic effects. In case of impedance control the specification of the force error due to friction requires additional hardware experiments for the identification of the maximum magnitude of uncompensated joint friction. For a reliable identification of the device stiffness as well as the force control and impedance fre-

quency response along with the corresponding signal distortion figures direct measurement seems to be essential.

5.3 Performances of the ViSHARD Devices

In the following, performance measures of the ViSHARD devices are presented. Results for the closed loop stiffness are not given because adequate hardware equipment for the direct measurement of the device closed loop endpoint stiffness has not been available. The determination of the workspace has been accomplished along with the study of the output capability. Section 5.3.1 illustrates the trade-off between workspace size and output capability. The results are presented for a workspace considered as dextrous. Performance figures for larger operating areas are provided in [Fri02] and [Ern02]. Information of the ViSHARD force precision is not included. As integral action is used in the force control law at zero joint motion the force precision corresponds to the accuracy and resolution of the force sensor. Specifications of the ViSHARD sensorial capabilities are given in appendix A.1. For a summary of technical hardware features see also table 2.1.

5.3.1 Output Capability

This section presents an output capability analysis for the ViSHARD3 and ViSHARD6 devices. For the ViSHARD10 interface no results are provided because the output capability depends strongly on the device nullspace configuration. Following the suggestions given in section 5.2 the ViSHARD peak force, velocity, and acceleration capability has been estimated, rather than directly measured, applying the algorithm detailed in appendix C. This analyzing technique computes for a given end-effector configuration the maximum output (L_2 norm) in the most adverse direction of manipulation.

ViSHARD3

The output analysis for the ViSHARD3 interface has been applied to a grid of end-effector positions in a rectangular workspace of $0.6 \times 0.25 \times 0.4$ m. Hardware limitations on the input capability of the joints are given by the limit for repeated peak torque and maximum speed of the harmonic drive gears with 54 N m and 7.64 rad/s.

The results for the force capability are shown in figure 5.1. As the force capability is best for end-effector heights at ± 0.20 m and worst for $z = 0$ m the results for these locations are shown in the left figure. They differ only at tip positions in the neighborhood of the device base where the distance to joint axis 2 is larger than the distance to axis 1. The right figure illustrates the contour plot of the worst case result. In the entire workspace the peak force capability is never less than 86.19 N. The calculation of the continuous force capability is straightforward when considering that the maximum continuous input torque due to hardware limitations of the motors is given with 20 N m. It is therefore obtained by the multiplication of the peak force results with the factor $20/54$ giving a worst case result of 31.92 N.

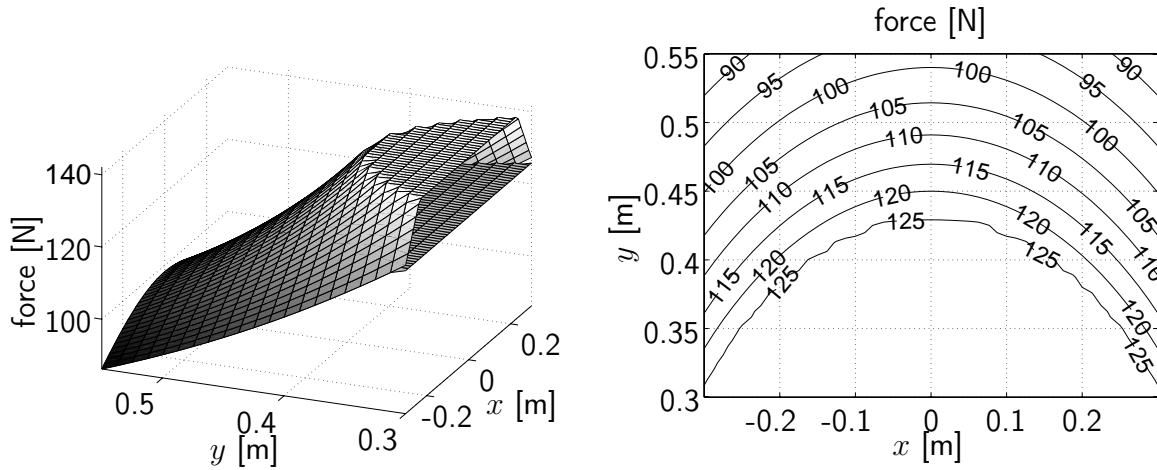


Figure 5.1: Peak force capability of VISHARD3; left: result for end-effector height $z = 0$ m (worst case) and $z = \pm 0.20$ m (best case); right: contour plot for worst case result

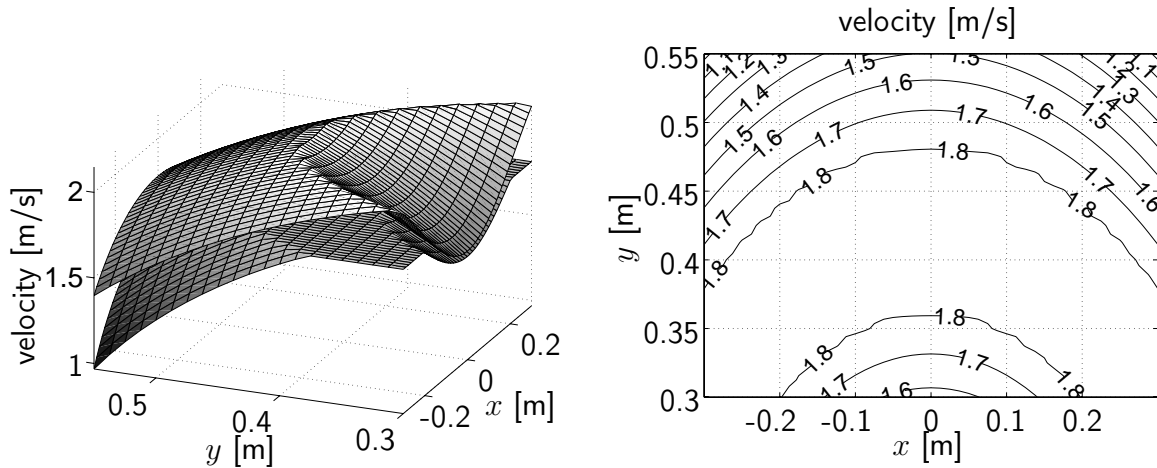


Figure 5.2: Velocity capability of VISHARD3; left: result for end-effector height $z = \pm 0.20$ m (worst case) and $z = 0$ m (best case); right: contour plot for worst case result

The velocity and acceleration capability is shown in figure 5.2 and 5.3. Here, the best results are obtained for the end-effector at the height of ± 0.20 m whereas the worst case is given with $z = 0$ m. The results reveal a significant performance decrease in the neighborhood of the device base and the workspace edges. The worst case results are 0.97 m/s and 14.69 m/s². The contour plot of figure 5.2 indicates a large increase of the velocity capability when reducing the workspace depth.

ViSHaRD6

As ViSHARD6 provides 6 DOF a separate output analysis for the translational and rotational DOF has been accomplished. This is achieved by the introduction of the constraint that either the rotational or translational output vector \mathbf{q}_{rot} and $\mathbf{q}_{\text{trans}}$ is zero as indicated in equation (C.8). This technique has been applied to a grid of end-effector orientations and positions in order to determine at each of these points the worst case output capability

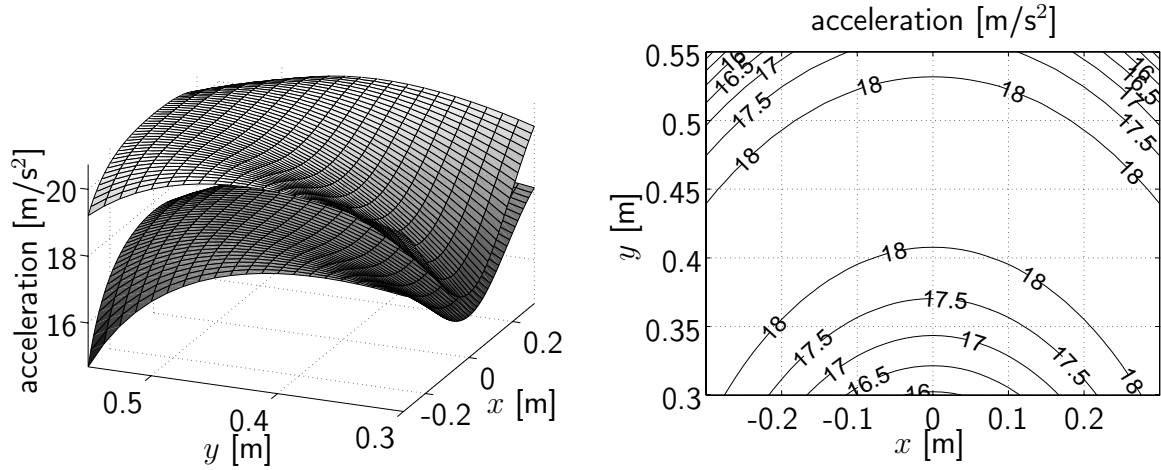


Figure 5.3: Acceleration capability of VISHARD3: ; left: result for end-effector height $z = \pm 0.20$ m (worst case) and $z = 0$ m (best case); right: contour plot for worst case result

by means of the performance in the most adverse direction of manipulation. The points with the orientation and height producing the lowest output capability are displayed in figure 5.4 to 5.8. These results are referred to the rectangular workspace of $86 \times 31 \times 31$ cm and an angle of pitch and roll of 360° .

The force capability of the haptic display is due to figure 5.4 in the entire workspace never less than 33.5 N for continuous force and 178 N for peak force. The torque capability is naturally limited by the moment of the least powerful actuator that is $20/54$ N m for the continuous/peak moment of pitch and jaw and $3.3/4.8$ N m for the moment of roll which is beyond the measuring range of the force-torque sensor of ± 12 N m.

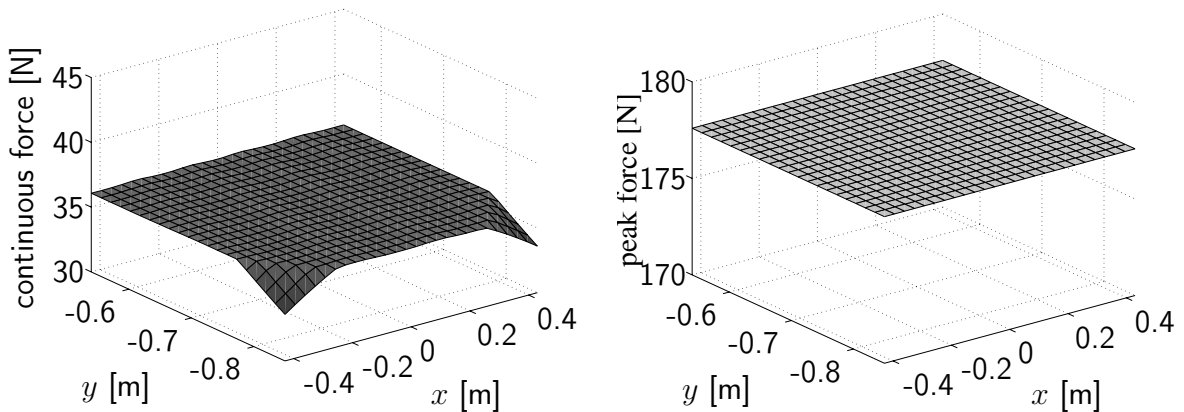


Figure 5.4: Continuous and peak force capability of VISHARD6 with $\alpha, \gamma \in [-180^\circ; 180^\circ]$ and $\beta \in [-45^\circ; 45^\circ]$

The performance of the device in terms of translational velocity is shown in figure 5.5. For an angular workspace with 90° of jaw the velocity is not less than 0.35 m/s which is rather low for simulating for instance free space. However, if the range of the jaw angle is reduced to 60° the dexterity of the device will be increased significantly permitting velocities of

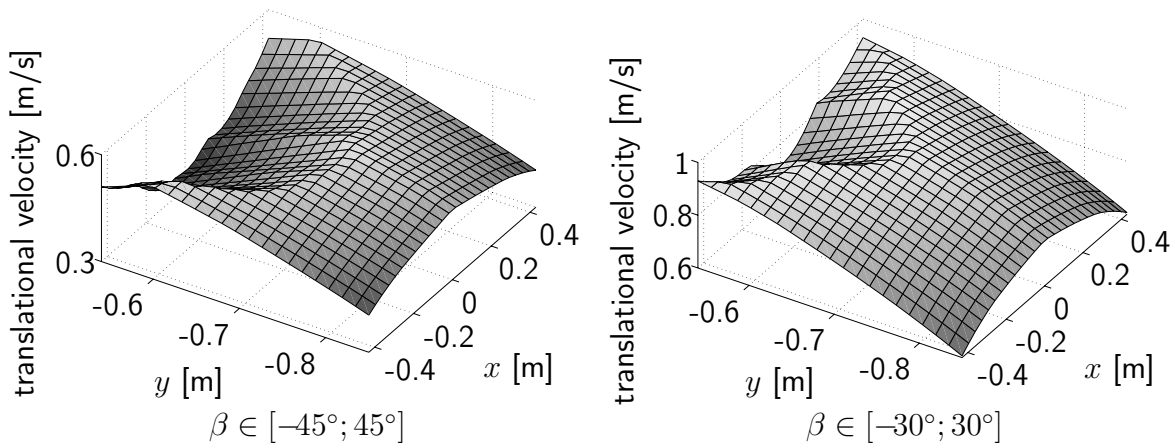


Figure 5.5: Translational velocity capability of ViSHARD6 with $\alpha, \gamma \in [-180^\circ; 180^\circ]$

more than 0.61 m/s. This also holds for the capability regarding angular velocity as the minimum is increased from 1.39 rad/s to 2.96 rad/s. As shown in figure 5.7 and 5.8 the translational and angular acceleration capability of the device is not less than 4.6 m/s^2 and 18.0 rad/s^2 for an angular workspace with 90° of jaw and 8.1 m/s^2 and 38.6 rad/s^2 for $\beta \in [-30^\circ; 30^\circ]$.

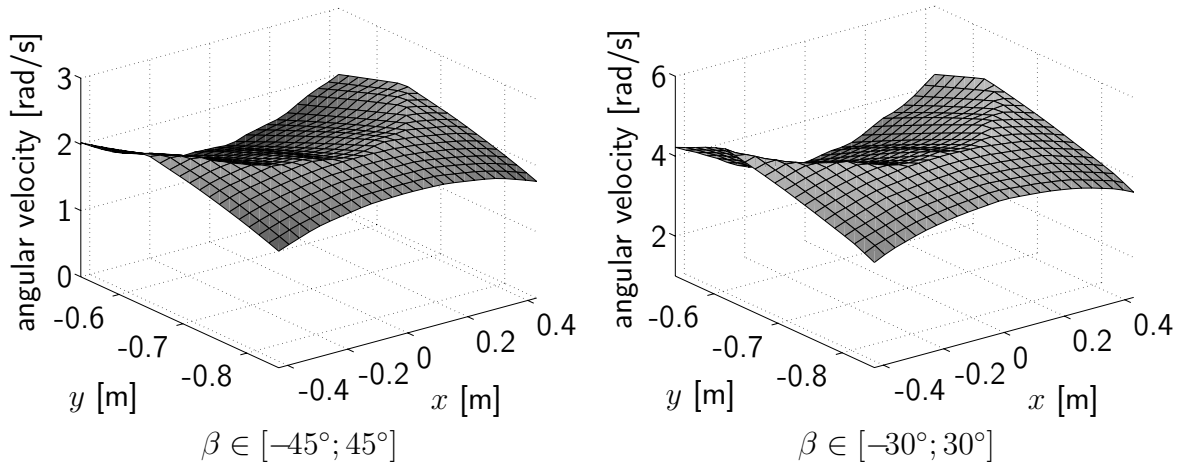


Figure 5.6: Angular velocity capability of ViSHARD6 with $\alpha, \gamma \in [-180^\circ; 180^\circ]$

5.3.2 Backdrivability

As proposed in section 5.2 the backdrivability of the ViSHARD devices is estimated using the dynamic device model along with the admissible control gains identified by hardware experiments. Due to the comparatively precise model-based friction compensation implemented in the ViSHARD control algorithms the closed loop backdrivability is expressed in terms of the minimum closed loop inertia. For a validation of the applicability of equation (3.3) and (3.6) to estimate the closed loop backdrivability, hardware experiments with the ViSHARD3 device involving direct measurement of the disturbance forces along a predefined motion trajectory have been accomplished.

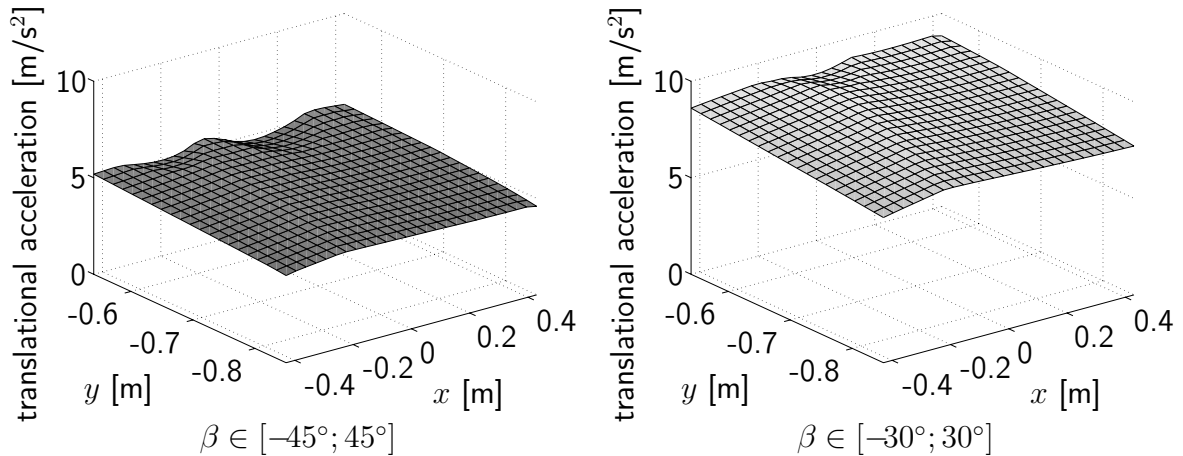


Figure 5.7: Translational acceleration capability of VISHARD6 with $\alpha, \gamma \in [-180^\circ; 180^\circ]$

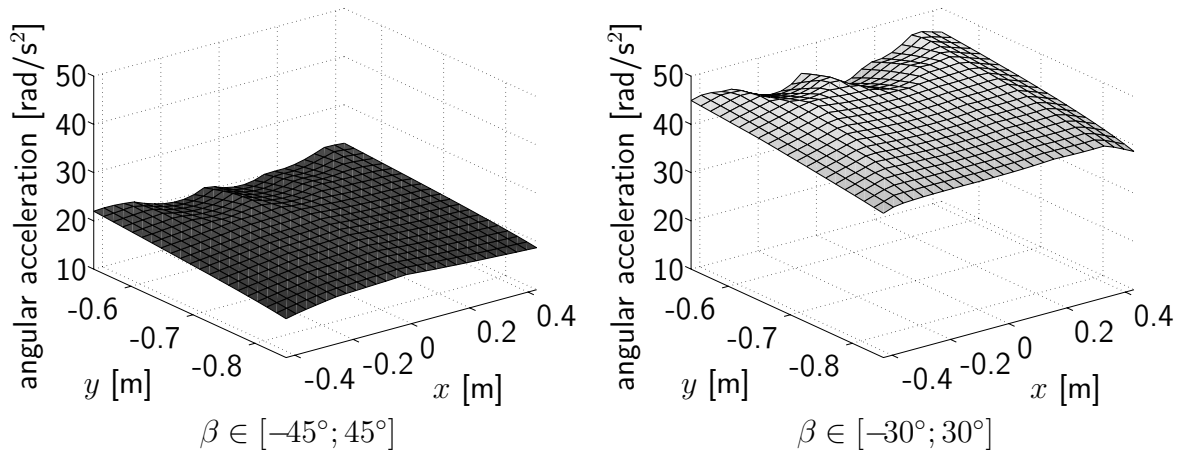


Figure 5.8: Angular acceleration capability of VISHARD6 with $\alpha, \gamma \in [-180^\circ; 180^\circ]$

Direct Measurement Results

These experiments are targeted at the direct measurement of the backdrivability by means of the interaction force at a dynamic interaction with the device. To provide repeatable experiments for the comparison of the closed loop results of different haptic control schemes it is either required to exert a dedicated force trajectory to the device and read the resulting motion or one has to force the device to perform a specified motion and read the interaction force. Because a pure force source is very hard to provide the latter option has been exercised.

In the experiments a position controlled linear guide has been used to move the end-effector of the VISHARD3 device, see figure 4.23. The difficulty with this approach is that a precise guidance of the tip motion necessitates a very stiff coupling to the guide. Because the required stiffness exceeds by far the stiffness of a human arm the control gains had to be reduced significantly for these experiments to maintain stability. Also experiments employing a more compliant coupling, which has been achieved by inserting shock absorbing polymers with different elasticities in the coupling mechanism, have been

tried. This, however, did not produce good results due to the additional significant flexible modes interfering the measurement results in high gear

The tested impedance control schemes are standard implementations of open loop impedance control and impedance control with force feedback, see figure 3.3. In both approaches a model-based friction and gravity feedforward but no dedicated shaping of the closed loop inertia has been applied. The virtual impedance \mathbf{Z}_d has been set to zero in order to render free space. The controller has been a PD control law with the diagonal gain matrices $\mathbf{K}_P = 1.5\mathbf{I}$ and $\mathbf{K}_D = 0.003\mathbf{I}$.

The tested admittance control schemes incorporate resolved acceleration, inverse Jacobian, and transposed Jacobian position control, see section 3.2.2. An experimental comparison of the position tracking performance of these algorithms is provided in appendix B. The controller gain matrices in equation 3.7 have been set to $\mathbf{K}_P = 500\mathbf{I}$ and $\mathbf{K}_D = 2\sqrt{500}\mathbf{I}$ aiming at a critically damped position control with 22.36 rad/s bandwidth. The virtual admittance has been chosen to render the dynamics of a 5 kg mass. Stability could only be maintained when using position control with acceleration feedforward. The approximate inertia and mass matrix of equation 3.11 and 3.13 has been set to $\widehat{\mathbf{M}}_q = \text{diag}(0.930, 0.416, 0.279) \text{ kg m}^2$ and $\widehat{\mathbf{M}}_x = \text{diag}(6.813, 9.350, 4.812) \text{ kg m}^2$ which are the mean values of the diagonal elements of \mathbf{M}_q and \mathbf{M}_x in the workspace of the haptic device. In all experiment the sampling rate was 2 kHz.

The end-effector has been forced to follow the trajectory illustrated in figure 5.9. The y and z position is held constant with $y = 0.364 \text{ m}$ and $z = 0.232 \text{ m}$. The trajectory shows segments with a comparatively high constant acceleration where a force error due to inertial effects is expected to dominate and phases with constant velocity revealing uncompensated friction and gyroscopic effects. Figure 5.9 shows also the actual motion obtained by measurement. Because the actual motion varies only little with the different haptic control schemes just the motion measured at the experiment with the admittance controller including resolved acceleration control is shown for the sake of clarity. Note, that a first order low-pass filter with 63 Hz cut-off frequency has been applied to the measured acceleration signal. This explains the phase lag of the measured acceleration trajectory.

The resultant interaction forces are given in figure 5.10. Again, a first order low-pass filter with 63 Hz cut-off frequency has been applied to the measured signals. The results indicate that in case of impedance control with force feedback (IMP1.5)³ the interaction force in x -direction due to acceleration varies significantly with the end-effector position; during the deceleration-acceleration phase it is around 12 N m but during the deceleration phase at the end just around 4 N m. Furthermore, the force trajectories in y and z -direction point to strong inertial couplings effects. The result of admittance control with resolved acceleration position control (RAC500) shows a comparatively good compensation of coupling effects and also of frictional and gyroscopic effects when viewing the periods with constant velocity. Transposed Jacobian control (TJC500) gives compared to resolved acceleration control inferior results; it tends to an underdamped response with reduced compensation of coupling effects. The result of inverse Jacobian control is omitted because no stable control could be achieved.

In figure 5.11 the force error of impedance control with force feedback and admittance control is compared. Whereas the force error \mathbf{f}_{err} of impedance control is equivalent to the

³the number indicates the proportional gain of the control law

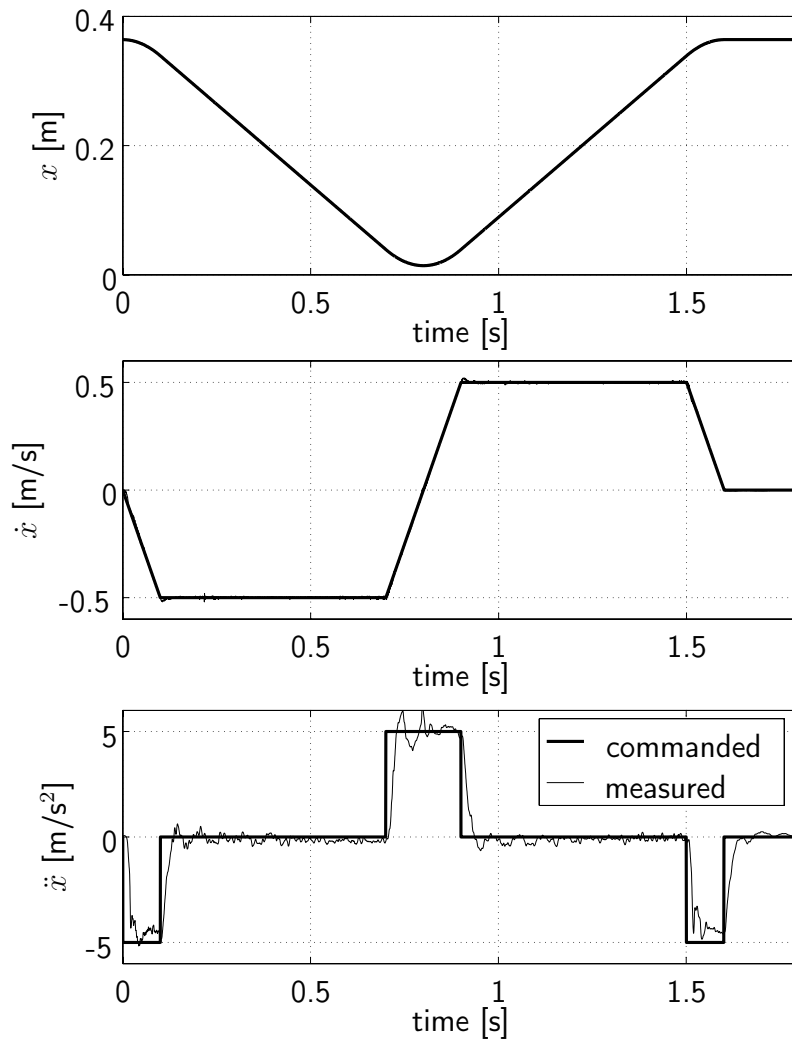


Figure 5.9: Commanded end-effector trajectory at backdrivability experiment

interaction force, the admittance force error is calculated with

$$\mathbf{f}_{\text{err}} = \mathbf{f}_m + 5\ddot{\mathbf{x}}_m, \quad (5.1)$$

where \mathbf{f}_m and $\ddot{\mathbf{x}}_m$ are the measured force and acceleration, respectively. Especially when the acceleration changes admittance control gives a large force error. This points to a reduced bandwidth when compared to impedance control. At most other times RAC500 has a smaller error than IMP1.5 indicating a comparatively accurate rendering of the dynamics specified by \mathbf{Z}_{d2}^{-1} . Again, RAC500 shows better results than TJC500.

Figure 5.12 aims at the validation of equation (3.3) predicting the closed loop impedance error of impedance controlled haptic interfaces. It compares the actual with the expected force error of open loop impedance control, which is according to equation (3.3) the force error of impedance control with force feedback multiplied with 2.5. The figure illustrates almost perfect conformance for f_x . The f_y -trajectory reveals the improved damping of the force feedback control due to the derivative action. The less accurate conformance for f_z can possibly be explained by stiction effects. The results shown in figure 5.10 and 5.12 indicate the appropriateness of equation (3.3) and (3.6) for the estimation of the closed loop backdrivability.

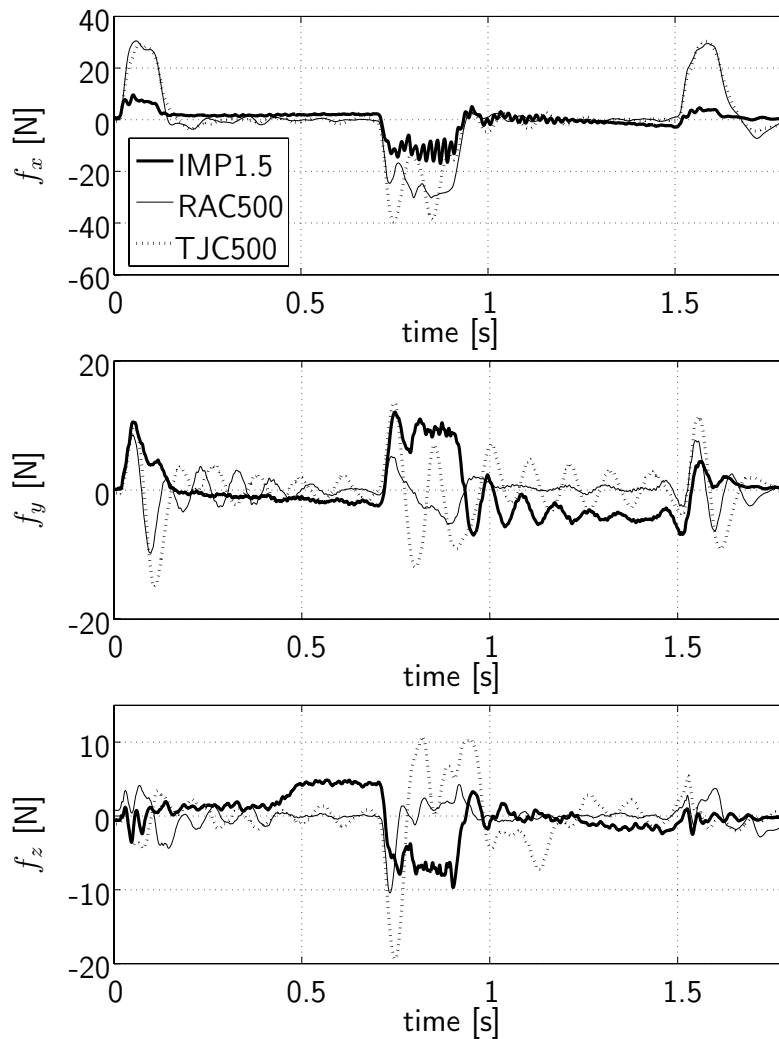


Figure 5.10: Interaction force at backdrivability experiment

Minimum Inertia

In case of admittance control the minimum closed loop inertia corresponds to the minimum pure inertia that can be commanded without producing instability at arbitrarily interactions performed by a human operator. In case of impedance control implementations, on the other hand, this performance criterion is derived from the inertial device properties along with the maximum admissible force control gain. As both, bounds for the minimum inertia and the maximum control gain are strongly dependent on the firmness of the operator's grasp and the bandwidth of the interaction, the minimum inertia can vary with the task to perform. In all experiments described below the test persons have been asked to try very hard to produce instability.

ViSHaRD3: The interaction with the ViSHaRD3 device has not been performed via the thimble but with a handhold in order to enable a firm grasp. The results of the admittance control experiments are summarized in table 5.2 and 5.3. Again, the inner position control algorithms resolved acceleration, inverse Jacobian, and transposed Jacobian control with gain matrices of the form $\mathbf{K}_P = k_p \mathbf{I}$ and $\mathbf{K}_D = 2\sqrt{k_p} \mathbf{I}$ have been applied. In case of using

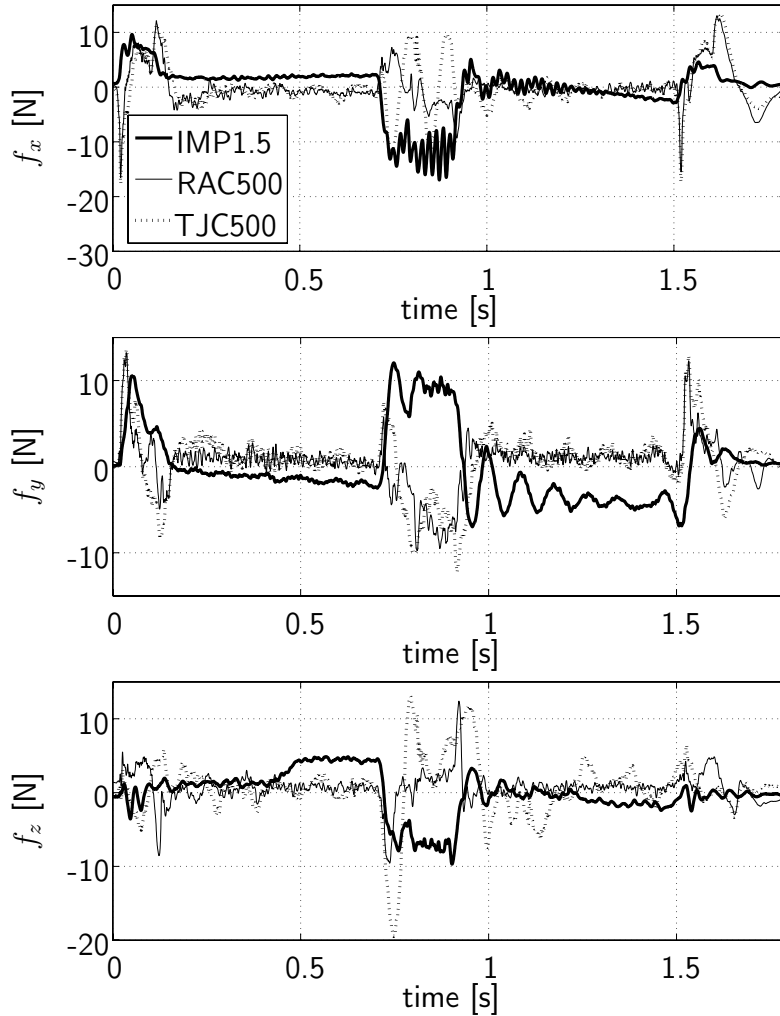


Figure 5.11: Force error at backdrivability experiment

a high gain position controller the introduction of acceleration feedback greatly improved the performance whereas the specific position control strategy did not seem to affect the minimum mass. It has, however, to be noted, that transposed jacobian control produced very high acoustic noise. All high gain implementations had in common that instability, appearing as low frequent oscillations, could be produced by a firm grasp when lowering the virtual mass. A loose grasp did not cause stability problems.

The benefit of acceleration feedforward could also be observed for the low gain implementations. Although the difference in minimum mass was less significant compared to high gain control, doing without feedforward decreased the bandwidth of the system; the test persons reported to feel a force response lagging in phase when performing high frequent motions. Whereas the implementations without acceleration feedforward tend to get unstable when grasping firmly, the others produced high frequent oscillations when holding the end-effector loosely and lowering the virtual mass.

The low gain approach allows a significant lowering of the mass when compared to high gain control. When using acceleration feedforward the test persons could not feel a difference between low and high gain in terms of the dynamic accuracy of the haptic feedback although the position control error is much larger in the low gain case. Moreover, the

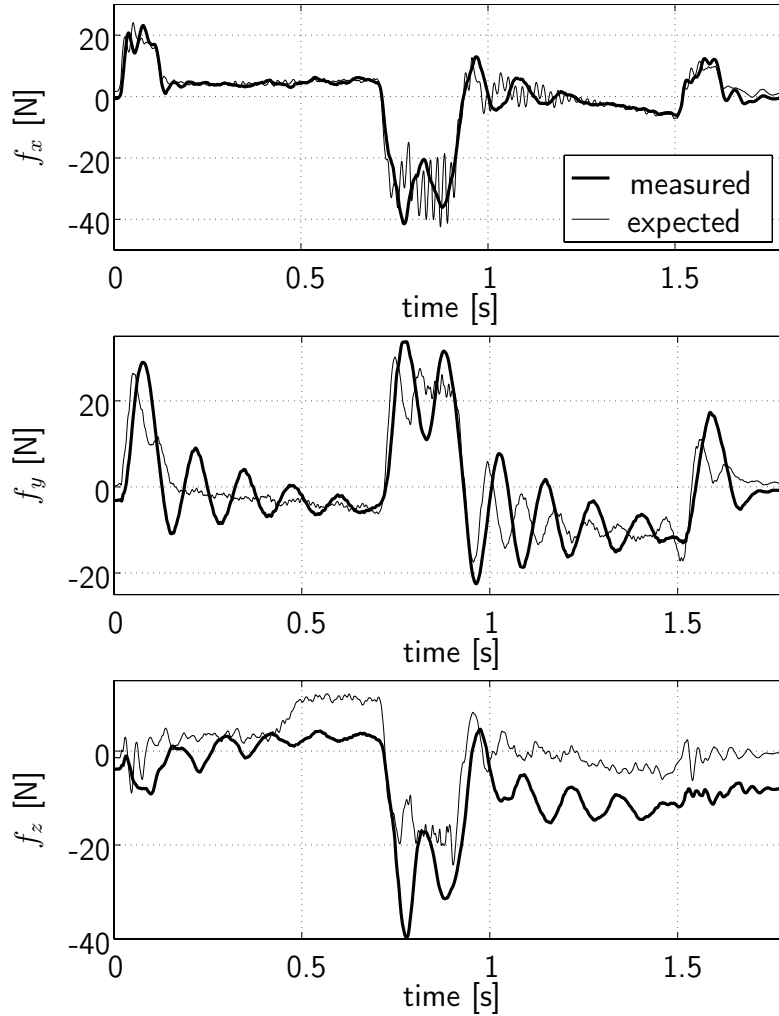


Figure 5.12: Expected versus measured interaction force of open loop impedance control

reduced acoustic noise in low gain control has been reported to improve user convenience. On the positive side the high gain control could slightly better compensate for stiction effects.

Operating the interface in the impedance mode allows for a force gain of 3.75. Considering that inertia of the uncontrolled interface varies between 18 and 1.9 kg the worst and best case minimum inertia is 3.8 and 0.4 kg, respectively. This large variation makes a comparison of admittance and impedance control difficult. The test persons, however, reported the impression of a lower closed loop impedance in the impedance display mode. On the negative side, the anisotropy of the apparent inertia and the inertial cross coupling effects give a somewhat strange feeling. The shaping of the closed loop inertia to a point mass feels more natural. Furthermore, the admittance display mode provides a better compensation of disturbances due to friction.

ViSHaRD6: Similar experiments have been accomplished with the ViSHaRD6 device. The compared admittance control schemes include computed torque and resolved acceleration control differing in whether the loop closure is made in joint or operational space. Again, the test persons have been asked to try to destabilize the system with arbitrary end-

Table 5.2: VISHARD3: minimum inertia of admittance control with $k_p = 10\,000$

Controller	Minimum Inertia
TJC with accel. fwd.	2.5 kg
TJC no accel. fwd.	4.2 kg
IJC with accel. fwd.	2.6 kg
IJC no accel. fwd.	4.3 kg
RAC with accel. fwd.	2.5 kg
RAC no accel. fwd.	4.5 kg

Table 5.3: VISHARD3: minimum inertia of admittance control with $k_p = 1\,000$

Controller	Minimum Inertia
TJC with accel. fwd.	1.75 kg
TJC no accel. fwd.	2 kg
IJC with accel. fwd.	3.4 kg
IJC no accel. fwd.	2.8 kg
RAC with accel. fwd.	2.0 kg
RAC no accel. fwd.	2.3 kg

effector motions at varying grip strengths. It turned out, that the most critical motions are stormy collisions with virtual walls strongly exciting the device flexible modes.

In good accordance with the observations at the experiments with VISHARD3 the inclusion of acceleration feedforward allowed the use of comparatively low gains in the inner position control loop without significant impairment of the perceived dynamic accuracy of the haptic sensation. The advantage of the moderate gains are an increase of the control robustness and a lowering of acoustic noise. Moreover, the reduction of the gains mitigated windup effects caused by hardware limitations of the device output capability. If the target acceleration or velocity exceeds the device output capability a high position error will be produced. Because the inner control loop is closed on position, the compensation of the control error can result in an undesired device response: At the render of a pure point inertia the device acceleration should have the same direction as the interaction force. For example in case of the reversal of the applied force the control output due to the produced position error can, however, result in a device acceleration in the opposite direction. The windup effect does in particular degrade the haptic sensation in case of high frequent oscillating end-effector motions where the device response appears to lag behind. A reduction of the control gains results in a larger contribution of the acceleration feedforward to the overall motor torque command mitigating the adverse effect of velocity or acceleration saturation. Needless to say, that windup effects can also be avoided by considering limitations of the output capability in the design of the target admittance (e.g. by the inclusion of integration limits).

For both algorithms, resolved acceleration and computed torque control, the gain could be reduced to $\mathbf{K}_P = 250\mathbf{I}$ and $\mathbf{K}_D = 2\sqrt{250}\mathbf{I}$ without significant decrease of the perceived dynamic accuracy at free space simulations. This parameter setting allowed for a highly robust render of a minimum translational inertia of 4.8 kg and a minimum rotational inertia of $\mathbf{M}_{\text{rot}} = \text{diag}(0.005, 0.5, 0.5)$ kg m² where the elements of \mathbf{M}_{rot} represent the target inertia for rotations around the axes $\mathbf{x}_E, \mathbf{y}_E, \mathbf{z}_E$ of the end-effector coordinate system shown in

figure 2.5. Comparing the performance of resolved acceleration and computed torque control no difference in terms of the minimum realizable inertia could be observed. In fact, the test persons could not feel any change in the haptic sensation when switching between these two position control implementations.

In a previous study by Ernst [Ern03] the closed loop performance of an admittance control implementation based on simple independent joint position control has been analyzed. Despite the identified minimum translational inertia of 8 kg does not allow a direct comparison due to minor hardware modifications⁴ the result indicates a performance improvement of approximately 40% by the inclusion of acceleration feedforward along with feedback linearization.

The maximum proportional gains of the PD force control law of the impedance control implementation has been determined with $\mathbf{K}_P = \text{diag}(1.1, 1.1, 3.0, 5.0, 6.6, 10)$. Due to the comparatively low gains for interactions in the x - and y -direction the closed loop inertia can be comparatively high. Another disadvantage of the impedance control scheme is the strong directional dependency of the impedance error and the heavy inertial cross couplings between the translational and rotational DOF. As a matter of these facts, the operation in the admittance mode seems to be much more convenient.

ViSHaRD10: For the identification of the minimum inertia of the ViSHARD10 the translational workspace has been constrained to end-effector positions with x -, y -, and z -coordinates within $[-0.3 \text{ m } 0.3 \text{ m}]$. The applied inverse kinematics was based on the inverse function technique for the motion of joint 1, 2, 3, 4, 6, 7, see equation (3.40), (3.44), (3.45), and Pseudoinverse control for the wrist motion applying the side criterion given in equation (3.43).

In case of using a simple independent joint control algorithm for the inner joint position control loop the minimum translational target has been found to be around $\mathbf{M}_{\text{trans}} = \text{diag}(10, 15, 4) \text{ kg}$ and the rotational inertia around $\mathbf{M}_{\text{rot}} = \text{diag}(0.05, 0.05, 0.01) \text{ kg m}^2$, where $\mathbf{M}_{\text{trans}}$ and \mathbf{M}_{rot} are defined respective the coordinate systems $\{B\}$ and $\{E\}$ shown in figure 2.7. The application of a more advanced computed torque scheme with acceleration feedforward significantly improved the results to $\mathbf{M}_{\text{trans}} = \text{diag}(5, 7, 2) \text{ kg}$ and $\mathbf{M}_{\text{rot}} = \text{diag}(0.01, 0.01, 0.005) \text{ kg m}^2$. The control gain has been set to $\mathbf{K}_P = 250\mathbf{I}$ and $\mathbf{K}_D = 2\sqrt{250}\mathbf{I}$. The significant dependence of the minimum mass and inertia on the direction is in accordance with the inertial device characteristics. This points to a potential benefit of more advanced inverse kinematics solution approaches optimizing the ViSHARD10 mass and inertial properties. A summary of the minimum inertia performances of the ViSHARD haptic interfaces using the most appropriate admittance control algorithm is presented in table 5.4

Important Remark: During the great many experiments for minimum inertia identification it turned out that the results are not perfectly reproducible. For example the minimum inertia of the ViSHARD3 device when using resolved acceleration control with acceleration feedforward varied from 1.6 to 2.0 kg at experiments accomplished within one day. It has to be noted, that these variations are not caused by changing operator interactions because highly robust inertia settings determined early in the mornings destabilized

⁴auxiliary bearing support at the base joint and the replacement of the direct drive actuation of the last joint by a geared actuation

Table 5.4: Minimum inertia of the ViSHARD devices operated in the admittance display mode

Device	Minimum Translational Inertia	Minimum Rotational Inertia
ViSHARD3	1.75 kg	not applicable
ViSHARD6	4.8 kg	diag(0.005, 0.5, 0.5) kg m ²
ViSHARD10	diag(5, 7, 2) kg	diag(0.01, 0.01, 0.005) kg m ²

the system without considerable operator effort at experiments carried out in the evenings. At the next morning the superior performance was recovered. This degradation of the device performance with time was repeatedly observed at several days. A connection of the varying performance with the device operating temperature could not be asserted because the device performance could not be recovered by switching the device off for several hours in order to cool down the joint components. The reason for the performance variations remains an open research question.

5.3.3 Dynamic Force Precision

This section presents experimental results of force control frequency response measurements accomplished with the ViSHARD3 device. The same experimental setup as for the direct measurement of the backdrivability (see section 5.3.2) has been used differing in that the linear guide has been controlled to keep its position to render isometric conditions. The force response has been derived from the measured interaction force in response to a sinusoidal force command in the x -direction. This procedure has been repeated for 60 frequencies ranging from 1 to 60 Hz. For all experiments the amplitude of the commanded force sine has been 5 N. The only exception are the measurements with open loop impedance control where the amplitude has been increased to 10 N in order to reduce the impact of stiction on the results. The force response is evaluated in terms of the amplitude and phase of the (in a least squares sense) best fit force sinusoid at the excitation frequency. As the investigated system is strongly nonlinear the actual force response can vary significantly from the fitted response. Therefore, also the signal distortion $D_{\text{rms}}^{\%}$, the percent RMS value of the deviation between these two signals, has been computed with

$$D_{\text{rms}}^{\%} = \frac{\sqrt{\frac{1}{n} \sum_{i=1}^n (f_i - \hat{f}_i)^2}}{\sqrt{\frac{1}{n} \sum_{i=1}^n \hat{f}_i^2}} \cdot 100 \%, \quad (5.2)$$

where n is the number of samples and \hat{f}_i and f_i the fitted and measured interaction force samples, respectively.

Clearly, the resultant frequency response is largely dependent on the end-effector position. Because the focus of this experiment is the influence of the control strategy on the closed loop frequency response the results are given for one device configuration only. Similar to the backdrivability experiments the requirement for a very stiff coupling to the environment requires comparatively low controller gains. Furthermore, active damping had to be introduced in y - and z -direction. It was not possible to analyze admittance control without acceleration feedforward due to stability problems. Again, a reduction of

the coupling stiffness by the inclusion of shock absorbing polymers did not produce useful results due to the added flexible modes.

The results shown in figure 5.13 confirm the reduction of the device closed loop bandwidth when operated in the admittance mode with loop closure on position. Both, resolved acceleration control with a high position gain of $k_P = 10\,000$ and low gain of $k_D = 1\,000$, have a sharp resonance at 21 Hz and 24 Hz, respectively. At both implementations the virtual mass has been set to 3 kg. The larger bandwidth of the low gain controller (28.5 Hz versus 26 Hz) can be explained by interpreting the gain as a weighting factor between the acceleration feedforward action, being equivalent to proportional force-based explicit force control, and the action of the position-based explicit force control, which is in this isometric experiment equivalent to double integral force-based explicit force control. Compared to the impedance control approaches the integral action improves, however, the force tracking capability at low frequencies; due to stiction effects the magnitude of the device under impedance control is less than 0 dB at low frequencies. The results also indicate that the inclusion of force feedback in impedance control can significantly increase the closed loop bandwidth (in this experiment it is increased from 33 Hz to more than 60 Hz); a PD controller with $k_P = 2.5$ and $k_D = 0.003$ has been used in these experiments.

Viewing the evaluation of the signal distortion reveals that the measured frequency response is largely different from the characteristics of linear systems. This is particularly true for the admittance control schemes showing a force response colored heavily by high frequency oscillations. At excitation frequencies exceeding the closed loop bandwidth the RMS value of the difference between the fitted and measured force response is orders of magnitudes higher than the RMS value of the fitted signal. Despite less susceptible to high frequency oscillations also the impedance control schemes exhibit significantly distorted output force signals. These facts point to a limited qualification of isometric measurement conditions and linear analyzing techniques for the characterization of the device force frequency response.

The effect of the derivative action in impedance control with force feedback is illustrated in figure 5.14. It shows the frequency response of a P and PD controller with $k_P = 1.5$ and $k_D = 0.003$. The diagram clearly exposes the increase in bandwidth due to the derivative action. Again, the distortion of the output signal is comparatively high. It has to be noted that these results cannot be directly compared to the results presented in figure 5.13 as the experiments have been accomplished at slightly different end-effector positions.

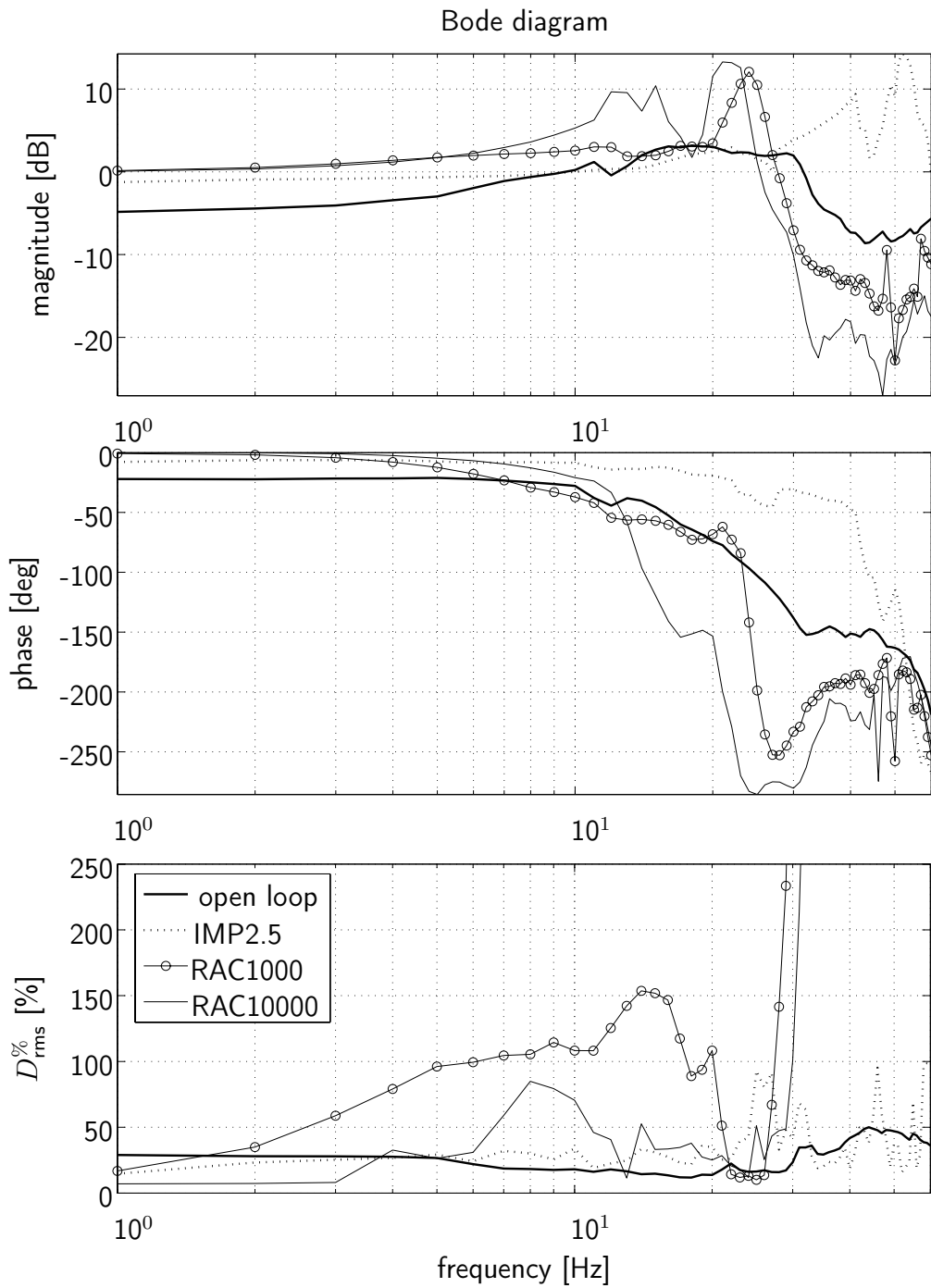


Figure 5.13: Force frequency response of impedance and admittance control laws: magnitude, phase, and signal distortion

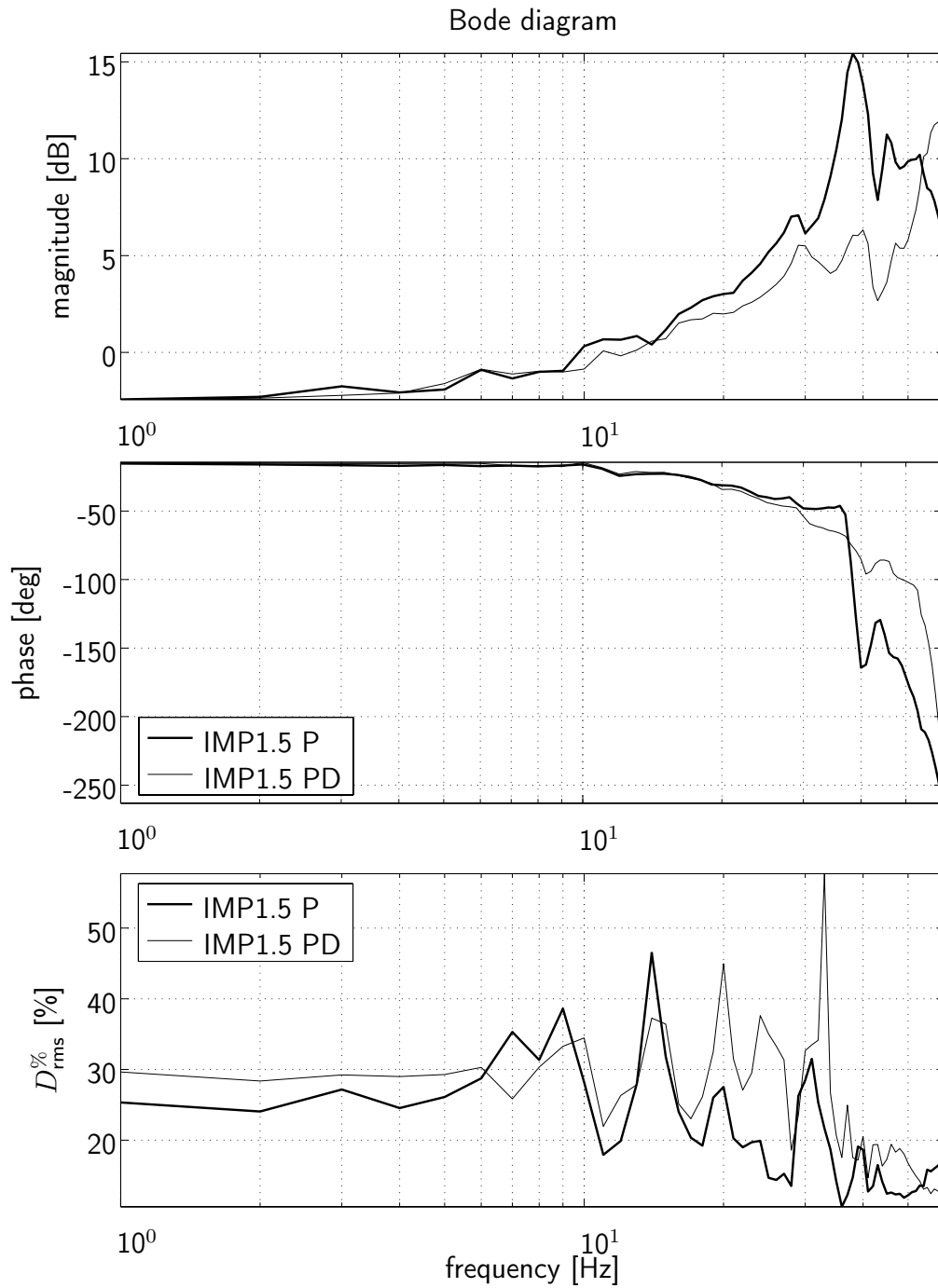


Figure 5.14: Force frequency response of impedance control with and without derivative action

5.4 Summary

The discussion of performance measures given in this chapter reveals that an evaluation of haptic interfaces is complicated by their nonlinear nature as well as the presence of a human operator in the feedback loop. The device nonlinearity renders many performance indices dependent on the device configuration, direction of interaction, and excitation amplitude. As a matter of this fact, measures solely for a ‘nominal configuration’ can be misleading. Instead, the performance should be expressed in terms of worst case figures in the entire specified workspace. Based on such a characterization the qualification of a haptic interface for a specific task can be verified. In order to avoid an excessive number of hardware experiments model-based analysis techniques should be applied for the identification of worst case figures whenever reliable. Such a procedure has been demonstrated for the evaluation of the output capability of the ViSHARD3 and 6 device. However, for the determination of the frequency response characteristics, control stability bounds, and the closed loop stiffness the application of direct measurement seems to be unavoidable. Device nonlinearities also reduce the explanatory power of linear frequency response analyzing techniques proposed in the literature for the evaluation of the device backdrivability. More descriptive seem to be performance measures considering explicitly the physical effects originating the disturbance forces in terms of, for instance, the maximum inertia or uncompensated friction force.

The second challenge, the presence of the operator in the control loop, makes in particular the evaluation of devices applying force feedback control difficult. Because stability bounds are deeply affected by the load characteristics isometric measurement conditions where the device is firmly coupled to a rigid reference device have been found to be inappropriate. The definition of more realistic testing conditions providing consistent results for devices using arbitrary haptic control schemes is still an open but very important research question.

For the evaluation of the performance of the ViSHARD3 interface a number of experiments with the device firmly coupled to a linear guide have been performed. Although the measurement results are of limited use for the identification of the device closed loop performance, because the isometric measurement conditions necessitated significant lowering of the control gains, they provide rich insight into the effect of the haptic control scheme on the closed loop behavior. Direct measurement of the backdrivability revealed an improved capability of admittance control to compensate for frictional and gyroscopic effects when compared to impedance control. Moreover, the compensation of inertial coupling effects enables the rendering of an isotropic closed-loop inertia. The results confirm the closed-loop impedance error predicted by the analysis of the impedance control scheme allowing the estimation of the device closed loop backdrivability from a model-based analysis using control gains determined by hardware experiments. The experiments for the device frequency response measurement highlight the significant increase in bandwidth when adding force feedback to impedance control. An additional improvement is achieved when using derivative action in the force control law. The admittance control implementations suffered from a largely reduced bandwidth. Moreover, they showed a high susceptibility to high frequency oscillation distorting strongly the force output signal.

A very plain and descriptive characterization of the backdrivability of haptic interfaces operated in the admittance mode is the specification of the minimum pure inertia that can be rendered without producing instability at arbitrary human interactions. Although the assumption of a perfect tracking capability of the inner motion control loop does not hold

in practice, the degradation of the perceived dynamic accuracy turned out to be comparatively low. In fact, the hardware experiments with the ViSHARD devices revealed that high gain position control implementations provided indeed a largely reduced control error but test persons could not recognize a significant difference in the accuracy of the haptic feedback compared to low gain implementations applying acceleration feedforward. The benefit of moderate gain position feedback is a significant increase of the control robustness permitting a reduction of the minimum inertia, a lowering of acoustic noise, and the mitigation of windup effects due to saturation of the device acceleration or velocity capability. It is, however, important to note, that low gain motion control implementations have to be accompanied with acceleration feedforward and the compensation of the interaction force in order to avoid significant impairment of the system bandwidth and control stiffness. The fact, that these observations hold for all ViSHARD devices, that vary strongly in terms of their inertial properties, indicates that the proposed control design is also useful for other haptic interfaces.

6 Conclusions and Future Work

6.1 Concluding Remarks

Viewing the state of the art of kinesthetic haptic interface design for the human hand one can observe that there is a lack of interfaces providing high force capability in large operating volumes. For applications with such requirements mostly off-the-shelf industrial robots showing major deficiencies regarding dynamic properties and safety aspects are used. The presented work provides a discussion of general design, control, and performance evaluation aspects of kinesthetic haptic interfaces with focus on human friendly devices with human matched output capacity and comparatively large workspace. The main innovation is the consideration of multiple redundant actuated joints in the kinematical design for the increase of the device versatility and performance. For the experimental evaluation of the proposed mechatronic concepts a family of kinesthetic haptic feedback devices has been designed and built by the author. The main contributions and results of this thesis are summarized in the following.

Based on the results of a review on hardware solutions for kinesthetic haptic feedback mechanisms the design concept of the ViSHARD device family has been developed. Striving for an experimental platform for the exploration of novel haptic applications the constructions are strongly influenced by considerations of versatility and extensibility. The high force capability is provided by joint components equipped with harmonic drive gears due to their superior stiffness characteristics and higher compactness when compared to alternative speed reduction mechanisms as for instance planetary gears or tendon based systems. For the increase of the payload capability all prototypes employ a horizontal SCARA segment at the base avoiding the need for compensation of gravitational load with motor torque. The requirement for large workspaces motivated purely serial instead of parallel or hybrid kinematical designs. An outstanding good ratio between workspace and device size has been achieved with the ViSHARD10 interface applying multiple actuated redundant joints to circumvent singular configurations by a dedicated control of the device null space motion. Moreover, ViSHARD10 features an unlimited rotational workspace free of singularities that cannot be achieved with nonredundant designs. Beneath workspace increase the redundant DOF offer a potential for collision avoidance (e. g. for the prevention of user interference or device collision at dual-arm haptics) and improvement of the dynamic properties and output capability. Because the control of the selfmotion can be adapted to the specific needs of the haptic interaction task the device is characterized by a high degree of versatility. The use of hyper-redundant kinematics for kinesthetic haptic interface design is considered novel.

As the ViSHARD devices provide force sensing capability both types of haptic control paradigms, impedance and admittance control, can be implemented to shape the closed loop dynamics. The discussion of these control schemes emphasized that admittance control implementations are advantageous for the render of inertia because, contrary to impedance control, neither acceleration measurement nor a dynamic device model is re-

quired to form the closed loop inertia. Another benefit is the superior disturbance rejection capability due to the high gain inner control loop closed on motion providing an effective elimination of nonlinear device dynamics as for instance friction. At the negative side, admittance control implementations suffer from inferior bandwidth characteristics. Viewing motion-based impedance control with acceleration feedforward it has been pointed out that this control scheme can be interpreted as impedance control and admittance control acting in parallel. For the purpose of comparison impedance and several distinct admittance control algorithms have been implemented for the operation of the ViSHARD devices.

The control of redundant haptic interfaces requires the definition of an inverse kinematics solution algorithm mapping operational motions or forces to the corresponding joint space quantities. The solution of the inverse kinematics of the ViSHARD10 device makes use of the advantageous property of the kinematical design that the decoupling of the translational from the rotational device motion can be achieved easily by dedicated control of certain joints. This enables the partitioning of the inverse kinematics problem into two separate problems: the inverse kinematics for the positioning (4R SCARA segment) and the orientation stage (4R spherical wrist). Two solution approaches, pseudoinverse control and the definition of an inverse function, have been discussed in detail. The inverse function approach applied to the SCARA or wrist control suffers (like all conservative inversion approaches) from fundamental restrictions on the invertible workspace. Pseudoinverse control does not have these limitations but results in non-conservative device motions. The implication is that a systematic performance analysis of pseudoinverse control is a major challenge because joint configurations are dependent on the end-effector path and speed of path following. As far as the control of the wrist motion is concerned hands-on experience at hardware experiments showed that pseudoinverse control with optimization of an appropriate side criterion can indeed offer an unlimited orientational workspace with a selfmotion simple to understand and anticipate for the operator. The redundant wrist concept can therefore be considered as very well suited for haptic applications. For the control of the SCARA segment the results using pseudoinverse control are less satisfactory as no robust singularity avoidance could be achieved for arbitrary end-effector motions. Good results could be achieved with the inverse function approach defined at a rectangular workspace of moderate size. Inverse functions constructed using numerical search algorithms indicate the feasibility of larger workspaces but have not yet been validated by hardware experiments.

Amongst the sources for disturbances of the haptic feedback friction is, in all probability, the most difficult to model. The good disturbance rejection capability of admittance control implementations usually reduces the need for dedicated friction compensation procedures. In case of impedance control the application of a model-based friction compensator in addition to force feedback control is rewarding due to stability bounds of the feedback gain. These permit only partial elimination of friction induced impedance errors with force feedback action alone. The model of the ViSHARD friction compensator does not account for presliding hysteresis and dynamic friction effects due to the low susceptibility of harmonic drive gears to stick-slip motion and the moderate requirements of haptic devices on positioning accuracy. More important seem to be the following effects revealed by hardware experiments but disregarded in most harmonic drive friction models reported in the literature: significant nonlinearity of the load dependent and viscous friction characteristics as well as a large change of the frictional behavior with time. The friction compensator proposed in this work accounts for all of these effects. The viscous and torque dependent

friction is described with fourth and second order polynomials, respectively. The time variability of the Stribeck curve is considered by adaptation of the friction parameters. As the change of the frictional behavior with operation time is comparatively slow the parameters are not adapted iteratively at each sampling instant but re-tuned after a specified number of samples. Experimental results indicate a convenient performance of the proposed adaptation scheme for joint 2 and 3. The results for joint 1 are less satisfactory pointing to a low reliability of the friction estimation. A possible explanation is the larger and more complex load dynamics around this joint. The compensation of stiction forces is accomplished by a variable structure force control law. Switching between PID and PD force control this algorithm aims at a good disturbance rejection for the joints at rest while maintaining a good dynamic behavior for moving joints. Hardware experiments showed, that this algorithm effectively removed any stiction effect allowing smooth motions at fine positioning tasks. Moreover, no degradation of robustness properties and dynamic performance could be observed.

The discussion on performance measures for haptic interfaces revealed that the standardized and systematic evaluation of devices with force feedback control is still an open research question. Whereas meaningful quantitative measures exist for performance properties not affected by the action of the controller no appropriate and well-defined experimental testing conditions are known for the identification of certain closed loop performance indices. Many authors propose isometric measurement conditions with the device tip firmly connected to a position source to directly measure the backdrivability and dynamic force precision. For most force feedback controlled haptic interfaces, including the VISHARD devices, this procedure does not work: Because the stiffness of the coupling exceeds by far the human arm stiffness the control gains have to be reduced to maintain stability. This, in turn, deteriorates the closed loop performance. The isometric measurements carried out with the VISHARD3 interface coupled to a linear guide enabled a comparative study of haptic control schemes. The backdrivability experiments confirmed the improved disturbance rejection capability of admittance control when compared to impedance control. The frequency response measurements showed that a significant higher force bandwidth can be achieved by adding force feedback with derivative action to open loop impedance control. Admittance control implementations showed a largely inferior closed loop bandwidth.

The evaluation of the VISHARD closed loop backdrivability in terms of the minimum inertia has been accomplished under realistic testing conditions with several human operators. Applying admittance control schemes the following observations have been made: The inclusion of acceleration feedforward permits a considerable lowering of the target inertia. Moreover, it allows the use of comparatively low position control gains without significant degradation of the perceived dynamic accuracy of the haptic sensation. Moderate gains of the position feedback have the advantage to reduce acoustic noise, to permit additional inertia reduction, and to mitigate windup effects due to output saturation. This is contrary to the usual recommendations given in the literature emphasizing the need for high inner feedback gains to increase the bandwidth of the inner position control loop beyond the bandwidth of the outer loop. These studies do, however, focus on simple admittance control implementations employing neither acceleration feedforward nor the compensation of interaction forces. Comparing resolved acceleration control with computed torque no difference in the haptic sensation could be perceived by the operator. Because these observations hold for all VISHARD devices I believe that they also provide useful hands-on experience for the control design of other haptic interfaces.

6.2 Future work

The driving motivation for the work presented in this thesis was the vision of general-purpose haptic interfaces applicable in a large variety of task domains. The ViSHARD family constitutes one important step towards this goal but by far not the final solution. Further improvement of the state of the art in kinesthetic haptic interface design will involve many exciting and challenging research directions, among the others:

Hardware design: A very rewarding and straightforward way for performance increase of haptic interfaces is the optimization of the mechatronic design of the joint components. This requires the development of highly integrated motor/gear modules optimized for haptic applications (e.g. low torque ripple, good backdrivability, high torque to mass ratio, low power loss at zero speed). A second promising line of research is the exploration of more complex design concepts such as parallel or serial macro/micro systems to overcome bandwidth limitations of large interfaces or to increase performance under safety constraints; the introduction of kinematical redundancies for singularity avoidance (see the ViSHARD10 design). The development of hardware prototypes is necessary to study the benefit and practicability of these concepts. Another rewarding research area seems to be the integration of tactile stimulation actuators in kinesthetic haptic hardware to provide collocated kinesthetic and tactile feedback to the operator.

Control design: Compared to robot force control in the framework of industrial applications much less theoretical and experimental research has been devised to haptic feedback control. The similarity of these control tasks suggests that many advanced control approaches successfully implemented for industrial robots can also be rewarding to enhance the closed loop performance of haptic interfaces. Promising candidates are for instance control algorithms based on advanced dynamic models considering joint or link flexibilities or approaches involving increased sensorial capabilities as for example combined joint and end-effector force/torque sensing or direct motor acceleration measurement. Acceleration sensing at the motor side seems to be an interesting alternative or addition to force sensing because the collocation of the sensor and the actuator possibly allows for a more robust active shaping of the device inertia. As far as the control of redundant haptic interfaces is concerned further in-depth studies of redundancy exploitation techniques specific to the goal of haptic human-device interaction are required. Viewing the results of this thesis the ability of ViSHARD10 to circumvent singular configurations and its applicability for haptic interactions could be demonstrated. The enormous versatility provided by the redundant DOF of the ViSHARD10 device does, however, not seem to be fully exploited. Rewarding future research directions are the development of task specific inverse kinematic solution algorithms providing for instance collision avoidance, improved dynamic properties, or higher output capability. This includes an in-depth study of full inverse kinematics solution algorithms solving for all 10 DOF simultaneously.

Applications: A driving factor for the research on hardware and control solutions for haptic interfaces with high force capability in large operating volumes is the development of application areas that benefit from this extended versatility. With the ViSHARD family an experimental platform for the exploration of such novel haptic application areas is provided. Future research may for example include bimanual collaborative virtual reality and telepresence tasks in large workspaces and open hand surgery training.

Evaluation: For the monitor of the research progress in haptic interface design as well as for the systematic comparison amongst devices a standardized performance evaluation

is required. As indicated in this work the definition of well-defined testing conditions replicating the load characteristics of human operators in an univocal and realistic way is still an open but very important research question. The solution to this problem is required for the measurement of physical closed loop performance parameters of haptic interfaces applying force feedback control. Another important research need are further investigations of the human haptic perceptual system. The definition of a meaningful standardized performance evaluation of haptic hardware requires the combined consideration of physical performance parameters and human perception characteristics.

A Technical Hardware Details

A.1 Specifications of Sensors and Joint Components

A.1.1 ViSHaRD3

Table A.1: ViSHARD3: Force/ Torque/ Acceleration Sensor Specifications

Property	Value
Type	85M35A-I40 (JR3)
Force Range	$F_x, F_y: \pm 200 \text{ N}; F_z: \pm 400 \text{ N}$
Torque Range	$\pm 12 \text{ N m}$
Linear Acc. Ratings	49 m/s^2
Rotational Acc. Ratings	100 rad/s^2
Force/Torque Resolution	1 : 4000 of the force/torque range
Linear Acc. Resolution	0.0981 m/s^2
Rotational Acc. Resolution	0.1 rad/s^2
Bandwidth	8 kHz

Table A.2: ViSHARD3: Harmonic Drive Gear Specifications

Joint #	Series-Vers.-Size-Ratio	M_R^1 [N m]	M_A^2 [N m]	k^3 [N m/rad]	v_{\max}^4 [rpm]
1-3	HFUC-2UH-17-100	54.0	39.0	$1.0 \cdot 10^4 - 1.6 \cdot 10^4$	7300

¹ limit for repeated peak torque

² limit for average torque

³ torsional stiffness; k is load dependent (see Harmonic Drive catalogue for details)

⁴ maximum input speed; applicable for Harmonic Drive 4B No.2 grease

Table A.3: ViSHARD3: Motor and Encoder Specifications

Joint #	Motor			Encoder		
	Type	M_H^1 [N m]	M_c^2 [N m]	Type	I^3	f_m^4 [kHz]
1-3	Maxon RE40 148877	2.5	0.201	HEDL-5540	500	100

¹ stall torque

² maximum continuous torque

³ impulses per turn

⁴ maximum operating frequency

A.1.2 ViSHaRD6

Table A.4: ViSHARD6: Force/ Torque Sensor Specifications

Property	Value
Type	67M25A-I40 (JR3)
Force Range	$F_x, F_y: \pm 200 \text{ N}; F_z: \pm 400 \text{ N}$
Torque Range	$\pm 12 \text{ N m}$
Resolution	1 : 4000 of the force range
Bandwidth	8 kHz

Table A.5: ViSHARD6: Harmonic Drive Gear Specifications

Joint #	Series-Vers.-Size-Ratio	M_R^1 [N m]	M_A^2 [N m]	k^3 [N m/rad]	v_{\max}^4 [rpm]
1-2	HFUC-2UH-25-160	176.0	108.0	$3.1 \cdot 10^4 - 5.7 \cdot 10^4$	5600
3-5	HFUC-2UH-17-100	54.0	39.0	$1.0 \cdot 10^4 - 1.6 \cdot 10^4$	7300
6	HFUC-2A-8-100	4.8	3.3	$0.91 \cdot 10^3 - 1.2 \cdot 10^3$	8500

¹ limit for repeated peak torque

² limit for average torque

³ torsional stiffness; k is load dependent (see Harmonic Drive catalogue for details)

⁴ maximum input speed; applicable for Harmonic Drive 4B No.2 grease

Table A.6: ViSHARD6: Motor and Encoder Specifications

Joint #	Motor			Encoder		
	Type	M_H^1 [N m]	M_c^2 [N m]	Type	I ³	f_m^4 [kHz]
1-5	Maxon RE40 148877	2.5	0.201	HEDL-5540	500	100
6	Maxon RE-max 29 226790	0.252	0.033	MR-Enc. Typ ML	1000	200

¹ stall torque

² maximum continuous torque

³ impulses per turn

⁴ maximum operating frequency

A.1.3 ViSHARD10

Table A.7: ViSHARD10: Force/ Torque Sensor Specifications

Property	Value
Type	67M25A-I40 (JR3)
Force Range	$F_x, F_y: \pm 200 \text{ N}; F_z: \pm 400 \text{ N}$
Torque Range	$\pm 12 \text{ N m}$
Resolution	1 : 4000 of the force range
Bandwidth	8 kHz

Table A.8: ViSHARD10: Harmonic Drive Gear Specifications

Joint #	Series-Vers.-Size-Ratio	M_R^1 [N m]	M_A^2 [N m]	k^3 [N m/rad]	v_{\max}^4 [rpm]
1	HFUC-2UH-25-160	176.0	108.0	$3.1 \cdot 10^4 - 5.7 \cdot 10^4$	5600
2	CSG-2UH-20-120	113.0	64.0	$1.6 \cdot 10^4 - 2.9 \cdot 10^4$	6500
3	HFUC-2UH-20-120	87.0	49.0	$1.6 \cdot 10^4 - 2.9 \cdot 10^4$	6500
4-7	HFUC-2UH-17-100	54.0	39.0	$1.0 \cdot 10^4 - 1.6 \cdot 10^4$	7300
8, 9	HFUC-2A-11-100	13.0	8.9	$2.7 \cdot 10^3 - 4.4 \cdot 10^3$	8500
10	HFUC-2A-8-100	4.8	3.3	$0.91 \cdot 10^3 - 1.2 \cdot 10^3$	8500

¹ limit for repeated peak torque

² limit for average torque

³ torsional stiffness; k is load dependent (see Harmonic Drive catalogue for details)

⁴ maximum input speed; applicable for Harmonic Drive 4B No.2 grease

Table A.9: ViSHARD10: Motor and Encoder Specifications

Joint #	Motor			Encoder		
	Type	M_H^1 [N m]	M_c^2 [N m]	Type	I ³	f_m^4 [kHz]
1,2,7	Maxon RE40 148877	2.5	0.201	MR-Enc. Type L	1024	320
3-6	Maxon RE35 118778	1.07	0.113	MR-Enc. Type L	1024	320
8-9	Faulhaber 3257048CR	0.538	0.070	HEDL-5540	500	100
10	Maxon RE-max 29 226790	0.252	0.033	MR-Enc. Typ ML	1000	200

¹ stall torque

² maximum continuous torque

³ impulses per turn

⁴ maximum operating frequency

A.1.4 Linear Guide

Table A.10: Linear Guide Specifications

Property	Value
Type	MOVOPART M55 (with Ball Screw Drive and Ball Guide)
Screw Lead	32 mm
Stroke Length	1.6 m
Linear Velocity, Maximum	1.6 m/s
Drive Shaft Torque, Maximum	12 N m
Repeatability	± 0.05 mm

Table A.11: Linear Guide: Motor and Encoder Specifications

Motor		Encoder		
Type	M_n^1 [N m]	Type	I ²	f_m^3 [kHz]
Mattke RS 330 E	0.667	MIG 5800	5000	300

¹ rated torque

² impulses per turn

³ maximum operating frequency

A.2 Dynamic Device Models

In the following, the dynamic models of the ViSHARD interfaces are presented using the Autolev¹ modeling language.

A.2.1 ViSHaRD3

```
%Problem: Dynamic Model Vishard3
%-----
%Newtonian, bodies, points
NEWTONIAN    N % Newtonian reference frame
BODIES       L1, L2, L3
POINTS       0, L1Q, L2Q, L3Q, EE
%-----
%Link lengths [m]:
CONSTANTS    L_L1=0.3, L_L2=0.075

%Link masses [kg]:
MASS         L1=M_L1=3.53732, L2=M_L2=1.60926 ,L3=M_L3=2.02199

%Link inertia [kg * m^2]
INERTIA      L1, 0.00820162, 0.07756594, 0.07152441, 0, 0, 0.01515538
INERTIA      L2, 0.00109135, 0.00253454, 0.00245410, 0, 0, 0.00022273
INERTIA      L3, 0.02949, 0.010543, 0.038194, 0.009881, 0.0001135, 0.000027702
%-----
%Motor and wavegenerator inertia [kg*m^2]
CONSTANTS    J_Wave_HD17    = 0.0000079
CONSTANTS    HD17_Ratio     = 100
CONSTANTS    J_Rotor_RE40   =0.0000134
%-----
%Rotation between the coordinate systems starting at newtonian
SIMPROT(N, L1, 3, TH1)
SIMPROT(L1, L2, 3, TH2)
SIMPROT(L2, L3, 1, TH3)
%-----
%Position vectors
P_O_L1Q> = L_L1*L11>           %from origin L1 to origin L2
P_O_L1o> = 0.15*L11>           %from origin L1 to CoM L1
P_L1Q_L2Q> = L_L2*L21>         %from origin L2 to origin L3
P_L1Q_L2o> = 0.02325*L21>      %from origin L2 to CoM L2
P_L2Q_EE> = 0.31*L32> + 0.22*L31> %from origin L3 to origin of EE
P_L2Q_L3o> = 0.184*L31> + 0.13369*L32> %from origin L3 to CoM L3
```

¹<http://www.autolev.com/>

A.2.2 ViSHaRD6

```

% Problem: ViSHaRD6
%-----
% Newtonian, bodies, frames, points
NEWTONIAN  N % Newtonian reference frame
BODIES     B1, B2, B3, B4, B5, B6
FRAMES     GREIF % from joint of B6 to handle
FRAMES     B3H, B4H % interframes for interim results
POINTS     0, S0, S1, S2, S3, S4, S5, SGREIF
POINTS     S2H, S3H % interpoints for interframes
%-----
%Link lengths [m] (length from joint to joint)
CONSTANTS L_0 = 0.534 , & % distance from N to S0 (only Z- direction)

          L_B1X = 0.6275 , & % distance from S0 to S1 in x-direction...
          L_B1Y = 0      , &
          L_B1Z = 0.139 , &

          L_B2X = 0.6275 , &
          L_B2Y = 0      , &
          L_B2Z = 0.221 , &

          L_B3X = 0      , &
          L_B3Y = -0.0165 , &
          L_B3Z = 0.2069 , &

          L_B4X = 0.084 , &
          L_B4Y = -0.0445 , &
          L_B4Z = 0.0165 , &

          L_B5X = 0.255 , &
          L_B5Y = 0      , &
          L_B5Z = 0.0189 , &

          L_B6X = 0      , &
          L_B6Y = 0      , &
          L_B6Z = -0.0634 % end-effector at height of joint 4
                        % (middle of handle at -0.105)
%-----
%Lengths from joint to center of mass of link
CONSTANTS COM_B1X = 0.18563 , &
          COM_B1Y = 0      , &
          COM_B1Z = 0.03056 , &

          COM_B2X = 0.26323 , &
          COM_B2Y = 0      , &

```

COM_B2Z = 0.10290 , &

COM_B3X = 0 , &

COM_B3Y = 0.02296 , &

COM_B3Z = 0.16915 , &

COM_B4X = 0.07440 , &

COM_B4Y = 0.00460 , &

COM_B4Z = 0.00663 , &

COM_B5X = 0.14539 , &

COM_B5Y = -0.00006 , &

COM_B5Z = 0.03242 , &

COM_B6X = 0 , &

COM_B6Y = 0 , &

COM_B6Z = -0.03776

%-----

%Link masses [kg]

CONSTANTS M_B1 = 7.52809 , &

M_B2 = 7.18310 , &

M_B3 = 2.24088 , &

M_B4 = 1.78136 , &

M_B5 = 1.04128 , &

M_B6 = 0.78057

MASS B1=M_B1, B2=M_B2, B3=M_B3, B4=M_B4, B5=M_B5, B6=M_B6

%-----

%Motor and wavegenerator inertia [kg*m^2]

CONSTANT J_WAVE_HFUC8 = 0.0000003

HFUC8_RATIO = 100

CONSTANTS J_WAVE_HFUC17 = 0.0000079

HFUC17_RATIO = 100

CONSTANTS J_WAVE_HFUC25 = 0.0000413

HFUC25_RATIO = 160

CONSTANTS J_ROTOR_REMAX29 = 0.00000127

CONSTANTS J_ROTOR_RE40 = 0.0000134

%-----

%Link inertia [kg*m^2]

CONSTANTS IB1_11 = 0.04769105 , &

IB1_22 = 0.78260941 , &

IB1_33 = 0.74881342 , &

IB1_12 = 0 , &

```

IB1_23 = 0           , &
IB1_31 = 0.12781952 , &

IB2_11 = 0.10580746 , &
IB2_22 = 1.15756998 , &
IB2_33 = 1.06281205 , &
IB2_12 = 0           , &
IB2_23 = 0           , &
IB2_31 = 0.28294264 , &

IB3_11 = 0.07739985 , &
IB3_22 = 0.07463462 , &
IB3_33 = 0.00423343 , &
IB3_12 = 0           , &
IB3_23 = 0.01051890 , &
IB3_31 = 0           , &

IB4_11 = 0.00271031 , &
IB4_22 = 0.01261225 , &
IB4_33 = 0.01320801 , &
IB4_12 = 0.00068868 , &
IB4_23 = 0.00013232 , &
IB4_31 = 0.00138278 , &

IB5_11 = 0.00184653 , &
IB5_22 = 0.03535640 , &
IB5_33 = 0.03411186 , &
IB5_12 = -0.00001633 , &
IB5_23 = -0.00000436 , &
IB5_31 = 0.00616587 , &

IB6_11 = 0.00184252 , &
IB6_22 = 0.00184252 , &
IB6_33 = 0.00037910 , &
IB6_12 = 0           , &
IB6_23 = 0           , &
IB6_31 = 0

INERTIA  B1, IB1_11, IB1_22, IB1_33, IB1_12, IB1_23, IB1_31
INERTIA  B2, IB2_11, IB2_22, IB2_33, IB2_12, IB2_23, IB2_31
INERTIA  B3, IB3_11, IB3_22, IB3_33, IB3_12, IB3_23, IB3_31
INERTIA  B4, IB4_11, IB4_22, IB4_33, IB4_12, IB4_23, IB4_31
INERTIA  B5, IB5_11, IB5_22, IB5_33, IB5_12, IB5_23, IB5_31
INERTIA  B6, IB6_11, IB6_22, IB6_33, IB6_12, IB6_23, IB6_31
%-----
%Rotation between the coordinate systems starting at newtonian
SIMPROT( N , B1, 3, Q1)

```

```

SIMPROT( B1, B2, 3, Q2)
SIMPROT( B2, B3, 3, Q3)
SIMPROT( B3, B3H, 1, -PI/2) % B3H's origin is located in B3's origin
SIMPROT( B3H, B4, 3, Q4)
SIMPROT( B4, B4H, 1, PI/2) % B4H's origin is located in B4's origin
SIMPROT( B4H, B5, 3, Q5)
SIMPROT( B5, B6, 3, Q6)
SIMPROT( B6, GREIF, 2, PI/2) % GREIF is end-effector
                                % with steady rotation from B

%-----
%Position vectors from origins "n-1" to "n"
%CAUTION: the index of the bodydeclaration Bi has an offset of +1 with
%respect to the origin declaration Si
P_0_S0> = L_0*N3>
P_S0_S1> = L_B1X*B11> + L_B1Y*B12> + L_B1Z*B13>
P_S1_S2> = L_B2X*B21> + L_B2Y*B22> + L_B2Z*B23>
P_S2_S2H> = L_B3X *B31> + L_B3Y*B32> + L_B3Z*B33>
P_S2H_S3> = 0*B3H1> + 0> + 0*B3H3>
P_S3_S3H> = L_B4X*B41> + L_B4Y*B42> + L_B4Z*B43>
P_S3H_S4> = 0*B4H1> + 0*B4H2> + 0*B4H3>
P_S4_S5> = L_B5X*B51> + L_B5Y*B52> + L_B5Z*B53>
P_S5_SGREIF> = L_B6X*B61> + L_B6Y*B62> + L_B6Z*B63>

%-----
%Position vectors from origin "n-1" to center of mass of "n"
P_S0_B10> = COM_B1X * B11> + COM_B1Y * B12> + COM_B1Z * B13>
P_S1_B20> = COM_B2X * B21> + COM_B2Y * B22> + COM_B2Z * B23>
P_S2_B30> = COM_B3X * B31> + COM_B3Y * B32> + COM_B3Z * B33>
P_S3_B40> = COM_B4X * B41> + COM_B4Y * B42> + COM_B4Z * B43>
P_S4_B50> = COM_B5X * B51> + COM_B5Y * B52> + COM_B5Z * B53>
P_S5_B60> = COM_B6X * B61> + COM_B6Y * B62> + COM_B6Z * B63>

```

A.2.3 ViSHaRD10

```

% Problem: ViSHaRD10
%-----
% Newtonian, bodies, frames, points
NEWTONIAN      N
BODIES         B1, B2, B3, B4, B5, B6, B7, B8, B9, B10, BKMS,BEE
FRAMES         B5H, B5HH, B8H, B9H, B9HH
POINTS         0, S0, S1, S2, S3, S4, S5, S5H, S5HH, S6, S7, S8, S9, S10, SKMS, SEE
%-----
%Link lengths [m] (lengths from joint to joint)
CONSTANTS L_0  = 0.1845   %distance from N to S0. (only z-direction)

CONSTANTS L_B1X = 0.250   %distance from S0 to S1 in x-direction ...
CONSTANTS L_B1Y = 0.0
CONSTANTS L_B1Z = 0.09975

CONSTANTS L_B2X = 0.250
CONSTANTS L_B2Y = 0.0
CONSTANTS L_B2Z = 0.09525

CONSTANTS L_B3X = 0.250
CONSTANTS L_B3Y = 0.0
CONSTANTS L_B3Z = 0.0945

CONSTANTS L_B4X = 0.250
CONSTANTS L_B4Y = 0.0
CONSTANTS L_B4Z = 0.1

CONSTANTS L_B5X = 0.340
CONSTANTS L_B5Y = 0.0
CONSTANTS L_B5Z = 0.7015

CONSTANTS L_B6X = 0.2122
CONSTANTS L_B6Y = 0.0
CONSTANTS L_B6Z = -0.022

CONSTANTS L_B7X = 0.2121
CONSTANTS L_B7Y = 0.0
CONSTANTS L_B7Z = -0.120

CONSTANTS L_B8X = 0.105
CONSTANTS L_B8Y = 0.0
CONSTANTS L_B8Z = -0.198

CONSTANTS L_B9X = 0.0969
CONSTANTS L_B9Y = 0.0

```

CONSTANTS L_B9Z =-0.105

CONSTANTS L_B10X= 0.0

CONSTANTS L_B10Y= 0.0

CONSTANTS L_B10Z= 0.047 %=KMS-force/torque sensor displacement

CONSTANTS L_BEEZ=0.0499

%-----

% Lengths from joint to center of mass of link

CONSTANTS Off_B1X = 0.05714

CONSTANTS Off_B1Y = 0

CONSTANTS Off_B1Z =0.08871

CONSTANTS Off_B2X = 0.06837

CONSTANTS Off_B2Y = 0

CONSTANTS Off_B2Z =0.08786

CONSTANTS Off_B3X = 0.07276

CONSTANTS Off_B3Y = 0

CONSTANTS Off_B3Z = 0.08586

CONSTANTS Off_B4X = 0.07348

CONSTANTS Off_B4Y = 0

CONSTANTS Off_B4Z =0.09096

CONSTANTS Off_B5X = 0.27521

CONSTANTS Off_B5Y = 0

CONSTANTS Off_B5Z = 0.37121

CONSTANTS Off_B6X = 0.08912

CONSTANTS Off_B6Y = 0

CONSTANTS Off_B6Z =0.0041

CONSTANTS Off_B7X = 0.07289

CONSTANTS Off_B7Y = 0

CONSTANTS Off_B7Z = -0.05604

CONSTANTS Off_B8X = 0.1273

CONSTANTS Off_B8Y = 0

CONSTANTS Off_B8Z =-0.1238

CONSTANTS Off_B9X = 0.11089

CONSTANTS Off_B9Y = 0

CONSTANTS Off_B9Z =-0.07183

CONSTANTS Off_B10X= 0

CONSTANTS Off_B10Y= 0

```
CONSTANTS Off_B10Z= 0.04380

%-----
%Link masses [kg]
CONSTANTS M_B1 =4.164
CONSTANTS M_B2 =3.474
CONSTANTS M_B3 =3.410
CONSTANTS M_B4 =2.888
CONSTANTS M_B5 =6.813
CONSTANTS M_B6 =0.682
CONSTANTS M_B7 =2.413
CONSTANTS M_B8 =1.152
CONSTANTS M_B9 =0.807
CONSTANTS M_B10=0.252
CONSTANTS M_BEE=0.137
CONSTANTS M_BKMS=0

MASS B1=M_B1, B2=M_B2, B3=M_B3, B4=M_B4, B5=M_B5, B6=M_B6, B7=M_B7, &
      B8=M_B8, B9=M_B9, B10=M_B10, BKMS=M_BKMS, BEE=M_BEE

%-----
%Motor und wavegenerator Inertia [kg*m^2]
CONSTANTS J_Wave_HD25 = 0.0000413
CONSTANTS HD25_Ratio = 160

CONSTANTS J_Wave_HD20 = 0.0000193
CONSTANTS HD20_Ratio = 120

CONSTANTS J_Wave_HD17 = 0.0000079
CONSTANTS HD17_Ratio = 100

CONSTANTS J_Wave_HD14 = 0.0000033
CONSTANTS HD14_Ratio = 50

CONSTANTS J_Wave_HD11 = 0.0000012
CONSTANTS HD11_Ratio = 100

CONSTANTS J_Wave_HD8 = 0.0000003
CONSTANTS HD8_Ratio = 100

CONSTANTS J_Rotor_RE40 =0.0000134

CONSTANTS J_Rotor_RE35 =0.00000696

CONSTANTS J_Rotor_Faul =0.0000040

CONSTANTS J_Rotor_REMAX29 =0.00000119
%-----
```

```
%Link inertia [kg * m^2]
CONSTANTS IB1_11 = 0.01737292645
CONSTANTS IB1_22 = 0.05000156183
CONSTANTS IB1_33 = 0.03832693659
CONSTANTS IB1_12 = 0.0
CONSTANTS IB1_23 = 0.0
CONSTANTS IB1_31 = 0.01572751860

CONSTANTS IB2_11 = 0.01205150423
CONSTANTS IB2_22 = 0.04204441670
CONSTANTS IB2_33 = 0.03455088661
CONSTANTS IB2_12 = 0.0
CONSTANTS IB2_23 = 0.0
CONSTANTS IB2_31 = 0.01188636688

CONSTANTS IB3_11 = 0.01122714403
CONSTANTS IB3_22 = 0.04181622042
CONSTANTS IB3_33 = 0.03508785792
CONSTANTS IB3_12 = 0.0
CONSTANTS IB3_23 = 0.0
CONSTANTS IB3_31 = 0.01148814075

CONSTANTS IB4_11 = 0.00877328074
CONSTANTS IB4_22 = 0.03379873722
CONSTANTS IB4_33 = 0.02836356648
CONSTANTS IB4_12 = 0.0
CONSTANTS IB4_23 = 0.0
CONSTANTS IB4_31 = 0.00883761932

CONSTANTS IB5_11 = 0.67185263155
CONSTANTS IB5_22 = 0.89099299671
CONSTANTS IB5_33 = 0.22882562546
CONSTANTS IB5_12 = -0.00023594478
CONSTANTS IB5_23 = -0.00026707941
CONSTANTS IB5_31 = 0.25891018149

CONSTANTS IB6_11 = 0.00054909428
CONSTANTS IB6_22 = 0.00442429241
CONSTANTS IB6_33 = 0.00469399244
CONSTANTS IB6_12 = 0.0
CONSTANTS IB6_23 = 0.0
CONSTANTS IB6_31 = -0.00006236027

CONSTANTS IB7_11 = 0.00329903283
CONSTANTS IB7_22 = 0.02457414879
CONSTANTS IB7_33 = 0.02293033587
CONSTANTS IB7_12 = 0.0
```

```

CONSTANTS IB7_23 = 0.0
CONSTANTS IB7_31 =-0.00222706549

CONSTANTS IB8_11 = 0.00984082811
CONSTANTS IB8_22 = 0.01237086138
CONSTANTS IB8_33 = 0.00292756506
CONSTANTS IB8_12 = 0.0
CONSTANTS IB8_23 = 0.0
CONSTANTS IB8_31 =-0.00342395927

CONSTANTS IB9_11 = 0.00156323252
CONSTANTS IB9_22 = 0.00295963420
CONSTANTS IB9_33 = 0.00166375930
CONSTANTS IB9_12 = 0.00000000006
CONSTANTS IB9_23 =-0.00000000001
CONSTANTS IB9_31 =-0.00095308184

CONSTANTS IB10_11= 0.00047020005
CONSTANTS IB10_22= 0.00047020005
CONSTANTS IB10_33= 0.00015350031
CONSTANTS IB10_12= 0
CONSTANTS IB10_23= 0
CONSTANTS IB10_31= 0

INERTIA      B1,  IB1_11, IB1_22, IB1_33, IB1_12, IB1_23, IB1_31
INERTIA      B2,  IB2_11, IB2_22, IB2_33, IB2_12, IB2_23, IB2_31
INERTIA      B3,  IB3_11, IB3_22, IB3_33, IB3_12, IB3_23, IB3_31
INERTIA      B4,  IB4_11, IB4_22, IB4_33, IB4_12, IB4_23, IB4_31
INERTIA      B5,  IB5_11, IB5_22, IB5_33, IB5_12, IB5_23, IB5_31
INERTIA      B6,  IB6_11, IB6_22, IB6_33, IB6_12, IB6_23, IB6_31
INERTIA      B7,  IB7_11, IB7_22, IB7_33, IB7_12, IB7_23, IB7_31
INERTIA      B8,  IB8_11, IB8_22, IB8_33, IB8_12, IB8_23, IB8_31
INERTIA      B9,  IB9_11, IB9_22, IB9_33, IB9_12, IB9_23, IB9_31
INERTIA      B10, IB10_11,IB10_22,IB10_33,IB10_12,IB10_23,IB10_31
INERTIA      BKMS,0,0,0,0,0,0      %included in B10
INERTIA      BEE,0,0,0,0,0,0      %included in B10

%-----
%Rotation between the coordinate systems starting at newtonian
%CAUTION: The index of the bodydeclaration (Bi) has an offset of +1 with
%respect to the declaration of the origins (Si). Thus, B10 is located at
%point S9 and P_S9_S10 has to be defined in the COS given by the
%declaration of the 10th Body (B10). Since the Mass of the Endeffector
%differs from the mass of B10, two bodies named BKMS and BEE have been
%introduced with the weight of only the endeffector. BKMS's origin is
%located at the origin of B_10, BEE's origin is located at the
%"Kardanpunkt".

```

```

SIMPROT(N , B1 , 3, Q1)
SIMPROT(B1 , B2 , 3, Q2)
SIMPROT(B2 , B3 , 3, Q3)
SIMPROT(B3 , B4 , 3, Q4)
SIMPROT(B4 , B5 , 3, Q5)
SIMPROT(B5 , B5H , 2, PI/2)
SIMPROT(B5H, B5HH, 3, PI)
SIMPROT(B5HH, B6 , 3, Q6)
SIMPROT(B6 , B7 , 3, Q7)
SIMPROT(B7 , B8 , 3, Q8)
SIMPROT(B8 , B8H , 2, PI/2)
SIMPROT(B8H, B9 , 3, Q9)
SIMPROT(B9 , B9H , 2, PI/2)
SIMPROT(B9H, B9HH, 1, PI)
SIMPROT(B9HH, B10 , 3, Q10)
%Sensor COS added
SIMPROT(B10, BKMS, 1, 0)
%EE COS
SIMPROT(BKMS, BEE, 1, 0)
%-----
%Position vectors (from origin "n-1" to origin "n")
P_0_S0> = L_0 * N3>
P_S0_S1> = L_B1x * B11> + L_B1y* B12> + L_B1z * B13>
P_S1_S2> = L_B2x * B21> + L_B2y* B22> + L_B2z * B23>
P_S2_S3> = L_B3x * B31> + L_B3y* B32> + L_B3z * B33>
P_S3_S4> = L_B4x * B41> + L_B4y* B42> + L_B4z * B43>
P_S4_S5> = L_B5x * B51> + L_B5y* B52> + L_B5z * B53>
P_S5_S5H> = 0 * B5H1> + 0 * B5H2> + 0 * B5H3>
P_S5H_S5HH> = 0 * B5HH1> + 0 * B5HH2> + 0 * B5HH3>
P_S5HH_S6> = L_B6x * B61> + L_B6y* B62> + L_B6z * B63>
P_S6_S7> = L_B7x * B71> + L_B7y* B72> + L_B7z * B73>
P_S7_S8> = L_B8x * B81> + L_B8y* B82> + L_B8z * B83>
P_S8_S9> = L_B9x * B91> + L_B9y* B92> + L_B9z * B93>
P_S9_S10> = L_B10x* B101> + L_B10y* B102> + L_B10z* B103>
P_S10_SKMS> = 0*BKMS1> + 0*BKMS1> + 0*BKMS3>
P_SKMS_SEE> = 0*BKMS1> + 0*BKMS1> + L_BEEz*BKMS3>
P_SEE_SKMS> = 0*BEE1> + 0*BEE2> - L_B10z*BEE3>
%-----
% Position vectors from origin "n-1" to center of mass of "n"
P_S0_B1o> = Off_B1x * B11> + Off_B1y * B12> + Off_B1z * B13>
P_S1_B2o> = Off_B2x * B21> + Off_B2y * B22> + Off_B2z * B23>
P_S2_B3o> = Off_B3x * B31> + Off_B3y * B32> + Off_B3z * B33>
P_S3_B4o> = Off_B4x * B41> + Off_B4y * B42> + Off_B4z * B43>
P_S4_B5o> = Off_B5x * B51> + Off_B5y * B52> + Off_B5z * B53>
P_S5_B6o> = Off_B6x * B61> + Off_B6y * B62> + Off_B6z * B63>
P_S6_B7o> = Off_B7x * B71> + Off_B7y * B72> + Off_B7z * B73>
P_S7_B8o> = Off_B8x * B81> + Off_B8y * B82> + Off_B8z * B83>

```

```
P_S8_B9o> = Off_B9x * B91> + Off_B9y * B92> + Off_B9z * B93>
P_S9_B10o> = Off_B10x* B101> + Off_B10y* B102> + Off_B10z* B103>
% Positions vector from Point SKMS to COG of the EE
P_SKMS_BKMSo> = Off_B10x* BKMS1> + Off_B10y* BKMS2> + Off_B10z* BKMS3>
% Positions vector from Point SEE to COG of the EE
P_SEE_BEEo> = 0*BKMS1> + 0*BKMS2> -(L_B10Z-Off_B10z)*BEE3>
```

B Tracking Performance of Operational Space Position Control Algorithms

The inner motion control loop of admittance control schemes can be accomplished with various different control algorithms. In this chapter hardware experiments with the VISHARD3 device for the comparison of the tracking performance of resolved acceleration, inverse Jacobian, and transposed Jacobian position control, see section 3.2.2, are described.

As VISHARD3 is a highly nonlinear and coupled system the accuracy of the approximated inverse dynamic model that is incorporated in the inverse Jacobian, and transposed Jacobian control law is strongly related to the manipulator configuration and velocity. Therefore, comparative performance results are highly dependent on the selection of the commanded end-effector trajectory.

In the following the results for a trajectory with strong coupling and gyroscopic effects are given. The end-effector has been commanded to follow a linear path in the x -direction as illustrated in figure B.1 while the y and z position is held constant with $y = 0.3$ m and $z = 0.215$ m (x , y , and z are respective the coordinate system {B} shown in figure 2.3). Traversing the neighborhood of a singular position the variation of the device mass matrix \mathbf{M}_x is comparatively high along this trajectory. This can be seen in figure B.2 presenting a decomposition of the required end-effector forces into inertial, gyroscopic¹, and friction together with gravitational components when moving the device along the reference trajectory assuming that no motor torque is applied; in the acceleration phase with -10 m/s² much less inertial force $f_{x,\text{inert}}$ is required than in the deceleration phase with 10 m/s². Please note, that this is not true for the diagonal elements of the inertia matrix \mathbf{M}_q varying only slightly along this trajectory. Figure B.2 also reveals coupling terms of the mass matrix; despite the end effector acceleration is zero in the y - and z -direction $f_{y,\text{inert}}$ and $f_{z,\text{inert}}$ are comparatively high. In the phase of constant end-effector velocity gyroscopic forces are dominating. The large deviation of the profile of the τ_2 and τ_3 trajectory, which is a mapping of the force trajectory into the joint space, when compared to the \ddot{q}_2 and \ddot{q}_3 profile points to coupling terms in \mathbf{M}_q . Especially during the end-effector deceleration phase τ_2 is dominated by inertial coupling torque.

For comparison the resolved acceleration, inverse Jacobian, and transposed Jacobian control algorithm has been tested along this trajectory with and without acceleration feedforward. The controller gain matrices in equation 3.7 have been set to $\mathbf{K}_P = k_P \mathbf{I}$ and $\mathbf{K}_D = 2\sqrt{k_P} \mathbf{I}$ with $k_P = 10\,000$ aiming at a critically damped position control with 100 rad/s bandwidth. The approximate inertia and mass matrix of equation 3.11 and 3.13 has been set to $\widehat{\mathbf{M}}_q = \text{diag}(0.930, 0.416, 0.279)$ kg m² and $\widehat{\mathbf{M}}_x = \text{diag}(6.813, 9.350, 4.812)$ kg which are the mean values of the diagonal elements of \mathbf{M}_q and \mathbf{M}_x in the workspace of the haptic device. In all experiment the sampling rate was 2 kHz.

¹ $\mathbf{J}^{-T}[\mathbf{C} - \mathbf{M}_q \mathbf{J}^{-1} \dot{\mathbf{J}}] \dot{\mathbf{q}}$

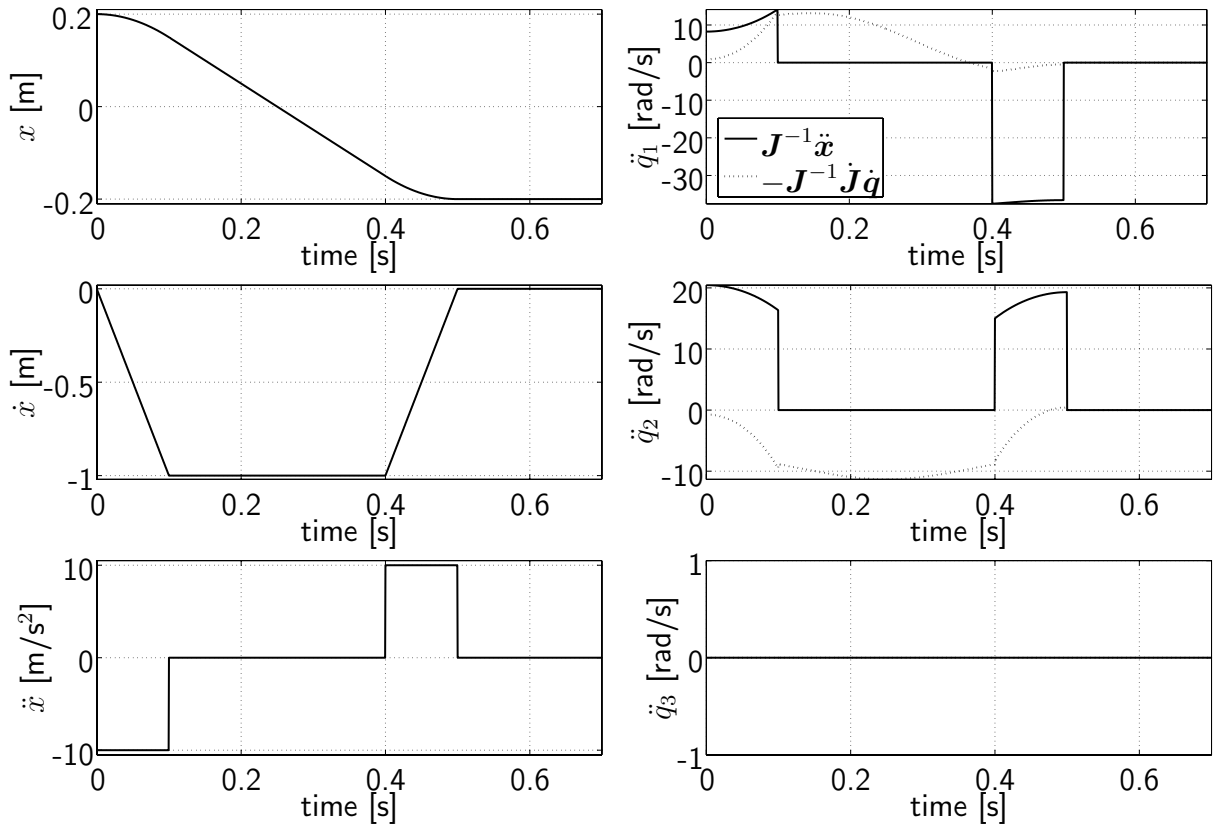


Figure B.1: Commanded end-effector trajectory and corresponding accelerations in the joint space

The results of the position control experiments are shown in figure B.3. One can clearly see that resolved acceleration control outperforms the other algorithms. The results also reveal the significant benefit of acceleration feedforward; the tracking errors in x -position are almost halved during the acceleration and deceleration phase when using acceleration feedforward. The decreased performance of transposed Jacobian control when compared to inverse Jacobian control is due to the fact that \mathbf{M}_x is stronger coupled than \mathbf{M}_q and varies heavily along the trajectory. Thus, the approximation with a constant diagonal matrix is less accurate. The increased y -position tracking error during the deceleration phase in case of inverse Jacobian control clearly indicates a connection between control performance and the accuracy of the approximated dynamic model; in this phase large inertial coupling torques in joint 2 are neglected in the inverse Jacobian control law.

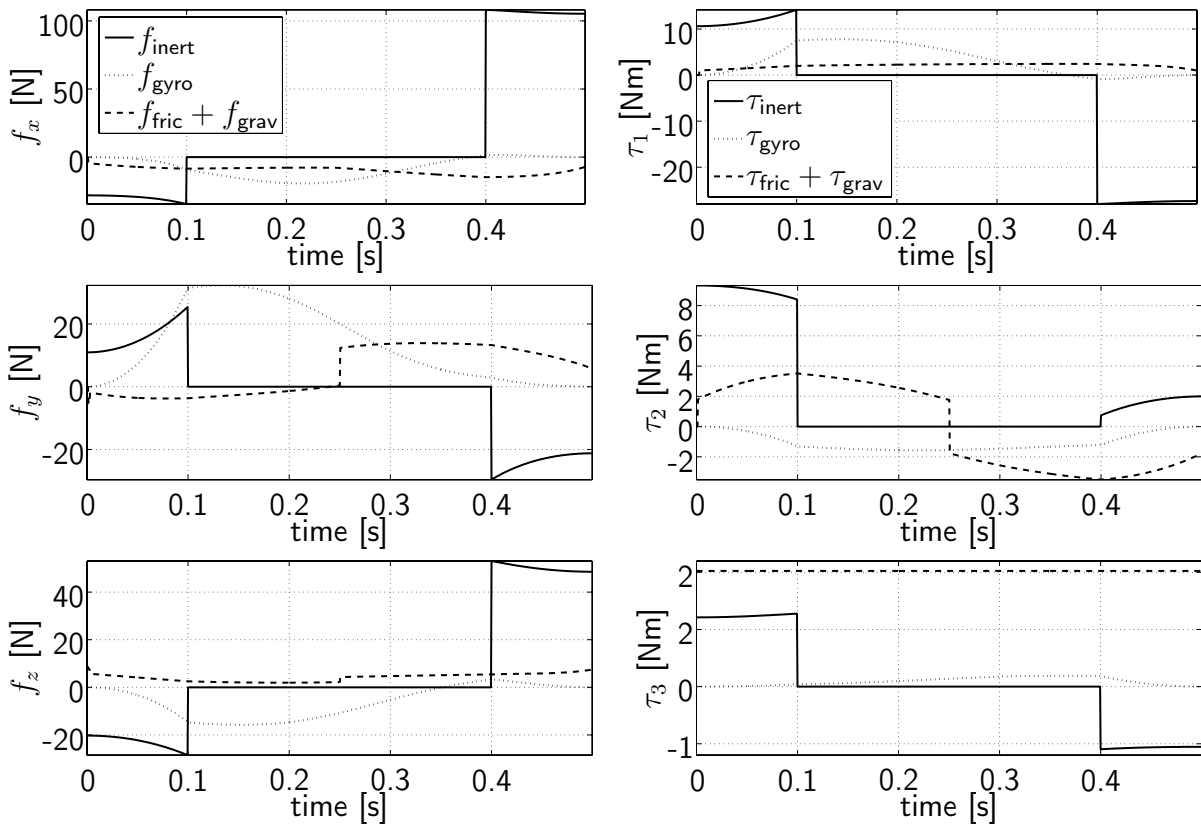


Figure B.2: Force/torque components due to inertial, gyroscopic, frictional, and gravitational effects

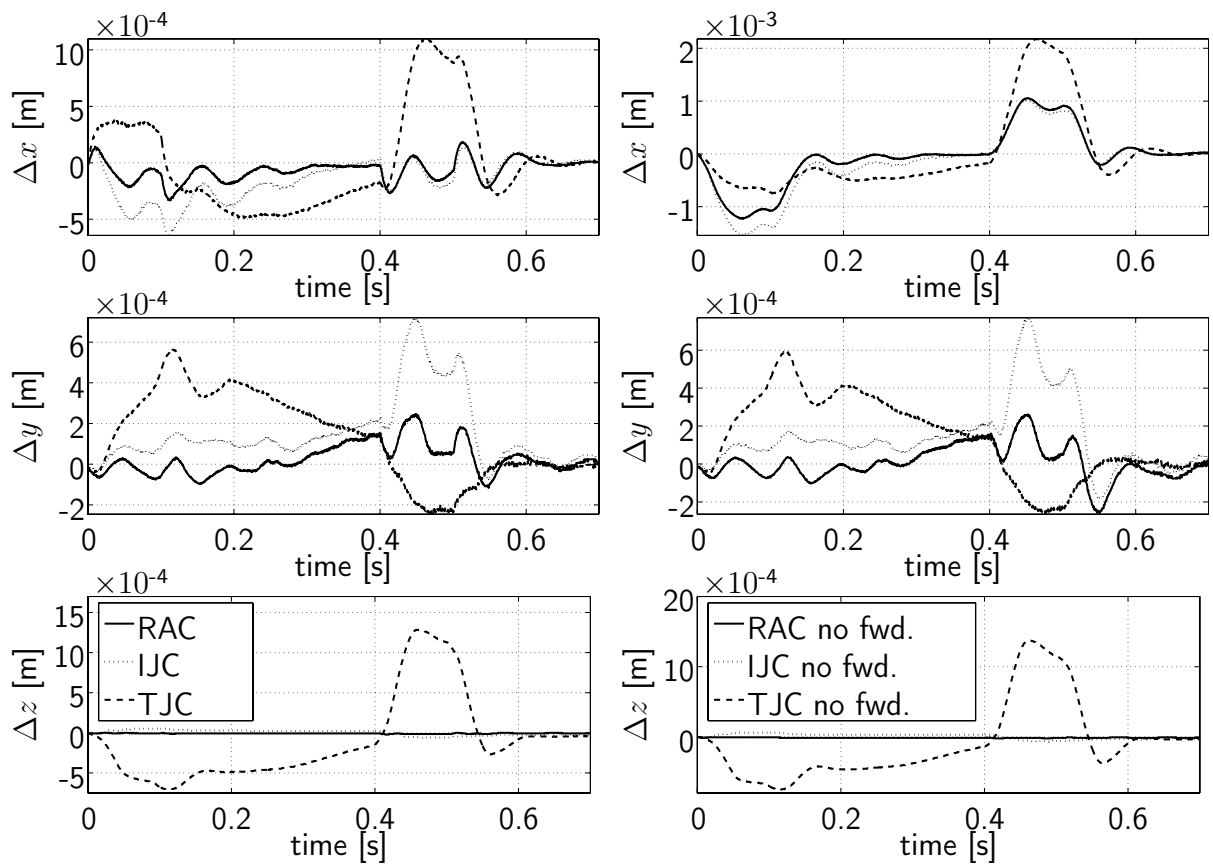


Figure B.3: Position tracking errors; left: control with acceleration feedforward; right: control without acceleration feedforward

C Output Performance Analysis

In this chapter a method to analyze the output capability of a haptic interface by means of force/moment, linear/angular velocity, or acceleration is proposed. Unlike commonly used techniques based on the manipulability ellipsoid (see e. g. [Yos91] and [HK00]), it addresses the problem of determining at a given working point the direction of manipulation in which the performance (maximum output) of the device is worst. Methods based on the manipulability ellipsoid usually focus on the evaluation of the input-output transmission of the device, which can be considered as the relation between the L_2 norm of the input vector the actuators produce and the corresponding L_2 norm of the output vector. With these methods the direction of manipulation in which the input-output transmission at a given working point is minimal can be determined. However, the calculation of the direction which minimizes the norm of the output vector (and thus the performance of the device) is not possible. This is because the absolutes of the elements of the input vector are limited corresponding to the specifications of the actuators and consequently the maximum norm of the input vector is dependent on the direction of manipulation. Hence, the technique described in the following is not based on the concept of the manipulability ellipsoid.

The relation between the input and output vector of the manipulator is given by the following equations:

$$\begin{pmatrix} \dot{\mathbf{x}} \\ \boldsymbol{\omega} \end{pmatrix} = \mathbf{J}\dot{\boldsymbol{\theta}} \quad (\text{C.1})$$

$$\begin{pmatrix} \mathbf{f}_{\text{trans}} \\ \mathbf{f}_{\text{rot}} \end{pmatrix} = (\mathbf{J}^{-1})^T \boldsymbol{\tau}; \quad \dot{\boldsymbol{\theta}} = \mathbf{0} \quad (\text{C.2})$$

$$\begin{pmatrix} \ddot{\mathbf{x}} \\ \dot{\boldsymbol{\omega}} \end{pmatrix} = \mathbf{J}\mathbf{M}^{-1}\boldsymbol{\tau}; \quad \dot{\boldsymbol{\theta}}, \mathbf{f}_{\text{trans}}, \mathbf{f}_{\text{rot}} = \mathbf{0} \quad (\text{C.3})$$

where \mathbf{J} is the Jacobian matrix, which maps the joint (actuator) velocities $\dot{\boldsymbol{\theta}}$ to the linear velocity $\dot{\mathbf{x}}$ and the angular velocity $\boldsymbol{\omega}$ of the end effector. Equation (C.2) and (C.3) assume that the resulting force/ torque caused by gravity and friction is comparatively small and thus can be neglected. Equation (C.2) gives the relation between the input moments $\boldsymbol{\tau}$ generated by the actuators and the resultant forces $\mathbf{f}_{\text{trans}}$ and moments \mathbf{f}_{rot} at the end-effector, assuming the system is in a static state (i. e. the velocity of all joints is zero). Equation (C.3) maps the input moments to the linear and angular acceleration of the end effector provided that no external forces $\mathbf{f}_{\text{trans}}$ and moments \mathbf{f}_{rot} are exerted to the system; $\mathbf{M}_q(\boldsymbol{\theta})$ denotes the inertia matrix.

As the analyzes of these three outputs proceed in an identical way only one representative is outlined. In the following, (C.1) to (C.3) are represented by

$$\begin{pmatrix} \mathbf{q}_{\text{trans}} \\ \mathbf{q}_{\text{rot}} \end{pmatrix} = \begin{bmatrix} \widehat{\mathbf{J}}_{\text{trans}} \\ \widehat{\mathbf{J}}_{\text{rot}} \end{bmatrix} \mathbf{p}, \quad (\text{C.4})$$

where $\widehat{\mathbf{J}}_t, \widehat{\mathbf{J}}_r \in \mathbb{R}^{3 \times 6}$ are the submatrices of $\widehat{\mathbf{J}}$ mapping the input vector \mathbf{p} generated by the actuators to the translational and rotational output vectors $\mathbf{q}_{\text{trans}}$ and \mathbf{q}_{rot} , the subvectors of the output vector \mathbf{q} . The objective of the proposed method to find the direction of manipulation in which the performance of the haptic device is worst, can be written as the following minimax optimization problem:

$$\min_{\mathbf{d}} \max_{\alpha > 0} \|\widehat{\mathbf{J}}\alpha\mathbf{d}\| \quad \text{such that } \alpha\mathbf{d} \in [\mathbf{p}_{\min}, \mathbf{p}_{\max}] \quad (\text{C.5})$$

where $\|\cdot\|$ is the L_2 norm and \mathbf{p}_{\min} and \mathbf{p}_{\max} the vectors with the minimal and maximal input the actuators can provide. The vector \mathbf{d} can be interpreted as the direction of the input vector \mathbf{p} with the scalar α adjusting its length. Since obviously α is to be chosen as large as possible, the solution $\alpha\mathbf{d}$ must be on the boundary of the rectangular search space restricted by \mathbf{p}_{\min} and \mathbf{p}_{\max} . Consequently, the minimax problem can be converted into six linear least squares problems, each probing one of the six hyperplanes forming the boundary of the search space, where the final solution is the minimum solution of these least squares problems. Defining $\widehat{\mathbf{J}}_i$ as the submatrix of $\widehat{\mathbf{J}}$ obtained by deleting the i -th column $\hat{\mathbf{j}}_i$, \mathbf{p}_i as the subvector of \mathbf{p} obtained by deleting the i -th element, and \bar{p}_i as either $p_{\min,i}$ or $p_{\max,i}$ deciding for the value with the lower absolute, one gets

$$\min_i \left\{ \min_{\mathbf{p}_i} \mathbf{F}_i^T \mathbf{F}_i \right\} \quad (\text{C.6})$$

$$\mathbf{F}_i = \widehat{\mathbf{J}}_i \mathbf{p}_i + \hat{\mathbf{j}}_i \bar{p}_i. \quad (\text{C.7})$$

The introduction of additional constraints is straightforward. To search for instance for a solution satisfying the equation $\mathbf{q}_{\text{rot}} = 0$ in order to evaluate the translational output the device can exert without generating rotational output, one obtains

$$\min_i \left\{ \min_{\mathbf{p}_i} \mathbf{F}_i^T \mathbf{F}_i \right\} \quad \text{such that } \widehat{\mathbf{J}}_{\text{rot},i} \mathbf{p}_i + \hat{\mathbf{j}}_{\text{rot},i} \bar{p}_i = \mathbf{0}. \quad (\text{C.8})$$

The resulting linear least squares problems with linear equality constraints can be solved efficiently by standard algorithms, see for example [LH74].

Bibliography

- [ABFB00] C.A. Avizzano, F. Barbagli, A. Frisoli, and M. Bergamasco. The hand force feedback: analysis and control of a haptic device for the human hand. In *IEEE International Conference on Systems, Man, and Cybernetics*, pages 989–994, 2000.
- [ABLS04] F. Al-Bender, V. Lampaert, and J. Swevers. Modeling of dry sliding friction dynamics: from heuristic models to physically motivated models and back. *CHAOS*, 14(2):446–460, 2004.
- [AH87] C.H. An and J.M. Hollerbach. Dynamic stability issues in force control of manipulators. In *Proceedings of the IEEE International Conference on Robotics & Automation*, pages 890–896, 1987.
- [AH91] B. Armstrong-Hélouvry. *Control of Machines with Friction*. The Kluwer International Series in Engineering and Computer Science. Robotics. Kluwer Academic Publishers, 1991.
- [AH94] B. Armstrong-Hélouvry. Dynamic friction in the control of robots. In *Proceedings of the IEEE International Conference on Robotics & Automation*, pages 1202–1207, 1994.
- [AH02] R.J. Adams and B. Hannaford. Control law design for haptic interfaces to virtual reality. *IEEE Transactions on Control Systems Technology*, 10(1):3–13, 2002.
- [AHDC94] B. Armstrong-Hélouvry, P. Dupont, and C. Canudas de Wit. A survey of models, analysis tools and compensation methods for the control of machines with friction. *Automatica*, 30(7):1083–1138, 1994.
- [Aki02] D. Akin. Sensational devices. *The Globe and Mail, Newspaper*, January 19, 2002.
- [AMH99] R.J. Adams, M. Moreyra, and B. Hannaford. Excalibur - a three axis force display. In *Proceedings ASME International Mechanical Engineering Congress and Exhibition*, 1999.
- [AS02] Albu-Schäffer. *Regelung von Robotern mit elastischen Gelenken am Beispiel der DLR-Leichtbauarme*. PhD thesis, Lehrstuhl für Steuerungs- und Regelungstechnik, Technische Universität München, 2002.
- [ASKH02] N. Ando, P.T. Szemes, P. Korondi, and H. Hashimoto. Friction compensation for a 6DOF cartesian coordinate haptic interface. In *Proceedings of the IEEE/RSJ International Conference on Intelligent Robots and Systems*, pages 2893–2898. 2002.

- [BAB⁺94] M. Bergamasco, B. Allotta, L. Bosio, L. Ferreti, G. Parrini, G.M. Prisco, F. Salsedo, and G. Sartini. An arm exoskeleton system for teleoperation and virtual environments applications. In *Proceedings of the IEEE International Conference on Robotics & Automation*, pages 1449–1454, 1994.
- [Bai85] J. Baillieul. Kinematic programming alternatives for redundant manipulators. In *Proceedings of the IEEE International Conference on Robotics & Automation*, pages 722–728, 1985.
- [BBPB02] M. Bouzit, G. Burdea, G. Popescu, and R. Boian. The Rutgers master II-new design force-feedback glove. *IEEE/ASME Transactions on Mechatronics*, 7(2):256–263, 2002.
- [BDHN93] B. Boulet, L. Daneshmend, V. Hayward, and C. Nemri. System identification and modelling of a high performance hydraulic actuator. In R. Chatila and G. Hirzinger, editors, *Experimental Robotics II*, volume 190 of *Lecture Notes in Control and Information Science*. Springer, 1993.
- [BDS95] D. Ben-Dov and S.E. Salcudean. A force-controlled pneumatic actuator. *IEEE Transactions on Robotics and Automation*, 11(6):906–911, 1995.
- [BH97] P. Berkelman and R.L. Hollis. Dynamic performance of a hemispherical magnetic levitation haptic interface device. In *SPIE International Symposium on Intelligent Systems and Intelligent Manufacturing, SPIE Proceedings*, volume 3602, 1997.
- [BI05] B. Bona and M. Indri. Friction compensation in robotics: an overview. In *Proceedings of the IEEE Conference on Decision and Control, and the European Control Conference*, pages 4360–4367, 2005.
- [BK00] H. Bruyninckx and O. Khatib. Gauss’ principle and the dynamics of redundant and constrained manipulators. In *Proceedings of the IEEE International Conference on Robotics & Automation*, pages 2563–2568, 2000.
- [BLP05] N.L. Bernstein, D.A. Lawrence, and L.Y. Pao. Friction modeling and compensation for haptic interfaces. In *Proceedings of the First Joint Eurohaptics Conference and Symposium on Haptic Interfaces for Virtual Environment and Teleoperator Systems*, pages 290–295, 2005.
- [BLTW04] D. Bi, Y.F. Li, S.K. Tso, and G.L. Wang. Friction modeling and compensation for haptic display based on support vector machine. *IEEE Transactions on Industrial Electronics*, 51(2):491–500, 2004.
- [BOYBK90] F. Brooks, M. Ouh-Young, J.J. Batter, and P.J. Kilpatrick. Project GROPE - haptic displays for scientific visualization. *Computer Graphics*, 24(4):177–185, 1990.
- [BP82] L.C. Bo and D. Pavelescu. The friction-speed relation and its influence on the critical velocity of the stick-slip motion. *Wear*, 82(3):277–289, 1982.

- [BRB99] A. Benali, P. Richard, and P. Bidaud. Design control and evaluation of a six dof force feedback interface for virtual reality applications. In *Proceedings of the IEEE International Workshop on Robot and Human Interaction*, pages 338–343, 1999.
- [Bro90] T.L. Brooks. Telerobotic response requirements. In *Proceedings of the IEEE Conference on Systems, Man and Cybernetics*, pages 113–120, 1990.
- [BS95] G.L. Beauregard and M.A. Srinivasan. The manual resolution of viscosity and mass. In *Proceedings of the ASME Dynamic Systems and Control Division, DSC-42*, pages 657–662, 1995.
- [BS02] S.J. Biggs and M.A. Srinivasan. Haptic interfaces. In K.M. Stanney, editor, *Handbook of Virtual Environments: Design, Implementation, and Applications*, chapter 5, pages 93–115. Lawrence Erlbaum Associates, 2002.
- [BSM02] P. Buttolo, P. Steward, and A. Marsan. A haptic hybrid controller for virtual prototyping of vehicle mechanisms. In *Proceedings of the 10th Symposium on Haptic Interfaces for Virtual Environments & Teleoperator Systems*, pages 249–254, 2002.
- [BT04] A Bicchi and G. Tonietti. Fast and ‘soft-arm’ tactics: dealing with the safety-performance tradeoff in robot arms design and control. *IEEE Robotics and & Automation Magazine*, 11(2):22–33, 2004.
- [Bur96] G. Burdea. *Force and Touch Feedback for Virtual Reality*. John Wiley & Sons, 1996.
- [BW88] D.R. Baker and C.W. Wampler. On the inverse kinematics of redundant manipulators. *The International Journal of Robotics Research*, 7(2):3–21, 1988.
- [CB94] J.E. Colgate and J.M. Brown. Factors affecting the Z-width of a haptic display. In *Proceedings of the IEEE International Conference on Robotics & Automation*, pages 3205–3210, 1994.
- [CC00] C.R. Carignan and K.R. Cleary. Closed-loop force control for haptic simulation of virtual environments. *Haptics-e*, 1(2), 2000.
- [CD95] T.F. Chan and R.V. Dubey. A weighted least-norm solution based scheme for avoiding joint limits for redundant joint manipulators. *IEEE Transactions on Robotics and Automation*, 11(2):286–292, 1995.
- [ÇFT02] M.C. Çavuşoğlu, D. Feygin, and F. Tendick. A critical study of the mechanical and electrical properties of the PHANToM haptic interface and improvements for high performance control. *Presence*, 11(6):555–568, 2002.
- [CL97] C. Canudas de Wit and P. Lischinsky. Adaptive friction compensation with partially known dynamic friction model. *International Journal of Adaptive Control and Signal Processing*, 11(1):65–80, 1997.

- [Cla91] R. Clavel. *Conception d'un robot parallèle rapide à 4 degrés de liberté*. PhD thesis, École Polytechnique Fédérale de Lausanne, 1991.
- [CLTM97] C.L. Clover, G.R. Luecke, J.J. Troy, and W.A. McNeely. Dynamic simulation of virtual mechanisms with haptic feedback using industrial robotics equipment. In *Proceedings of the IEEE International Conference on Robotics & Automation*, pages 724–730, 1997.
- [CNA⁺89] C. Canudas de Wit, P. Noel, A. Aubin, B. Brogliato, and P. Drevet. Adaptive friction compensation in robot manipulators: low-velocities. In *Proceedings of the IEEE International Conference on Robotics & Automation*, pages 1352–1357, 1989.
- [CNSV99] F. Caccavale, C. Natale, B. Siciliano, and L. Villani. Six-DOF impedance control based on angle/axis representations. *IEEE Transactions on Robotics and Automation*, 15(2):289–300, 1999.
- [CO^rL95] C. Canudas de Wit, H. Olsson, K.J. Åström, and P. Lischinsky. A new model for control of systems with friction. *IEEE Transactions on Automatic Control*, 40(3):419–425, 1995.
- [CPE57] J. Courtney-Pratt and E. Eisner. The effect of tangential force on the contact of metallic bodies. In *Proceedings of the Royal Society*, volume A238, pages 529–550, 1957.
- [CS94] C.R. Carignan and J.A. Smith. Manipulator impedance accuracy in position-based impedance control implementations. In *Proceedings of the IEEE International Conference on Robotics & Automation*, pages 1216–1221, 1994.
- [CSK04] S. Chatterjee, T.K. Singha, and S.K. Karmakar. Effect of high-frequency excitation on a class of mechanical systems with dynamic friction. *Journal of Sound and Vibration*, 269(1-2):61–89, 2004.
- [CSV99] S. Chiaverini, B. Siciliano, and L. Villani. A survey of robot interaction control schemes with experimental comparison. *IEEE/ASME Transactions on Mechatronics*, 4(3):273–285, 1999.
- [Cut93] P. Cutt. Tactile displays: adding the sense of touch to virtual environments. In *Proceedings of Virtual Reality Systems'93 Conference*, pages 120–122, 1993.
- [CWH05] G. Campion, Q. Wang, and V. Hayward. The panograph Mk-II: a haptic instrument. In *Proceedings of the IEEE/RSJ International Conference on Intelligent Robots and Systems*, pages 723–728, 2005.
- [Dah68] P. Dahl. A solid friction model. Technical Report TOR-158(3107-18), The Aerospace Corporation, El Segundo, California, 1968.
- [DGG03] R. Dhaouadi, F.H. Ghorbel, and P.S. Gandhi. A new dynamic model of hysteresis in harmonic drives. *IEEE Transactions on Industrial Electronics*, 50(6):1165–1171, 2003.

- [DHA00] P. Dupont, V. Hayward, and B. Armstrong. Elasto-plastic friction model: contact compliance and stiction. In *Proceedings of the American Control Conference*, pages 1072–1077, 2000.
- [Dha03] R. Dhaouadi. Nonlinear friction compensation in harmonic drives with hysteresis. In *Proceedings of the IEEE/ASME International Conference on Advanced Intelligent Mechatronics*, pages 278–283, 2003.
- [DLR94] C. Dede, R.B. Loftin, and J.W. Regian. The design of artificial realities to improve learning Newtonian mechanics. In *Proc. of the East-West International Conference on Multimedia, Hypermedia, and Virtual Reality*, Moscow, Russia, 1994.
- [DMH99] F.B.M. Duarte, J.A.T Machado, and L. Horváth. A trajectory planning algorithm for redundant manipulators. In *Proceedings of the IEEE International Symposium on Industrial Electronics*, pages 1002–1007, 1999.
- [DNB⁺05] N. Diolaiti, G. Niemeyer, F. Barbagli, J.K. Salisbury, and C. Melchiorri. The effect of quantization and Coulomb friction on the stability of haptic rendering. In *Proceedings of the First Joint Eurohaptics Conference and Symposium on Haptic Interfaces for Virtual Environment and Teleoperator Systems*, pages 237–246, 2005.
- [Dup90] P.E. Dupont. Friction modeling in dynamic robot simulation. In *Proceedings of the IEEE International Conference on Robotics & Automation*, pages 1370–1376, 1990.
- [EDS90] P. Elosegui, R.W. Daniel, and P.M. Sharkey. Joint servoing for robust manipulator force control. In *Proceedings of the IEEE International Conference on Robotics & Automation*, pages 246–251, 1990.
- [EIL96] R.E. Ellis, O.M. Ismaeil, and M.G. Lipsett. Design and evaluation of a high-performance haptic interface. *Robotica*, 14:321–327, 1996.
- [Elo91] P. Elosegui. *Analysis of the Compliant Motion Achievable with an Industrial Robot: Identification, Feedback, and Design*. PhD thesis, Department of Engineering Science, University of Oxford, 1991.
- [Elo93] P. Elosegui. A study of force control transfer functions identified on a PUMA 560 arm. In *Proceedings of the IEEE/RSJ International Conference on Intelligent Robots and Systems*, pages 1545–1552, 1993.
- [Epp88] S.D. Eppinger. *Modelling Robot Dynamic Performance for Endpoint Force Control*. PhD thesis, Artificial Intelligence Laboratory, Massachusetts Institute of Technology, 1988. Also available as Massachusetts Institute of Technology, Artificial Intelligence Laboratory Technical Report No. AITR-1072.
- [Ern02] M. Ernst. Entwurf und Simulation eines haptischen Displays mit sechs Freiheitsgraden. Studienarbeit, Fachgebiet für Regelungssysteme, Technische Universität Berlin, 2002.

- [Ern03] M. Ernst. Entwurf und Implementierung von Regelungsverfahren für das haptische Display ViSHARD 6. Diplomarbeit, Fachgebiet für Regelungssysteme, Technische Universität Berlin, 2003.
- [EYB04] H. Esen, K. Yano, and M. Buss. A virtual environment medical training system for bone drilling with 3 DOF force feedback. In *Proceedings of the IEEE/RSJ International Conference on Intelligent Robots and Systems*, pages 3631–3636, 2004.
- [EYB06] H. Esen, K. Yano, and M. Buss. Interaction with virtual deformable objects for surgery simulation using a hyper redundant haptic display. In *Eurohaptics'06*, pages 519–522, 2006.
- [EYB07] H. Esen, K. Yano, and M. Buss. Training strategies allowing haptic interaction in multi-user virtual environments. In *Proceedings of the IEEE International Conference on Robotics & Automation*, 2007. in review.
- [FB03] A. Frisoli and M. Bergamasco. Experimental identification and evaluation of performance of a 2dof haptic display. In *Proceedings of the IEEE International Conference on Robotics & Automation*, pages 3260–3265, 2003.
- [FBLG96] L. Fabiani, G. Burdea, N. Langrana, and D. Gomez. Human interface using the Rutgers Master II force feedback interface. In *Proceedings of the IEEE Virtual Reality Annual International Symposium*, pages 54–59, 1996.
- [FEB06] M. Fritschi, M.O. Ernst, and M. Buss. Integration of kinesthetic and tactile display - modular design concept. In *Eurohaptics'06*, pages 607–612, 2006.
- [FK97] R. Featherstone and O. Khatib. Load independence of the dynamically consistent inverse of the Jacobian matrix. *The International Journal of Robotics Research*, 16(2):168–170, 1997.
- [FM00] B.F. Feeny and F.C. Moon. Quenching stick-slip chaos with dither. *Journal of Sound and Vibration*, 237(1):173–180, 2000.
- [Fri02] M. Fritschi. Aufbau eines Trainingssimulators für die digitale rektale Untersuchung von Prostatakarzinomen. Diplomarbeit, Institut für Flugmechanik und Flugregelung, Universität Stuttgart, 2002. Prepared at: Fachgebiet für Regelungssysteme, Technische Universität Berlin.
- [FRM⁺05] A. Frisoli, F. Rocchi, S. Marcheschi, A. Dettori, F. Salsedo, and M. Bergamasco. A new force-feedback arm exoskeleton for haptic interaction in virtual environments. In *Proceedings of the First Joint Eurohaptics Conference and Symposium on Haptic Interfaces for Virtual Environment and Teleoperator Systems*, pages 195–201, 2005.
- [GBB99] M.J. Girone, G.C. Burdea, and M. Bouzit. The "Rutgers ankle" orthopedic rehabilitation interface. In *Proceedings of the ASME Haptics Symposium*, volume 67, pages 305–312, 1999.

- [GGB05] F. Gosselin, C. Bidard, and J. Brisset. Design of a high fidelity haptic device for telesurgery. In *Proceedings of the IEEE International Conference on Robotics & Automation*, pages 206–211, 2005.
- [GCH⁺01] S. Grange, F. Conti, P. Helmer, P. Rouiller, and C. Baur. The Delta Haptic Device as a nanomanipulator. In *Microrobotics and Microassembly III*, volume 4568 of *Proceedings of SPIE*, pages 100–111, Boston, MA, 2001.
- [GCR⁺01] S. Grange, F. Conti, P. Rouiller, P. Helmer, and C. Baur. Overview of the Delta Haptic Device. In *Eurohaptics'01*, 2001.
- [GGD02] P.S. Gandhi, F.H. Ghorbel, and J. Dabney. Modeling, identification, and compensation of friction in harmonic drives. In *Proceedings of the 41st IEEE Conference on Decision and Control*, pages 160–166, 2002.
- [GLR03] A. Guerraz, C. Loscos, and H. Ritter Widenfeld. How to use physical parameters coming from the haptic device itself to enhance the evaluation of haptic benefits in user interface? In *Eurohaptics'03*, 2003.
- [GW92] J.J. González and G.R. Widmann. Investigations of nonlinearities in the force control of real robots. *IEEE Transactions on Systems, Man, and Cybernetics*, 22(5):1183–1193, 1992.
- [GW95] J.J. González and G.R. Widmann. A force commanded impedance control scheme for robots with hard nonlinearities. *IEEE Transactions on Control Systems Technology*, 3(4):398–408, 1995.
- [GZ88] A. Gomes de S and G. Zachmann. Integrating virtual reality for virtual prototyping. In *Proceedings of the ASME Design Engineering Technical Conference*, 1988.
- [HACH⁺04] V. Hayward, O.R. Astley, M. Cruz-Hernandez, D. Grant, and G. Robles-De-La-Torre. Haptic interfaces and devices. *Sensor Review*, 24(1):16–29, 2004.
- [Han02] Hansen2002. *Controlled Mechanical Systems with Friction*. PhD thesis, Technische Universiteit Eindhoven, 2002.
- [Has01] C.J. Hasser. *The Effects of Displacement Quantization and Zero-Order Hold on the Limit Cycle Behavior of Haptic Knobs*. PhD thesis, Department of Mechanical Engineering, Stanford University, 2001.
- [Hay96] O.R. Hayward, V. Astley. Performance measures for haptic interfaces. In G. Giralt and G. Hirzinger, editors, *Robotics Research: The 7th International Symposium*, pages 195–207. Springer, 1996.
- [HCH97] V. Hayward and M. Cruz-Hernández. Parameter sensitivity analysis for design and control of tendon transmissions. In O. Khatib and J.K. Salisbury, editors, *Experimental Robotics IV*, volume 223 of *Lecture Notes in Control and Information Science*, pages 241–252. Springer, 1997.

- [HCT⁺] J.M. Hollerbach, E. Cohen, E. Thompson, W.B. Freier, D.E. Johnson, A. Nahvi, D.D. Nelson, T.V. Thompson II, and S.C. Jacobsen. Haptic interfacing for virtual prototyping of mechanical CAD designs. In *ASME Design for Manufacturing Symposium*. CDROM proceedings.
- [HGG⁺98] V. Hayward, P. Gregorio, S. Greenish, M. Doyon, L. Lessard, J. McDougall, I. Sinclair, S. Boelen, X. Chen, J.-P. Demers, and J. Poulin. Freedom-7: A high fidelity seven axis haptic device with application to surgical training. In A. Casals and A.T. de Almeida, editors, *Experimental Robotics V*, Lecture Notes in Control and Information Sciences 232, pages 445–456. Springer, 1998.
- [HHB92] J. Hollerbach, I. Hunter, and J. Ballantye. A comparative analysis of actuator technologies for robotics. In O. Khatib, J. Craig, and T. Lozano-Perez, editors, *The Robotics Review 2*, pages 299–342. MIT Press, 1992.
- [HHM04] J.P. Hauschild, G. Heppler, and J. McPhee. Friction compensation of harmonic drive actuators. In *Proceedings of the 6th International Conference on Dynamics and Control of Systems and Structures in Space*, pages 683–692, 2004.
- [Hir05] S. Hirche. *Haptic Telepresence in Packet Switched Communication Networks*. PhD thesis, Lehrstuhl für Steuerungs- und Regelungstechnik, Technische Universität München, 2005.
- [HK00] K.-S. Hong and J.-G. Kim. Manipulability analysis of a parallel machine tool: application to optimal link length design. *Journal of Robotic Systems*, 17(8):403–415, 2000.
- [HL92] I.W. Hunter and S. Lafontaine. A comparison of muscle with artificial actuators. In *5th Technical Digest of the IEEE Solid-State Sensor and Actuator Workshop*, pages 178–185, 1992.
- [Hog85] N. Hogan. Impedance control: an approach to manipulation: part I-theory; part II-implementation; part III-applications. *ASME Journal of Dynamic Systems, Measurement, and Control*, 107(1):1–24, 1985.
- [Hog89] N. Hogan. Controlling impedance at the man/machine interface. In *Proceedings of the IEEE International Conference on Robotics & Automation*, pages 1626–1631, 1989.
- [Hol84] J.M. Hollerbach. Optimum kinematic design for a seven degree of freedom manipulator. In *2nd International Symposium of Robotics Research*, pages 215–222, 1984.
- [Hol02] J.M. Hollerbach. Locomotion interfaces. In K.M. Stanney, editor, *Handbook of Virtual Environments: Design, Implementation, and Applications*, chapter 11, pages 239–254. Lawrence Erlbaum Associates, 2002.
- [HR02] B. Hannaford and J.-H. Ryu. Time-domain passivity control of haptic interfaces. *IEEE Transactions on Robotics and Automation*, 18(1):1–10, 2002.

- [HRS02] J. Hoogen, R. Riener, and G. Schmidt. Control aspects of a robotic haptic display for kinesthetic knee joint simulation. *IFAC Journal on Control Engineering Practice*, 10(11):1301–1308, 2002.
- [HS85] J. Hollerbach and K. Suh. Redundancy resolution of manipulators through torque optimization. In *Proceedings of the IEEE International Conference on Robotics & Automation*, pages 1016–1021, 1985.
- [HS90] D.P. Hess and A. Soom. Friction at a lubricated line contact operating at oscillating sliding velocities. *Journal of Tribology*, 112(1):147–152, 1990.
- [HSAS⁺] G. Hirzinger, N. Sporer, A. Albu-Schäffer, M. Hähle, R. Krenn, A. Pascucci, and M. Schedl. DLR’s torque-controlled light weight robot iii - are we reaching the technological limits now? In *Proceedings of the IEEE International Conference on Robotics & Automation*, pages 1710–1716.
- [HT95] R. Hooper and D. Tesar. Motion coordination based on multiple performance criteria with a hyper-redundant serial robot example. In *Proceedings of the IEEE International Symposium on Intelligent Control*, pages 133–138, 1995.
- [HZS01] K. Hashtrudi-Zaad and S.E. Salcudean. Analysis of control architectures for teleoperation systems with impedance/admittance master and slave manipulators. *International Journal of Robotics Research*, 20(6):419–445, 2001.
- [Iwa93] H. Iwata. Pen-based haptic virtual environment. In *Proceedings of the IEEE Virtual Reality Annual International Symposium*, pages 287–292, 1993.
- [JGB73] V.I. Johannes, M.A. Green, and C.A. Brockley. The role of the rate of application of the tangential force in determining the static friction coefficient. *Wear*, 24(5):381–385, 1973.
- [JH92] L.A. Jones and I.W. Hunter. Human operator perception of mechanical variables and their effects on tracking performance. In *Proceedings of the Winter Annual Meeting of the American Society of Mechanical Engineers: Dynamic Systems and Control, DSC-42*, pages 49–53, 1992.
- [JKID90] S.C. Jacobsen, H. Ko, E.K. Iversen, and C.C. Davis. Control strategies for tendon-driven manipulators. *IEEE Control Systems Magazine*, 10(2):23–28, 1990.
- [JL92] C.T. Johnson and R.D. Lorenz. Experimental identification of friction and its compensation in precise, position controlled mechanisms. *IEEE Transactions on Industry Applications*, 28(6):1392–1398, 1992.
- [Jon89] L.A. Jones. Matching forces: constant errors and differential thresholds. *Perception*, 18(5):681–687, 1989.
- [JS02] M. Jungmann and H.F. Schlaak. Miniaturised electrostatic tactile display with high structural compliance. In *Eurohaptics’02*, 2002.

- [JSBI91] S. Jacobsen, F. Smith, D. Backman, and E. Iversen. High performance, high dexterity, force reflecting teleoperator II. In *ANS Topical Meeting on Robotics and Remote Systems*, 1991.
- [Kam03] P. Kammermeier. *Verteilte taktile Stimulation zur Vermittlung mechanischer Berührungsinformation in Telepräsenzanwendungen*. PhD thesis, Lehrstuhl für Steuerungs- und Regelungstechnik, Technische Universität München, 2003.
- [Kar85] D. Karnopp. Computer simulation of stick-slip friction in mechanical dynamic systems. *ASME Journal of Dynamic Systems, Measurement and Control*, 107(1):100–103, 1985.
- [KBS03] S. Kim, J.J. Berkley, and M. Sato. A novel seven degree of freedom haptic device for engineering design. *Virtual Reality*, 6(4):217–228, 2003.
- [KcC⁺04] U. Kühnappel, H.K. Çakmak, B. Chantier, H. Maaß, G. Strauss, C. Trantakis, E. Novatius, J. Meixensberger, K. Lehmann, H. Buhr, M. Lawo, and G. Bretthauer. HapticIO: haptic interface-systems for virtual-reality training in minimally-invasive surgery. In *Proceedings of Internationale Statustagung Virtuelle und Erweiterte Realität*, 2004.
- [KD02] A.E. Kirkpatrick and S.A. Douglas. Application-based evaluation of haptic interfaces. In *Proceedings of the 10th Symposium on Haptic Interfaces for Virtual Environments and Teleoperator Systems*, pages 32–39, 2002.
- [KD05] C.W. Kennedy and J.P. Desai. Modeling and control of the Mitsubishi PA-10 robot arm harmonic drive system. *IEEE/ASME Transactions on Mechatronics*, 10(3):263–274, 2005.
- [KDLS90] K. Kreutz-Delgado, M. Long, and H. Seraji. Kinematic analysis of 7 dof anthropomorphic arms. In *Proceedings of the IEEE International Conference on Robotics & Automation*, pages 824–830, 1990.
- [KG97] N.M. Kircanski and A.A. Goldenberg. An experimental study of nonlinear stiffness, hysteresis, and friction effects in robot joints with harmonic drives and torque sensors. *The International Journal of Robotics Research*, 16(2):214–239, 1997.
- [KH83] C.A. Klein and C.-H. Huang. Review of pseudoinverse control for use with kinematically redundant manipulators. *IEEE Transactions on Systems, Man, and Cybernetics*, SMC-13(3):245–250, 1983.
- [KH94] H. Kazerooni and M.-G. Her. The dynamics and control of a haptic interface device. *IEEE Transactions on Robotics and Automation*, 10(4):453–464, 1994.
- [Kha95] O. Khatib. Inertial properties in robotic manipulation: an object-level framework. *The International Journal of Robotics Research*, 13(1):19–36, 1995.

- [Kim05] C.-H. Kim. Entwurf und Bewertung von modellbasierten Admittanzreglern für das haptische Display ViSHARD6. Diplomarbeit, Fachgebiet für Regelungssysteme, Technische Universität Berlin, 2005.
- [KKO94] K. Kaneko, K. Komoriya, and K. Ohnishi. Manipulator control based on a disturbance observer in the operational space. In *Proceedings of the IEEE International Conference on Robotics & Automation*, pages 902–909, 1994.
- [KLLK05] Y.S. Kim, J. Lee, S. Lee, and M. Kim. A force reflected exoskeleton-type masterarm for human-robot interaction. *IEEE Transactions on System, Man and Cybernetics, Part A*, 35(2):198–212, 2005.
- [Koe04] H. Koenen. Leichtbau bei spielfreien Getrieben. In R. Slatter, editor, *Leichtbau in der Antriebstechnik*, chapter 4, pages 63–101. Shaker, Aachen, 2004.
- [Kro04a] A. Kron. *Beiträge zur bimanuellen und mehrfingerigen haptischen Informationsvermittlung in Telepräsenzsystemen*. PhD thesis, Lehrstuhl für Steuerungs- und Regelungstechnik, Technische Universität München, 2004.
- [Kro04b] J.-P. Kropp. Optimierung von Leichtbaugetrieben. In R. Slatter, editor, *Leichtbau in der Antriebstechnik*, chapter 5, pages 103–117. Shaker, Aachen, 2004.
- [KW00] D.-S. Kwon and K.Y. Woo. Control of the haptic interface with friction compensation and its performance evaluation. In *Proceedings of the IEEE/RSJ International Conference on Intelligent Robots and Systems*, pages 955–960, 2000.
- [LA92] S. Luo and S. Ahmad. Predicting the drift motion for kinematically redundant robots. *IEEE Transactions on Systems, Man, and Cybernetics*, 22(4):717–728, 1992.
- [Law93] D.A. Lawrence. Stability and transparency in bilateral teleoperation. *IEEE Transactions on Robotics and Automation*, 9(5):624–637, 1993.
- [LC94] D.A. Lawrence and J.D. Chapel. Performance trade-offs for hand controller design. In *Proceedings of the IEEE International Conference on Robotics & Automation*, pages 3211–3216, 1994.
- [LD03] S.D. Laycock and A.M. Day. Recent developments and applications of haptic devices. *Computer Graphics Forum*, 22(2):117–132, 2003.
- [LGZY01] L. Li, W.A. Gruver, Q. Zhang, and Z. Yang. Kinematic control of redundant robots and the motion optimizability measure. *IEEE Transactions on Systems, Man, and Cybernetics*, 31(1):155–160, 2001.
- [LH74] C.L. Lawson and R.J. Hanson. *Solving Least Squares Problems*. Prentice-Hall, Inc., Englewood Cliffs, New Jersey, 1974.
- [Lié77] A. Liégeois. Automatic supervisory control of the configuration and behaviour of multibody mechanisms. *IEEE Transactions on Systems, Man, and Cybernetics*, 7(12):868–871, 1977.

- [LKCC91] K.F. Laurin-Kovitz, J.E. Colgate, and S.D.R. Carnes. Design of components for programmable passive impedance. In *Proceedings of the IEEE International Conference on Robotics & Automation*, pages 1476–1481, 1991.
- [LSAB02] V. Lampaert, J. Swevers, and F. Al-Bender. Modification of the Leuven integrated friction model structure. *IEEE Transactions on Automatic Control*, 47(4):683–687, 2002.
- [Mar05] J. Martins, J. Savall. Mechanisms for haptic torque feedback. In *Proceedings of the First Joint Eurohaptics Conference and Symposium on Haptic Interfaces for Virtual Environment and Teleoperator Systems*, pages 611–614, 2005.
- [MB86] J.A. Maples and J.J. Becker. Experiments in force control of robotic manipulators. In *Proceedings of the IEEE International Conference on Robotics & Automation*, pages 695–702, 1986.
- [MFAB05] S. Marcheschi, A. Frisoli, C.A. Avizzano, and M. Bergamasco. A method for modeling and control complex tendon transmissions in haptic interfaces. In *Proceedings of the IEEE International Conference on Robotics & Automation*, pages 1785–1790, 2005.
- [MH95] F. Mougnet and V. Hayward. Limit cycle characterization, existence and quenching in the control of a high performance hydraulic actuator. In *Proceedings of the IEEE International Conference on Robotics & Automation*, pages 2218–2223, 1995.
- [Moc04] N. Mock. Design eines haptisches Eingabegerätes mit redundanten Freiheitsgraden. Studienarbeit, Fachgebiet für Regelungssysteme, Technische Universität Berlin, 2004.
- [Moc05] N. Mock. Entwurf und Implementierung einer Admittanzregelung für ein hyper-redundantes haptisches Eingabegerät. Diplomarbeit, Fachgebiet für Regelungssysteme, Technische Universität Berlin, 2005.
- [Mor96] J.B. Morrell. Parallel coupled micro-macro actuators. Technical Report AITR-1563, Artificial Intelligence Laboratory, Massachusetts Institute of Technology, 1996.
- [MOSo90] J.A.C. Martins, J.T. Oden, and F.M.F Simões. A study of static and kinetic friction. *International Journal of Engineering Science*, 28(1):29–92, 1990.
- [MPM99] C. Mavroidis, C. Pfeiffer, and M. Mosley. Conventional actuators, shape memory alloys, and electrorheological fluids. In Y. Bar-Cohen, editor, *Automation, Miniature Robotics, and Sensors for Nondestructive Evaluation and Testing*, pages 189–214. The American Society for Nondestructive testing, Inc. (ASNT), 1999.
- [MS94] T.H. Massie and J.K. Salisbury. The PHANTOM haptic interface: a device for probing virtual objects. In *Proceedings of the ASME Winter Annual Meeting, Symposium on Haptic Interfaces for Virtual Environment and Teleoperator Systems, DSC-55-1*, pages 295–300, 1994.

- [MVA⁺04] J.D.W. Madden, N.A. Vandersteeg, P.A. Anquetil, P.G.A. Madden, A. Takshi, R.Z. Pytel, S.R. Lafontaine, P.A. Wieringa, and I.W. Hunter. Artificial muscle technology: physical principles and naval prospects. *IEEE Journal of Oceanic Engineering*, 29(3):706–728, 2004.
- [Nak91] Y. Nakamura. *Advanced Robotics - Redundancy and Optimization*. Addison-Wesley, 1991.
- [Nem97] B. Nemeč. Pseudoinverses and null space velocity controller. In *IEEE International Conference on Intelligent Engineering Systems*, pages 107–111, 1997.
- [Nit06] N. Nitzsche. *Weiträumige Telepräsenz: Uneingeschränkte Fortbewegung und haptische Interaktion*. PhD thesis, Lehrstuhl für Steuerungs- und Regelungstechnik, Technische Universität München, 2006.
- [NS01] N. Niksefat and N. Sepehri. Designing robust force control of hydraulic actuators despite system and environmental uncertainties. *IEEE Control Systems Magazine*, 21(2):66–77, 2001.
- [NSV99] C. Natale, B. Siciliano, and L. Villani. Spatial impedance control of redundant manipulators. In *Proceedings of the IEEE International Conference on Robotics & Automation*, pages 1788–1793, 1999.
- [Or96] H. Olsson and K.J. Åström. Observer-based friction compensation. In *Proceedings of the 35th IEEE Conference on Decision and Control*, pages 4345–4350, 1996.
- [OrC⁺98] H. Olsson, K.J. Åström, C. Canudas de Wit, M. Gäfert, and P. Lischinsky. Friction models and friction compensation. *European Journal of Control*, 3:176–195, 1998.
- [PB97] G.M. Prisco and M. Bergamasco. Dynamic modelling of a class of tendon driven manipulators. In *Proceedings of the 8th International Conference on Advanced Robotics*, pages 893–899, 1997.
- [Pee03] A. Peer. Modellierung und Regelung eines Force-Feedback Aktuators für Steer-by-Wire Systeme. Diplomarbeit, Lehrstuhl für Steuerungs- und Regelungstechnik, Technische Universität München, 2003.
- [PKAS⁺01] C. Preusche, R. Koeppel, A. Albu-Schäffer, M. Hähle, N. Sporer, and G. Hirzinger. Design and haptic control of a 6 dof force-feedback device. In *Proceedings of the Workshop on Advances in Interactive Multimodal Telepresence Systems*, 2001.
- [PPBD06] A. Pillarisetti, M. Pekarev, A.D. Brooks, and J.P. Desai. Evaluating the role of force feedback for biomanipulation tasks. In *Proceedings of the 14th International Symposium on Haptic Interfaces for Virtual Environment and Teleoperator Systems*, pages 11–18, 2006.

-
- [PUB06] A. Peer, U. Unterhinninghofen, and M. Buss. Tele-assembly in wide remote environments. In *Proceedings of the 2nd International Workshop on Human-Centered Robotic Systems*, pages 75–80, 2006.
- [PW95] G. Pratt and M. Williamson. Series elastic actuators. In *Proceedings of the IEEE/RSJ International Conference on Intelligent Robots and Systems*, pages 399–406, 1995.
- [QD92a] H.P. Qian and J. De Schutter. Introducing active linear and nonlinear damping to enable stable high gain force control in case of stiff contact. In *Proceedings of the IEEE International Conference on Robotics & Automation*, pages 1374–1379, 1992.
- [QD92b] H.P. Qian and J. De Schutter. The role of damping and low pass filtering in the stability of discrete time implemented robot force control. In *Proceedings of the IEEE International Conference on Robotics & Automation*, pages 1368–1373, 1992.
- [QD92c] H.P. Qian and J. De Schutter. Stabilizing robot force control through low pass filtering with low cut off frequency. In *Proceedings of the 31th Conference on Decision and Control*, pages 1893–1896, 1992.
- [RC81] M.H. Raibert and J.J. Craig. Hybrid position/force control of manipulators. *ASME Journal of Dynamic Systems, Measurement, and Control*, 103(2):126–133, 1981.
- [RC99] P. Richard and P. Coiffet. Dextrous haptic interaction in virtual environments: human performance evaluations. In *Proceedings of the 8th IEEE International Workshop on Robot and Human Interaction*, pages 315–320, 1999.
- [Rea94] M.C. Readman. *Flexible Joint Robots*. CRC Press, Boca Raton, 1994.
- [RHMS99] J. Rosen, B. Hannaford, P. MacFarlane, and M.N. Sinanan. Force controlled and teleoperated endoscopic grasper for minimally invasive surgery - experimental performance evaluation. *IEEE Transactions on Biomedical Engineering*, 46(10):1212–1221, 1999.
- [Rim04] D. Rimmelspacher. Entwurf eines adaptiven Verfahrens zur Reibungskompensation von Harmonic Drive Getrieben für das haptische Display VISHARD3. Studienarbeit, Fachgebiet für Regelungssysteme, Technische Universität Berlin, 2004.
- [RN76] R.S.H. Richardson and H. Nolle. Surface friction under time-dependent loads. *Wear*, 37(1):87–101, 1976.
- [Rob00] D.W. Robinson. *Design and Analysis of Series Elasticity in Closed-Loop Actuator Force Control*. PhD thesis, Massachusetts Institute of Technology, 2000.

- [ROC97] C. Richard, A.M. Okamura, and M.R. Cutkosky. Getting a feel for dynamics: using haptic interface kits for teaching dynamics and control. In *ASME IMECE 6th Annual Symposium on Haptic Interfaces*, Dallas, Texas, 1997.
- [Ros95] T. Rosenbauer. *Getriebe für Industrieroboter: Beurteilungskriterien, Kenndaten, Einsatzhinweise*, volume 32 of *Berichte aus der Produktionstechnik*. Shaker Verlag, Aachen, 1995.
- [RPH85] R.K. Roberts, R.P. Paul, and B.M. Hillberry. The effect of wrist force sensor stiffness on the control of robot manipulators. In *Proceedings of the IEEE International Conference on Robotics & Automation*, pages 269–274, 1985.
- [SAB05a] W. Symens and F. Al-Bender. Dynamic characterization of hysteresis elements in mechanical systems. I. Theoretical analysis. *CHAOS*, 15(013105), 2005.
- [SAB05b] W. Symens and F. Al-Bender. Dynamic characterization of hysteresis elements in mechanical systems. II. Experimental validation. *CHAOS*, 15(013106), 2005.
- [SABGP00] J. Swevers, F. Al-Bender, C.G. Ganseman, and T. Prajogo. An integrated friction model structure with improved presliding behavior for accurate friction compensation. *IEEE Transactions on Automatic Control*, 45(4):675–686, 2000.
- [Sal80] J.K. Salisbury. Active stiffness control of a manipulator in cartesian coordinates. In *Proceedings of the 19th IEEE Conference on Decision and Control*, pages 95–100, 1980.
- [SB04] B. Stanczyk and M. Buss. Development of a telerobotic system for exploration of hazardous environments. In *Proceedings of the IEEE/RSJ International Conference on Intelligent Robots and Systems*, pages 2532–2537, 2004.
- [Sha88] J.E.E. Sharpe. Technical and human operational requirements for skill transfer in teleoperation. In *Proceedings of the International Symposium on Teleoperation and Control*, pages 175–187, 1988.
- [She92] T.B. Sheridan. *Telerobotics, Automation, and Human Supervisory Control*. MIT Press, 1992.
- [SHH88] A. Sharon, N. Hogan, and D.E. Hardt. High bandwidth force regulation and inertia reduction using a macro/micro manipulator system. In *Proceedings of the IEEE International Conference on Robotics & Automation*, pages 126–132, 1988.
- [SMA95] W. Seyfferth, A.J. Maghzal, and J. Angeles. Nonlinear modeling and parameter identification of harmonic drive robotic transmissions. In *Proceedings of the IEEE International Conference on Robotics & Automation*, pages 3027–3032, 1995.

-
- [SS00] L. Sciavicco and B. Siciliano. *Modelling and Control of Robot Manipulators*. Advanced Textbooks in Control and Signal Processing. Springer, 2nd edition, 2000.
- [Str02] R. Stribeck. Die wesentlichen Eigenschaften der Gleit- und Rollenlager. *Zeitschrift des Vereins deutscher Ingenieure*, 46(38,39):1342–1348, 1432–1437, 1902.
- [Tag97] H.D. Taghirad. On the modelling and identification of harmonic drive systems. Technical Report TR-CIM-97-02, Centre for Intelligent Machines, McGill University, 1997.
- [TB88] H.D. Taghirad and P.R. Bélanger. Robust friction compensator for harmonic drive transmission. In *Proceedings of the IEEE International Conference on Control Applications*, pages 547–551, 1988.
- [TGTC98] M. Turner, D. Gomez, M. Tremblay, and M. Cutkosky. Preliminary tests of an arm-grounded haptic feedback device in telemanipulation. In *Proceedings of the Winter Annual Meeting of the American Society of Mechanical Engineers: Dynamic Systems and Control, DSC-64*, pages 145–149, 1998.
- [Tho99] J.J. Thomsen. Using fast vibrations to quench friction-induced oscillations. *Journal of Sound and Vibration*, 228(5):1079–1102, 1999.
- [TN99] M. Takaiwa and T. Noritsugu. Application of pneumatic parallel manipulator as haptic human interface. In *Proceedings of the IEEE/ASME International Conference on Advanced Intelligent Mechatronics*, pages 185–190, 1999.
- [TNNU98] Y. Tsumaki, H. Naruse, D.N. Nenchev, and M. Uchiyama. Design of a compact 6-dof haptic interface. In *Proceedings of the IEEE International Conference on Robotics & Automation*, pages 2580–2585, 1998.
- [Tol67] D.M. Tolstoi. Significance of the normal degree of freedom and natural normal vibrations in contact friction. *Wear*, 10:199–213, 1967.
- [Tow88] W.T. Townsend. *The effect of transmission design on force-controlled manipulator performance*. PhD thesis, Artificial Intelligence Laboratory, Massachusetts Institute of Technology, 1988. Also available as Massachusetts Institute of Technology, Artificial Intelligence Laboratory Technical Report No. AITR-1054.
- [TPD92] H.Z. Tan, X.D. Pang, and N.I. Durlach. Manual resolution of length, force and compliance. In *Proceedings of the Winter Annual Meeting of the American Society of Mechanical Engineers: Dynamic Systems and Control, DSC-42*, pages 13–18, 1992.
- [TSEC94] H.Z. Tan, M.A. Srinivasan, B. Eberman, and B. Cheng. Human factors for the design of force-reflecting haptic interfaces. In *Proceedings of the Winter Annual Meeting of the American Society of Mechanical Engineers: Dynamic Systems and Control, DSC-55(1)*, pages 353–359, 1994.

- [Tut92] T.D. Tuttle. Understanding and modeling the behavior of a harmonic drive gear transmission. Master's thesis, Artificial Intelligence Laboratory, Massachusetts Institute of Technology, 1992. Also available as Massachusetts Institute of Technology, Artificial Intelligence Laboratory Technical Report No. AITR-1365.
- [UB02] M. Ueberle and M. Buss. Design, control, and evaluation of a new 6 dof haptic device. In *Proceedings of the IEEE/RSJ International Conference on Intelligent Robots and Systems*, pages 2949–2954, 2002.
- [UB06] M. Ueberle and M. Buss. Design and control of a hyper-redundant haptic interface. In M.H. Ang and O. Khatib, editors, *Experimental Robotics IX: The 9th International Symposium on Experimental Robotics*, volume 21 of *Springer Tracts in Advanced Robotics*, pages 523 – 532. Springer, 2006.
- [UMB03] M. Ueberle, N. Mock, and M. Buss. Towards a hyper-redundant haptic display. In *Proceedings of the Workshop on High-fidelity Telepresence and Teleaction, jointly with the conference HUMANOIDS*, Munich, 2003.
- [UMB04] M. Ueberle, N. Mock, and M. Buss. VisHaRD10, a novel hyper-redundant haptic interface. In *Proceedings of the 12th International Symposium on Haptic Interfaces for Virtual Environment and Teleoperator Systems*, pages 58–65, 2004.
- [VAL01] A. Visioli, R. Adamini, and G. Legnani. Adaptive friction compensation for industrial robot control. In *Proceedings of the IEEE/ASME International Conference on Advanced Intelligent Mechatronics*, pages 577–582, 2001.
- [VEF06] M.P. Vitello, M.O. Ernst, and M. Fritschi. An instance of tactile suppression: Active exploration impairs tactile sensitivity for the direction of lateral movement. In *Eurohaptics'06*, pages 351–356, 2006.
- [Vis94] A. Visintin. *Differential Models of Hysteresis*, volume 111 of *Applied Mathematical Sciences*. Springer, 1994.
- [VLFR] R.Q. Van der Linde, P. Lammertse, E. Frederiksen, and B. Ruiters. The HapticMaster, a new high-performance haptic interface. In *Eurohaptics'02*, pages 1–5.
- [Vol90] R.A. Volpe. *Real and Artificial Forces in the Control of Manipulators: Theory and Experiments*. PhD thesis, Robotics Institute, Department of Physics, Carnegie Mellon University, Pittsburgh, PA, USA, 1990.
- [Wam88] C.W. Wampler. Winding number analysis of invertible workspaces for redundant manipulators. *The International Journal of Robotics Research*, 7(5):22–31, 1988.
- [Wam92] C. Wampler. Wrist singularities: theory and practice. In O. Khatib, J. Craig, and T. Lozano-Pérez, editors, *The Robotics Review 2*, pages 173–189. MIT Press, 1992.

-
- [Whi69] D. E. Whitney. Resolved motion rate control of manipulators and human prostheses. *IEEE Transactions on Man-Machine Systems*, MMS-10:47–53, 1969.
- [Whi77] D.E. Whitney. Force feedback control of manipulator fine motions. *ASME Journal of Dynamic Systems, Measurement, and Control*, 99(2):91–97, 1977.
- [Whi85] D.E. Whitney. Historical perspective and state of the art in robot force control. In *Proceedings of the IEEE International Conference on Robotics & Automation*, pages 262–268, 1985.
- [Wil94] R.L. Williams II. Local performance optimization for a class of redundant eight-degree-of-freedom manipulators. In *Proceedings of the IEEE International Conference on Robotics & Automation*, pages 992–997, 1994.
- [WLW⁺05] X. Wang, P.X. Liu, D. Wang, B. Chebbi, and M. Meng. Design of bilateral teleoperators for soft environments with adaptive environmental impedance estimation. In *Proceedings of the IEEE International Conference on Robotics & Automation*, pages 1127–1132, 2005.
- [YJN⁺96] C. Youngblut, R.E. Johnston, S.H. Nash, R.A. Wienclaw, and C.A. Will. Review of virtual environment interface technology. IDA Paper P-3186, Institute for Defense Analysis (IDA), 1996.
- [Yos85a] T. Yoshikawa. Dynamic manipulability of robotic manipulators. *Journal of Robotics Systems*, 2(1):113–124, 1985.
- [Yos85b] T. Yoshikawa. Manipulability of robotic mechanism. *The International Journal of Robotics Research*, 4(5):3–9, 1985.
- [Yos91] T. Yoshikawa. Translational and rotational manipulability of robotic manipulators. In *IECON'91*, pages 1170–1175, 1991.
- [ZD04] W.-H. Zhu and M. Doyon. Adaptive control of harmonic drives. In *Proceedings of the 43rd IEEE Conference on Decision and Control*, pages 2602–2608, 2004.
- [ZKRS02] M. Zinn, O. Khatib, B. Roth, and J.K. Salisbury. A new actuation approach for human friendly robot design. In *Proceedings of the International Symposium of Experimental Robotics*, Santa Angelo d'Ischia, Italy, 2002.